Thesis Submitted for the Degree of

Doctor Of Philosophy

COLLOIDAL GOLD NANOPARTICLES FOR HIGH SENSITIVITY ECL BIOSENSORS: EFFECT OF SIZE AND SHAPE

Author

Anitha Devadoss M.Sc

Supervisors

Prof. Robert J. Forster

Prof. Tia E. Keyes

Dublin City University

Biomedical Diagnostics Institute

School of Chemical Sciences

January 2011

DECLARATION

I hereby certify that this material, which I now submit for assessment on the programme of study leading to the award of Doctor of Philosophy is entirely my own work, that I have exercised reasonable care to ensure that the work is original, and does not to the best of my knowledge breach any law of copyright, and has not been taken from the work of others save and to the extent that such work has been cited and acknowledged within the text of my work.

Signed: _____ Student ID No: _____

Candidate

Date: _____

This thesis is dedicated to my beloved Parents.

ACKNOWLEDGEMENTS

Gratitude is the memory of heart. It is a great pleasure to thank the people who played an important role in my life. First of all, I owe my deepest gratitude to my supervisors Prof. Robert Forster and Prof. Tia Keyes for giving me this wonderful opportunity for stepping into an exciting research field. I would like to extend my special thanks to Robert for his constant encouragement and critical guidance throughout the course of my research work. Many thanks to Prof. Dermot Brougham for his assistance in acquisition of Zeta potential values. I would like to thank Dr. David Tanner and Dr. Calum Dickinson at University of Limerick for their support in recording the TEM images. I would like to extend my sincere thanks to Biomedical Diagnostics Institute for their crucial financial support and excellent research facilities that exposed me to a challenging but an interesting field of biosensors.

Past three years in my life gave me lots of treasurable memories and self-confidence. I would like to thank my best friends Anita, Bincy, Claudio, Colm and Karthika for sharing most of my cheerful as well as gloomy moments and of course their presence and support gave me comfort. I would like to thank Amy and Paolo for their vital support during the early stages of my PhD. Most of the stories I shared with Elaine and Brian during the coffee breaks were memorable. Special thanks to Chuck, Vlad, Robbie, Stephen, Emmet, Lynda, Andrea, Barry, Rajani, Sithara, Cedric, Ram, Lynn, Michele, Gennaro, Suraj, Damien, Rob, Tib, Ciaran, Reena, Dolan, Eoin, Emma, Nikki, Qiang, Zoe, Jammie, Jie, Gavin, Shane, Julie and Brendan. I would also like to thank all the technical staff of BDI and school of chemical sciences for their timely help.

Although the last but not the least, I thank my mom and dad for their everlasting love and affection, which guided and motivated me in all stages of my life. I am grateful to my sister (Ramya), brother-in-law (Promoth) and Sudhagar for their constant encouragement without which my dreams would not have been possible.

CONTENTS

Chapter 3: Colloidal Nanomaterials

Chapter 6: ECL Biosensor for the Detection of NADH

Chapter 7: Conclusions and Future Work

Colloidal Gold Nanoparticles for High Sensitivity ECL Biosensors: Effect of Size and Shape

Anitha Devadoss

Abstract

Electrochemiluminescent metallopolymers of the form $[M(bpy)_2PVP_{10}]^{2+}$, M is osmium or ruthenium, bpy is 2,2'-bipyridyl and PVP is poly-(4-vinylpyridine) have been synthesised. Colloidal gold nanoparticles and nanorods were synthesised using a phase transfer protocol and seed mediated growth techniques, respectively. The diameter of the colloidal gold nanoparticles was tuned from 4 ± 0.5 nm to 12.5 ± 1 nm by varying the reducing agent ($NaBH_4$) concentration from 0.4 M to 0.1 M. The presence of silver nitrate in the growth solution is found to enhance the percentage yield of gold nanorods. The percentage yield increases nearly three-fold with a maximum of 88% being obtained by increasing the concentration of silver nitrate from 60 μM to 300 μM.

Metallopolymer-gold nanocomposites have been synthesised with controlled metal centre: Au NP molar ratio by mixing solutions of 4-(Dimethylamino) pyridine protected gold nanoparticles and a $[Ru(bpy)_2PVP_{10}]^{2+}$ metallopolymer. The impact of changing the gold nanoparticle diameter from 4 ± 0.5 nm to 12.5 ± 1 nm has been investigated. The luminescence of the metallopolymer undergoes static quenching by the metal nanoparticles irrespective of their size. The quenching efficiency increases from 38% to 93% with the nanoparticle diameter at 1:1 volume ratio of Au NP:Ru whilst the size of the quenching sphere remains unaffected with a 75 ± 5 Å radius. Consistent with percolation theory, the conductivity is initially unaffected by nanoparticle incorporation until reaching a certain molar ratio, 4.95×10^{-2}, after which the conductivity increases and reaches its maximum. In contrast to optically driven emission, the electrochemiluminescence intensity of the nanocomposite initially increases as nanoparticles are added before decreasing for the highest loadings. The electrochemiluminescence increases with increasing nanoparticle diameter. The ECL emission intensity of the nanocomposite formed using 12.5 nm particles at

molar ratios between $5x10^{-3}$ and $10x10^{-3}$ is approximately seven fold higher than that found for the parent metallopolymer.

The effect of gold nanorods on optically and electrochemically driven emission of osmium metallopolymer has been investigated. The controlled loading of gold nanorods quenches the luminescence of the Os metallopolymer by a static quenching mechanism. The quenching efficiency is found to be 72% at Au NR:Os molar ratio of 1.5×10^{-3}. The radius of quenching sphere is estimated to be 89Å using Perrin's model. No change in the charge transport rate or the ECL intensity of the metallopolymer is observed, suggesting that the osmium metal centres did not effectively mediate the electron transport. Moreover, it is found that the complete insulation of gold nanorods from electrochemical activity hindered the charge transport through nanocomposite films.

Finally, ECL based detection of reduced nicotinamide adenine dinucleotide (NADH) was demonstrated using electrodes modified with ruthenium metallopolymer nanocomposites formed by incorporating 12.5 nm DMAP-protected gold nanoparticles. A lower limit of detection was achieved using nanocomposite films when compared to the parent metallopolymer. The ECL biosensor developed with the Ru metallopolymer nanocomposite showed a linear response over a wide dynamic range from 1 μM to 1 mM with a detection limit of 10 fM. The ECL biosensor showed a sensitivity of 1 pM. The implications of these findings and the possibility of extending such high sensitivity detection technique for detecting other biologically significant molecules are discussed.

GLOSSARY OF ACRONYMS

Acronym:	**Explanation**
AA:	Ascorbic acid
ABEI:	N-(amino butyl)-N-ethylsoluminol
ACN:	Acetonitrile
AFM:	Atomic force microscopy
Au NP:	Gold Nanoparticles
bpy:	2,2'-bipyridyl
CV:	Cyclic voltammetry
CCD:	Charge-coupled device
C_{16}TAB:	Cetyltrimethyl ammonium bromide
DMAP:	4-(N, N'-Dimethylamino) pyridine
DMF:	Dimethylformamide
D_{CT}:	Charge transfer diffusion coefficient
DMSO-d_6:	N, N'-Dimethylsulfoxide (Deuterated)
DNA:	Deoxyribo nucleic acid
DTB:	Dodecyltrimethyl ammonium bromide
ECL:	Electrochemiluminescence
EDS:	Energy dispersive spectrum
FE-SEM:	Field emission-scanning electron microscopy
FRET:	Fluorescence or Förster resonance energy transfer
GCE:	Glassy carbon electrode
HPLC:	High performance liquid chromatography
ITO:	Indium tin oxide
IHP:	Inner Helmholtz plane

L:	Monodentate ligand
LOD:	Limit of detection
LSPR:	Localised surface plasmon resonance
MLCT:	Metal to ligand charge transfer
MUA:	Mercapto undecanoic acid
MWNTs:	Multiwalled carbon nanotubes
NADH:	Nicotinamide adenine dinucleotide, reduced form
NAD^+:	Nicotinamide adenine dinucleotide, oxidised form
NHS:	N-hydroxysuccinimide
NMR:	Nuclear magnetic resonance
pI:	Isoelectric point
PIGE:	Paraffin-impregnated graphite electrodes
PVP:	Poly (4-vinyl pyridine)
PMMA:	Poly methyl methacrylate
PMT:	Photo multiplier tube
PNIPAAm:	Polymerised N-polyacrylamide
PSS:	Polystyrene sulfonate
PZC:	Potential of zero charge
RuPVP:	$[Ru(bpy)_2PVP_{10}]^{2+}$ metallopolymer
SERS:	Surface enhanced Raman scattering
TCSPC:	Time-correlated single photon counting system
TEM:	Transmission electron microscopy
TOAB:	Tetraoctyl ammonium bromide
TPrA:	Tripropylamine
UV:	Ultraviolet
UCD:	University College Dublin

UPD:	Under potential deposition
Vis:	Visible

Symbols	Explanation	Units
A	Area of the working electrode	cm^2
A_{ec}	Electrochemically active area	-
b	Path length	cm
C^*	Bulk concentration	M
C_{dl}	Double layer capacitance	F
D_{CT}	Charge transfer diffusion coefficient	cm^2s^{-1}
ε	Molar extinction coefficient	$M^{-1}cm^{-1}$
ζ	Zeta potential	mV
η	Viscosity	Kg/s.m
υ	Speed of the particle	cm/s
e^-	Electron	-
E	Electrochemical potential	V
$E^{\circ\prime}$	Standard electrochemical potential	V
E_Q	Luminescence quantum efficiency -	
F	Faraday constant	C
ΔG^o	Gibbs free energy	eV
h	Planck's constant	m^2kgs^{-1}
i	Current	A
i_p	Peak current	A
I_{DA}	Intensity of the donor-acceptor pair	-
I_D	Intensity of the donor alone	-
κ	Relative orientation in space of transition dipoles	-
K_{SV}	Stern-Volmer constant	-
k_{nr}	Rate of non-radiative decay	-
MW	Molecular weight	g/mol

n	Refractive index of the medium	-
n	Number of electrons exchanged	-
N_a	Avogadro number	mol^{-1}
N_{atom}	Number of gold atoms per single nanoparticles	-
N_{moles}	Number of moles of gold	mol
Φ	Luminescence quantum yield	-
Ox	Oxidised species	-
Q_D	Quantum yield of the donor	-
Q	Charge passed in an electrochemical experiment	C
r_{NP}	Radius of nanoparticles	nm
r_{Au}	Radius of gold atom	nm
R	Universal gas constant	$J\ K^{-1}\ mol^{-1}$
Red	Reduced species	-
R_0	Förster distance	nm
Γ	Surface coverage	$mol\ cm^{-2}$
Γ_r	Radiative decay rate	-
τ	Lifetime of Ru/Os metallopolymers	s
T	Temperature	C
υ	Scan rate in a cyclic voltammetry experiment	$mV\ s^{-1}$
V_q	Volume of the sphere of effective quenching	cm^3
X	Initial amount of the gold salt	mg

PUBLICATIONS AND PRESENTATIONS

Peer-Reviewed Journals

- *Anitha Devadoss*, Anna-Maria Spehar-Deleze, David A.Tanner, Paolo Bertoncello, Reena Marthi, Tia E. Keyes, Robert J. Forster, Enhanced Electrochemiluminescence and Charge Transfer through a Metallopolymer- Gold Nanocomposite. ***Langmuir***, **2010**, 26 (3), 2130.

- *Anitha Devadoss*, Calum Dickinson, Tia E. Keyes, Robert, J. Forster, Electrochemiluminescence and charge transport properties of metallopolymer-gold nanocomposites, ***ECS Transactions***, **2010**, 25 (24), 137.

- *Anitha Devadoss*, Calum Dickinson, Tia E. Keyes, Robert, J. Forster, Optimisation of Gold Nanoparticle Size for Enhanced Electrochemiluminescence from Metallopolymer-Nanoparticle Composites, ***Submitted to Analytical Chemistry***.

- Anita Venkatanarayanan, Barry O'Connell, *Anitha Devadoss*, Tia E. Keyes, Robert J. Forster, Potential Modulated Electrochemiluminescence of Ruthenium Metallopolymer Films, ***Submitted to Electrochemistry Communications***.

Oral Presentations

- Electrochemiluminescence and Charge Transport Properties of Metallopolymer-Gold Nanocomposite, *Anitha Devadoss*, Tia E. Keyes, Robert J. Forster, ***216th ECS Meeting***, Vienna- Austria, October, **2009**.

- Nanoparticle-Metallopolymer Nanocomposites for High Brightness Electrochemiluminescence Assays, Robert J. Forster, *Anitha Devadoss*, Anna-Maria Spehar-Deleze, Tia E. Keyes, ***16th International Symposium on Bioluminescence and Chemiluminescence***, Lyon, France, April, **2010**.

- Electrochemiluminescence and Charge Transport Properties of Metallopolymer-Gold Nanocomposites, *Anitha Devadoss*, Tia E. Keyes, Robert J. Forster, ***62nd Irish university chemistry colloquium***, Belfast, Northern Ireland, July, **2010**.

Poster Presentation

- Optimizing Electrochemiluminescence and Charge Transfer Modulations in Metallopolymer-Gold Nanocomposites, *Anitha Devadoss*, Anna-Maria Spehar-Deleze, David A. Tanner, Paolo Bertoncello, Reena Marthi, Tia E. Keyes, Robert J. Forster, ***International workshop on Nanotechnology-enabled sensors & diagnostics,*** Dublin City University, Ireland, June **2009.**

Chapter 1

Literature Review

1.1. Introduction

Due to the increasing challenges in the field of medical sciences, early stage diagnosis is crucial for the successful treatment of many diseases.[1] Biomarkers have been widely in use for early stage detection of bio molecular analytes whose presence in the body indicates a particular disease.[2,3,4] Several diagnostic methods have been developed over the past few decades, however, highly sensitive and selective detection techniques are still needed for the successful detection of ultra-low concentration of disease biomarkers at the early stages of any disease. Various types of detection strategies including optical, electrochemical and mass sensitive detection techniques are commonly used.[5] However, electrochemiluminescence (ECL), an electrochemically-induced process that leads to the generation of light at the electrode surface[6,7] is increasingly gaining attention in the field of biosensors.

ECL has several attractive features such as compatibility with solution phase and thin-film formats, precise control over the time and position of the light emitting reaction, high signal to noise ratio and the possibility to enhance the signals with nanomaterials such as metal nanoparticles and nanotubes. ECL can be more selective than other fluorescence based detection techniques as the change in electrode potential can effectively control the generation of the excited state species. ECL is considered to be a non-destructive technique in most cases as ECL emitters can be regenerated even after the emission.[8] Taken together, these features make ECL a very powerful analytical technique. By employing ECL active species as biological labels, ECL has found applications in immunoassays[9,10,11] and DNA analysis.[12]

The key objective of biosensor research is to develop the low cost biosensors that can attain lower limits of detection. Enhancing the electrochemiluminescence intensity is a significant approach to improving the limits of detection. Polymeric material offer enhanced performance than the monomeric luminophores as the biomolecule label

can contain multiple metal centres and thin films can be formed, which simplifies the assay design and minimises reagent consumption. However, while the redox response associated with the metal centre within a metallopolymer may be ideal, the rate of homogeneous charge transport is generally rather slow and it typically takes tens of seconds to electrolyse a film that is a few hundred nanometres thick.[13]

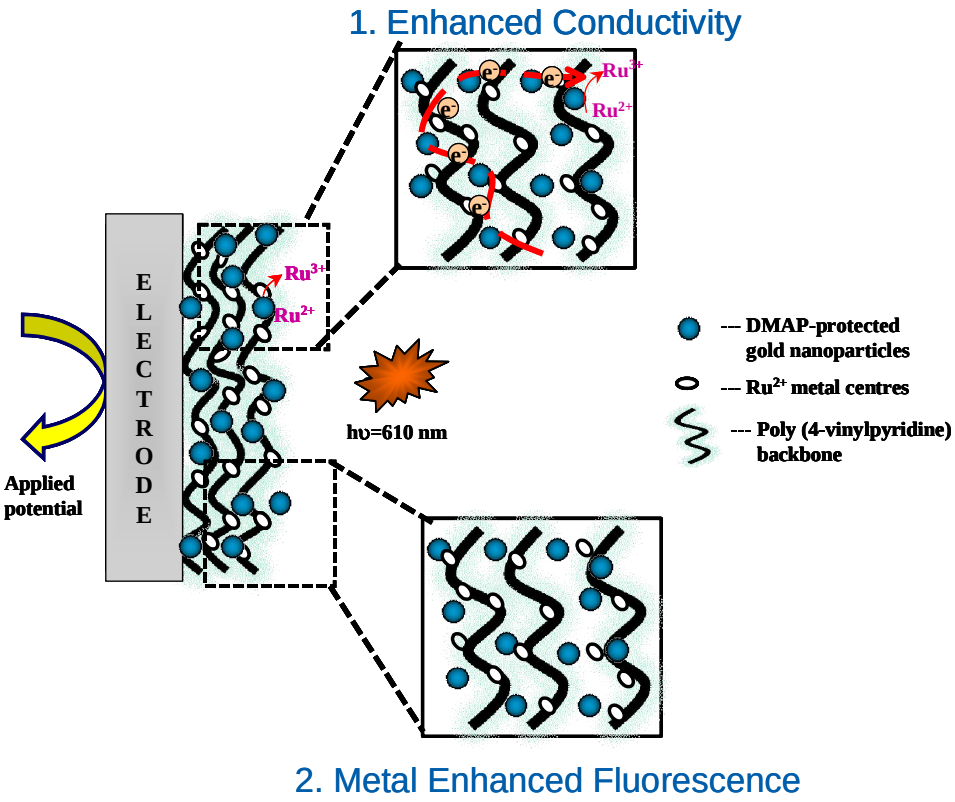

Figure 1.1: Schematic diagram representing the two major possible effects in metallopolymer-gold nanoparticle composite films due to the presence of colloidal gold nanoparticles. Here, ● represents DMAP-protected gold nanoparticles and O represents Ru metal centres conjugated to poly (4-vinylpyridine) backbone. Here, the red coloured dashed line (---) represents the electron transport pathway between randomly distributed gold nanoparticles.

The time taken to electrolyse a film can be expressed using equation (1.1).

$$t = \frac{\delta^2}{\pi D_{CT}} \quad \text{.....(1.1)}$$

where D_{CT} is the rate of homogeneous charge transport, δ is the thickness of the film and t is the time taken to electrolyse the film. Therefore, in order to increase the ECL intensity by immobilising more material on the electrode surface, the rate of charge transport must be increased if a reasonable response time is to be maintained.

One attractive strategy to achieving this goal is to incorporate metallic nanoparticles that could simultaneously increase the film conductivity leading to the electro generation of more luminophores per unit time[14] and perhaps enhancing the emission efficiency through metal enhanced fluorescence effects. Colloidal gold nanoparticles are increasingly gaining interest due to their interesting spectroscopic properties and biocompatibity.[15] The size, shape and distribution of gold nanoparticles play a vital role in determining the performance of the nanocomposite systems.

This thesis specifically focuses on the utilisation of colloidal gold nanostructures for enhancing the sensitivity and selectivity of ECL detection. Figure 1.1 shows the schematic diagram representing two possible major effects due to the presence of colloidal gold nanoparticles that could significantly enhance the ECL emission intensity. As a part of the work, an ECL based biosensor for the detection of reduced nicotinamide adenine dinucleotide (NADH) has been demonstrated.

This thesis is presented in several sections. Chapter 1 is a survey of the relevant literature. Various strategies of synthesising metallopolymers and colloidal gold nanoparticles with various size and shape are described. The generation of enhanced electrochemiluminescence using nanoparticles is reviewed. Finally, the theory behind the major techniques used in the course of the work is described in detail.

Chapter 2 deals with the synthesis and characterisation of ruthenium and osmium containing polypyridyl complexes. In particular, the synthesis of metallopolymers of the form $[M(bpy)_2PVP_{10}](ClO_4)_2$, where M may be Ru or Os, bpy is 2,2'-bipyridyl and PVP is poly(4-vinylpyridine); is described in detail and the spectroscopic and electrochemical properties of monomeric and polymeric ruthenium/osmium polypyridyl complexes are presented.

The synthetic strategies followed to control the size and shape of gold nanoparticles are summarised in Chapter 3. Specifically, the synthesis of size mono dispersed 4-(N, N'-Dimethylamino) pyridine (DMAP)-protected spherical gold nanoparticles with various mean diameters ranging from 4 ± 0.5 nm to 12.5 ± 1 nm is described. The effect of the reducing agent (0.1 to 0.4 M) on the diameter of gold nanoparticles is presented. Cetyl trimethyl ammonium bromide (C_{16}TAB)-protected gold nanorods have been synthesised using seed-mediated growth techniques. An attempt to increase the percentage yield of gold nanorods by altering the synthetic parameters is described. The basic properties and the effect of various synthetic parameters on spherical and rod shaped gold nanoparticles are discussed.

Chapter 4 describes the formation of ruthenium metallopolymer-gold nanoparticle composites. The loading of DMAP-protected gold nanoparticles is controlled and the role of loaded gold nanoparticles on the photo physical and electrochemical properties of the parent metallopolymer are addressed. The influence of the nanoparticle diameter on the rate of charge transport through the metallopolymer films is probed for different sized gold nanoparticles. The optimal size of the dispersed gold nanoparticles and molar ratio of ruthenium metal centres to gold nanoparticles is determined so as to achieve maximum ECL.

The formation of osmium metallopolymer-gold nanorod composites is discussed in Chapter 5. The interaction of the surface capping ligands of gold nanorods with the polymer backbone is analysed using electron microscopy and electrochemical techniques. The significance of the distribution of the gold nanorods and communication between the metallopolymer and the filler nanoparticles are discussed in detail.

Finally, Chapter 6 outlines the application of Ru metallopolymer-gold nanoparticle composites for the ECL based detection of β-nicotinamide adenine dinucleotide (β-NADH). In particular, the effect of enhanced charge transport in metallopolymer nanocomposites on ECL based detection of NADH is described.

1.2. ECL Biosensors

A biosensor can be generally defined as the device that consists of a biological recognition system, often called a bio receptor, and a transducer. The interactions of the analytes with the bio receptor are designed to produce an effect that can be measured by the transducer, which converts the signals into measurable electrical signals.[5] Based on the transduction methods used, biosensors are classified as optical, thermal and electrochemical sensors. Among them, electrochemiluminescence (ECL) has found a wide range of applications in clinical and biomedical diagnostics.[16,17]

Numerous chemical and biochemical analytes can be effectively detected at very low concentrations (pico to femto molar) and over a wide linear range with ECL.[18,19] Luminol and tris (2,2'-bipyridyl) ruthenium (II) ($[Ru(bpy)_3]^{2+}$) are the most commonly used ECL luminophores or labels.[9,20,21] Recently, semiconductor nanocrystals based ECL-generation have gained attention.[22,23] However, the semiconductor nanocrystals are generally toxic and hence may not be suitable for bio related applications.

Amongst various other ECL luminophores, $[Ru(bpy)_3]^{2+}$ is the most widely used for analytical applications due to its ability to produce ECL in aqueous solutions and its good chemical, electrochemical and photochemical stability.[6,24,25] The potential advantage of ECL based detection is that an ECL assay can be designed either as a sandwich assay with two different monoclonal antibodies or as a competiting binding assay with a single antibody. These strategies are commonly used for the detection of several significant biomolecules including enzymes,[26,27] antibody/antigen,[28,29] nucleic acid/DNA,[30] and cellular structures.

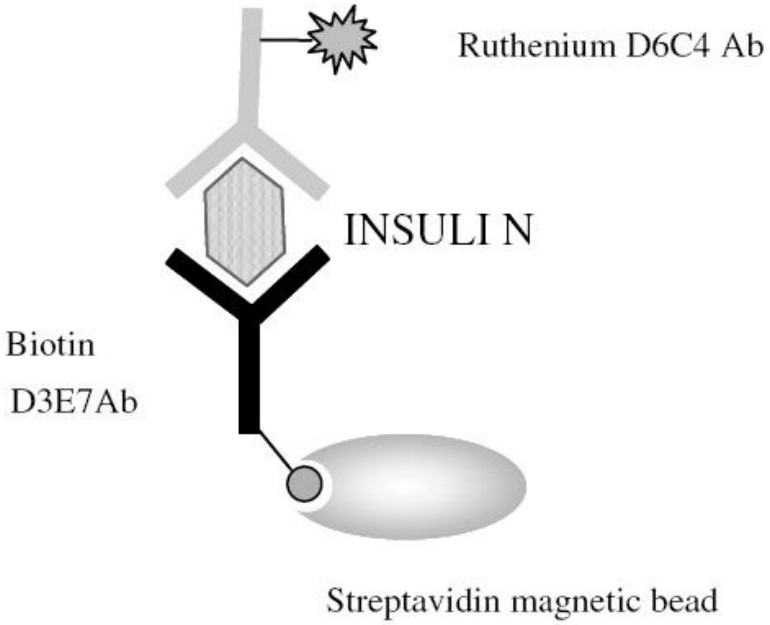

Figure 1.2: Scheme representing electrochemiluminescence based insulin sandwich type immunoassay. Adapted from Rajasree Golla, Ramakrishna Seethala, *A Sensitive, Robust High-Throughput Electrochemiluminescence Assay for Rat Insulin*, J. Biomol Screen, **2004**, 9, 62.

Figure 1.2 shows a typical ECL insulin sandwich immunoassay.[31] Here the $[Ru(bpy)_3]^{2+}$NHS ester was used for labelling a primary amino group of the primary monoclonal antibody and biotin-NHS ester for labelling the secondary antibody. At optimal concentrations, the antibodies bind to insulin and the entire complex is bound to streptavidin-coated magnetic beads. The beads serve as the solid phase through the biotin moiety of the antibody, which gives stability to the entire complex for the washing steps, which are performed to remove the unbounded ruthenium moieties. When the stabilised complex is exposed to tripropyl amine, ECL is generated and the intensity produced provides information on insulin concentration.

However, the general barrier in using $[Ru(bpy)_3]^{2+}$ is the difficulty of immobilising the complex on solid substrates. Recently, considerable efforts have been paid towards the effective immobilisation of $[Ru(bpy)_3]^{2+}$ moieties on solid surface as this could lead to reduced reagent consumption and allow simpler instrumentation. Monolayers of $[Ru(bpy)_3]^{2+}$ have been produced by Langmuir-Blodgett techniques.[32] Also, Meyer *et al* has introduced an additional approach for immobilisation of

ruthenium complexes using sol-gel networks. Indium tin oxide (ITO) electrodes were coated with $[Ru(bpy)_3]^{2+}$ modified polystyrene entrapped in SiO_2 sol-gel.[33] ECL was observed from the ruthenium complex in a silica gel host with gel-entrapped TPA.[34]

Another popular method of immobilising $[Ru(bpy)_3]^{2+}$ is the use of a cation exchange polymer. Bard *et al* has reported that the immobilisation of $[Ru(bpy)_3]^{2+}$ moieties in Nafion increases the concentration of the immobilised luminophores in thin films.[35] Martin and co-workers demonstrated the co-immobilisation of the ruthenium complex in a Nafion polymer along with enzymes.[36] The covalent attachment of the luminophores with the polymer backbone could overcome the difficulty of immobilisation. Due to the presence of a macromolecular polymer backbone, metallopolymers could lend themselves easily to forming thin films that provide greater stability in a wide range of solvents.

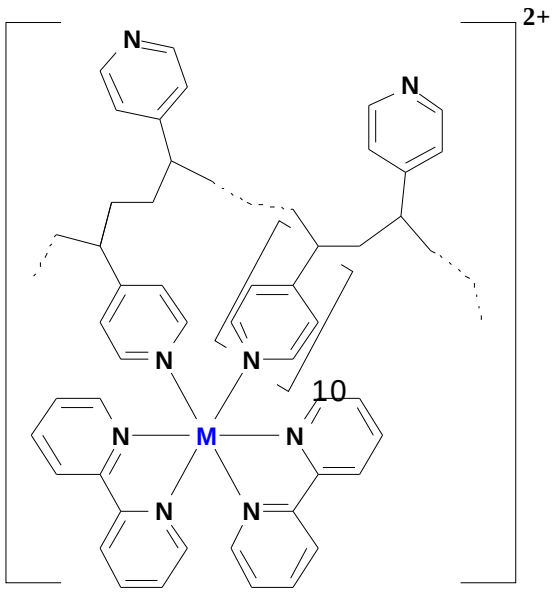

Figure 1.3: Structure of $[M(bpy)_2PVP_{10}](ClO_4)_2$ metallopolymer, where M is ruthenium or osmium, bpy is 2,2'-bipyridyl and PVP is poly(4-vinylpyridine).[37]

Metallopolymers of the form $[M(bpy)_2PVP\ L]^{2+}$, where bpy is 2,2'-bipyridyl, M is ruthenium or osmium, PVP is poly(4-vinylpyridine) and L denotes the ligands attached show interesting photo physical and electrochemical properties. Figure 1.3 shows the structure of $[M(bpy)_2PVP_{10}](ClO_4)_2$ metallopolymer. Ruthenium and osmium-based metallopolymers are the two typical redox polymers that are widely

used in chemical sensors[38,39] because of their electrochemical activities. The spectroscopy and electrochemistry of such metallopolymers can be tuned by the selection of metal centres and ligands conjugated to the polymer backbone.[40]

Achieving lower limits of detection is a significant criterion to improving the sensitivity of biosensors. Several attempts have been made to enhance the emission intensity of the ECL luminophores. Dennany *et al* reported that effective immobilisation of metallopolymers on electrode surface could enhance the ECL emission intensity. It is found that the efficiency of the ECL reaction for the Ru metallopolymer film is almost four times higher than in solution.[37] This could be due to the presence of the polymer matrix that could decrease the rate of radiative decay and also effectively block the access of quencher like molecular oxygen from solution.

Another interesting way to improve the electrochemiluminescence intensity of ECL metallopolymers is by forming nanocomposites by introducing nanoparticles into a metallopolymer matrix. Nanocomposites have gained much attention in the field of biosensors for enhancing the electrochemiluminescence intensity of the ECL luminophores.[27,41] Specifically, gold nanoparticles have been widely used to enhance the ECL intensity of the luminophores for biosensor applications, which are listed and reviewed in Section 1.5.

1.3. Nanocomposites

The integration of polymers and nanoparticles is a promising pathway for manufacturing flexible composites that exhibit advantageous electrical, optical or mechanical properties.[42] The term *nanocomposite* is used if one of the structural units, either the organic or inorganic, is in the size range of 1-100 nm. Examples are the incorporation of inorganic clusters or nanoparticles with special optical, electronic or magnetic properties in polymer matrices. The most obvious advantage of nanocomposites is that they can favourably combine often-dissimilar properties of discrete components in one material.[43] Another driving force in this field is the possibility to create new multifunctional materials that can be easily processed.

General preparative method involves the intimate mixing (self-assembly) of the functional materials (nanoparticles) with a processable matrix (polymer).[44] The capping ligands, size and structure of the nanoparticles play an important role in the nanocomposite because they govern the interaction of the nanoparticles with the polymer backbone.[42] Thus, the self-assembly method is considered to be simple and flexible since the individual components can be tuned separately for achieving the required nanocomposites property.

1.4. Gold Nanoparticles

Plasmonic nanostructures have been used in a wide range of applications such as biological optical imaging,[45,46] sensing applications,[47] optoelectronic nanodevices[48] etc., due to their special properties. The optical properties of these nanostructures are tuneable throughout the visible and near infrared region by tuning the composition, size, shape, aggregation state and the nature of the medium in which they are dispersed. For electroanalytical applications, most attention has been paid to gold nanostructures because of its good biocompatibility, excellent conductivity and excellent stability.[49] Gold nanoparticles can play the following roles in an electrochemical sensing system:

1. Biomolecule immobilisation;
2. Electrochemical catalysis;
3. Electron transfer rate enhancement;
4. Biomolecule tagging

The morphology of the nanoparticles can be controlled by the choice of the synthesis procedure. The synthesis of gold nanoparticles with various size[50] and shape[51,52] has been extensively studied over the past few decades.[53,54,55] Greater attention has been paid to the synthesis of noble metal nanoparticles.[56] In particular, gold nanoparticles are brilliantly coloured due to the localised surface plasmon resonance absorption. The colour of gold nanoparticles depends on the size and shape of the nanoparticles and the dielectric constant of the surrounding medium, leading to many novel studies on their synthesis and applications.[15] As the morphology of the nanoparticles greatly depends on the synthetic procedure, development of improved synthesis protocols is a significant aspect of nanotechnology.[57]

The interaction of nanoparticles with the polymer backbone is influenced by the ligands attached to the nanoparticles. The desired ligands for protecting the nanoparticles can be achieved by the appropriate synthetic procedure. Colloidal gold nanoparticles are widely synthesised via chemical reduction techniques resulting in nucleation and growth of metallic particles in solution including the most common citrate reduction.[57] A two-phase reduction technique has been extensively used for

the generation of very small nanoparticles (1-5 nm) with narrow dispersity. Inverse micelles have also been found to generate nanoparticles with controlled size and shape.[58,59] However, these methods generally suffer from poor monodispersity due to the challenge of initiating and arresting the growth of all the particles at the same time.

The *Brust and Schiffrin method*,[60] a new recipe was developed in the early 1990s to produce metal nanoparticles in organic solvents that are not miscible with water e.g., toluene. Tetraoctyl ammonium bromide (TOAB) in toluene is added to the aqueous solution of gold salt which leads to the phase transfer of gold salt into organic media. Sodium borohydride, a strong reducing agent, is added to the mixture, which leads to the immediate reduction of the gold salt. The organic phase can be separated and washed with dilute sulphuric acid for neutralisation. This method results in gold nanoparticles less than 5-6 nm. Highly monodisperse nanoparticles can be obtained using this approach.

1.4.1. Phase Transfer Protocols

Colloidal nanoparticles are dispersed in a solvent, which can be either water or an organic solvent, depending on the synthetic procedure. Each approach has certain advantages and disadvantages that are summarised in Table 1.1. The ability to disperse gold nanoparticles in various polar and non-polar solvents is governed by the hydrophilic or hydrophobic nature of the capping ligands. The amphiphilic nanoparticles can be dispersed in both kinds of solvents.

Table 1.1: Merits and demerits of aqueous and non-aqueous based gold nanoparticles synthesis.[61]

S.No	Water based gold nanoparticle synthesis	Organic solution based gold nanoparticle synthesis
1	***Advantages:*** Water is a good solvent for a number of metal ions and capping ligands. Reduction of metal ions occurs in a single step.[62]	High concentrations can be achieved with ease. Chemical nature of the nanoparticle surface can be easily constrained.[63]
2	Shape control can be obtained by using suitable micelles.[64,65]	High degree of control over the size and monodispersity.[66]
3	Bio conjugation with DNA,[67] enzymes,[68] etc. may be easily accomplished.	Functionalised nanoparticles can be stored as powder.
4	***Disadvantages:*** Concentration of the nanoparticles is limited due to ionic interactions.	Multi- step process. However, bio conjugation is generally not possible in an organic solvent.

In summary, it is clear that both methods of synthesising gold nanoparticles have characteristic advantages and disadvantages. Based on the application, both methods

can be conveniently used for producing gold nanoparticles using a *phase transfer protocol*. Appropriate selection of hydrophilic or hydrophobic capping ligands results in the transfer of nanoparticles from one medium to another, which is termed as *phase transfer*. Possibly the first report on phase transfer of gold nanoparticles from water to an organic solvent was achieved by transferring the nanoparticles prepared by *Turkevich method*[69] into butyl acetate by complexing with a "comb stabiliser", which is essentially a copolymer consisting of a backbone of methyl methacrylate and glycidyl methacrylate with pendant side chains of poly (12-hydroxstearic acid) present in the organic solvent.

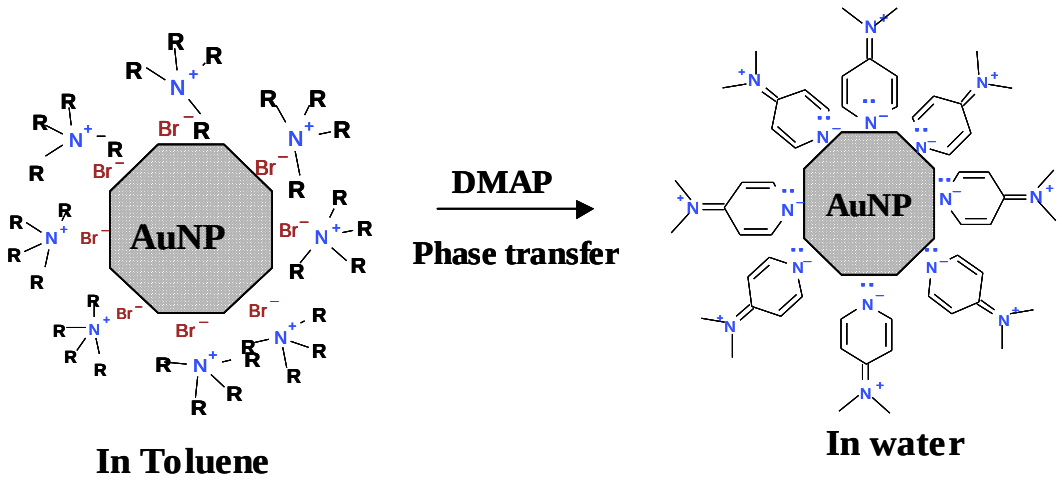

Figure 1.4: Schematic diagram representing the phase transfer of gold nanoparticles from toluene to water by the addition of DMAP. Adapted from David Gittins and Frank Caruso, *Spontaneous Phase Transfer of Nanoparticulate Metals from Organic to Aqueous media*, Angew Chem. Int, **2001**, 40, 3001.

The ligand molecules bound to the nanoparticle surface not only control the growth of the particles during synthesis, but also prevent aggregation of the nanoparticles. The repulsive force between particles can in principle be due to electrostatic repulsion, steric exclusion or a hydration layer on the surface.[15] Depending on the particle system, *i.e.* the core material, and the solvent in which the particles are dispersed, the choice of the right ligands can yield stable particles.[70] For example, hydrophobic ligand molecules prevent the aggregation of the particle cores in organic solvents by covering the nanoparticle surface.

The key point in achieving phase transfer is *via* replacing the hydrophobic group bound to the nanoparticle surface with polar functional groups, thus rendering the nanoparticles water-soluble. Figure 1.4 shows the proposed scheme of phase transfer of gold nanoparticles. Gittins and Caruso demonstrated the synthesis of metal nanoparticles by the phase transfer protocol (toluene to water).[49] In particular, the authors showed that the gold and palladium nanoparticles prepared in toluene by *Brust-Schiffrin method* could be rapidly and effectively phase transferred to water by using aqueous solution of 4-(N,N'-Dimethylamino) pyridine (DMAP).

1.5. Gold Nanorods

Gold nanorods exhibit strong optical absorption at visible and near-infrared regions, which can be tuned based on their dimensions.[54] The localised surface plasmon resonance of gold nanorods has two bands that correspond to the transverse and longitudinal vibrations of electrons at the surface of the nanorods.[71] The existence of longitudinal absorption modes in the longer wavelength region is attractive for forming nanocomposites with osmium-based metallopolymers. As the osmium metallopolymer emits at 760 nm, a well-defined spectral overlap can be achieved between the osmium emission and gold nanorod absorption. This could result in interesting metal enhanced fluorescence effects in the resultant composite system.

Gold nanorods are particularly suitable for photonics, optoelectronic and electrochemical studies due to the strong dependence of the surface plasmon absorption band on the aspect ratio (length of the rod / width of the rod).[72] Due to the recent advances in nanoscience, high-yield synthesis, functionalisation and surface chemistry of gold nanorods are well established.[73,74] The surface plasmon resonance band corresponding to the transverse vibrations is similar to that of spherical gold nanoparticles, which can be observed around 520 nm. The plasmon bands that arises due to the longitudinal vibrations of gold nanorods strongly depend on the aspect ratio of the nanorods.[75] Hence, any change in the dimension of the gold nanorods results in a considerable change in the localised surface plasmon resonance, which can be observed between 600-1000 nm. This is an attractive feature but is difficult to achieve the required monodispersity and control over the length and width. However, monodispersity is essential since even a very small change in size and shape of the nanoparticles can alter the behaviour of the entire system.

Thus, the synthesis of gold nanorods has received much attention because of the existing challenge of increasing monodispersity and total percentage yield. Many groups have reported various methods of producing gold nanorods, including templated synthesis,[76] wet synthesis,[77,78] photochemical[79,80] and electrochemical synthesis at room temperature. Chon *et al* showed that the growth rate of the gold nanorods increases nearly 3 orders of magnitude at 97°C using seedless high temperature synthesis.[81] However, achieving control over the growth of

nanostructures leading to proper dimensional confinement is a challenging task, which can be overcome by introducing templates.[82]

Solution phase preparation of the gold nanorods using surface-capping agents, such as cetyltrimethyl ammonium bromide (C_{16}TAB),[58] hydroxyl amine,[83] tetraoctyl phosphine oxide, oleic acid[84] etc. has been successfully used to obtain rod shaped particles. Among various methods of producing gold nanorods, seed-mediated growth is attractive since the growth of the nanorods can be arrested using surfactants and nanorods with the required aspect ratio can be synthesised with ease and low cost.

1.5.1. Seed-mediated Synthesis

The synthesis of monodispersed gold nanorods in high yield is a challenging task as the formation of spherical gold nanoparticles is thermodynamically more favourable due to the higher surface energy of the spheres. Thus, by attaching surface capping ligands, the surface energy of the nanoparticles can be altered. Hence, an appropriate surface capping ligands is essential for synthesising nanoparticles with various dimentions. The seed mediated synthesis protocol gives fairly monodisperse, high yield (>75%) and stable gold nanorods with different aspect ratios (2-7.5) depending on the synthetic parameters.[85] The seeds serve as the nucleation sites for the anisotropic growth of gold nanorods.[86] In the seed-mediated route, gold seeds of size range 3-4 nm are first synthesised by chemical reduction of a gold salt with a strong reducing agent (sodium borohydride) in the presence of surface capping ligands. These seeds are then added to a solution containing a mixture of metal salt, a weak reducing agent (ascorbic acid) and a surfactant (C_{16}TAB) that acts as a growth-directing agent.

Murphy and co-workers have demonstrated that the tail length of the surfactant is important in controlling the nanorod growth, presumably due to stabilisation of a bilayer on the long faces of gold nanorods.[87] They also reported that the size and nature of the seeds determines the length and thickness and hence the aspect ratio of the resultant nanorods. It has been shown that the kinetics of reduction of gold ions to atomic gold can be controlled by the silver nitrate content.[88] Silver adsorbs selectively to Au {110} facets by underpotential deposition (UPD) and inhibits Au deposition on those surfaces but allows Au deposition on {100} and {111} surfaces, leading to nanorod growth in the {100} direction.[89]

The role of C_{16}TAB on gold nanorod growth has been debated over the past few years.[87,90,91] Recently, it has been reported that the presence of iodide in C_{16}TAB prevents the growth of nanorods as the iodide adsorbs strongly on the surface of the gold and prevents the C_{16}TAB binding and hence hinders nanorod growth.[92] Mulvaney and co-workers has proposed that the growth mechanism invokes the local electric field at the tip of the growing nanorod and C_{16}TAB micelles.[90] It is reported that C_{16}TAB directs the growth by blocking long axis crystal faces, and hence

promotes the metal growth in short axis faces[93] to make nanorods. Moreover, the polar head groups of C_{16}TAB molecules inhibit the attachment of C_{16}TAB to the gold surface and provide aqueous dispersity.

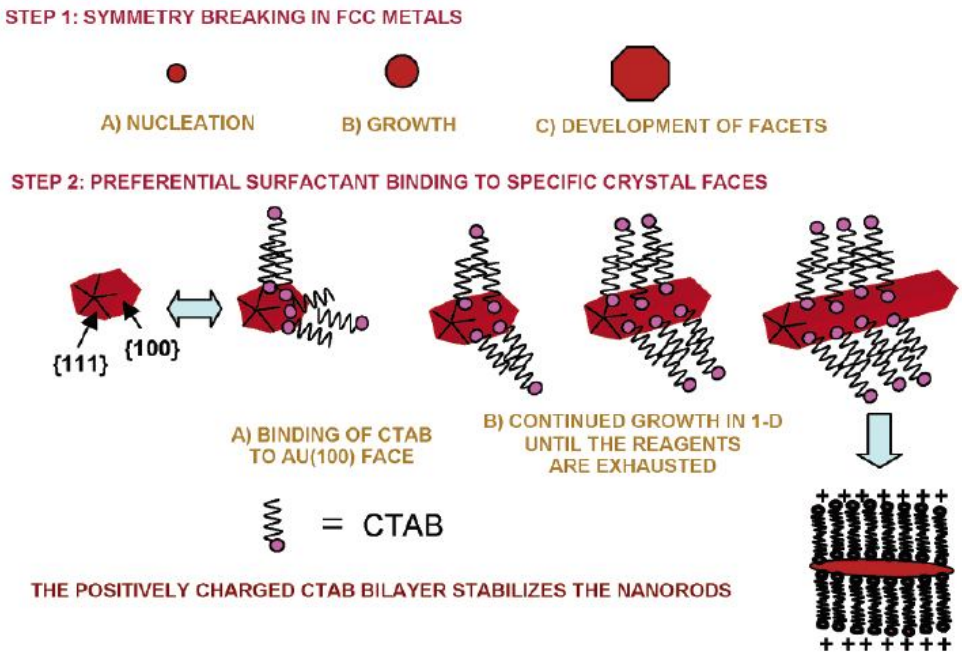

Figure 1.5: Proposed mechanism of surfactant-directed gold nanorod growth. Adapted from Catherine J. Murphy, Tapan K Sau, Anand M Gole, Christopher J Orendorff, Jinxin Gao, Linfeng Gao, Simona E Hunyadi, and Tan Li, *Anisotropic Metal Nanoparticles: Synthesis, Assembly and Optical Applications,* J. Phys. Chem. B, **2005,** *109,* 13857.

Murphy *et al* have postulated a general mechanism that describes the formation of gold nanorods using C_{16}TAB as a soft template.[54] Figure 1.5 shows the mechanism of surfactant assisted seed-mediated growth of gold nanorods. The single crystalline seed particles have facets that are differentially blocked by surfactant (or an initial halide layer that then electrostatically attracts the cationic surfactant). Thus the subsequent addition of metal ions and a weak reducing agent leads to metallic growth at the exposed particle faces. Mulvaney *et al* has reported that the local electric field at the tip of the growing nanorod and CTAB micelles invokes the growth mechanism.[94] Specifically, the model finds that the Au(III) and Au(I) intermediates bind strongly to CTAB micelles, which are carried to the seed particles, and

delivered preferentially at the tips to promote the growth of nanorods instead of nanospheres.

1.6. Gold Nanoparticles in ECL Bioassays

Electrochemical biosensors have been fabricated mostly using metal nanoparticles of various size and shape because of their excellent biocompatibility, good conductivity and higher stability. Due to the higher surface area of the nanoparticles, colloidal gold has been used to enhance the immobilisation of biomolecules on the electrode surface.[95] Moreover, the presence of gold nanoparticles in ECL based sensors/assays can produce lower detection limits by enhancing the ECL emission properties of the luminophores used.[96] This is a significant outcome, as the sensitivity of a biosensor greatly depends on the lower limits of detection (LOD). Lower limits of detection could also facilitate early stage diagnosis, as the concentration of the analytes can be at ultra low levels ($< 10^{-15}$ M).

ECL based detection techniques generally uses ECL active species as the biomarkers. Thus, enhancing the ECL emission intensity of such species could increase the sensitivity of detection by facilitating lower limits of detection. Hence, several works have been devoted to achieving enhanced emission from a wide range of ECL active species including luminol,[97] quantum dots, *monomeric*[98] and polymeric polypyridyl complexes[99] etc. using gold nanoparticles. The surface modification of working electrodes using gold nanoparticles is the most extensively used technique for enhancing the emission properties of ECL moieties.

ECL emission from $[Ru(bpy)_3]^{2+}$ moieties have been investigated from the early 1970s.[100] Wang and co-workers proposed a simplified method of immobilising $[Ru(bpy)_3]^{2+}$ on electrode surface using citrate capped gold nanoparticles.[101] Besides effective immobilisation, this technique also resulted in enhanced ECL emission from the ruthenium moieties due to the presence of gold nanoparticles. Figure 1.6 shows the schematic representation of the preparation process for electrode modification.

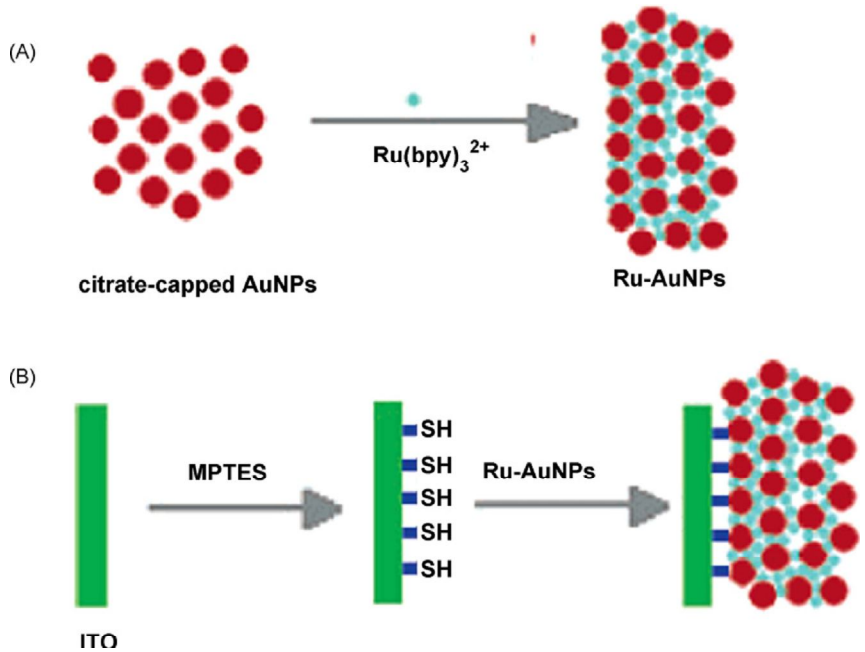

Figure 1.6: Scheme illustrating (A) the formation of Ru-gold nanoparticle composite (Ru-Au NPs) in aqueous medium due to electrostatic interaction between $[Ru(bpy)_3]^{2+}$ and citrate capped gold nanoparticles (Au NPs) and (B) the immobilisation of Ru-Au NPs on the surface of sulfhydryl-derivatised ITO electrode. Reproduced from Xuping Sun, Yan Du, Shaojun Dong, and Erkang Wang, *Method for Effective Immobilization of* $Ru(bpy)_3^{2+}$ *on an Electrode Surface for Solid State Electrochemiluminescence Detection,* Anal. Chem. **2005**, 77, 8166.

Here, the gold nanoparticles act as conducting sites to improve the electron transfer through the film. Hence, the modified electrodes produced an intense ECL signal with tripropyl amine as co-reactant, which was stable for several scans. Later, Dong and co-workers used the same approach to develop an alcohol dehydrogenase biosensor. The alcohol dehydrogenase biosensor displayed a wide linear range, good stability and high sensitivity with a detection limit of 3.33 μM.[102]

Fang *et al* has reported the electrodeposition of $[Ru(bpy)_3]^{2+}$/Chitosan and $[Ru(bpy)_3]^{2+}$/Au NPs/Chitosan composite films on glassy carbon electrodes.[103] As shown in Figure 1.7(A), positively charged $[Ru(bpy)_3]^{2+}$ was adsorbed on the surface of negatively charged gold nanoparticles due to electrostatic interactions. Proton consumption that occurs at the electrode surface during electro deposition alters the

pH close to the electrode surface. At higher pH, the chitosan molecules entrapping the Au NPs-$[Ru(bpy)_3]^{2+}$ deposit on the cathode.

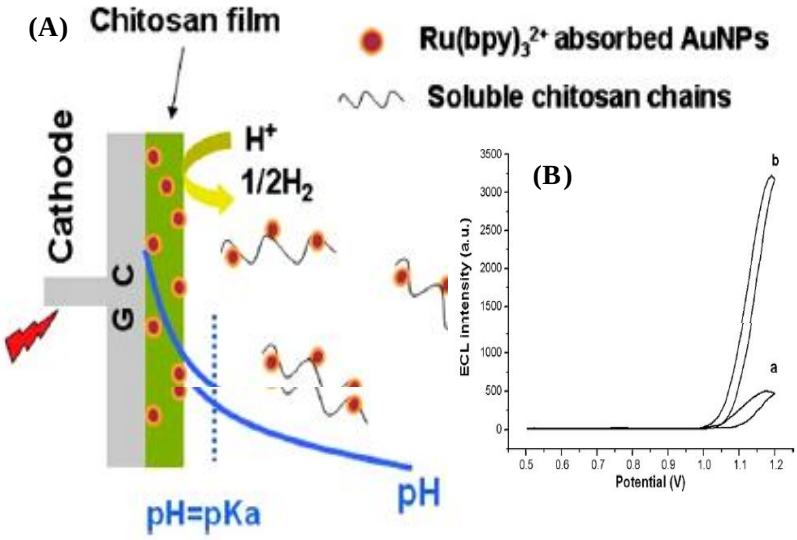

Figure 1.7: (A) Schematic representation of illustration of the electrodeposition of $[Ru(bpy)_3]^{2+}$/Au NPs/Chitosan composite film onto cathode using two electrode systems. (B) ECL curves of $[Ru(bpy)_3]^{2+}$/Chitosan composite film modified electrode (a) and $[Ru(bpy)_3]^{2+}$/Au NPs/Chitosan composite film modified electrode (b) in 0.1 M PBS (pH=7.5) with 1 μM TPrA. Reproduced from Wen Yun, Ying Xu, Ping Dong, Xiongxiong Ma, Pingang He, Yuzhi Fang, *Solid-State Electrochemiluminescence Sensor through the Electrodeposition of* $Ru(bpy)_3^{2+}$ */ AuNP / Chitosan Composite Film onto Electrode,* Anal. Chim. Acta, **2009**, 635, 58.

The ECL activity of the nanocomposite-modified electrodes is shown in the inset to Figure 1.7(B). It has been reported that $[Ru(bpy)_3]^{2+}$/Au NPs/Chitosan nanocomposite films produces ECL nearly 10 times more than the emission intensity of $[Ru(bpy)_3]^{2+}$/Chitosan modified electrodes. It has been reported that the presence of gold nanoparticles enhances the penetration of TPrA molecules from aqueous solution through the porous $[Ru(bpy)_3]^{2+}$/Au NPs/Chitosan composite film to enhance the ECL signal. It is important to consider the possibility of achieving metal enhanced effects due to the presence of gold nanoparticles that could also result in enhanced ECL emission from the nearby luminophore. The nanocomposite-modified electrodes were used to detect lower concentrations of tripropyl amine.[103] A

detection limit of nearly 0.5 nM of TPrA can be achieved in the presence of gold nanoparticles. This approach shows the possibility of using gold nanoparticles for enhancing the detection limit of solid-state ECL sensors that can be extended for the detection of various biomolecules.

A wide range of surface capping ligands can be immobilised on gold nanoparticles that facilitates their binding to solid surfaces. Zu *et al* has reported an attractive and simple method of immobilising gold nanoparticles capped with fluorosurfactant ligands (i.e.; Zonyl FSO) on indium tin oxide (ITO) electrodes.[104] It has been observed that modifying an ITO electrode with 4 nm gold nanoparticles enhances the TPrA oxidation nearly 300 times compared to a bare ITO electrode. Thus, gold nanoparticle modified electrodes can be used for more efficient and flexible ECL analyses.

Gold nanoparticles are also used to enhance the emission properties of various other ECL tags that have been widely used in immunoassays. It has been demonstrated that the sensitivity of ECL signals at electrodes modified with gold nanoparticles was much improved when compared with conventional electrodes. For example, Zhang *et al* reported that the sensitivity of immunoassay can be enhanced nearly 5-fold using a N-(amino butyl)-N-ethylsoluminol (ABEI) luminescent label at a gold nanoparticles modified paraffin-impregnated graphite electrodes (PIGE).[105]

Figure 1.8 shows (a) the cyclic voltammetric response of a bare gold electrode, (b) a PIGE modified electrode and (c) a PIGE electrode modified with gold nanoparticles. The oxidation peak current at +0.5 V increases in sequence from bulk to a bare PIGE electrode and then to a gold nanoparticles modified PIGE electrode. This indicates that the gold nanoparticles on the surface of modified PIGE electrode can catalyse an electrochemically oxidising process of ABEI, which results in enhanced ECL emission. Similarly, gold nanorods are also widely used for biosensor applications because of the higher surface area and longitudinal surface plasmon bands.

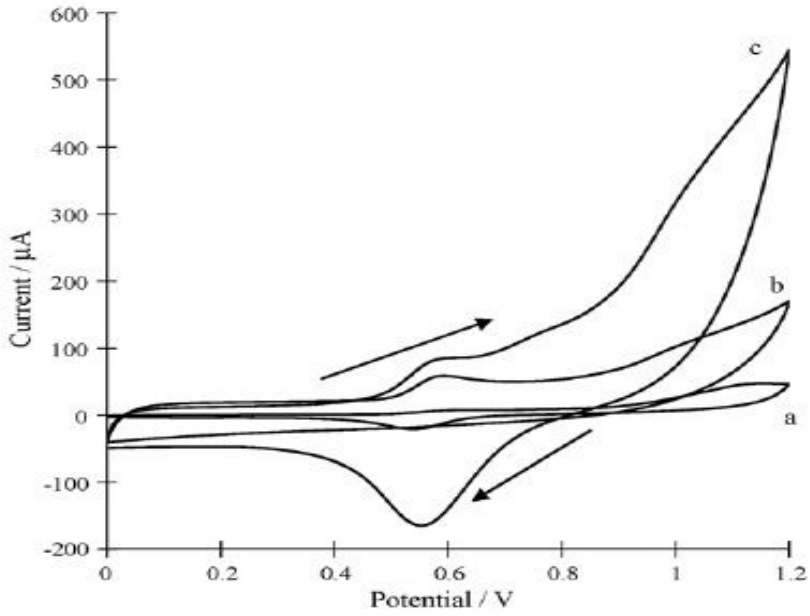

Figure 1.8: Voltammogram of ABEI at a bulk gold electrode (a), at the bare PIGE (b) electrode and at a gold nanoparticles modified PIGE (c) electrode in 0.1 M PBS containing 0.18 mM ABEI. The CVs were recorded at a scan rate of 10 mVs^{-1}. Reprinted from Honglan Qi, Yi Zhang, Yange Peng, and Chengxiao Zhang, *Homogenous Electrogenerated Chemiluminescence Immunoassay for Human Immunoglobulin G using N-(aminobutyl)-N-ethylisoluminol as Luminescence Label at Gold Nanoparticles Modified Paraffin-Impregnated Graphite Electrode*, Talanta, **2008**, 75, 684.

Dong and co workers demonstrated the influence of shape of the nanoparticles over the reaction pathways of generating ECL in the presence of luminol.[106] It has been reported that in AC imedence measurements, electrodes modified with gold nanorods show the smallest diameter from the Nyquist plot when compared to both a bare gold electrode and the electrode modified with spherical gold nanoparticles. The charge transfer rate through the gold nanorod modified electrode is larger than that for the spherical gold nanoparticles modified electrode. As the ECL emission properties greatly depends on charge transfer rates of ECL active species at the electrode surface, nearly 3-4 fold enhancement in the ECL emission of luminol on spherical gold nanoparticles modified gold electrode was achieved in comparison with the bare gold electrode. Whereas, the gold nanorod modified electrode shows nearly three-fold increase in ECL in comparison with gold nanosphere modified electrodes.

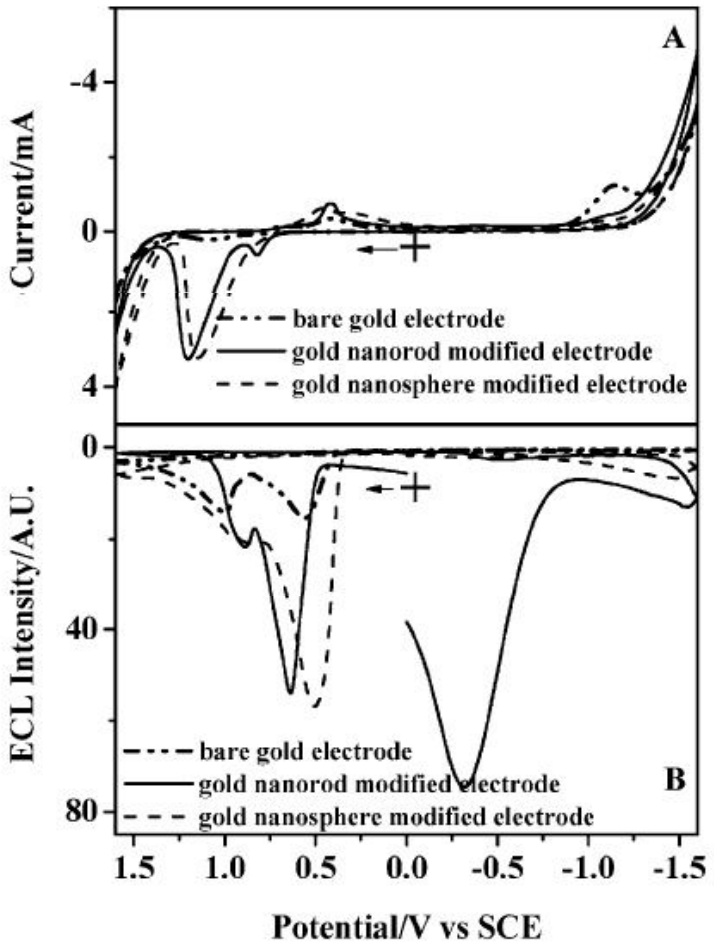

Figure 1.9: (A) CV curves and (B) ECL intensity of luminol on bare gold electrode dashed-dotted-dotted line), a gold nanorod modified electrode (solid line) and a spherical gold nanoparticles modified electrode (dashed line) under air saturated conditions. (KBr, 0.1 M; pH 8; PBS, 0.1 mol/L; luminol, 1 mM; scan rate 40 mV/s). Adapted from Yong-Ping Dong, Hua Cui, and Cheng-Ming Wang, *Electrogenerated Chemiluminescence of Luminol I a Gold Nanorod-Modified Gold Electrode*, J. Phys. Chem. B, **2006**, 110, 18408.

The electrodes were also modified with gold nanorods (aspect ratios 3.2 ± 0.5 and 7.5 ± 1.1) in order to study the influence of shape of the nanoparticles on the ECL emission characteristics. Figure 1.9 shows the ECL response of luminol observed at the bare gold electrode (-••-) and for electrodes modified with spherical gold nanoparticles (---) and gold nanorods (—), respectively. It has been observed that the ECL response of gold nanorods showed similar behaviour as that observed for spherical gold nanoparticles modified electrodes. Significantly, the emission

intensities of the ECL peaks were enhanced nearly 2-10 fold at an electrode modified with gold nanorods, which is nearly thrice the intensity observed for spherical gold nanoparticles.[109]

Moreover, a new ECL emission peak has been observed at –0.28 V (*vs* SCE) only for electrodes modified with gold nanorods in both neutral and alkaline solutions and the emission intensity enhanced with increase in pH. The generation of the ECL peak at –0.28 V is likely due to the reaction of the luminol anion (LH^-) with various electrogenerated species such as OOH^- and $Br_2^{\bullet-}$.[106] Hence, a new reaction pathway has been proposed which is related to LH^-, $Br_2^{\bullet-}$ and $O_2^{\bullet-}$.[107,108] They also suggested the gold nanorods play a significant role in stabilising $Br_2^{\bullet-}$ and $O_2^{\bullet-}$ and hence the shape of the gold nanoparticles plays a vital role in ECL generation.

The ultimate goal of achieving enhanced ECL emission is to develop clinical assays capable of detecting disease biomarkers within the human body. Examples of potential bio molecular analytes include hormones, proteins secreted by cancer cells, enzymes, antibodies generated through the immune system. The detection of such biomolecular analytes using ECL based assays requires higher sensitivity and lower detection limits. Clinical applications of ECL detection can be achieved by detecting either the label or co-reactant concentration that is related to the analyte concentration.[12]

ECL detection of DNA hybridisation shows a very high sensitivity and such reactions can be controlled and manipulated by the applied potential.[109] Bard *et al* has developed a new ECL method for the detection of single strand DNA (ss-DNA) by immobilising DNA on gold electrode and using $[Ru(bpy)_3]^{2+}$ as an ECL label.[110] It has been reported recently that gold nanoparticles can de directly used as an ECL enhancing agent for the electrochemical detection of DNA.[111] Zhang *et al* proposed a highly sensitive ECL method for the detection of DNA hybridisation using gold nanoparticles as a carrier for the ECL label and ss-DNA.[112]

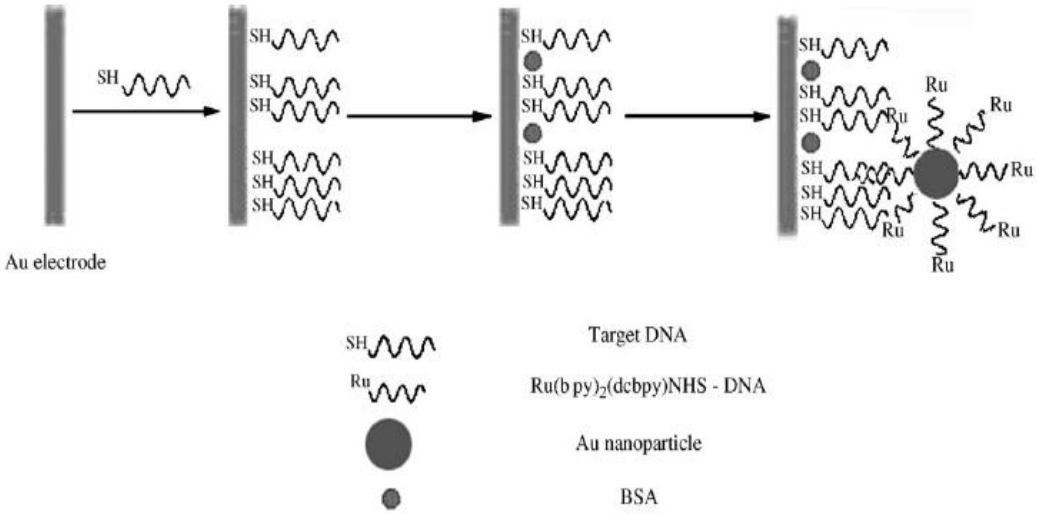

Figure 1.10: Schematic diagram of ECL detection using gold nanoparticles for DNA hybridisation. Reprinted from Hui Wang, Chengxiao Zhang, Yan Li, and Honglan Qi, *Electrogenerated Chemiluminescence Detection for Dioxyribinucleic Acid Hybridization Based on Gold Nanoparticles Carrying Multiple Probes*, Anal. Chim. Acta, **2006**, 575, 205.

Figure 1.10 shows the schematic diagram of ECL based detection of DNA hybridisation. In a model system, a 12-base synthetic ss-DNA (with 3'-thiol modification) was used as a target analyte while ruthenium bis (2,2'-bipyridine)(2,2'-bipyridine-4, 4'-dicarboxylic acid)-*N*-hydroxysuccinimide ester (abbreviated to $Ru(bpy)_2(dcbpy)NHS$) served as ECL label and gold nanoparticles acted as carrier. The presence of gold nanoparticles showed an enhanced ECL emission and the detection limit for the complementary sequence achieved was 5 pM, which is more sensitive than the ECL methods reported earlier.[113]

The ruthenium metal complexes have the ability to produce ECL signals in the presence of some biomolecules such as amino acids and nicotinamide adenine dinucleotide (NADH) as a co-reactant. Thus, the ECL intensity is directly related to the concentration of the biomolecules. Such electrochemical methods can be used as an alternative for the detection of biomolecules with high accuracy. Dennany *et al* have demonstrated the detection of amino acid e.g., proline and hydroxy-proline, using $[Ru(bpy)_2dcb]Cl_2$ monolayers, where bpy is 2,2'-bipyridine and dcb is 4,4'-dicarboxy-2, 2'-bipyridine.[114] It was shown that the ECL and current response

depend linearly on the concentration of analytes over a dynamic range from 1 to 10 nM.

Dihydronicotinamide adenine dinucleotide (NADH) is an important coenzyme involved in metabolic, photosynthetic and respiratory processes in every living cell.[115] This class of coenzyme alternates between the oxidised state NAD^+ and reduced state, NADH, for the production and transport of ATP in living cells.[116] These coenzymes find their application in the field of bioanalytical sciences mainly in enzymatic assays and enzymatic electrodes.[117,118] Several researchers have reported the electrochemical detection of NADH using modified electrodes. However, direct electrochemical oxidation of NADH at the bare electrode requires a high (~ 1 V) overpotential. The high overpotential for the oxidation of NADH results in electrode fouling and causes interference from easily oxidisable species present in the sample.

Considerable efforts have been made to reduce the overpotential for NADH oxidation using mediators. One approach is to modify the electrode surface with a catalyst or mediator. Electrochemical methods were used to reduce the overpotential of NADH oxidation by using various nanomaterials including carbon nanotubes,[119] graphite[120] and gold nanoparticles.[121] An attractive alternative to enhance the sensitivity of detection of NADH is to use the ECL pathway in which the coenzyme is re-oxidised by an ECL species, such as ruthenium (II) tris (2,2'-bipyridine).[122,36]

$[Ru(bpy)_3]^{3+}$ moieties mediate the oxidation of NADH and result in an excited state that emits light. Therefore, NADH can act as a co-reactant for ECL generation. In such cases, the amount of light emitted is proportional to the concentration of NADH present. Moreover, the presence of amine groups in NADH helps to enhance the sensitivity of detection using $[Ru(bpy)_3]^{2+}$ by producing intense ECL. Figure 1.11 shows the detection of NADH or NADPH using $[Ru(bpy)_3]^{2+}$ *via* generating ECL signals.

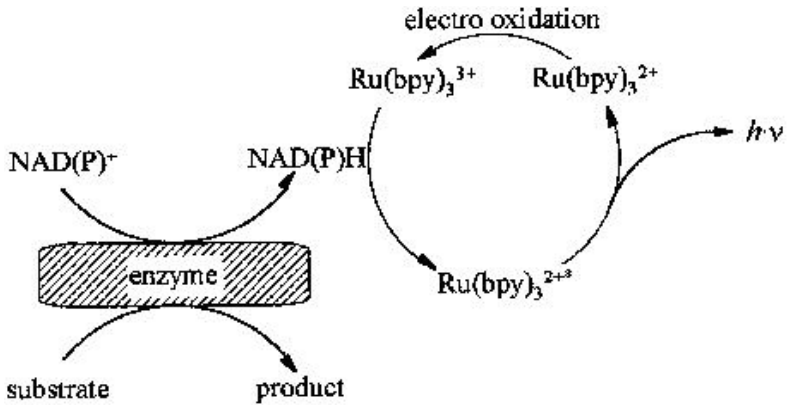

Figure 1.11: Enzymatic detection using $[Ru(bpy)_3]^{2+}$ ECL; NADH or NADPH are produced during a highly specific enzymatic reaction and detection using ECL. Adapted from Karsten Fahnrich, Miloslav Pravda, and George Guilbault, *Recent Applications of Eelectrogenerated Chemiluminescence in Chemical Analysis*, Talanta, **2001**, 54, 531.

However, co-immobilisation of the enzyme and $[Ru(bpy)_3]^{2+}$ affects the hydrophilicity of the film, which can reduce the enzymatic activity.[36] In addition, the positive charges of $[Ru(bpy)_3]^{2+}$ could effectively interact with the negative charges of the enzyme leading to reduced activity. Hence, the best results were obtained only by separately immobilising $[Ru(bpy)_3]^{2+}$ moieties and the enzyme in two different polymer layers rather than immobilising both as a single layer.

A new method of immobilising $[Ru(bpy)_3]^{2+}$ in a sol-gel network along with gold nanoparticles has been developed.[26] Due to this unique immobilisation, the gold nanoparticles act as conducting nanoelectrodes and hence increases the oxidation of NADH, which resulted in a higher ECL signal. It has been reported that the NADH can be detected typically over a range from 2.5 nM to 586 μM, with a sensitivity of 1 nM. This detection sensitivity using gold nanoparticles is found to be nearly two orders lower than the electrodes modified with carbon materials.[123,124]

Dehydrogenases are widely used in bioanalytical chemistry mainly in enzymatic assays. It has been reported that the nicotinamide coenzyme (NAD^+/NADH) controls the enzymatic activity of more than 300 dehydrogenases in cells.[125] Thus, it is believed that efficient sensing of NADH in the biological systems might provide

more information about the enzymatic activities that occurs in cells. Thus, there is a need to produce more stable, highly sensitive, selective and rapid ECL based detections for NADH.

1.7. Theoretical Background

The present section deals with the theoretical predictions, which supports all the major experimental work reported in this thesis. This section introduces surface plasmon resonance, luminescence, theory of energy transfer between a donor and an acceptor, basics of cyclic voltammetry and the mechanisms of electrochemiluminescence generation.

1.7.1. Origin of Surface Plasmon Resonance

The bright colours of gold nanoparticles are due to the collective oscillation of electrons in the conduction band of the particles excited by the incident electromagnetic field, known as localised surface plasmon oscillation.[15] As the wave front of the light passes through the solution, the electron density in the particle is polarised to one surface and oscillates in resonance with the incident light's frequency. As the positive charges in the particles are assumed to be immobile, the conduction band electrons move under the influence of the external fields (Figure 1.12).

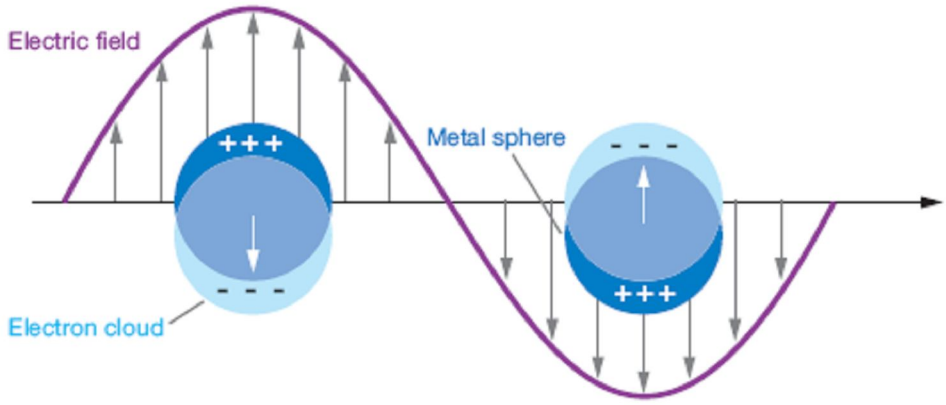

Figure 1.12: Origin of surface plasmon resonance due to coherent interaction of the electrons in the conduction band with the incident light. Reprinted from Katherine Willets, and Richard Van Duyne, *Localised Surface Plasmon Resonance Spectroscopy and Sensing*, Annu. Rev. Phys. Chem. **2007**, 58, 267.

This interaction results in the displacement of the negative charges from the positive ones, which results in a net charge difference at the nanoparticle boundaries. This in turn gives a restoring force to the system and as a consequence dipolar oscillation of

the electrons is created, this is known as *surface plasmon oscillations*.[126] The oscillation frequency is usually in the visible region for gold and silver nanoparticles. The free electrons in the metal (d electrons for gold) are free to move through the material which can cause a standard resonance condition as shown above when interacting with the wavelength of light much larger than the nanoparticle size.

The term "surface" arises from the fact that although all the electrons are oscillating with respect to the positive-ion background, the main effect observed is the restoring force due to surface polarisation. The surface, thus, plays an important role for the observation of surface plasmon resonance as it alters the boundary conditions for the polarisability of metal and therefore shifts the resonance to optical frequencies.[127] The resonance condition is determined from absorption and scattering spectroscopy. The change in surface geometry due to the size and shape of the particle results in a shift in the electric field density on the surface, which alters the respective surface plasmon oscillations.

When metal nanoparticles and a luminophore are in close vicinity, the electric field created by the metal nanoparticles interacts with the excited state of the luminophore and alters its emission. Such interactions can have a number of useful effects, including increased quantum yields, photo stability, absorption cross-section, and distances for resonant energy transfer and decreased luminescence lifetime of the luminophore. These effects are called *Metal Enhanced Fluorescence* (MEF). Figure 1.13 shows the Jablonski diagram representing metal enhanced fluorescence.[128] The quantum yield and lifetime of the luminophore in the absence of metal nanoparticles is given as follows:

$$Q_0 = \frac{\Gamma_r}{(\Gamma_r + k_{nr})} \quad \text{.....(1.2)}$$

$$\tau_0 = (\Gamma_r + k_{nr})^{-1} \quad \text{.....(1.3)}$$

where Γ_r is radiative decay rate, k_{nr} is the nonradiative decay rate, and Q_0 and τ_0 are the quantum yield and lifetime of the luminophore, respectively.

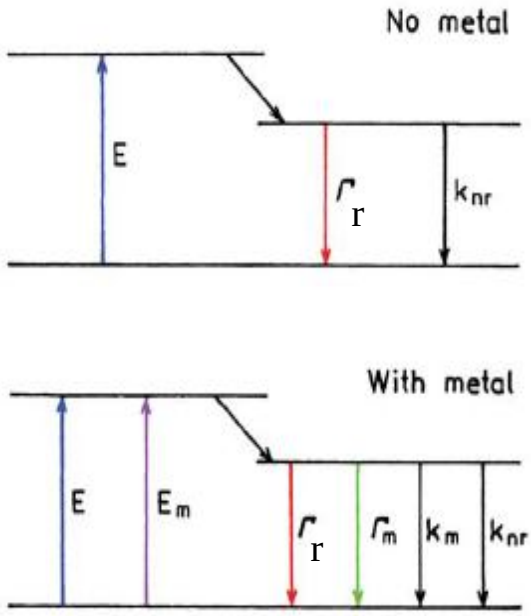

Figure 1.13: Jablonski diagram without (top) and with (bottom) the effects of near metal nanoparticles. Reproduced from Joseph Lackowicz, *Radiative Decay Engineering: Biophysical and Biomedical Applications,* Anal.Biochem. **2001**, 298, 1.

The quantum yield (Q) and the lifetime (τ_0) of the luminophore near metal nanoparticles changes due to the increase in the radiative decay due to the presence of metal nanoparticles. Thus, the quantum yield and lifetime in presence of metal nanoparticles can be expressed as follows:[128]

$$Q_0 = \frac{\Gamma_r + \Gamma_m}{(\Gamma_r + \Gamma_m + k_{nr})} \quad \text{.....(1.4)}$$

$$\tau_0 = (\Gamma_r + \Gamma_m + k_{nr})^{-1} \quad \text{.....(1.5)}$$

where Γ_m is the radiative decay induced by metals. The effect of metal enhanced luminescence is found to be higher for the luminophores with lower quantum yields. It is essential to analyse the nature of interaction observed between luminophore and metal nanoparticles and the factors influencing those interactions. There are three different kinds of interactions that are possible between the luminophore and a metal nanoparticle. Figure 1.14 shows the effect of metallic nanoparticles on transitions of a luminophore that are present in close vicinity.

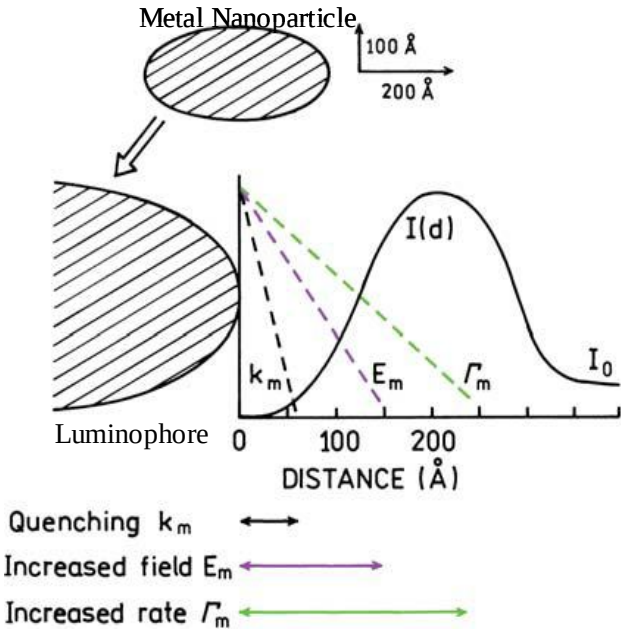

Figure 1.14: Effect of metallic nanoparticles on transitions of a luminophore. Metallic particles can cause quenching (k_m), can concentrate the incident light field (E_m) and can increase the radiative decay rate (Γ_m). Reproduced from Joseph Lackowicz, *Radiative Decay Engineering: Biophysical and Biomedical Applications,* Anal. Biochem. **2001**, 298, 1.

Metal nanoparticles can quench the luminescence at short distances from the metal. Apart from that, metal nanoparticles can increase both the excitation rate and the radiative decay rate. All these possible effects are related to the distance between the metal nanoparticles and the luminophores and to the extent of spectral overlap between the metal nanoparticles absorption and luminophore emission.

1.7.2. Luminescence Quenching

Quenched luminescence can occur between a luminophore and neighbouring metal nanoparticles. As described in the previous section, luminescence quenching is a short-range phenomenon (<100 Å).[128] Bimolecular quenching typically occurs via one of two mechanisms (1) dynamic (collisional) quenching and (2) static quenching. Dynamic quenching can occur when the excited state luminophore is deactivated upon contact with some other molecule in solution, which is called quencher.[129] Static quenching occurs as a result of formation of nonfluorescent complexes with the quenchers.

Bimolecular quenching data are usually presented as Stern-Volmer plots (F_0/F *versus* [Q], where [Q] is the concentration of the quencher). Comparison of the ratios of luminescence intensities (F_0/F) and lifetimes (τ_0/τ) for the luminophores in the presence and absence of nanoparticles is the indicator of the nature of quenching. The lifetimes of the luminophore depends on the concentration of the quencher in dynamic quenching due to the possibility of depopulating the excited state. The dynamic quenching can be expressed as follows:[129]

$$\frac{F_0}{F} = \frac{\tau_0}{\tau} = 1 + k_q \tau_0 [Q] \quad \text{.....(1.6)}$$

where F_0 and τ_0 are the luminescence intensity and lifetime in the absence of quencher, F and τ are the luminescence intensity and lifetime in the presence of the quencher molecules, k_q is the decay rate and [Q] is the concentration of the quencher.

The Perrin model applies where luminophores and quencher reside in a rigid matrix where diffusion does not occur during the lifetime of the luminophores. Depending upon the mechanism (energy or electron transfer), quenching depends on the sixth power or exponentially on the distance between luminophores and quencher. Generally to cover both possibilities, a critical interaction distance at which quenching efficiency is 50% is defined and the Perrin model then describes the volume of the sphere in which the quencher must reside in order to act as a quencher.

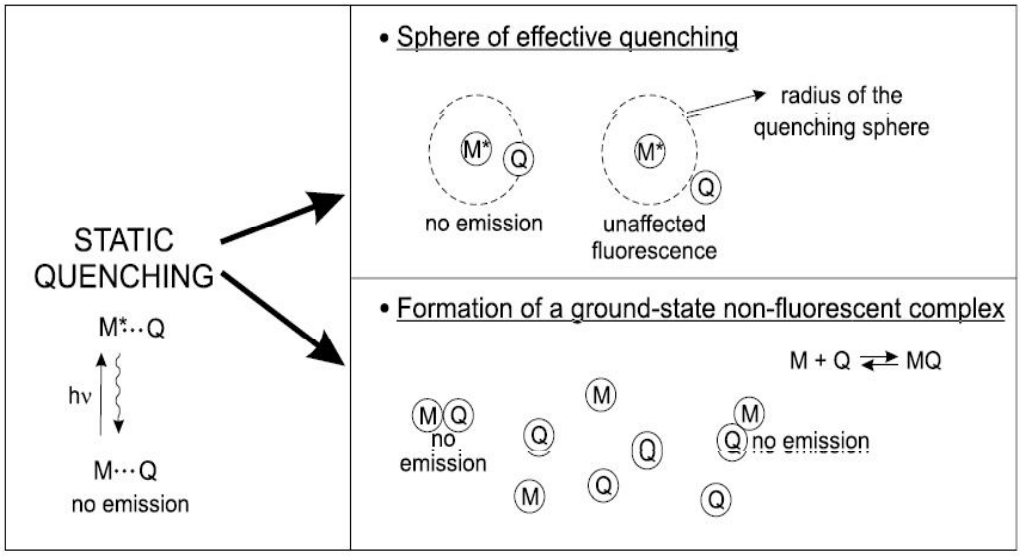

Figure 1.15: Illustration of static quenching due to the sphere of effective quenching and ground state complexing. Reproduced from Bernard Valeur, *Molecular Fluorescence: Principles and Applications*, **2001**.

The quenching of luminophore due to the formation of sphere of effective quenching can be explained as follows. According to Perrin, the quenching is assumed to be complete when the quencher molecule is present inside a quenching sphere of volume (V_q). In contrast, when the quencher molecules are present outside the sphere there is no influence on the emission properties of the luminophores. The Stern-Volmer equation for such kind of quenching can be expressed by an exponential dependence of F_0/F on [Q]:

$$\frac{F_0}{F} = \exp(V_q N_a [Q]) \quad \text{.....(1.7)}$$

where V_q is the volume of the quenching sphere and N_a is Avogadro's number. A decrease in the luminescence is also observed in static quenching, which could be either due to the formation of a non-fluorescent complex or a sphere of effective quenching.[129] The sphere of effective quenching is observed generally when the dimension of the quencher is in the nanometer range. Figure 1.15 represents the sphere of effective quenching and formation of non-fluorescent complex. The quenching occurs in the first case when the quencher is present inside the quenching sphere, when the quenchers reside outside the sphere does not show any quenching.

In the second case, the quencher forms a non-fluorescent complex with the liminophore and hence results in quenched emission. The radius of the quenching sphere can be obtained from equation (1.6) and is typically about 10 Å.

1.7.3. Photo Induced Energy Transfer

The spectral overlap of absorbance of metal nanoparticles with the emission spectrum of luminophore could result in efficient energy transfer, which might result in metal-enhanced fluorescence effects. Fluorescent or Förster Resonance Energy Transfer (FRET) can be explained by classical theory.[130] FRET occurs between the donor molecule (D) in the excited state and an acceptor (A) in the ground state. The energy transfer is the result of long-range dipole-dipole interactions between the donor-acceptor pair. The rate of energy transfer depends on the extent of spectral overlap of the emission of donor with the absorption spectrum of acceptor, the quantum yield of the donor, relative orientation of the donor and the acceptor transition dipoles, and the distance between the donor and acceptor molecules.

As represented in Figure 1.14, the interaction of metal nanoparticles with the luminophore is greatly influenced by the distance between them and the spectral overlap. The metallopolymer- gold nanocomposite system has a well-defined spectral overlap between the emission spectrum of the donor Ru ($\lambda_{max} \approx 610$ nm) with that of the absorbance spectrum of the DMAP-protected gold nanoparticles around 550-650 nm. Non-radiative transfer of electronic excitation from a donor molecule to an acceptor molecule can be descrined as follows:

$$D^* + A = D + A^* \quad \text{.....(1.8)}$$

where D and A represents the donor and acceptor molecules and the * represents the excited state of the respective molecules. The distance at which resonant energy transfer is 50% efficient is called the Förster distance, which is typically in the range 20-100 Å.[130] Energy transfer is assumed to occur whenever the donors and acceptors are within the characteristic Förster distance, and whenever suitable spectral overlap occurs. The value of R_0 can be predicted from the spectral properties of donors and acceptors. Förster energy transfer is a through-space interaction that is mostly independent of the intervening solvents and/or the macromolecules. The transfer arises from dipole-dipole coupling, but does not involve a light field.

Consider that the donor is already in the excited state and the acceptor is in the ground state. In such case, the rate of transfer from a donor to the acceptor separated by a distance *r* is given by equation (1.9):[130]

$$k_T(r) = \frac{Q_D \kappa^2}{\tau_D r^6}\left(\frac{9000(\ln 10)}{128\pi^5 N n^4}\right)\int_0^\infty F_D(\lambda)\varepsilon_A(\lambda)\lambda^4 d\lambda \quad \text{.....(1.9)}$$

where Q_D is the quantum yield of the donor in the absence of acceptor, *n* is the refractive index of the medium, N is the Avogadro number, *r* is the distance between the donor and acceptor, and τ_D is the lifetime of the donor in the absence of acceptor. F_D (λ) is the intensity normalised luminescence intensity of the donor in the wavelength range λ to λ + Δλ with the total intensity (area under the curve) normalised to unity. ε_A (λ) is the molar extinction coefficient of the acceptor at λ, which is *typically* in units of M^{-1} cm^{-1}. The term κ^2 is a factor describing the relative orientation in space of the transition dipoles of the donor and acceptor. κ^2 is usually assumed to be equal to 2/3, which is appropriate for dynamic random averaging of the donor and acceptor orientations.

The Förster distance (R_0) can be calculated from the spectral properties of the donor and the acceptor and the donor quantum yield from the following equation:[130]

$$R_0^{\,6} = \frac{9000(\ln 10)\kappa^2 Q_D}{128\pi^5 N n^4}\int_0^\infty F_D(\lambda)\varepsilon_A(\lambda)\lambda^4 d\lambda \quad \text{.....(1.10)}$$

where R_0 is the Förster distance and Q_D is the quantum yield of the donor. Once the value of R_0 is known, the rate of energy transfer can be easily calculated using

$$k_T(r) = \frac{1}{\tau_D}\left(\frac{R_0}{r}\right)^6 \quad \text{.....(1.11)}$$

If the transfer rate is much faster than the decay rate, then energy transfer will be efficient. If the transfer rate is slower than the decay rate, then there is insufficient time for the transfer to occur during the excited-state lifetime, and RET will be inefficient.

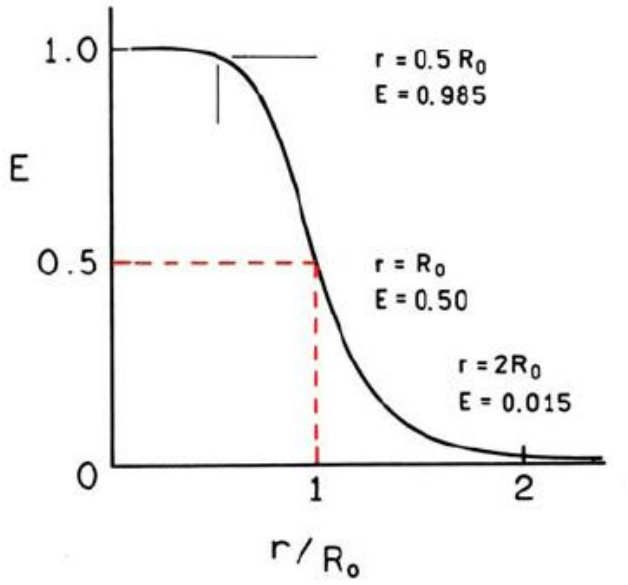

Figure 1.16: Dependence of the energy transfer efficiency (E) on distance. R_0 is the Förster distance. From Joseph R. Lakowicz, *Principles of Fluorescence Spectroscopy,* **1999**.

The efficiency of energy transfer (E) is the fraction of photons absorbed by the donor, which are transferred to the acceptor.

$$E = \frac{R_0^{\,6}}{R_0^{\,6} + r^6} \qquad \text{.....(1.12)}$$

Equation 1.12 shows that the transfer efficiency is strongly dependent on distance when the D–A distance is near R_0 (Figure 1.16). The efficiency quickly increases to 1.0 as the D–A distance decreases below R_0. The transfer efficiency is typically measured using the relative fluorescence intensity of the donor, in the absence (F_D) and presence (F_{DA}) of acceptor:

$$E = 1 - \frac{F_{DA}}{F_D} \qquad \text{.....(1.13)}$$

Thus, the transfer efficiency can be measured once the luminescence intensity of the donor and donor-acceptor couple is known.

1.7.4. Zeta Potential

The particles at the colloidal suspension usually carry an electric charge due to the presence of chemical groups at the surface. The development of net charge at the particle surface might be due to the ionisation of the surface groups or adsorbed species. The presence of charge affects the distribution of ions in the surrounding interfacial region that leads to the existence of electrical double layer around the particle. The liquid layer surrounding the particle can be described in two parts: an inner *"Stern layer"* and an outer *"Diffuse layer"*. Figure 1.17 shows the distribution of charge around the negatively charged particle.

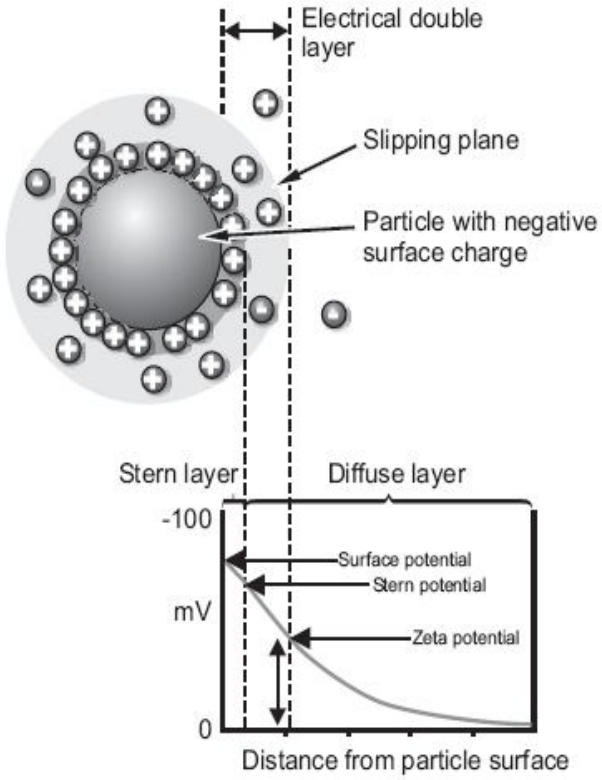

Figure 1.17: Distribution of the ions around the negatively charged particle. Adapted from Chapter 16, *Zetasizer Nano Series manual*.

Within the diffuse layer there is a theoretical boundary inside which the ions and particles form a stable entity. When the particles move, the ions within the boundary move with the particle whereas the ions present outside the boundary do not move

with the particle. This boundary is called the surface of hydrodynamic shear or *slipping plane*. The potential that exists at this boundary is called the *"Zeta potential"*. The Zeta potential can be calculated using Smoluchowski's formula: [131]

$$\zeta = \frac{4\pi\eta}{\varepsilon} \times U \times 300 \times 300 \times 1000 \quad \text{.....(1.14)}$$

where ζ is the zeta potential (mV), η is the viscosity of the solution, ε is the dielectric constant and U is the electrophoretic mobility. Here,

$$U = \frac{\upsilon}{V/L} \quad \text{.....(1.15)}$$

where υ is speed of the particle (cm/s), V is the voltage (V) and L is the distance to the electrode. The magnitude of the zeta potential gives an indication of the potential stability of colloidal system. If the particles in suspension have a large positive or negative zeta potential then they will tend to repel each other and hence there will be no tendency to aggregate. However, if the particles have a low zeta potential there is no electrostatic force to prevent the particle from coming together and aggregating. Thus, it is important to have higher Zeta potential values for a greater stability.

1.7.5. Cyclic Voltammetry

Cyclic voltammetry is the most widely used electrochemical technique, which gives qualitative information about the electrochemical reactions. It offers a rapid means of determining the redox potentials of the electroactive species, and is convenient for evaluating the effect of media upon redox process.[132] Voltammetry provides information about the thermodynamics and kinetics of electron transfer across the electrode/film interface. Figure 1.18 shows the potential-time excitation signal for a cyclic voltammogram experiment.

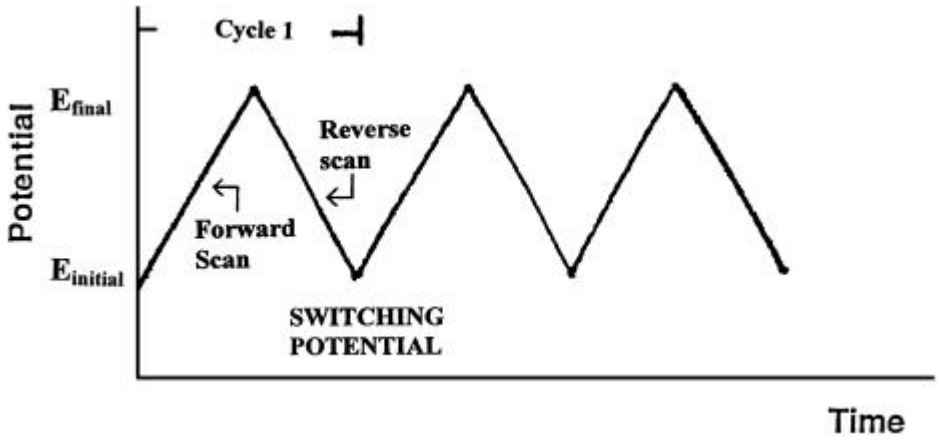

Figure 1.18: Potential-time excitation signal in cyclic voltammetric experiment. Adapted from Joseph Wang, *Analytical Electrochemistry*, **2000**.

In linear sweep voltammetry, the scan stops at E_{final}, whereas in cyclic voltammetry, the sweep direction is reversed when the potential reaches E_{final} and the potential returns to $E_{initial}$. This constitutes one complete cycle in cyclic voltammetry. A cyclic voltammogram, a plot of current *versus* applied voltage is recorded by scanning linearly the potential of a stationary working electrode. As the electron transfer process is not a purely thermodynamically controlled process, the current response is often dominated by kinetics. The kinetics is fast in a reversible system and hence the Nernst equation can be used to describe the current response. By contrast, slow kinetics results in irreversible systems in which the current is dominated by the rate of electron transfer. In such cases, the diffusion of the electro-active species also greatly influences the current.

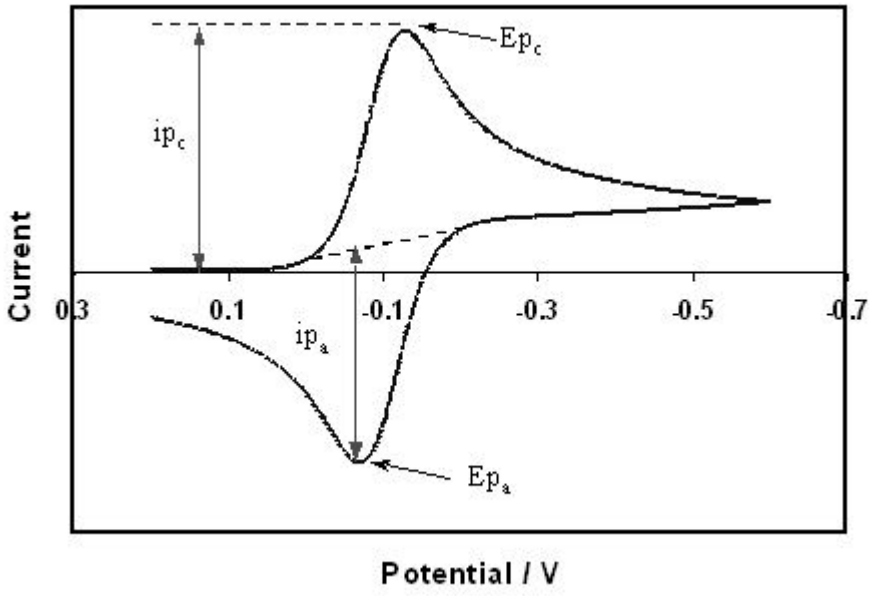

Figure 1.19: Solution phase cyclic voltammogram response of a reversible system. Adapted from Bard and Faulkner, *Electrochemical Methods: Fundamentals and Applications*, **2001**.

Figure 1.19 shows the cyclic voltammogram of a fully reversible process in solution.[133] The voltammogram in Figure 1.19 shows important parameters such as i_{pa} and i_{pc} (anodic and cathodic peak current), E_{pa} and E_{pc} (anodic and cathodic peak potentials) respectively. These parameters could provide all the significant details about the reaction that takes place at the electrode surface. Consider a solution containing the reduced form of the redox couple, R. As the electrode is scanned in the positive potential direction, initially no Faradaic current is observed. When the potential approaches the point where oxidation of the species can occur, the anodic current increases rapidly due to the oxidation of R. Equal concentrations of oxidised and reduced species exist at the formal potential. When the potential is switched, the current still remains anodic until the applied potential becomes sufficiently negative. Once the potential becomes sufficiently negative, the Faradaic current becomes zero and reduction process begins.

Adsorption of redox materials on the electrode surface leads to changes in the shape of the cyclic voltammogram when compared to solution-phase reactants since the

redox-active material does not have to diffuse to or from the electrode surface.[134] A change in the orientation of the oxidised and reduced species can affect peak splitting while the non-uniformity of the adsorbed species results in peak broadening. Slow electron transfer can also cause deviation form the ideal behaviour, as these systems are not in equilibrium. Figure 1.20 illustrates the theoretical cyclic voltammogram expected for an adsorbed monolayer under finite diffusion conditions, where the dynamics of heterogeneous electron transfer across the electrode/film interface do not influence the observed response.

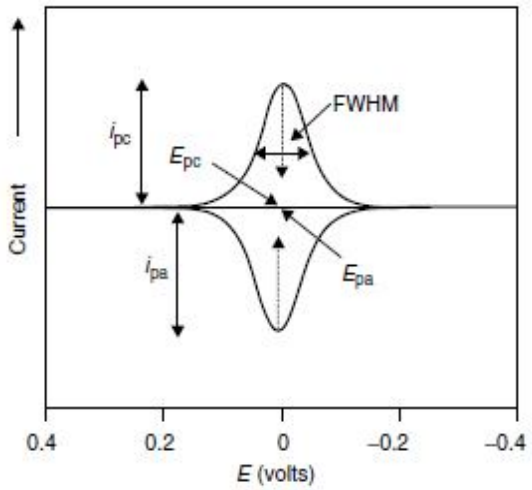

Figure 1.20: Current–potential curves obtained from cyclic voltammetry measurements for the reduction and oxidation of an adsorbed interfacial supramolecular assembly under finite diffusion conditions. Reproduced from Robert J. Forster, Tia E. Keyes, Johannes G. Vos, *Interfacial Supramolecular Assemblies*, **2003**.

The peaks of surface confined species are sharp and symmetrical unlike the solution phase species. This behaviour is due to the existence of fixed amounts of species on the electrode surface, which is not influenced by mass transport. Thus, for an ideal system, no peak-to-peak separation is expected. The peak current i_p is related to the surface coverage by the following equation:[133]

$$i_p = \frac{n^2 F^2}{4RT} \upsilon A \Gamma \quad \text{.....(1.16)}$$

where n is the number of electrons transferred, F is the Faraday constant, υ is the scan rate, R is the gas constant, T is the absolute temperature, A is the real or microscopic area of electrode and Γ is the surface coverage or concentration of redox active adsorbate (mol cm^{-2}). The peak current (i_p) varies linearly with the scan rate (υ). Under conditions of exhaustive oxidation and reduction, the surface coverage can be obtained from the following equation:[134]

$$\Gamma = \frac{Q}{nFA} \quad \text{.....(1.17)}$$

where Q is the charge passed during exhaustive electrolysis of the film after correction for double layer charging. In many films, electrochemical charge transport occurs by electron self-exchange reactions between neighbouring oxidised and reduced sites. The movement of charge compensating counter ions that are mobile within the layer accompanies this electron hopping process. The effective diffusion coefficient, D_{CT}, corresponding to the diffusion of either electron or charge compensating counter ions, can be estimated using the Randles-Sevcik equation.

The concentration profile of fixed oxidised and reduced species depends on the dimensionless parameter $D_{CT}t/d^2$, where t is the time for the potential scan to traverse the wave and d is the thickness of the layer. When $D_{CT}t/d^2 >> 1$, the electro active sites are in equilibrium and finite diffusion is observed. When $D_{CT}t/d^2 << 1$, the oxidised scan direction is reversed before the reduced sites within the film are completely oxidised. This is called *semi-infinite linear diffusion condition*. Under this semi-infinite linear diffusion condition, the peak current becomes dependent on the square root of scan rate ($\upsilon^{1/2}$) which can be expressed as follows:[133]

$$i_p = \left(2.69 \times 10^5\right) n^{3/2} A D^{1/2} \upsilon^{1/2} C \quad \text{.....(1.18)}$$

where n is the number of electrons transferred, A is the area of the electrode, C is the effective fixed site concentration and i_p is the anodic to cathodic peak current. If ohmic effects and slow electron transfer are absent and under semi-infinite diffusion conditions, $\Delta E_p = 57.0/n$ mV at 25°C, and $i_{pa}/i_{pc} = 1$ where ΔE_p is the difference in the anodic and cathodic peak potentials and i_{pa} and i_{pc} are the anodic and cathodic peak heights respectively.

1.7.6. Mechanisms of ECL Generation

Typically ECL systems are divided into two mechanisms: Annihilation and co-reactant ECL systems. In each case, two species are generated electrochemically, and those two species undergo an electron-transfer reaction to produce an emissive species. Here, the focus is on the oxidative co-reactant route to ECL production that is typical of $[Ru(bpy)_3]^{2+}$ systems.

1.7.6.1. Co-reactant ECL System

The co-reactant is the species which can either be oxidised or reduced by the same potential pulse that oxidises the ECL species, e.g. oxalate and tripropylamine (TPrA).[135,136] The co-reactant forms an intermediate species that reacts with the ECL luminophores to generate an excited state which results in the emission of light. However, the intermediates should have sufficient oxidising and reducing energy to react with the oxidised or reduced ECL luminophores to form the excited state species.[7] In addition, the intermediates should undergo a rapid reaction with the oxidised species and should not be a good quencher of ECL.[11] It is significant that the co-reactant should not emit any ECL signal over the potential range scanned.[137]

The generation of ECL using TPrA as a co-reactant was first observed in the 1980s.[12] The most common advantage of the TPrA system is the possibility of generating ECL in aqueous solutions. The maximum optimal ECL using TPrA is found at pH 7.5.[138] The TPrA/$[Ru(bpy)_3]^{2+}$ system is the most commonly used ECL systems for practical and analytical applications. In this case, ECL is produced upon simultaneous oxidation of $[Ru(bpy)_3]^{2+}$ and TprA and Figure 1.21 shows the most common mechanism that has been proposed for the generation of ECL signals. The oxidation or reduction of the co-reactant occurs at the same potential as $[Ru(bpy)_3]^{2+}$. The co-reactant then form a new species, which reacts with $[Ru(bpy)_3]^{3+}$ to generate ECL.

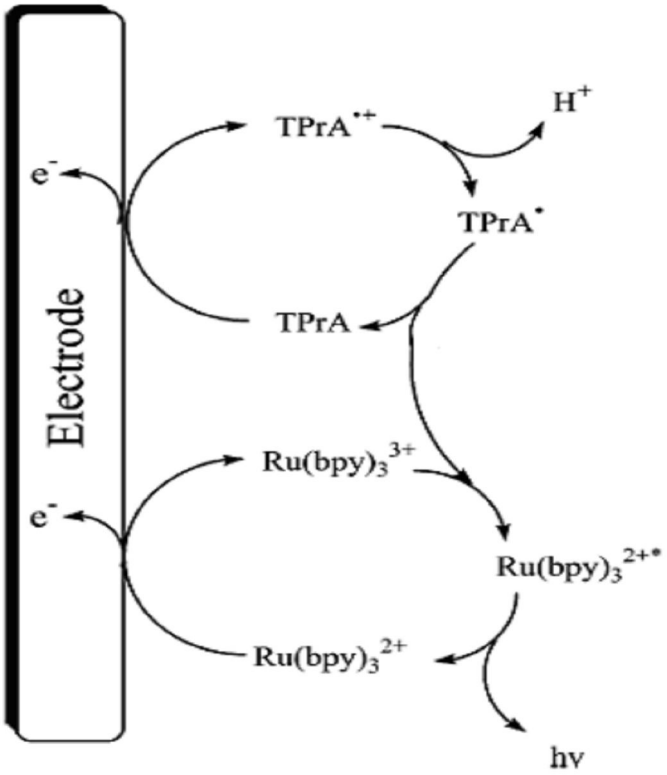

Figure 1.21: Proposed mechanism for TPrA/$[Ru(bpy)_3]^{2+}$ ECL system. Adapted from Mark Richter, *Electrochemiluminescence (ECL)*, Chem. Rev., **2004**, 104, 3003.

Besides this common mechanism, at least four distinct reaction mechanisms have been proposed for the co-reactant pathway between $[Ru(bpy)_3]^{2+}$ and TPrA.[139,140] Figure 1.22 shows the scheme for ECL generation from $[Ru(bpy)_3]^{2+}$ upon reaction with tripropylamine. For efficient ECL generation, the deprotonation of the ammonium ion (R_3NH^+) of the original tertiary amine before the reaction is significant.

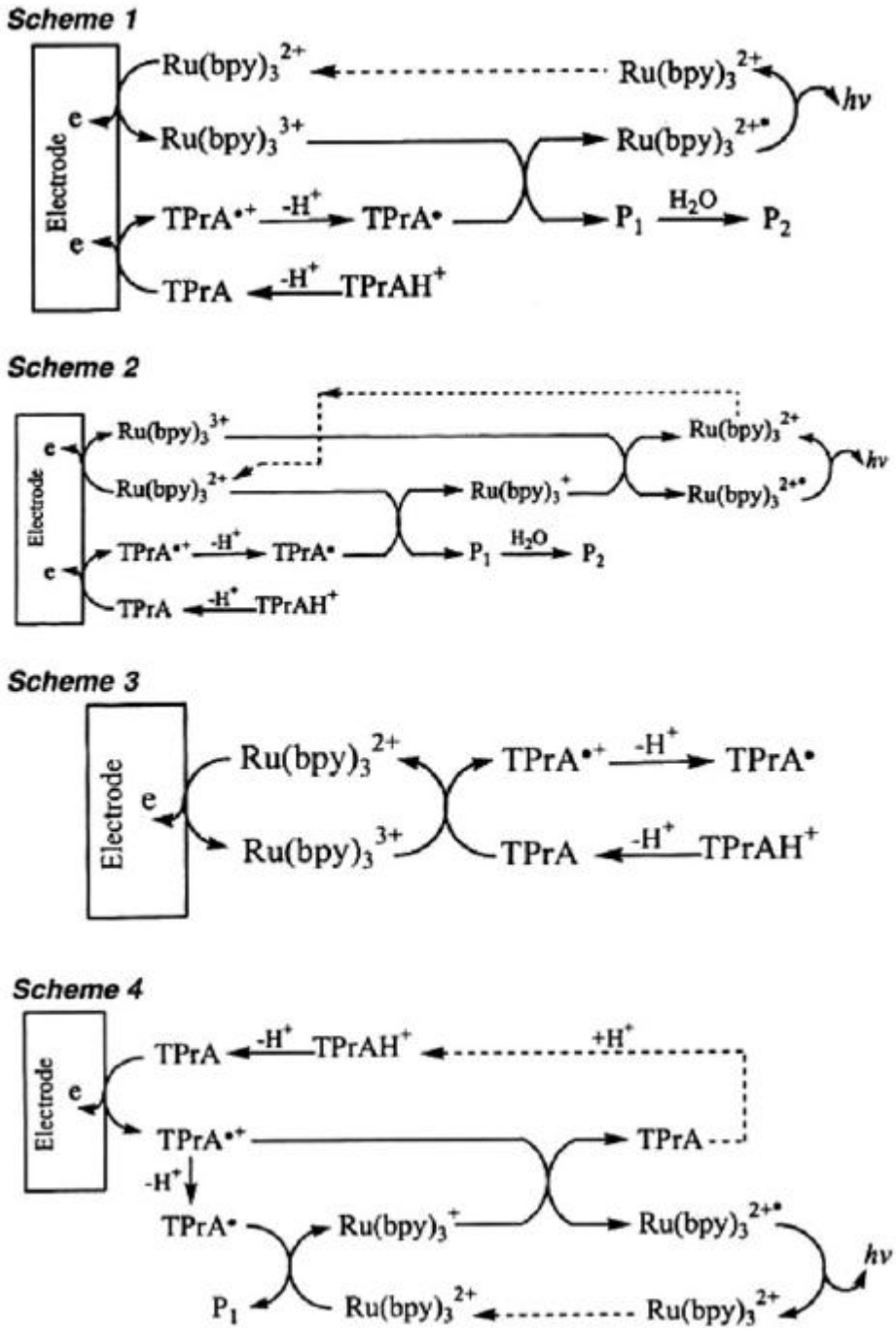

Figure 1.22: Schemes for tripropylamine co-reactant reaction with $[Ru(bpy)_3]^{2+}$. Reproduced from Wujian Miao, Jai-Pil Choi, and Allen J. Bard, *Electrogenerated Chemiluminescence 69: The Tris (2,2'-bipyidine) ruthenium (II), $(Ru(bpy)_3^{2+})$/Tri n-propylamine (TPrA) system Revisited- A New Route Involving TPrA Cation Radicals*, J. Am. Chem. Soc. **2002**, 124, 14478.

Whist in the case of a polymer film containing ruthenium/osmium metal centres, there are several processes that could limit the production of overall current due to

the reaction of Ru^{3+} with the co-reactant including the rate of charge transport (D_{CT}), rate of mass transport of the analytes within the polymer film (t_s) and the kinetics of cross-reaction (k_{cross}).[141] As an elaborate study has been already made on analysing the mass transport and the kinetics of metallopolymers,[141] this thesis focuses on elucidating the significance of charge transport rates through metallopolymer films on the ECL intensity.

1.8. Conclusions

In conclusion, this chapter describes the recent advancements in electrochemiluminescence-based biosensors for the detection of biologically important molecules. This chapter initially introduces the basic concepts of ECL biosensors and the potential ways to enhance the performance of biosensors using colloidal gold nanostructures. A brief description on the synthesis of spherical and rod shaped colloidal gold nanoparticles has been reviewed. Finally, relevant literature on the application of gold nanoparticles in ECL assays has been elaborately discussed.

ECL has potential advantages in the detection of disease biomarkers even at ultra low concentrations of analytes. The solid state ECL generation has proven numerous added advantages over the solution phase measurements, which includes enhanced ECL emission intensities from the ECL luminophores, reduced consumption of the solvents and ease of device designs. Though many efforts have been made to enhance the sensitivity of ECL biosensors, still there is an increased requirement to enhance the performance, sensitivity and selectivity of these devices to achieve highly sensitive biosensors at low cost. Due to the recent advancements in the scientific research, applications of nanometer-sized particles can be used to improve the ECL emission properties.

1.9. References

1 Wang, J. *Biosensors & Bioelectronics,* **2006,** 21, 1887.

2 Wolf, M.; Juncker, D.; Michel, B.; Hunziker, P.; Delamarche, E. *Biosens. Bioelectron,* **2004**, 19, 1193.

3 Zakynthinos, E.; Pappa, N. *J. Cardiol.* **2009**, *53*, 317.

4 Mani, V.; Chikkaveeraiah, B. V.; Patel, V.; Gutkind, J. S.; Rusling, J. F. *ACS Nano* **2009**, *3*, 585.

5 Vo-Dinh, T.; Cullum, B. Fresenius J. *Anal. Chem*. **2000**, 366, 540.

6 Knight, A. *Trend Anal. Chem*. **1999**, 18, 47.

7 Richter, M. *Chem. Rev*. **2004**, 104, 3003.

8 Bard, A. J.; *Electrogenerated Chemiluminescence*, 2nd edition, Marcel Dekker Inc, New York, **2004**.

9 Knight, A. W.; Greenway, G. M. *Analyst*, **1994**, 119, 879.

10 Hsueh, Y.; Collins, S. D.; Smith, R. L., *Sensor Actuat B- Chem*, **1998**, 49, 1.

11 Pyati, R.; Mark, R. M., *Annu. Rep. Prog. Chem., Sect C,* **2007**, *103*, 12.

12 Bard, A. J.; Debad, J. D.; Leland, J. K.; Sigal, G. B.; Wilbur, J. L.; Wohlstadter, J. N. *Encyclopedia of Analytical Chemistry*; Meyers, R. A., Ed.; Wiley: Chichester, U.K., **2000**.

13 Huang, T.; Murray, R. W. *Langmuir*. **2002**, 18, 7077.

14 Chen, Z.F., Zu, Y.B., *Langmuir*, **2007**, 23, 11387.

15 Eustis, S.; El-Sayed, M. A. *Chem. Soc. Rev*. **2006**, 35, 209.

16 Faulkner, L. R.; Bard, A. J. *Electroanalytical Chemistry*, Marcel Dekker, New York, **1977**.

17 Kulmala, S.; Suomi, J. *Anal. Chim. Acta*, **2003**, 500, 21.

18 Miao, W. *Chem. Rev* **2008**, 108, 2506.

19 Fahnrich, K. A.; Pravda, M.; Guilbault, G. G. *Talanta,* **2001**, 54:531.

20 Gorman, B. A.; Francis, P. S.; Barnett, N. W. *Analyst,* **2006,** 131, 616.

21 Borisov, S. M.; Wolfbeis, O. S.; *Chem. Rev.* **2008**, 108, 423.

22 Myung, N.; Ding, Z. F.; Bard, A. J. *Nano Lett*. **2002**, 2, 1315.

23 Jiang, H.; Ju, H. X. *Chem. Comm.* **2007**, 4, 404.

24 Gerardi, R. D.; Barnett, N. W.; Lewis, S. W. *Anal. Chim. Acta,* **1999**, 378, 1.

25 Chang, Z.; Zhou, J. M.; Zhao, K.; Zhu, N. N.; He, P. G.; Fang, Y. Z. *Electrochim. Acta* , **2006**, 52, 575.

26 Deng, L.; Zhang, L.; Shalng, L.; Guo, S.; Wen, D.; Wang, F.; Dong, S. *Biosens. Bioelectron.*, **2009**, 24, 2273.

27 Liu, X.; Niu, W.; Li, H.; Han, S.; Hu, L.; Xu, G. *Electrochem. Commun*, **2008**, 10, 1250.

28 Tian, D.; Duan, C.; Wang, W.; Li, N.; Zhang, H.; Cui, H.; Lu, Y. *Talanta,* **2009**, 78, 399.

29 Lin, J-M.; Tsuji, A.; Maeda, M. *Anal. Chim. Acta* **1997**, *339*,139.

30 Li, Y.; Qi, H.; Yang, J.; Zhang, C. *Microchim Acta*, **2009,** 164, 69.

31 Golla, R.; Seethala, R. *J. Biomol Screen,* **2004**, 9, 62.

32 Obeng, Y. S.; Bard, A. J. L*angmuir*, **1991**, 7, 191.

33 Sykora, M.; Meyer, T. J. *Chem. Mater*. **1999**, 11, 1186.

34 Collinson, M. M.; Taussig, J. S.; Martin, S. A. *Chem. Mater.* **1999**, 11, 2594.

35 Fan, F-R. F.; Mau, A.; Bard, A. J. *Chem. Phys. Lett*. **1985**, 116, 400.

36 Martin, A. F.; Nieman, T. A. *Biosens. Bioelectron.*, **1997**, 12, 479.

37 Dennany, L.; Hogan, C. F.; Keyes, T. E.; Forster, R, J. *Anal. Chem*. **2006**, 78, 1412.

38 Rustling, J.; Forster, R.J. *Colloids & Int Sci*, **2003**, 262, 1.

39 Poherty, A. P.; Stanley, M. A.; Vos, J. G. *Analyst*, **1995**, 120, 2371.

40 Forster, R. J.; Vos, J. G. *Macromolecules*, **1990**, 23, 4372.

41 Qi, H.; Peng, Y.; Gao, Q.; Zhang, C. *Sensors*, **2009,** 9, 674.

42 Kickelbick, G. *Hybrid materials synthesis, characterisation and Applications*, Wiley VCH Verlag GmbH & Co. KgaA, **2007**.

43 Fahmi, A.; Pletch, T.; Mendoza, C.; Cheval, N. *Materials. Today*, **2009**, 12, 44.

44 Beecroft, L. L.; Ober, C. K. *Chem. Mater*, **1997**, 9, 1302.

45 Schultz, D. A. *Curr. Opin. Biotechnol*. **2003,** 14, 13.

46 Hashmi, A. S. K, *Chem. Rev*., **2007**, 107, 3180.

47 Yu, A.; Liang, Z.; Cho, J.; Caruso, F, *Nano Lett*., **2003,** 3, 9**.**

48 Niemeyer, C. M. *Angew. Chem., Int. Ed.* **2001**, 40, 4128.

49 Gittins, D. I.; Caruso, F, *Angew. Chem. Int. Ed.* **2001,** 40, 3001.

50 Chen, S.; Liu, Y.; GuozhongWu, *Nanotechnology* **2005,** 16, 2360.

51 Chang, C.; Wu, H.; Kuo, C.; Huang, M. H, *Chem. Mater*., **2008,** 20, 7570.

52 Hu, M.; Chen, J.; Li, Z.; Au, L.; Hartland, G. V.; Li, X. Marqueze, M.; Xia, Y. *Chem. Soc. Rev*., **2006**, 35, 1084.

53 Yuan, H.; Ma, W.; Chen, H.; Zhao, J.; Liu, J.; Zhu, H.; Gao, X, *Chem. Mater***. 2007**, 19, 1592.

54 Murphy, C. J.; Sau, T. K.; Gole, A. M.; Orendorff, C. J.; Gao, J.; Gou, L.; Hunyadi, S. E.;Li, T, *J. Phys. Chem. B*, **2005**, 109, 13857.

55 Skrabalak, S. E.; Au, L.; Li, X.; Xia, Y. *Nature Protocols*, **2007**, 2, 2182.

56 Goubet, N.; Ding, Y.; Brust, M.; Wang, Z. L.; Pileni, M-P. *ACS Nano*, **2009**, 3, 3622.

57 Daniel, M-S.; Astruc, D. *Chem. Rev.* **2004**, 104, 293.

58 Gole, A.; Murphy, C. J. *Chem. Mater*. **2004**, 16, 3633.

59 Pileni, M. P. *Langmuir*, **1997**, 13, 3266.

60 Brust, M.; Walker, M.; Bethell, D.; Schiffrin, D.; Whyman, R, *J. Chem. Soc. Commun*. **1994**, 801.

61 Sastry, M. *Current science*, **2003,** 85, 1735.

62 Handley, D. A., *Colloidal Gold: Principles, Methods and Applications*, Academic Press, San Diego, **1989**.

63 Templeton, A. C., Hostetler, M. J., Kraft, C. T. and Murray, R. W., *J. Am. Chem. Soc.*, **1998,** 120, 1906.

64 Esumi, K., Matsuhisa, K. and Torigoe, K., *Langmuir*, **1995**, 11, 3285.

65 Johnson, C. J., Dujardin, E., Davis, S. A., Murphy, C. J.; Mann, S., *J. Mater. Chem.*, **2002**, 12, 1765.

66 Leff, D. V., Ohara, P. C., Heath, J. C. and Gelbart, W. M., *J. Phys. Chem.*, **1995**, 99, 7036.

67 Elghanian, R., Storhoff, J. J., Mucic, R. C., Letsinger, R. L.; Mirkin, C. A., *Science*, **1997**, 277, 1078.

68 Gole, A.; Dash, V.; Ramakrishnan, V.; Mandale, A. B.; Sainkar, S. R.; Rao, M. Sastry, M., *Langmuir*, **2001**, 17, 1674

69 Underwood, S.; Mulvaney, P., *Langmuir*, **1994**, 10, 3427

70 Heath, J. R.; Knobler, C. M.; Leff, D. V. J. Phys. Chem. B **1997**, 101, 189.

71 Guo, H.; Ruan, F.; Lu, L.; Hu, J.; Pan, J.; Yang, Z.; Ren, B. *J. Phys. Chem. C.* **2009,** 113, 10459.

72 Ni, W.; Kou, X.; Yang, Z.; Wang, J. *ACS Nano*. **2008,** 2, 677.

73 Wu, H-Y.; Huang, W-L.; Huang, M. H. *Chem. Mater*. **2005**, 17, 6447.

74 Wu, H-Y.; Huang, W-L.; Huang, M. H. *Cryst. Growth Des.*, **2007**, 7, 831.

75 Perez-Juste, J.; Pastoriza-Santos, I.; Liz-Marzan, L. M.; Mulvaney, P. *Coord Chem Rev*, **2005**, 249, 1870.

76 Van Der Zande, B. M.; Bohmer, M. R.; Fokkink, L. G. J.; Scho¨nenberger, C. *Langmuir* **2000**, *16*, 451.

77 Jana, N. R.; Gearheart, L.; Murphy, C. J. *J. Phys. Chem. B* **2001**, *105*, 4065.

78 Nikoobakht, B.; El-Sayed, M. A. *Chem. Mater.* **2003**, *15*, 1957.

79 Yu, Y. Y.; Chang, S. S.; Lee, C. L.; Wang, C. R. C. *J. Phys. Chem. B* **1997**, *101*, 6661.

80 Kim, F.; Song, J. H.; Yang, P. *J. Am. Chem. Soc.*, **2002,** 124, 14316.

81 Zijlstra, P.; Bullen, C.; Chon, J. W. M.; Gu, M. *J. Phys. Chem. B.* **2006**, 110, 19315.

82 Yong, K-T.; Sahoo. Y.; Swihart, M. T.; Schneeberger, P. M.; Prasad, P. N. *Top. Catal.* **2008**, 47, 49.

83 Brown, K. R.; Natan, M. J. *Langmuir* , **1998**, 14, 726.

84 Mohamed, M. B.; AbouZeid, K. M.; Abdelsayed, V.; Aljarash, A. A.; El-Shall, M. S. *ACS Nano*, **2010**, 4, 2766.

85 Jana, N. R.; Gearheart, L.; Murphy, C. J. *Chem. Mater.* **2001**, 13, 2313.

86 Perez-Juste, J.; Pastoriza-Santos, I.; Liz-Marzan, L. M.; Mulvaney, P. *Coord. Chem. Rev.* **2005**, 249, 1870.

87 Gao, J.; Bender, C. M.; Murphy, C. J. *Langmuir* **2003**, *19*, 9065.

88 Rao, P.; Doremus, R. *J. Non-cryst. Solids*, **1996**, 203, 202.

89 Liu, M. Z.; Guyot-Sionnest, P. *J. Phys. Chem. B* **2005**, 109, 22192.

90 Perez-Juste, J.; Liz-Marzan, L. M.; Carnie, S.; Chan, D. Y. C.; Mulvaney, P. *Adv. Funct. Mater.* **2004**, 14, 571.

91 Hubert, F.; Testard, F.; Spalla, O. *Langmuir* **2008**, 24, 9219.

92 Smith, D. K.; Miller, N. R.; Korgel, B. A. *Langmuir*, **2009**, 25, 9518.

93 Johnson, C. J.; Dujardin, E.; Davis, S. A.; Murphy, C. J.; Mann, S. *J. Mater. Chem*. **2002**, *12*, 1765.

94 Perez-Juste, J.; Liz-Marzan, L. M.; Carnie, S.; Chan, D. Y. C.; Mulvaney, P. *Adv. Funct. Mater*. **2004**, *14*, 571.

95 Hernandez-Santos, D.; Gonzalez-Garcia, M. B.; Garcia, A. C. *Electroanalysis*, **2002**, 14, 1225.

96 Cai, H.; Xu, C.; He, P.; Fang, Y. J. *Electroanal. Chem*. **2001**, 510, 78.

97 Dong, Y-G.; Ciu, H.; Wang, C-M. *J. Phys. Chem. B.* **2006**, 110, 18408.

98 Wang, J.; Yang, Z.; Wang, X.; Yang, N. *Talanta*, **2008**, 76, 85.

99 Devadoss, A.; Sphere-Deleze, A-M.; Bertoncello, P.; Marthi, R., Keyes, T. E.; Forster, R. J. *Langmuir*, **2010,** 26, 2130.

100 Tokel-Takvoryan, N. E.; Hemingway, R. E.; Bard, A. J. *J. Am. Chem. Soc*. **1973**, 95, 6582.

101 Sun, X.; Du, Y.; Dong, S.;Wang, E. *Anal. Chem*. **2005**, 77, 8166.

102 Zhang, L.; Xu, Z.; Sun, X.; Dong, S.; *Biosens. Bioelectron***, 2007**, 22, 1097.

103 Yun, W.; Xu, Y.; Dong, P.; Ma, X.; He, P.; Fang, Y. *Anal. Chim. Acta*, **2009,** 635, 58.

104 Chen, Z.; Zu, Y. *Langmuir*, **2007**, 23, 11387.

105 Qi, H.; Zhang,Y.; Peng,Y.; Zhang, C. *Talanta* **2008**, 75, 684.

106 Dong, Y-P.; Cui, Y.; Wang, C-M. *J. Phys. Chem. B.* **2006,** 110, 18408.

107 Vitt, J. E.; Johnson, D. C.; Engstrom, R. C. *J. Electrochem. Soc.* **1991**, *138*, 1637.

108 Sawyer, D. T.; Valentine, J. S. *Acc. Chem. Res.* **1981**, *14*, 393.

109 Qi, H. L.; Zhang, C. X.; *Anal. Chim. Acta*, **2004**, 501, 31.

110 Miao, W. J.; Bard, A. J. *Anal. Chem*. **2003**, 75, 5825.

111 Ozsoz, M.; Erdem, A.; Kerman, K.; Ozkan, D.; Tugrul, B.; Topcuoglu, N.; Ekren, H. M. Taylan, *Anal. Chem*. **2003,** 75, 2181.

112 Wang, H.; Zhang, C.; Li, Y.; Qi, H, *Anal.Chim. Acta*, **2006**, 575, 205.

113 Yang, M. L.; Liu, C. Z.; Qian, K. J.; He, P. G.; Fang, Y. Z. *Analyst,* **2002**, 127, 1267.

114 Dennany. L.; O'Reilly, E. J.; Keyes, T. E.; Forster, R. J. *Electrochem. Commun*. **2006**, 8, 1588.

115 Huang, X.; El-Sayed, I. H.; Yi, X.; El-Sayed, A. J. *Photochem Photobio B. Biology,* **2005,** 81, 76.

116 Gorton, L.; Dominguez, E. rev. *Mol. Biotech*. **2002**, 82, 371.

117 Bartlett, P. N.; Simon, E.; Toh, C. S. *Bioelectrochem*, **2002**, 56, 117.

118 Munteanu, F. D.; Mano, N.; Kuhn, A.; Gorton, L. *Bioelectrochem*, **2002**, 56, 67.

119 Wang, J.; Musame. M. *Anal. Chem*. **2003**, 75, 2075.

120 Zhu, L. *Sensors. Actuat B.Chem.* **2007**, 125, 254.

121 Mahesh, K. M.; Santhosh, P.; Gopalan, A.; Lee, K. P. *Talanta*, **2008**, 75, 1307.

122 Lee, W-Y.; Nieman, T. A. *Anal. Chem.* **1992**, 64, 261.

123 Choi, H. N.; Yoon, S. h.; Lyu, Y. K.; Lee, W. Y. *Electroanalysis*, **2007**, 19, 459.

124 Zhuang, Y. F.; Ju, H. X. *Anal. Lett.* **2005**, 38, 2077.

125 Tang, L.; Zeng, G.; Shen, G.; Zhang, Y.; Li, Y.; Fan, C.; Liu, C.; Niu, C. *Anal. Bioanal. Chem*. **2009**, 393, 1677.

126 Willets, K. A.; Van Duyne, R. P. *Annu. Rev. Phys. Chem.* **2007**. 58:267.

127 Ghosh, S. K.; Pal, T. *Chem. Rev*. **2007**, 107, 4797.

128 Lakowicz, J. R.; *Anal Biochem* ,**2001**, 298, 24.

129 Valeur, B.; *Molecular Fluorescence Principles and Applications*, Wiley-VCH Verlag GmbH, **2001**.

130 Lakowicz, J.R. *Principles of fluorescence spectroscopy*, Springer, 2nd Edition, **1999**.

131 Hunter, R. J. *Zeta potential in colloid science*, Academic, London, **1981**.

132 Wang, J. *Analytical electrochemistry*, 2nd edition, Wiley-VCH, **2000.**

133 Bard, A. J.; Faulkner, L. R. *Electrochemical Methods: Fundamental and Applications*, 2nd Edition, Wiley, New York, **2001**.

134 Forster, R. J.; Keyes, T. E.; Vos, J. *Interfacial supramolecular assemblies.* Wiley and Sons, **2003.**

135 Noffsinger, J. B.; Danielson, N. D. *Anal. Chem*., **1987**, 59, 865.

136 Leland, J. K.; Powell, M. J. *J. Electrochem. Soc.*, **1990**, 137, 3127.

137 Bard, A. J., *Fundamentals of ECL: Co-reactants; Electrogenerated Chemiluminescence*; Marcel Dekker.Inc, USA, **2004**.

138 Ala-Kleme, T.; Kulmana, S.; Jiang, Q. *Luminescence*, **2006**, 21, 118.

139 Miao, W.; Choi, J.; Bard, A. J. *J. Am. Chem. Soc.* **2002,** 124, 14478.

140 Wightman, R.; Forry, S.; Maus, R.; Badoco, D.; Pastore, P. *J. Phys. Chem. B* **2004**, 108, 19119.

141 Hogan, C. F.; Forster, R. J. *Anal. Chim. Acta*, **1999**, 396, 13.

Chapter 2

ECL Metallopolymers

2.1. Introduction

Electrogenerated chemiluminescence (ECL) involves the electron transfer reaction between two species resulting in an excited species that emits light.[1] Inorganic complexes are the focus of research because of their high ECL efficiency.[2] Among them, bipyridyl substituted ruthenium complexes like $[Ru(bpy)_3]^{2+}$ has gained momentum in the field of ECL due to their chemical stability, redox properties, excited state reactivity and lifetimes.[3] Balzani and co-workers have shown that by appropriate selection of the counter ion, $[Ru(bpy)_3]^{2+}$ can be dissolved in a variety of solvents ranging from dichloromethane to water.[2] Similarly, upon absorption of light $[Ru(bpy)_3]^{2+}$ undergoes a metal to ligand charge transfer (MLCT) in which one of the bipyridyl ligands is reduced and ruthenium is oxidised to form Ru(III), a strong oxidant and bpy^-, a strong reductant.[4]

$[Ru(bpy)_3]^{2+}$ produces ECL signals in the presence of oxalate based on direct oxidation of Ru at the anode, followed by the production of the emitting species.[5] There have been several reports on the ECL emission of the confined species at the electrode surface, e.g., Langmuir - Blodgett[6] or self assembled.[7] The concept of introducing $[Ru(bpy)_3]^{2+}$ in a micrometer thick polymer matrix e.g., a nafion layer, has showed maximum ECL emission,[8] which indeed has given a new dimension to the area of electrochemiluminescence. A new class of metallopolymers have been developed by covalently attaching the metal centres to the polymer backbone. Metallopolymers combine the processing advantages of polymers with the functionality provided by the presence of metal centres.[9] These metallopolymers are thermodynamically stable and show an intense ligand centred absorption peak in the visible region.

In particular, metallopolymers of the form $[M(bpy)_2PVP_n]^{2+}$ have been produced by coordinating $[M(bpy)_2Cl_2]$ to the conjugated polymer backbones, where M is Ru or Os; bpy is 2,2'-bipyridyl; PVP is poly(4-vinylpyridine) and n shows the number of

PVP units per metal centre.[10] Figure 2.1 shows the structure of *monomeric* Ru or Os substituted bipyridyl complex. Polymer backbones that have been utilised include poly(4-vinylpyridine) (PVP),[11,12] poly(N-vinylimidazole) (PVI),[10] poly(4-vinylpyridine/polystyrene) copolymer (PVP/PS)[13] and polystyrene with amide linkers.[14] Metallopolymers with different ratios of metal to polymer loadings ranging from 1:5 to 1:25 have been reported.[15]

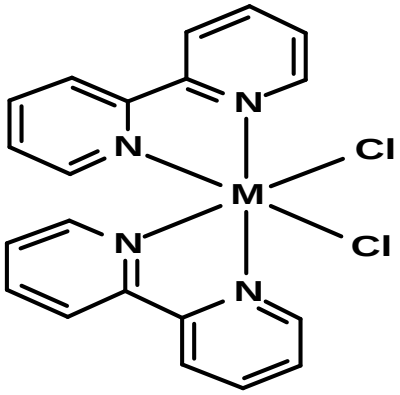

Figure 2.1: Chemical structure of $[M(bpy)_2Cl_2]$ monomer, where M may be ruthenium or osmium, bpy is 2,2'bipyridyl.

Amongst the various kinds of polymers, the poly (4-vinylpyridine) backbone is attractive due to the stronger affinity of pyridine groups towards the metal.[16] These metallopolymers formed with PVP backbone can be used to produce ECL in the presence of suitable co-reactants e.g., oxalate and Tripropyl amine (TPrA).[17] The ECL emission intensity from $[M(bpy)_2PVP_n]^{2+}$ metallopolymers depends on the concentration of the luminophores immobilised inside the polymer. However, the ECL efficiency is found to decrease at very high loading due to self-quenching.[18] Hence, it is important to maintain optimum loading of the metal centres in the polymer matrix. Metallopolymers with an optimum M:PVP loading of about 1:10 shows close to ideal electrochemical properties.[19]

The formation of various metallopolymers depends on the ability to replace the chloride ions in the $[M(bpy)_2Cl_2]$ complex. The replacement of chloride ion depends on the experimental conditions and the process of formation of pure $[M(bpy)_2PVP_{10}]^{2+}$ metallopolymer is described in Section 2.3.5 in detail. However,

one of the major barriers regarding the metallopolymers is that high molecular weight materials tend to be rather insoluble in common solvents. However, sonicating the metallopolymers for few hours in DMF makes them fairly soluble.

This chapter describes the synthesis and basic characterisation of monomeric and polymeric ruthenium and osmium polypyridyl complexes. The spectroscopic, electrochemical and electrochemiluminescence properties of these metallopolymers are investigated and presented in detail.

2.2. Experimental

2.2.1. Materials

Ruthenium (III) chloride (99.98%), lithium chloride (99%), 2,2'-bipyridine (99%), poly (4-vinylpyridine) (98%), silver nitrate (99.99%), sodium dithionite (86%), sodium perchlorate (99%), dimethylformamide (99.8%), methanol (99.9%) and ethanol (99.53%) were received from Sigma-Aldrich. Potassium hexachloro osmate (IV) (metal content 38.7% min) was received from Alfa Aesar. All the reagents were used as received. The aqueous solutions were prepared from Milli-Q reagent water (Millipore Corp.,), 18 MΩ cm.

2.2.2. Ruthenium Metallopolymer Synthesis

2.2.2.1. *cis*-$[Ru(bpy)_2Cl_2]$

cis-$[Ru(bpy)_2Cl_2]$ was synthesised by following the standard literature method.[20] $RuCl_3$ (0.78 g, 30mmol) was heated in dimethylformamide (DMF) (25 cm^3) and LiCl (0.18 g) was added while the reaction was maintained under a nitrogen atmosphere. 2,2'- bipyridyl (0.93 g, 59.66 mmol) was added slowly over a 25 min period and the solution was heated to reflux for 8 hours. The reaction mixture was cooled and acetone (500 cm^3) was added and the solution placed in freezer overnight. The purple powder that developed was collected by vacuum filtration and thoroughly washed with water to remove traces of $[Ru(bpy)_3]^{2+}$. The product was then washed with excess iced water and diethyl ether to aid drying. Typical yield was 80%.

^1H NMR (400 MHz, DMSO-d_6) numbering scheme shown in Figure 2.2 for $[Ru(bpy)_2Cl_2]$: δ = 9.96 (2-H, s), 8.65 (2-H, d), 8.5 (2-H, d), 8.1 (2-H, t), 7.7 (2-H, t), 7.68 (2-H, t), 7.5 (2-H, d), 7.4 (2-H, t). ES MS m/z (expt): 449.3.

2.2.2.2. Ruthenium Metallopolymer

The metallopolymer, $[Ru(bpy)_2PVP_{10}] (ClO_4)_2$, where PVP is poly(4-vinylpyridine), was synthesised using a modified literature method.[21] *cis*-$[Ru(bpy)_2Cl_2]$ (60 mg, 0.13 mmols) were added to $AgNO_3$ (39.2 mg, 0.23 mmols) in 10 cm^3 of reagent grade methanol followed by vigorous stirring for 1h.[22] The resulting precipitate of AgCl was removed by vacuum filtration and the filtrate, $[Ru(bpy)_2(H_2O)Cl]$, was evaporated to dryness. A 10-fold molar excess of poly (4-vinylpyridine) (average molecular weight = 160,000 g mol^{-1}) was dissolved in 50 cm^3 of 80:20 (v/v) water: ethanol, and this was added to the solid filtrate. The mixture was refluxed in the dark up to 72 h and was periodically monitored by cyclic voltammetry every 24h until reaction completion. The solvent was evaporated and adding 1 M $NaClO_4$ precipitated the product. Typical yield is 83%. Elemental analysis was C, 60; H, 4.7; N, 13.9. Anal. Calcd for $RuC_{70}H_{66}N_{14}Cl_2O_8$ was C, 69.8; H, 5.5, N, 16.2.

2.2.3. Osmium Metallopolymer synthesis

2.2.3.1. *cis*-$[Os(bpy)_2Cl_2]$

cis-$[Os(bpy)_2Cl_2]$ was prepared by the standard procedure[23] except that potassium hexachloro osmate, K_2OsCl_6, was used as the osmium precursor. In a typical preparation, K_2OsCl_6 (0.547 g) and 2,2'-bipyridyl (0.36 g) in 25 cm^3 ethylene glycol were heated to reflux for 8 hours under N_2. Since the crude reaction mixture contained both *cis*-$Os(bpy)_2Cl_2$ and *cis*-$[Os(bpy)_2Cl_2]^+$, an equal amount of saturated aqueous sodium dithionite was added to the cooled reaction mixture in order to reduce excess Os(III) to Os(II). The purple black powder that formed was isolated by vacuum filtration, washed with large excess of water to remove $[Os(bpy)_3]^{2+}$ and other ionic products, and washed with large volumes of ether to aid drying. Typical yield is 66%.

^1H NMR (400 MHz, D_6-DMSO) numbering scheme shown in Figure 2.3 for $[Os(bpy)_2Cl_2]$: δ = 9.57 (2-H, s), 8.6 (2-H, d), 8.4 (2-H, d), 7.6 (4-H, dt), 7.3 (4-H, d, t), 6.85 (2H, t). ES MS m/z (expt): 574.1.

2.2.3.2. Osmium Metallopolymer

The metallopolymer, $[Os(bpy)_2PVP_{10}] (ClO_4)_2$, where PVP is poly(4-vinylpyridine), was synthesised using a modified literature method.[21] The synthesis of osmium polymer is similar to that of the ruthenium metallopolymer synthesis except longer reflux times were required. *cis*-$[Os(bpy)_2Cl_2]$ (60 mg, 0.13 mmols) were added to $AgNO_3$ (39.2 mg, 0.23 mmols) in 10 cm^3 of reagent grade methanol followed by vigorous stirring for 1h.[22] The resulting precipitate of AgCl was removed by vacuum filtration and the filtrate, $[Os(bpy)_2(H_2O)Cl]$, was evaporated to dryness. A 10-fold molar excess of poly (4-vinylpyridine) (average molecular weight = 160,000 g mol^{-1}) was dissolved in 50 cm^3 of 80:20 (v/v) water: ethanol, and this was added to the solid filtrate. The mixture was refluxed in the dark and was periodically monitored by cyclic voltammetry for every 24h until completion. The solvent was evaporated and adding 1 M $NaClO_4$ precipitated the product. Typical yield is 89%. Elemental analysis was C, 50.9; H, 8; N, 7.5. Anal. Calcd for $OsC_{70}H_{66}N_{14}Cl_2O_8$ was C, 56.3, H, 4.45, N, 13.1.

2.2.4. Apparatus and Procedures

Absorbance measurements for all the samples were recorded using a Shimadzu UV-240 spectrophotometer using 1-cm optical path length quartz cuvette, which allows measurement in the spectral range from 300 to 1100 nm. The emission spectrum for all the samples was recorded using a Perkin-Elmer LS-50 luminescence spectrometer. The excitation wavelength used was 460 nm and 355 nm for Ru and Os, respectively. The slit width was maintained at 10 nm for all the measurements. Luminescence lifetime studies were made on a PicoQuant PDL-800B pulsed diode laser controller and FluoTime 100 time-correlated single photon counting system (TCSPC) with pulsed laser source with cut-on filter of 530 nm. The laser used for exciting the ground state Ru and Os molecules are 460 nm and 355 nm, respectively. TCSPC analysis was preformed using PicoQuant FluoFit software.

^{1}H NMR spectra were recorded on Bruker Advance 400 NMR spectrometer and the free induction decay (FID) profiles processed using XWIN-NMR software package. The measurements were carried out in deuterated dimethyl sulfoxide (d_6-DMSO).

The molecular mass of the Ru/Os monomers was found using Bruker-Esquire-LC/MS series mass spectrometer. The Cole Parmer 74900 series software was used to analyse the data. A small amount (~2 mg) of the monomers was dissolved in 2 cm^3 HPLC grade acetonitrile. Approximately 200 µl of the sample was injected per hour and the spectra were recorded. Elemental analysis was performed in University College Dublin using an Exeter Analytical CE440 CHN analyser. High Performance Liquid Chromatography (HPLC) was used to analyse the purity of the compounds. C_{18} columns were used with the UV-Vis spectrophotometer as the detector.

Cyclic voltammetry was performed using a CH Instrument Model 600c electrochemical workstation and conventional three-electrode cell. A glassy carbon electrode of 3 mm diameter was used as the working electrode and a platinum wire as the counter electrode. Glassy carbon electrodes were cleaned by successive polishing using 3 µm and 0.5 µm alumina slurry, followed by sonication for 15 minutes in acetone, ethanol, and water, respectively. All potentials are quoted versus a Ag/AgCl/3M KCl reference electrode and all the measurements were recorded at room temperature. Adherent layers of the $[M(bpy)_2PVP_{10}](ClO_4)_2$ where M is Ru or Os, were obtained by drop-casting 100 µl of 20 µM Ru/Os metallopolymer solution on the glassy carbon electrode and then evaporating to dryness in the dark overnight. Surface coverages were experimentally determined by graphical integration of background corrected cyclic voltammograms recorded at a slow scan rate (5 mV s^{-1}).

The ECL measurements involving the simultaneous detection of light and current were performed using the CH instrument model 720b connected to an Oriel 70680 photo multiplier tube (PMT). The PMT was biased at -850 V by a high voltage power supply (Oriel, model 70705) and amplifier/recorder (Oriel, model 70701). During the experiments the cell was kept in a light-tight box in a specially designed holder so that the working electrode was always positioned opposite the fibre optic bundle, the other end of which was coupled to the PMT.

2.3. Results and Discussion

2.3.1. Spectroscopic Analysis

Nuclear Magnetic Resonance (NMR) Spectroscopy is one of the principle techniques used in analytical chemistry to obtain the physical, chemical and structural information about the molecules due to the observed chemical shifts or Zeeman effects on the resonant frequencies of the nuclei present in the compounds.[24] The ruthenium and osmium bipyridyl complexes are diamagnetic and hence sharp NMR spectra can be obtained. The NMR spectrum was recorded for $[M(bpy)_2Cl_2]$ monomers, where M is Ru or Os; bpy is 2,2'-bipyridyl. Approximately 10 mg of the sample dissolved in approximately 700 µl of deuterated dimethyl sulfoxide (DMSO-d_6) was used for ^{1}H NMR measurements.

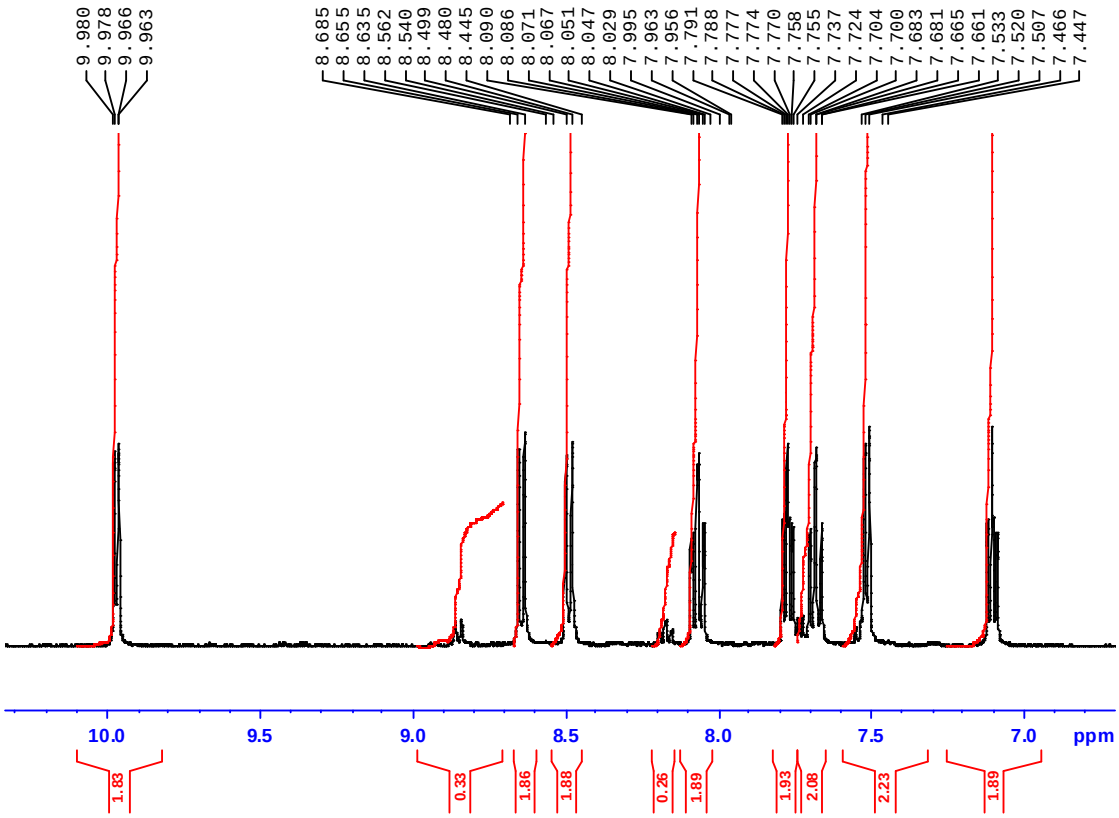

Figure 2.2: Proton nuclear magnetic resonance spectra for $[Ru(bpy)_2Cl_2]$. The concentration of $[Ru(bpy)_2Cl_2]$ was 0.043 M. Deuterated DMSO-d_6 was used as the solvent.

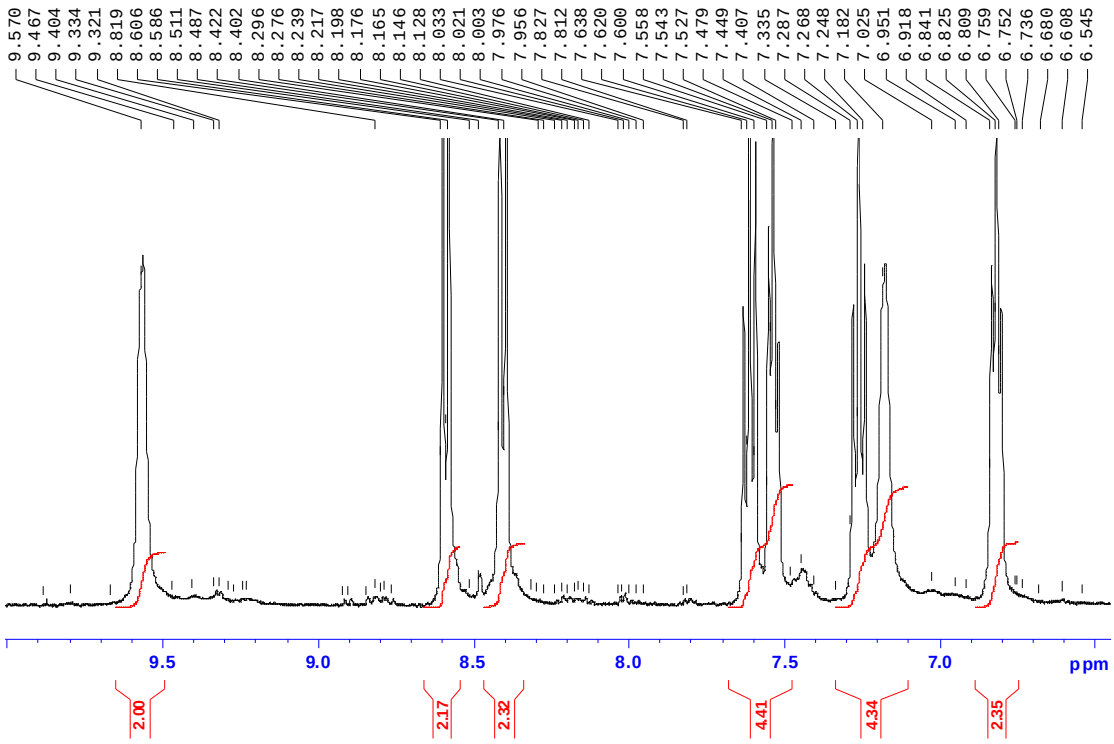

Figure 2.3: Proton nuclear magnetic resonance spectra for $[Os(bpy)_2Cl_2]$. The concentration of $[Os(bpy)_2Cl_2]$ complex was 0.034 M. Deuterated DMSO-d_6 was used as the solvent.

Sharp well-defined ^1H NMR resonances were observed for the ruthenium and osmium bipyridyl compounds. Figure 2.2 and 2.3 shows the proton nuclear magnetic resonance spectra for $[Ru(bpy)_2Cl_2]$ and $[Os(bpy)_2Cl_2]$, respectively. The x-axis of NMR spectrum was calibrated against the solvent and hence, any effects due to the solvent identity were removed. The structure of $[M(bpy)_2Cl_2]$, where M is Ru or Os, is shown in Figure 2.1.

The integration of the peaks in NMR spectra can provide the information on the purity of the samples. Here, for both ruthenium and osmium dichloride complexes, the proton integration confirms the existence of 16 protons, which is in agreement with the chemical structure. The proton adjacent to the coordinated nitrogen in the bipyridyl ligand corresponds to the singlet peak at 9.95 ppm, which is shifted downfield due to the higher electron affinity of the nearby chloride ions in $[Ru(bpy)_2Cl_2]$.

The single peak in the NMR spectrum of $[Os(bpy)_2Cl_2]$ shows a similar downfield shift of around 9.5 ppm, yet the magnitude of the shift is lesser than that of its Ru analogue. The splitting of NMR peaks can be assigned to the presence of interacting nuclei that must be bonded in relatively close proximity, which perturbs the observed nuclei. The NMR spectra observed for Ru and Os bipyridyl complexes shows aromatic protons between 6.5 and 9 ppm. These peaks arise due to the presence of bipyridyl ligands and are consistent with previously reported data. The NMR spectra for Ru and Os metallopolymers are complex and are not discussed here.

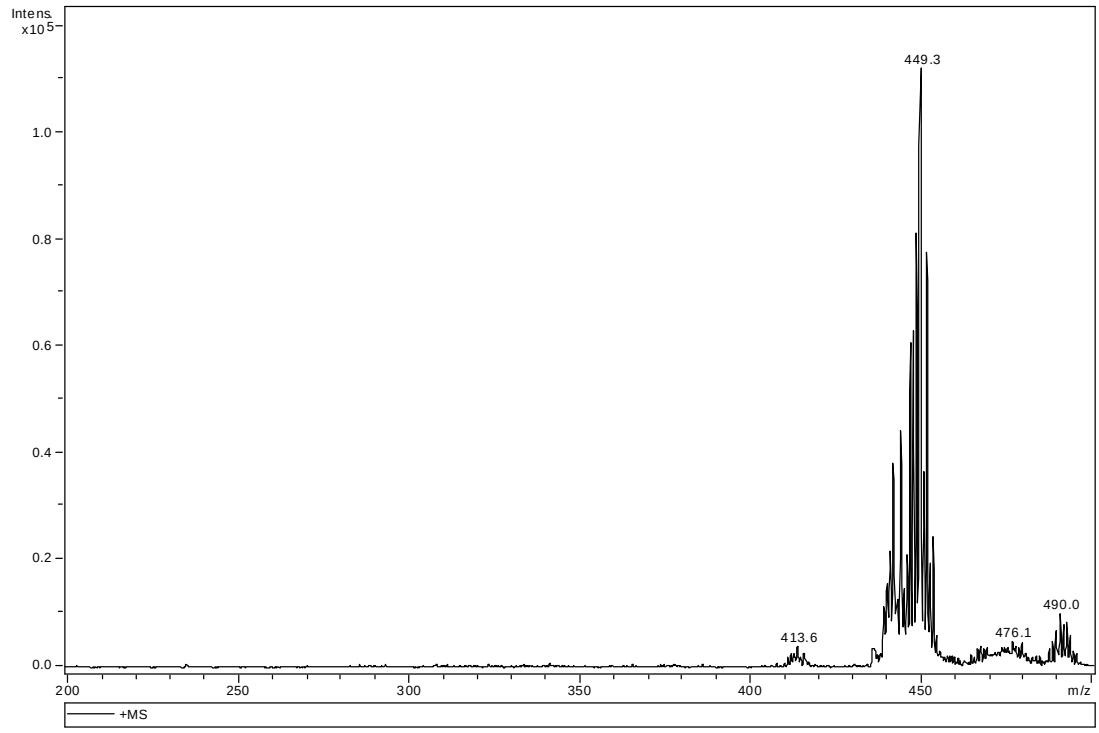

Figure 2.4: Mass spectra for 15 mM $[Ru(bpy)_2Cl_2]$ in HPLC grade Acetonitrile.

Also the structural characterisation of Ru and Os dichloro complexes were conducted using elemental analysis, mass spectrometry and high performance liquid chromatography. The molecular mass of the monomeric ruthenium and osmium complex can be evaluated from the mass spectra. Figure 2.4 and 2.5 gives the spectrum obtained from the mass spectrometric analysis for $[Ru(bpy)_2Cl_2]$ and $[Os(bpy)_2Cl_2]$, respectively. The presence of isotope structures at 450 m/z (Figure 2.4) and 575 m/z (Figure 2.5) in the mass spectrum confirms the presence of Ru and Os. The molecular weight obtained from the experiments is indistinguishable from the anticipated value. The molecular weight of metallopoymers is very large due to

the high molecular weight of the poly (4-vinylpyridine) polymer backbone (M_w= 160,000). Hence, the molecular weight of the monomers was experimentally calculated.

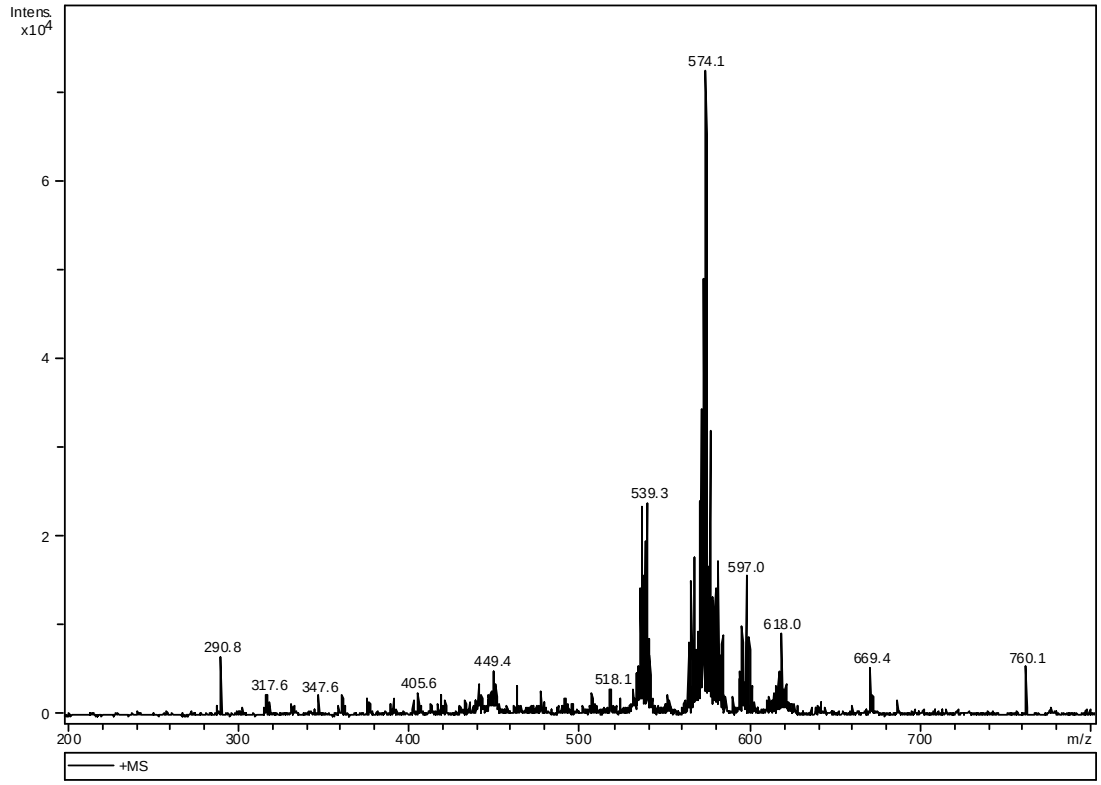

Figure 2.5: Mass spectra for 12 mM [$Os(bpy)_2Cl_2$] in HPLC grade Acetonitrile.

High-Performance Liquid Chromatography was used to analyse the purity of the compounds. [$Ru(bpy)_2Cl_2$] and [$Os(bpy)_2Cl_2$] were dissolved in HPLC grade acetonitrile. The solution purity was checked with the chromatographic technique using C_{18} columns. The UV absorption spectrophotometer (200-900 nm) was used as the detector. Figure 2.6 shows the chromatogram obtained for the monomers of Ru (dashed line) and Os (solid line) bipyridyl metal complexes.

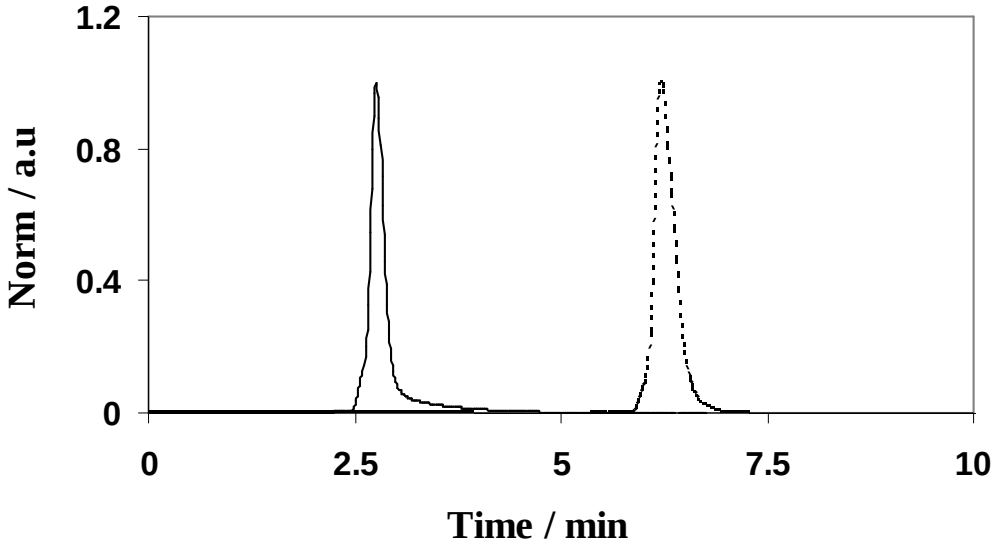

Figure 2.6: HPLC traces obtained for $[Ru(bpy)_2Cl_2]$ (dashed line) and **[**$Os(bpy)_2Cl_2$] (solid line). C_{18} columns were used and the samples were dissolved in HPLC grade acetonitrile. Mobile phase was 80:20 v/v, HPLC grade acetonitrile and water.

The chromatogram intensities were normalised to unity. The single peak in the chromatogram shows that only one component is present in the compound, which is attributed to the high purity of the samples. The retention time is different for Ru and Os monomers because of the difference in the solubility of the complexes in the mobile phase. The detector employed in the HPLC study is a diode array UV-Visible absorption spectrophotometer. Figure 2.7 and 2.8 shows the UV-Vis-NIR absorption spectrum obtained at the detector for $[Ru(bpy)_2Cl_2]$ and $[Os(bpy)_2Cl_2]$ complexes, respectively.

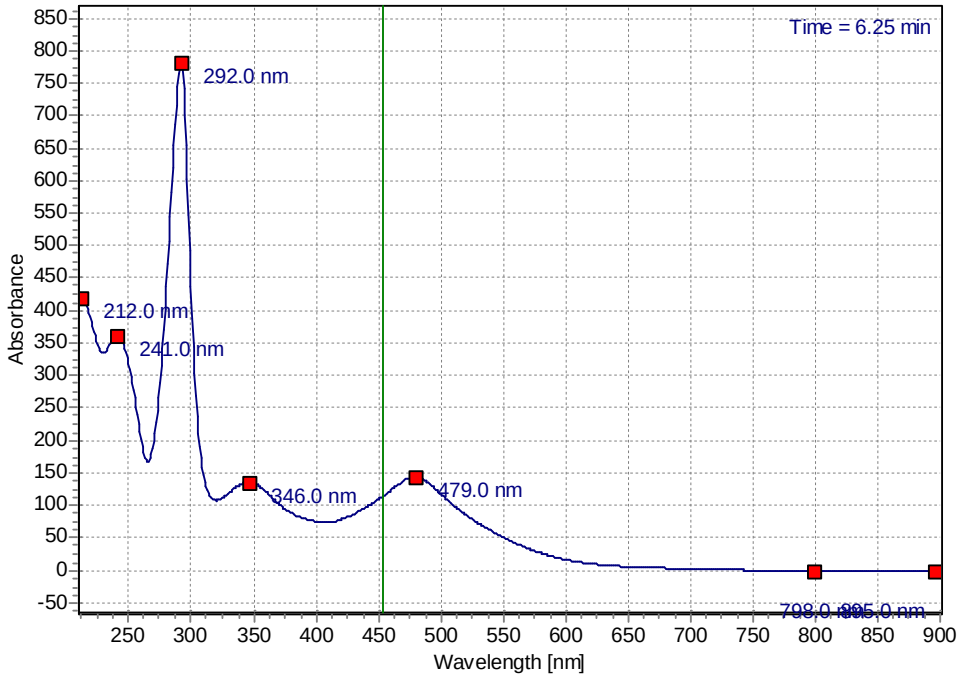

Figure 2.7: UV-Vis spectra obtained at the HPLC detector for $Ru(bpy)_2Cl_2$ solution.

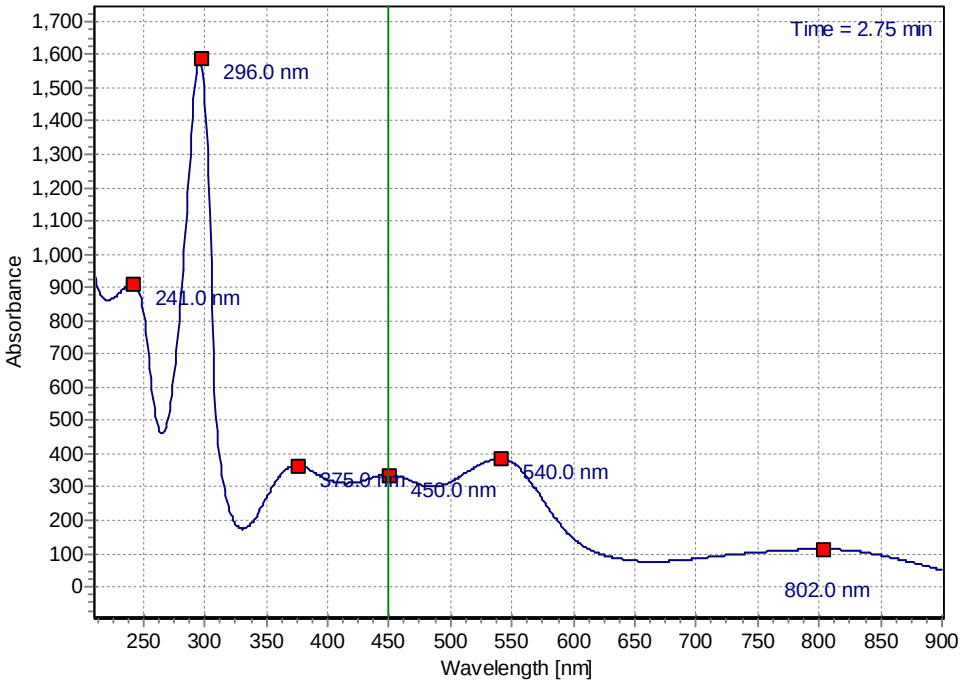

Figure 2.8: UV-Vis spectra obtained at the detector of HPLC for $Os(bpy)_2Cl_2$ solution.

The UV-Vis-NIR spectrum obtained from the detector is in good agreement with the solution phase extinction spectrum obtained for Ru (Figure 2.10) and Os (Figure 2.11) dichloride samples, respectively. Thus, the presence of single peak in the chromatogram and the output absorption spectra obtained at the detector are sufficient enough to confirm the high purity of the monomeric bipyridyl metal complexes.

2.3.2. Elemental Analysis

The elemental analysis for ruthenium and osmium substituted metallopolymer was carried out in University College Dublin using an Exeter Analytical CE440 CHN analyser. During the measurement, the samples are combusted in oxygen and passed through a series of traps and detectors. The signals were recorded for the amount of carbon dioxide (C), water (H) and nitrogen (N). The experimental and theoretical CHN values for Ru and Os substituted polymers are listed in Table 2.1.

Table 2.1. CHN values for Ru and Os containing metallopolymers showing both the experimental and theoretical values.

Compounds	Experimental values (Mass percent %)			Theoretical values (Mass percent %)		
	C	H	N	C	H	N
$[Ru(bpy)_2PVP_{10}](ClO_4)_2$	48.6	7.08	2.7	59.9	4.74	13.97
$[Os(bpy)_2PVP_{10}](ClO_4)_2$	48.32	3.93	7.45	56.3	4.45	13.1

A slight discrepancy between the theoretical CHN values and the experimentally evaluated CHN values might be due to the presence of some traces of the solvents (water molecules) that has been used during the synthesis. The presence of water could also be due to the highly hygroscopic nature of Ru and Os polymers, which will tend to form hydrogels that could affect the CHN ratios. Hence the experimentally estimated CHN values were corrected to the solvent effects. It was found that the experimentally calculated CHN values coincides (~ 95%) with the theoretically predicted CHN values by eliminating the presence of solvent molecules. Assuming no losses occur during the extraction of metallopolymer, the ratio of Ru to pyridine units was maintained to be 1:10 by controlling the initial amounts of $Ru(bpy)_2Cl_2$ and poly(4-vinylpyridine).

2.3.3. Absorption and Emission Spectroscopy

Electronic spectroscopy is a useful technique to characterise the metallopolymers. The absorption bands observed in the UV-Visible spectrum can provide a limited insight into the coordination sphere of the metal centre. The UV-Visible absorption spectrum was recorded for both ruthenium and osmium containing monomeric bipyridyl complexes. Figure 2.9 shows the absorption spectra corresponding to the monomeric $[Ru(bpy)_2Cl_2]$ (— - pink line) and $[Os(bpy)_2Cl_2]$ (— - blue line), respectively.

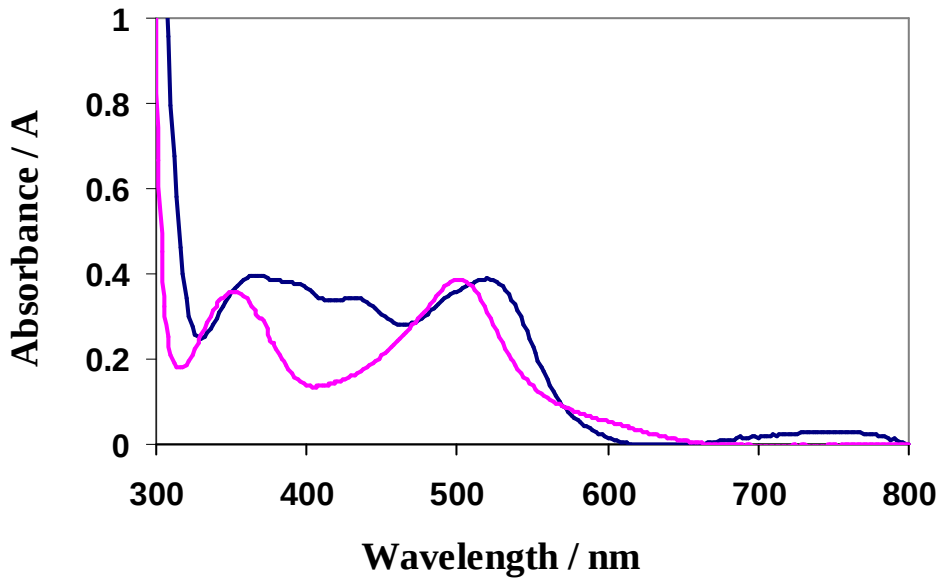

Figure 2.9: UV-Vis absorption spectrum recorded for 50 µM solutions of $[Ru(bpy)_2Cl_2]$ (— - pink line) and $[Os(bpy)_2Cl_2]$ (— - blue line) in acetonitrile.

The absorption bands observed between 200-300 nm correspond to the ligand centred $\pi \rightarrow \pi^*$ transition. The metal-to-ligand charge transfer (MLCT) corresponds to the transition from $d \rightarrow \pi^*$ appears in the region 300-800 nm.[25] Figure 2.10 and 2.11 shows the UV-Vis spectrum (solid line) for $[Ru(bpy)_2PVP_{10}]^{2+}$ and $[Os(bpy)_2PVP_{10}]^{2+}$ metallopolymers, respectively.

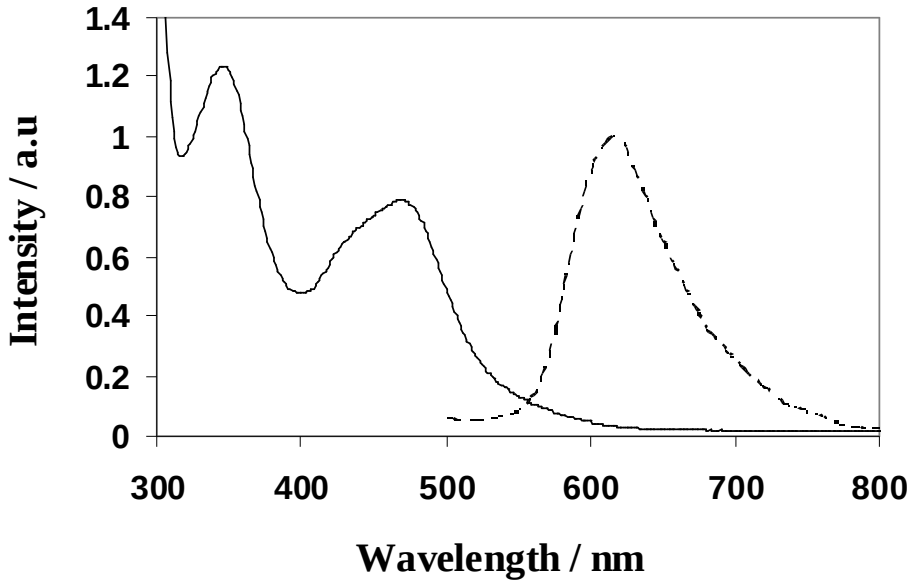

Figure 2.10: UV-Visible absorption and luminescence spectra for 50 µM $[Ru(bpy)_2PVP_{10}]^{2+}$ dissolved in ethanol showing the absorption maximum (solid line) due to MLCT and luminescence (dash line) arises from the triplet state.

The absorption spectrum for the ruthenium metallopolymer is dominated by two characteristic peaks around 350 nm and 460 nm, which can be attributed to the metal to ligand charge transfer ($d \rightarrow \pi^*$) transitions. Using the reported molar extinction coefficient, the concentration of Ru metallopolymer was calculated using the Beer-Lambert's law. The molar extinction coefficient of $[Ru(bpy)_2PVP_{10}]^{2+}$ metallopolymer is found to be ~11,220 $M^{-1}cm^{-1}$.[10] The analogous $[Os(bpy)_2PVP_{10}]^{2+}$ metallopolymer exhibits MLCT transitions around 350 nm and 460 nm (solid line in Figure 2.11) with an additional broad feature with absorption maximum at 650 nm. The presence of an additional peak at longer wavelength has been assigned to a spin forbidden triplet-MLCT transition, which is partially allowed by the considerable spin-orbit coupling present due to the heavy Os metal ion.[10] The molar extinction coefficient for osmium metallopolymer is found to be ~16,982 $M^{-1}cm^{-1}$.[10]

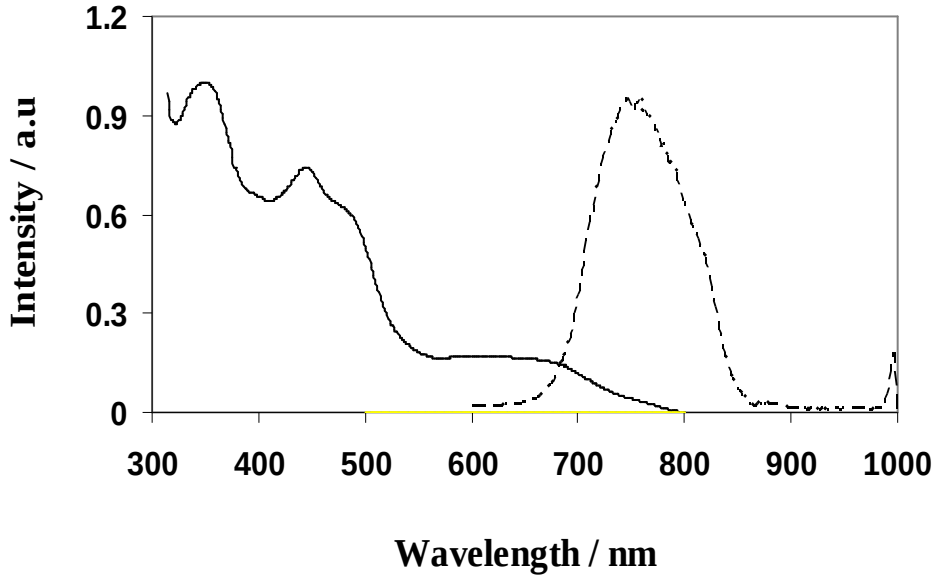

Figure 2.11: The normalised UV-Visible absorption and luminescence spectra of 50 μM $[Os(bpy)_2PVP_{10}]^{2+}$ metallopolymer in DMF showing the absorption maximum (solid line) due to MLCT and luminescence (dash line) due to triplet state.

The luminescence occurs from a triplet MLCT states.[4] The monomeric Ru and Os dichloride complex do not show any luminescence. When the Ru metallopolymer is excited at a wavelength corresponding to the MLCT band, an electron is promoted from the metal ground state to the π^*-orbital of 2,2'-bipyridyl ligand, which then decays back to the ground state by emitting at 610 nm. The $[Os(bpy)_2PVP_{10}]^{2+}$ metallopolymer emits at 760 nm upon excitation at 355 nm. The observed emission in both Ru and Os metallopolymer strongly suggests the presence of $[MN_6]^{2+}$ moieties in the polymer, so that the two nitrogen units from the polymer backbone are bonded to the metal centres. However, it is important to consider the fact that the observed emission does not mean all the N_6 moieties are excited as the possibility of excitation of the metal centres depends on the quantum efficiency of the sample.

The emission quantum yields and lifetimes of ruthenium and osmium metallopolymers can yield a wealth of information on the relative efficiencies of radiative and non-radiative process, as well as the rates of competing photochemical reactions.[26] The quantum yield of $[Ru(bpy)_2PVP_{10}]^{2+}$ and $[Os(bpy)_2PVP_{10}]^{2+}$ metallopolymer was measured using a standard procedure.[27] The same number of

photons was absorbed by the standard and the respective ruthenium and osmium metallopolymer by matching the absorbance at the excitation wavelength. Hence, a sample ratio of the integrated luminescence intensities of the two solutions will yield the ratio of their quantum yield.

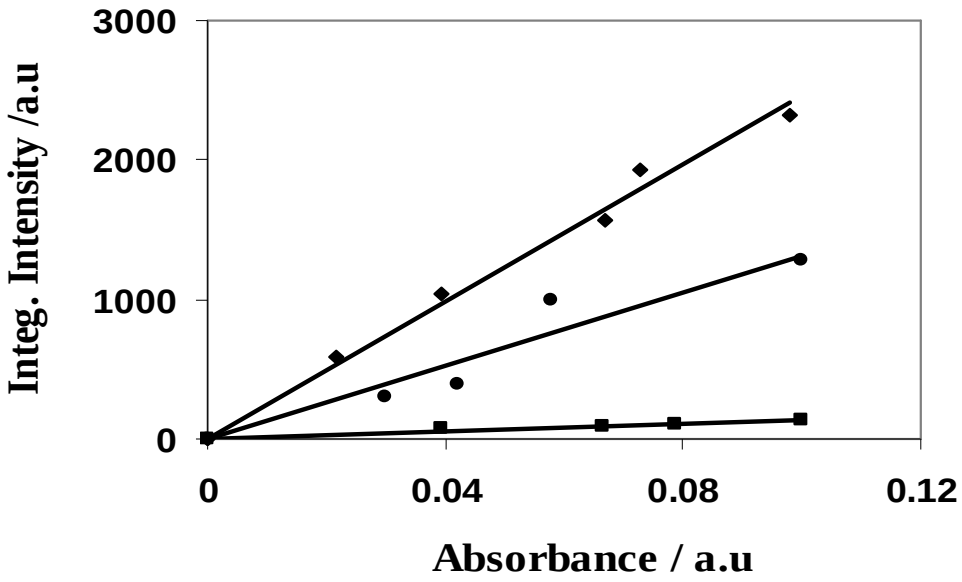

Figure 2.12: Linear plots of area of the emission spectrum *versus* the absorbance for $[Ru(bpy)_2PVP_{10}]^{2+}$ metallopolymer (■),$[Os(bpy)_2PVP_{10}]^{2+}$ metallopolymer (●) and standard $Ru(bpy)_3Cl_2$ (♦). All the samples were prepared in 18 MΩ Millipore water.

Figure 2.12 shows the integrated area of the luminescence spectrum plotted *versus* the absorbance maximum for ruthenium (■) and osmium metallopolymers (●), respectively. The gradient for each sample is proportional to that sample's luminescence quantum yield. Absolute values of quantum yield for $[Ru(bpy)_2PVP_{10}]^{2+}$ and $[Os(bpy)_2PVP_{10}]^{2+}$ metallopolymers are calculated using the following equation 2.1: [28]

$$\phi_X = \phi_{ST}\left(\frac{A_X}{A_{ST}}\right)\left(\frac{n_X^2}{n_{ST}^2}\right) \quad \text{.....(2.1)}$$

where the subscripts ST and X represent the standard and the test samples respectively, Φ is the luminescence quantum yield, *A* is the gradient of the plot of

integrated area of emission spectrum *vs* absorbance and n is the refractive index of the solvent.

It has been reported that the nature of the solvent exerts an important influence on quantum yields.[29] Whilst the excitation coefficient and radiative decay rates are independent of the solvent polarity, the rates of non-radiative decay (k_{nr}) greatly depend on solvent polarity and hence affect the quantum yield.[4] Hence, the quantum yield of all the samples was measured in de-aerated aqueous medium. $[Ru(bpy)_3]Cl_2$ was used as the standard sample, which has a quantum yield of 0.042 in deaerated aqueous solution.[30]

As described earlier, the slopes of the graph in Figure 2.12 are proportional to the quantum yield of $[Ru(bpy)_3]Cl_2$ (♦), $[Os(bpy)_2PVP_{10}]^{2+}$ (●) and $[Ru(bpy)_2PVP_{10}]^{2+}$ (■), respectively. The quantum yield of $[Ru(bpy)_2PVP_{10}]^{2+}$ metallopolymer was calculated as 0.0024. The quantum yield of $[Os(bpy)_2PVP_{10}]^{2+}$ metallopolymer was found to be 0.022.

2.3.4. Luminescence Lifetimes

The luminescent lifetime can provide useful insights into the excited-state electron or energy transfer processes. The lifetimes of the Ru and Os metallopolymer solutions were measured using the FluoTime 100 Time-Correlated Single Photon Counting (TCSPC) instrument. The metallopolymer was dissolved in DMF:ethanol mixture (1:1, v/v). 20 µM ruthenium and osmium metallopolymer solutions were used to measure the lifetimes.

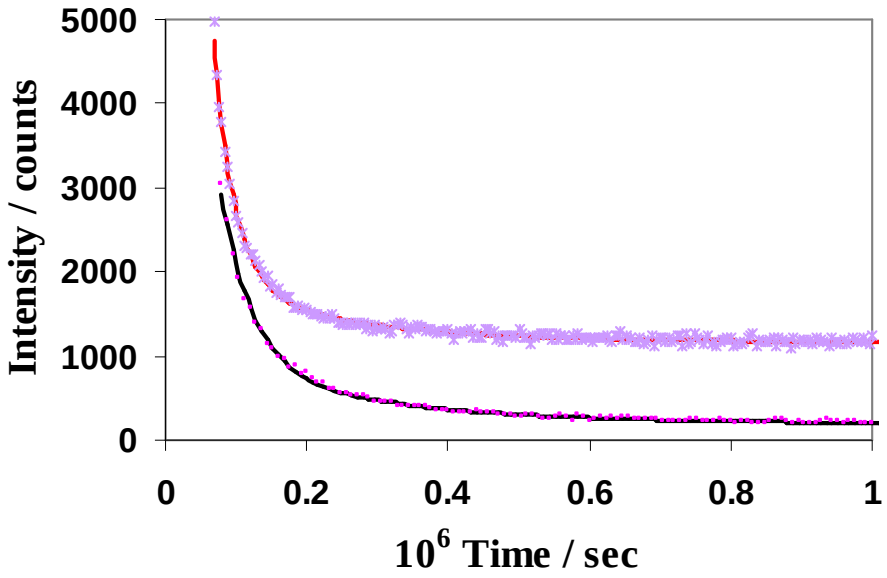

Figure 2.13: Luminescence decay of 20 µM $[Ru(bpy)_2PVP_{10}]^{2+}$ metallopolymer in aerated (■- pink dots) and de-aerated (×- purple cross) solution. The black line (—) and the red line (—) shows the exponential tail fit for the aerated and de-aerated samples respectively.

The excitation wavelength for ruthenium and osmium metallopolymer solutions is 460 nm and 355 nm, respectively. Figure 2.13 shows the exponential decay curve for the 20 µM ruthenium metallopolymer in both aerated and de-aerated solutions.

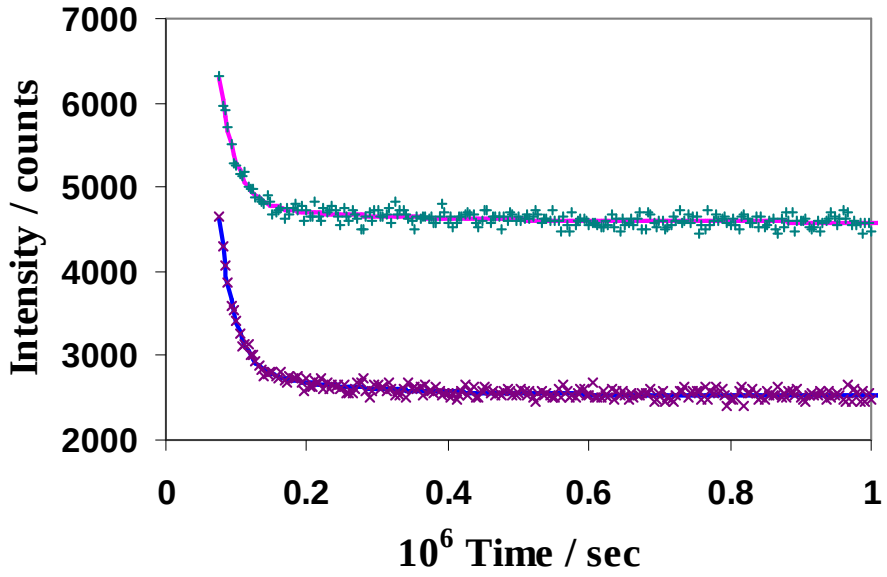

Figure 2.14: Luminescence decay of 20 µM $[Os(bpy)_2PVP_{10}]^{2+}$ metallopolymer in aerated (×- purple cross) and de-aerated (+- green plus) solution. The solid lines of blue (—) and pink (—) shows the exponential tail fit for the aerated and de-aerated samples respectively.

Figure 2.14 shows the best fit obtained for 20 µM osmium containing metallopolymer solutions. The time-correlated single photon counting experiments reveal that the excited state decays for the pure metallopolymer, $[M(bpy)_2PVP_{10}](ClO_4)_2$, where M are Ru or Os, is bi-exponential. This multi-exponential behaviour may arise due to the different microenvironments that exist in the samples including cross-linked chains that increase the rigidity of the complex and decrease the rate of vibrational relaxation.[31] Atmospheric oxygen is an efficient quencher of luminescence lifetime.[4] Hence, the samples were de-aerated by purging with nitrogen for at least 15 minutes before the excited state lifetimes were recorded. Table 2.2 shows the lifetimes obtained in triplet measurements for ruthenium and osmium metallopolymers in both aerated and de-aerated conditions.

Table 2.2: Luminescence lifetimes for metallopolymer solutions of the kind $[M(bpy)_2PVP_{10}]^{2+}$, where M may be Ru or Os in the presence and absence of oxygen.

Compound	Lifetimes in aerated sample (ns)		Lifetimes in de-aerated sample (ns)	
	τ_1	τ_2	τ_1	τ_2
$[Ru(bpy)_2PVP_{10}]^{2+}$	49±5 (75%)	332±8 (24%)	55±7 (60%)	190±21 (38%)
$[Os(bpy)_2PVP_{10}]^{2+}$	17±0.8 (90%)	138±5 (9.9%)	22±2 (87%)	230±10 (12%)

The lifetimes of ruthenium and osmium metallopymers were found to be higher in the degassed samples. This is attributed to the elimination of collisional oxygen quenching in the nitrogen environment. The average lifetimes for the ruthenium metallopolymer under aerated and de-aerated conditions were around 49±5 ns (75%): 332±8 ns (24%) and 55±7 ns (60%): 190±21 ns (38%) respectively. As expected, the longer lifetime component of Ru is more oxygen sensitive as they persist for longer and is more easily quenched by oxygen. It has been shown that $[Ru(bpy)_2PVP_{10}]^{2+}$ metallopolymer shows a luminescent decay lifetime of about 69±5 ns.[31] The observed lifetime for the metallopolymer is lower than $[Ru(bpy)_3]^{2+}$. This might be due to the self-quenching of the spatially close ruthenium centres in the polymer but also significantly might be due to the lower luminescence quantum yield

Significantly, the lifetimes in the aerated and de-aerated osmium metallopolymer solutions were found to be around 17.4±0.8 (90%): 138±5 (9.9%) and 22±2 ns (87%): 230±10 ns (12%), respectively. The reported excited state lifetime of osmium metallopolymer in solution exhibits a dual-exponential decay with an average lifetime of about 45±7 ns.[31] The deviation of osmium metallopolymer lifetimes from these values may be due to the difference in the solvent, which can influence the rigidity of the polymer and therefore the rate of non-radiative decay.

2.3.5. Electrochemical Characterisation

Cyclic voltammetry gives qualitative information about the species under study.[32] The position of the peak and the shape of the peak give kinetic information that takes place at the electrode surface. The Figure 2.15 shows the cyclic voltammogram of monomeric *cis*-[$Ru(bpy)_2Cl_2$] and *cis*-[$Os(bpy)_2Cl_2$] (Inset figure) films formed by drop-casting 50 µl solution on 3 mm glassy carbon electrode.

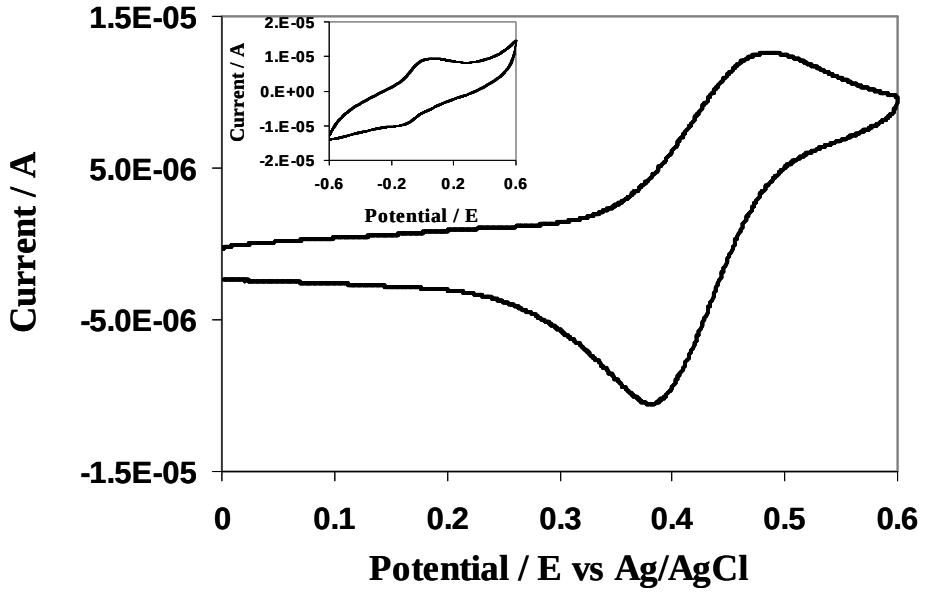

Figure 2.15: Cyclic voltammogram of [$Ru(bpy)_2Cl_2$] dissolved in dimethyl sulfoxide. The inset figure shows the voltammetric response of [$Os(bpy)_2Cl_2$] film. The films were prepared by drop-casting 50 µl solution on 3 mm glassy carbon electrode. 0.5 M H_2SO_4 was used as the supporting electrolyte. The scan rate is 50 mV s^{-1}.

The redox couples of both ruthenium and osmium monomeric bipyridyl complex exhibits the oxidation at a far low potential when compared to ruthenium/osmium tris-bipyridyl systems. Metallopolymers of the type $[M(bpy)_2PVP_{10}]^{2+}$ were synthesised using [$M(bpy)_2Cl_2$] as the starting materials, where M is Ru or Os. During the process of synthesis, the reaction solutions were periodically monitored using cyclic voltammetry. Figure 2.16 shows the voltammetric response (every 24

hours) of the ruthenium metallopolymer at a scan rate of 100 mV s^{-1}. 0.5 M H_2SO_4 is used as the supporting electrolyte.

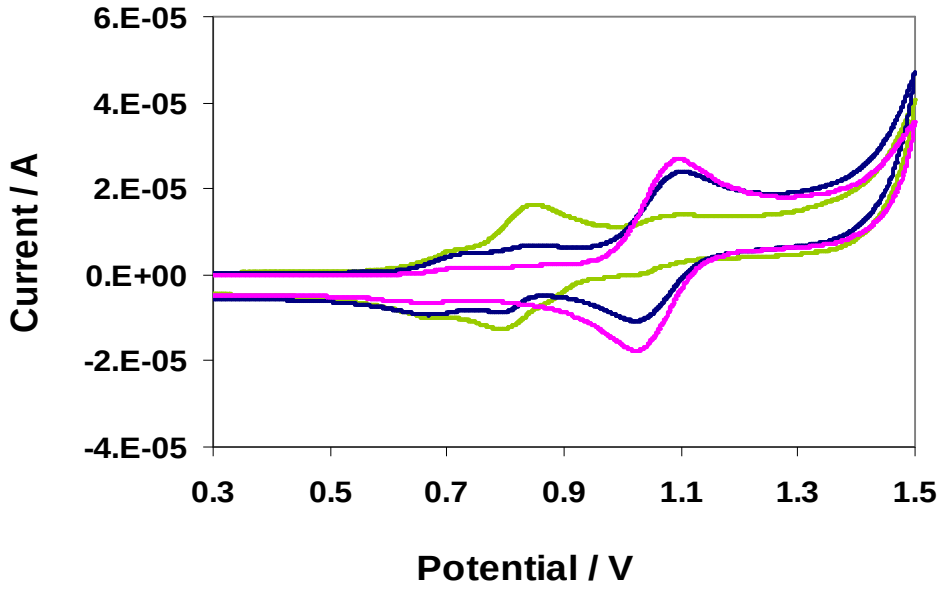

Figure 2.16: Cyclic voltammetric response (24 hrs- green line (—), 48hrs- blue line (—) and 72 hrs- pink line (—)) of the ruthenium metallopolymer films at a scan rate of 100 mV s^{-1} in 0.5 M H_2SO_4 as electrolyte.

The changes in the oxidation potential indicate the reaction progress. The peak around 0.8 V corresponds to the mono substituted compound (N5Cl moieties), which is formed due to the removal of one Cl from $[Ru(bpy)_2Cl_2]$ moiety. The voltammetric response (— - green line) shows that [N5Cl] moieties are formed at the early stage of the synthesis. This indicates that the removal of Cl resulted in the binding of monomeric Ru metal complex to the PVP backbone. Increased reflux times clearly lead to the suppression of the peak at 0.8 V whereas that at 1.1 V increases (— - blue line). The peak at 1.1 V corresponds to the N6 moieties.[17] This shows that the [N5Cl] moieties formed at the initial stage are converted into N6 moieties by replacing the chloride with a pyridine unit. Significantly, prolonged reflux results in the formation of pure $[Ru(bpy)_2PVP_{10}]^{2+}$ which is likely to have the redox peak at 1.1V.

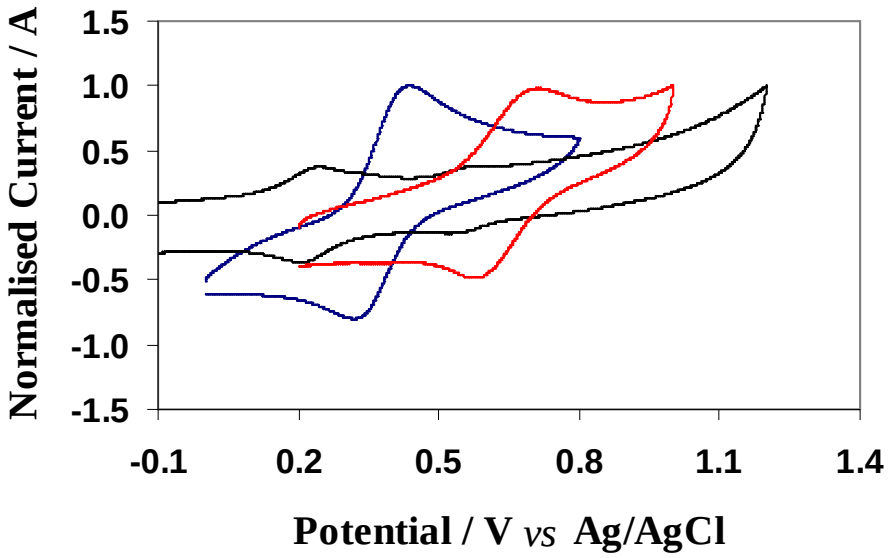

Figure 2.17: Voltammetric response (week 1- black line (—), week 2- blue line (—) and week 3- red line (—)) of the osmium metallopolymer at a scan rate of 100 mVs^{-1}. 0.5 M H_2SO_4 was used as the supporting electrolyte.

The synthesis of Os metallopolymer is similar to that of the Ru metallopolymer except longer reflux times were required for the former because of the inertness of osmium metal centre. Figure 2.17 shows the cyclic voltammetric response of the Os metallopolymer recorded for different reaction times. As the volumes deposited on the electrode surface are not consistent between the reflux times and hence the associated charge cannot be interpreted quantitatively. Yet, the information on the reaction progress can be achieved from the clear shift in the redox peaks in the voltammogram. The peak at 0.2 V observed in the first week of the reaction corresponds to $[Os(bpy)_2Cl_2]$, the starting material (as shown in Figure 2.15). The peak observed at 0.4 V confirms the formation of the monochloro substituted complex of osmium, $[Os(bpy)_2PVPCl]^+$,[34] which in the presence of water and further reflux results in the formation of pure $[Os(bpy)_2PVP_{10}]^{2+}$. The pure Os metallopolymer powder was precipitated by adding 0.1 M $NaClO_4$.

The general reaction mechanism during the formation of the Ru and Os containing metallopolymers can be expressed as follows:

$$[M(bpy)_2Cl_2] + AgNO_3 \longrightarrow [M(bpy)_2(H_2O)Cl] + AgCl\downarrow \text{.....(2.2)}$$

$$[M(bpy)_2(H_2O)Cl]^+ + PVP \xrightarrow{80:20, H_2O:EtOH} [M(bpy)_2PVPCl]^+ + solvent \text{.....(2.3)}$$

$$[M(bpy)_2PVPCl]^+ + H_2O \rightarrow [M(bpy)_2PVP(H_2O)]^{2+} + Cl^- \text{.....(2.4)}$$

$$[M(bpy)_2PVP(H_2O)]^{2+} + PVP \rightarrow [M(bpy)_2PVP]^{2+} + H_2O \text{.....(2.5)}$$

where PVP is poly (4-vinylpyridine) and EtOH is Ethanol.

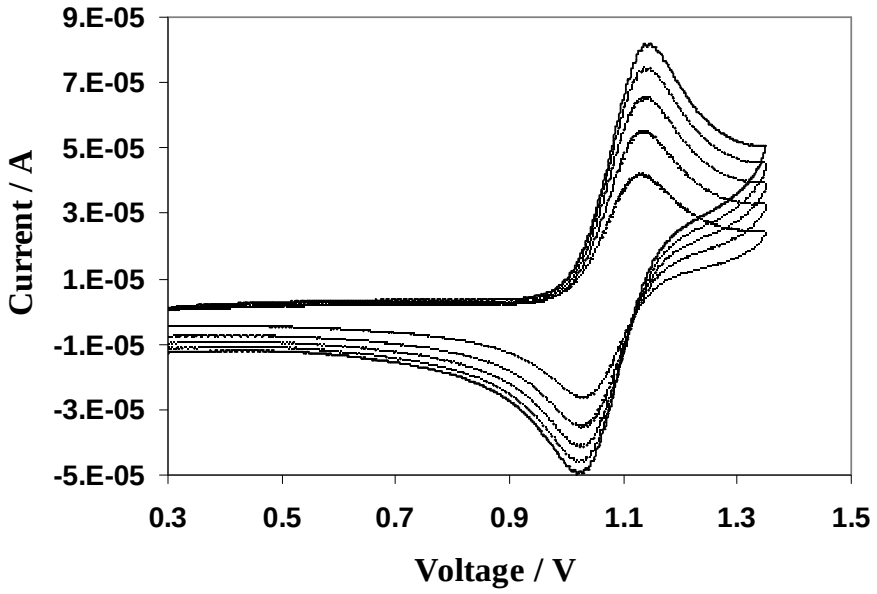

Figure 2.18: Cyclic voltammogram for Ru metallopolymer film formed by drop-casting 100 µl on 3 mm glassy carbon electrode recorded at scan rates between 100-500 mVs^{-1} (bottom to top) with 0.1 M $LiClO_4$ as the supporting electrolyte.

Figures 2.18 and 2.19 show the cyclic voltammograms of $[Ru(bpy)_2PVP_{10}]^{2+}$ and $[Os(bpy)_2PVP_{10}]^{2+}$ metallopolymer film, respectively at scan rates between 100-500 mV s^{-1} in 0.1M $LiClO_4$. The films were formed by drop-casting 100 µl solution on a 3 mm glassy carbon electrode and the solvent was evaporated to dryness overnight in the dark. For an ideal surface confined species, the anodic and cathodic peak

potentials should be identical and the full width at half maximum (FWHM) should be 90.6/n mV.

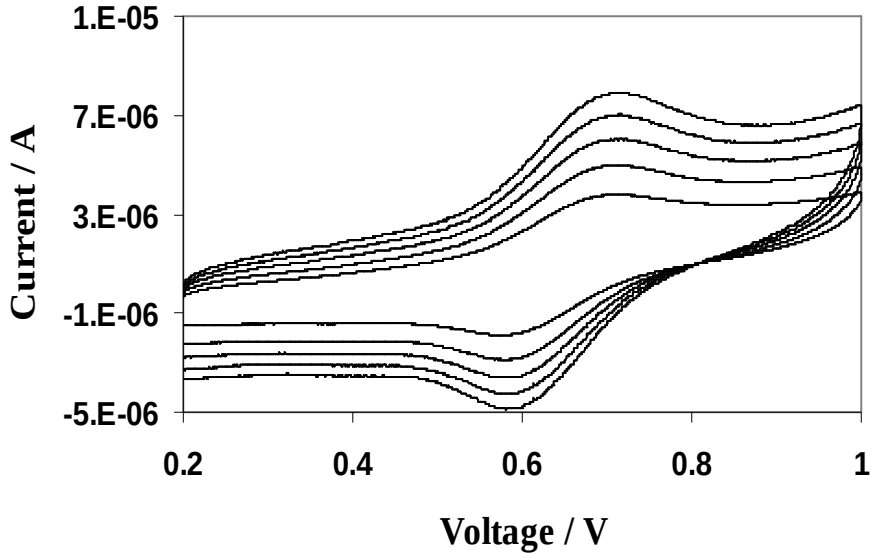

Figure 2.19: Cyclic voltammogram for $[Os(bpy)_2PVP_{10}]^{2+}$ metallopolymer film formed by drop-casting 100 µl on 3 mm glassy carbon electrode recorded at scan rates from 100-500 mVs^{-1} (bottom to top) with 0.1 M $LiClO_4$ as the supporting electrolyte.

However, the cyclic voltammogram response of Ru and Os containing metallopolymer films shows a larger FWHM (>120 mV) and a peak-to-peak separation between the anodic and cathodic waves (ΔE_p= ~60 mV). Under these conditions, the peak current (i_p) does not depend on the scan rate (υ); instead i_p is directly proportional to $\upsilon^{1/2}$. Thus, the electrochemical charge transport occurs by electron self exchange reactions between the neighbouring reduced and oxidised sites.

It is clear from the cyclic voltammograms recorded for ruthenium (Figure 2.18) and osmium (2.19) containing metallopolymers that linear semi-infinite diffusion control is more appropriate. Under such conditions, the homogeneous charge transfer coefficient, D_{CT}, can be determined using Randles-Sevcik Equation 1.18 as described in Section 1.7.5.[33]

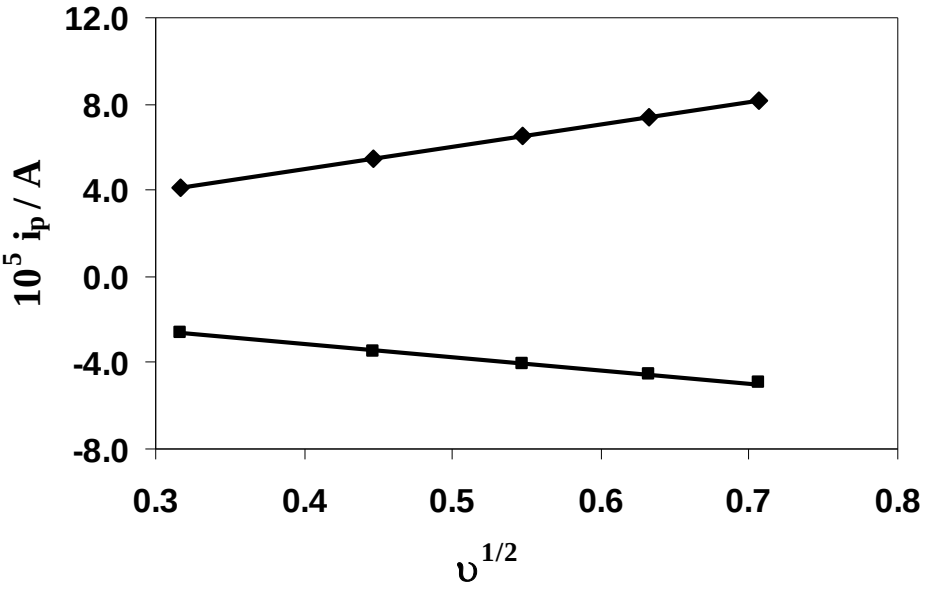

Figure 2.20: Linear plot of peak current (i_p) versus the square root of scan rate ($\upsilon^{1/2}$) for $[Ru(bpy)_2PVP_{10}]^{2+}$ metallopolymer film. Here (♦) and (■) represents the peak currents observed during the anodic and cathodic process, respectively. The electrode was scanned at a rate of 100-500 mV s^{-1} with 0.1 M $LiClO_4$ as the supporting electrolyte.

As mentioned earlier, the rate of charge transfer through the polymer layer may be quantified by measuring charge transfer diffusion coefficients (D_{CT}) through the polymer films using cyclic voltammetry. Plots of peak current (i_{pa} and i_{pc}) *vs* square root of scan rate ($\upsilon^{1/2}$) are linear from 100-500 mV s^{-1} for both the ruthenium and osmium metallopolymer. Figure 2.20 and 2.21 shows the plot of peak current (i_p) *versus* the square root of scan rate ($\upsilon^{1/2}$) $[Ru(bpy)_2PVP_{10}]^{2+}$ and $[Os(bpy)_2PVP_{10}]^{2+}$ metallopolymers, respectively. The slope obtained for ruthenium and osmium metallopolymer is used to calculate the value of D_{CT}.

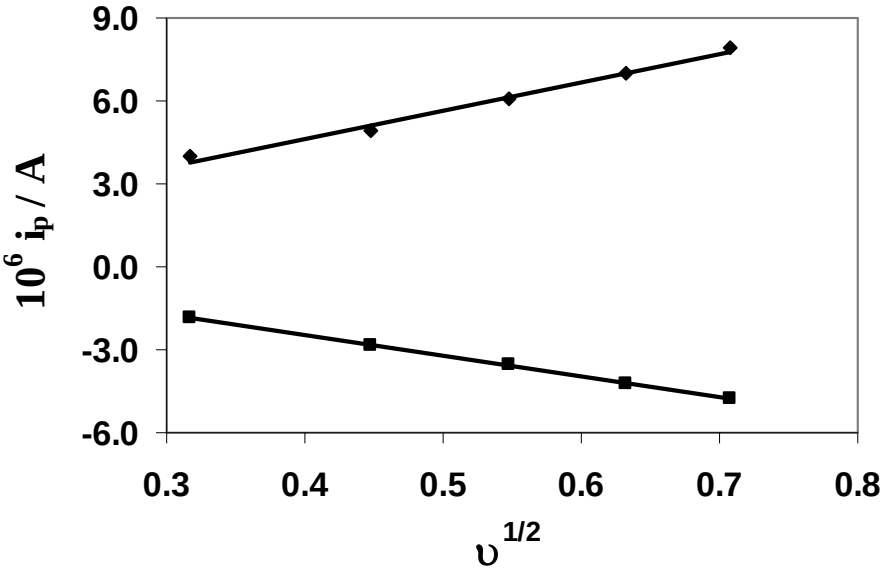

Figure 2.21: Linear plot of peak current (i_p) *versus* the square root of scan rate ($\upsilon^{1/2}$) for $[Os(bpy)_2PVP_{10}]^{2+}$ metallopolymer film. Here the shapes (♦) and (■) represents the peak currents observed during the anodic and cathodic process. The electrode was scanned at a rate of 100-500 mV s^{-1} with 0.1 M $LiClO_4$ as the supporting electrolyte.

Using a fixed site concentration of 0.8 M,[34] the D_{CT} for anodic and cathodic peak currents is calculated for both ruthenium and osmium metallopolymers. The charge transfer diffusion coefficient for ruthenium metallopolymer for anodic and cathodic peak currents is found to be around $3.7\pm0.5\times10^{-12}$ cm^2 s^{-1} and $4.5\pm0.3\times10^{-12}$ cm^2 s^{-1}, respectively in 0.1 M $LiClO_4$ solution. Whereas, the charge transfer diffusion coefficients for the osmium metallopymer are found to be around $4.3\pm0.3\times10^{-13}$ cm^2 s^{-1} and $2.2\pm0.1\times10^{-13}$ cm^2 s^{-1} as calculated from the anodic and cathodic peak currents.

2.3.6. Electrochemiluminescence

The electrochemiluminescence produced by metallopolymer films with a co-reactant system is well established.[35] These Ru and Os metallopolymer films produce moderately intense ECL through the co-reaction of Ru/Os^{3+} with Tri-propyl amine (TPrA). The electro generation of ECL from ruthenium and osmium metallopolymers upon reacting with a co-reactant (TPrA) can be explained using oxidative-reduction pathway.

Here, the oxidation of the co-reactant (TPrA) occurs initially upon applying potential. This results in the production of $TPrA^{\bullet}$, which is a strong reducing agent. The oxidised form of the co-reactant reduces $[M(bpy)_2PVP_{10}]^{3+}$ to form $[M(bpy)_2PVP_{10}]^{2+*}$, an excited state molecule that emits light. A general mechanism of ECL production in the $[M(bpy)_2PVP_{10}]^{2+}$ metallopolymer through the co-reactant pathway is as follows:

$$TPrA \rightarrow TPrA^{\bullet+} + e^{-} \quad \text{.....(2.6)}$$

$$TPrA^{\bullet+} \rightarrow TPrA^{\bullet} + H^{+} \quad \text{.....(2.7)}$$

$$[M(bpy)_2PVP_{10}]^{2+} \rightarrow [M(bpy)_2PVP_{10}]^{3+} + e^{-} \quad \text{.....(2.8)}$$

$$[M(bpy)_2PVP_{10}]^{3+} + TPrA^{\bullet} \rightarrow [M(bpy)_2PVP_{10}]^{2+*} + \text{products} \quad \text{.....(2.9)}$$

$$[M(bpy)_2PVP_{10}]^{+} + [M(bpy)_2PVP_{10}]^{3+} \rightarrow [M(bpy)_2PVP_{10}]^{2+*} + \text{products} \quad \text{.....(2.10)}$$

$$[M(bpy)_2PVP_{10}]^{2+*} \rightarrow [M(bpy)_2PVP_{10}]^{2+} + h\upsilon \quad \text{.....(2.11)}$$

The electrodes were modified with thin layers of the $[Ru(bpy)_2PVP_{10}]^{2+}$ and $[Os(bpy)_2PVP_{10}]^{2+}$ metallopolymers by drop-casting 100 µl of 20 µM DMF:Ethanol (v/v, 1:1) solution. Figure 2.22 shows the ECL response obtained from the Ru and Os metallopolymer films immobilised on a glassy carbon electrode. 0.1 M TPrA is used as the co-reactant.

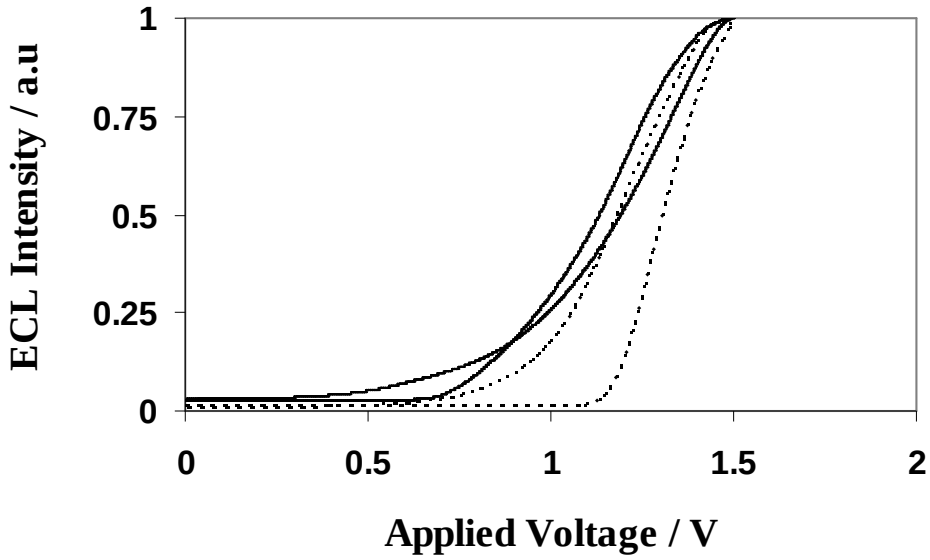

Figure 2.22: The normalised electrochemiluminescence response for Ru (dotted line) and Os (solid line) metallopolymer film on 3 mm glassy carbon electrode. 0.1 M TPrA was used as the co-reactant. The electrode was poised at 1.2 V.

The ECL emission intensity was recorded using a photo multiplier tube. The redox potentials of both the luminophores and co-reactant play a significant role in ECL production. From Figure 2.22, it is observed that no ECL emission was observed until the applied potential reaches 0.6 V after which the ECL emission intensity increases drastically. This might be because of the oxidation of the co-reactant. According to Bard *et al*, the direct oxidation of TPrA at platinum electrodes occurs beyond 0.6 V that is inhibited by the growth of electrode surface oxide.[36] Thus in $[M(bpy)_2PVP_{10}]^{2+}$/TPrA system, the ECL emission is observed as explained in Figure 2.22 only beyond 0.7 V which means the oxidation of TPrA is accelerated due to the applied potential. Moreover, the ECL emission process in the Os metallopolymer gets initiated at a lower voltage to ruthenium polymers, which might be due to the less positive (0.7V) oxidation potential of Os metallopolymer than for the ruthenium analogue (1.1 V).

2.4. Conclusions

The metallopolymers containing covalently attached ruthenium and osmium bipyridyl complexes have attractive ECL properties. Metallopolymers of the form $[M(bpy)_2PVP_{10}](ClO_4)_2$, where M is ruthenium or osmium, have been synthesised and the basic spectroscopic and electrochemical properties were explored. The purity of the compounds is confirmed using various spectroscopic analytical techniques. It is observed that the spectroscopic and electrochemical properties of these metallopolymers greatly depend on the metal centres that are attached to the polymer backbone. The intense electrochemiluminescence properties of these ruthenium and osmium containing metallopolymers are promising in the field of biosensors.

2.5. References

1 Richter, M. M. *Chem. Rev*. **2004**, 104, 3003.

2 Balzanico, V.; Juris, A. *Coord. Chem. Rev*. **2001**, 211, 97.

3 Kalyanasundaram. K. *Photochemistry of Polypyridine and Porphyrin Complexes*, Academic Press, London, **1992**.

4 Lakowicz, J. R. *Principles of Fluorescence Spectroscopy*, Kluwer Academic, Plenum Press, New York, **1999.**

5 Rubinstein, I.; Bard, A. J. *J. Am. Chem. Soc*. **1981**, 103, 512.

6 Zhang, X.; Bard, A. J. *J. Phys. Chem*. **1988**, 92, 556.

7 Obeng, Y. S.; Bard, A. J. *Langmuir* **1991**, 7, 195.

8 Fan, F-R. F.; Mau, A.; Bard, A. J. *Chem. Phys. Lett.* **1985**, 116, 400.

9 Eloi, J.; Chabanne, L.; Whittel, G. R.; Manners, I. *Materials today*, **2008**, 11, 28.

10 Forster, R. J.; Vos, J. G. *Macromolecules*, **1990**, 23, 4372.

11 Doherty, A. P.; Forstre, R. J.; Smyth, M. R.; Vos, J. G. *Anal. Chim. Acta*, **1991**, 255, 45.

12 Larsson, H.; Sharp, M. *J. Electroanal. Chem*. **1995**, 381, 133.

13 Luxton, A. R.; Quig, A.; Delvaux, M.; Fetters, L. J. *Polymer* **1978**, 19, 1320.

14 Friesen, D. A.; Kajita, T.; Danielson, E.; Meyer, T. *J. Inorg. Chem.* **1998**, *37*, 2756.

15 Geraty, S. M.; Vos, J. G. *J. Chem. Soc. Dalton Trans.* **1987**, 3073.

16 Malynych, S.; Luzinov, I.; Chumanov, G. *J. Phys. Chem. B* **2002**, *106*,1280.

17 Dennany, L; Forster, R. J.; Rusling, J. F. *J. Am. Chem. Soc*. **2003**, 125, 5213.

18 Dennany, L.; Hogan, C. F.; Keyes, T. E.; Forster, R. J. *Anal. Chem.* **2006**, *78*, 1412.

19 Forster, R. J.; Hogan, C. F. *Anal. Chem*. **2000,** 72, 5576.

20 Sullivan, B. P.; Salmon, D. J.; Meyer, T. J. *Inorg. chem*, **1978**, 17, 12.

21 Hogan, C. F.; Forster, R. J. *Analyt. chim. Acta*, **1999**, 396, 13.

22 Pellegrin, Y.; Berg, K. E.; Blondin, G.; Anxolabéhère-Mallart, E.; Leibl, W.; Aukauloo, A. *Eur. J. Inorg. Chem.* **2003**, 1900.

23 Buckingham, D.; Dwyer, F. P.; Goodwin, H.A.; Sargeson, A.M., *Aust. J. Chem.* **1964**, 17, 325.

24 Gilbert, B. C.; Norman, R. *An Introduction to NMR Spectroscopy*, RSC, London, **1977**.

25 Ghosh, S. Y. *Chem. Phys. Lett.* **1994**, 226, 344.

26 Vos, J. G.; Forster, R. J.; Keyes, T. E. *Interfacial Supramolecular assemblies*, John Wiley & sons, **2003**.

27 Williams, A.T. R.; Winfield, S. A.; Miller, J.N. *Analyst*, **1983,** 108, 1067.

28 Dhami, S.; De Mello, A. J.; Rumbles, G.; Bishop, S. M.; Phillips, D.; Beeby, A. *Photochem. Photobiol.*, **1995**, 61, 341.

29 Lima, J. F.; Murakami Iha, N. Y. *Can. J. Chem.* **1996**, 74, 476.

30 Juris, A.; Balzani, V.; Barigelletti, F.; Campagna, S.; Belser, P.; Von Zelewsky, A. *Coord. Chem. Rev.* **1988**, *84*, 85.

31 Dennany, L.; Keyes, T. E.; Forter, R. J. *Analyst.* **2008**, 133, 753.

32 Wang, J.; *Analytical electrochemistry*, Wiley, 2nd ed. New York, **2000.**

33 Bard, A. J.; Faulkner, L. R. *Electrochemical Methods: Fundamental and Applications*, 2nd ed.; Wiley, New York, **2001**.

34 Forster, R. J.; Keane, L.; *J. Electroanal. chem.*, **2003**, 554-555, 345.

35 Pyatia, R.; Richter, M. M. *Annu. Rep. Prog. Chem., Sect. C*, **2007**, 103, 12.

36 Zu, Y. Bard, A. J.; *Anal. Chem.* **2000**, 72, 3223.

Chapter 3

Colloidal Nanomaterials

3.1. Introduction

The chemistry and physics of gold nanomaterials has emerged as a new discipline. The biocompatibility and stability of gold is very attractive feature in many fields such as interfacial science, molecular devices and biosensors.[1] Nanocomposites developed by incorporating gold nanoparticles within polymers have gained significant attention over the past few years.[2] Changes in the size and shape of the nanoparticles result in different kinds of interactions with the polymer systems that lead to some remarkable electrochemical and energy transfer properties.[3] The selection of the capping ligands and the method of producing the gold nanoparticles play an important role in controlling the morphology.[4] This chapter focuses on the synthetic strategies used to produce monodispersed stable spherical and rod shaped gold nanoparticles.

Gold nanoparticles can be synthesised using both organic and water based synthetic techniques.[5] The merits and demerits were listed and analysed in Section 1.4.1. As the ultimate goal of this work is to develop ECL biosensor, gold nanoparticles dispersed in water will be ideal. Water-soluble spherical gold nanoparticles can be synthesised using hydrophilic ligands such as 4-(N, N'-Dimethylamino) pyridine (DMAP).[6] It has been reported that the addition of DMAP helps to phase transfer the spherical gold nanoparticles from the toluene to the water phase. The present study focuses on the synthetic aspects of producing spherical gold nanoparticles with different size and monodispersity using a phase transfer approach.

The production of monodispersed colloidal nanoparticles depends on controlling both the nucleation and growth processes.[7] The formation of colloidal nanoparticles can be explained in three stages such as (a) reduction of gold salt, (b) formation of nuclei and (c) the particle growth.[8] In a typical synthesis, the reduction of gold salt results in the formation of nucleation centre that is followed by the growth process. If strong reducing agents such as sodium borohydrate are used, the reduction rate is

too fast that makes it difficult to detect the ionic species that are involved in the reduction and formation of nuclei. Indeed, homogeneous nucleation is a significant criterion to produce monodispersed nanoparticles.[9] To achieve the requirement of homogeneous nucleation, the synthesis of colloids is highly specific and the reaction conditions (metal ion concentration) are restricted to a very narrow regime.

After nucleation, there are two main growth mechanisms that control the size of the nanoparticles such as (a) kinetically limited and (b) diffusion limited. If the incorporation of the surface atom is slow, growth is kinetically limited and hence results in larger particles.[10] Measuring the surface plasmon resonance at regular intervals using a conventional spectrophotometer provides information on the growth process of the larger particles.[7] For diffusion-limited growth, the growth rate is expected to depend on the diffusion of the ions to the nucleation centres resulting in smaller particles at a higher growth rate.[11] Thus, by controlling the synthetic parameters, the particle growth can be easily altered. The reducing agent employed in the synthesis plays an important role in controlling the size of the nanoparticles by controlling the growth mechanism.[12] Thus, the concentration of the reducing agent was changed systematically to change the size of the resultant spherical gold nanoparticles.

The spectral overlap between the emission and absorption spectra of luminophore and the localised surface plasmon resonance (LSPR) band of nanoparticles is very important for optimum luminescence enhancement.[13] The LSPR band of the spherical gold nanoparticles can be tuned to longer wavelength by changing the size, and surrounding dielectric medium.[14,15] In the case of spherical gold nanoparticles, the surface plasmon resonance band is observed at 520 nm, which can be shifted to a longer wavelength region (~600 nm) by increasing the size of the nanoparticles from 4 to 100 nm.[14]

A fascinating feature in nanoscience is that the change in the morphology of the materials will result in unique optical properties. For example, gold nanorods have two different plasmon resonances. The transverse oscillation of the electrons can be observed around 520 nm for gold and the other due to the longitudinal plasmon resonance at longer wavelengths. The transverse plasmon resonance does not depend

on the aspect ratio (length/width) of the nanorods and are similar to that of the spherical gold nanoparticles.[16] The longitudinal vibration modes of the nanorods can be tailored easily since it increases by increasing the aspect ratio of the nanorods. This is an attractive feature in our case, because the aspect ratio of the gold nanorod can be tuned easily to match the emission spectra of various luminophores even in the longer visible wavelengths and far IR region.

The synthesis of gold nanorods has been very well established over the past few years.[17,18] It has been reported that the seed-mediated growth technique results in the production of gold nanorods with a wide range of aspect ratios. This method has proven to provide a high degree of control over mono dispersity and yield.[19,20] Hence, cetyltrimethyl ammoniumbromide (C_{16}TAB) protected gold nanorods were prepared using seed-mediated growth technique.[21] The influence of the synthetic parameters on the morphology and the yield of gold nanorods were systematically studied. The aspect ratio of the gold nanorods was tuned in such a way that the longitudinal absorption matches the emission of $[Os(bpy)_2PVP_{10}]^{2+}$ metallopolymer (~760 nm).

In this present chapter, the synthesis and basic characterisation of spherical gold nanoparticles and gold nanorods are addressed. The impact of the synthetic conditions on controlling the size and shape of the gold nanoparticles are reported. The advantages and limitations in tuning the size and shape of the nanomaterials are discussed. Each of the characterisation techniques used for analysing both the spherical gold nanoparticles and gold nanorods are also briefly discussed.

3.2. Experimental

3.2.1. Materials

Gold (III) chloride trihydrate (99.9%), sodium borohydride (99%), sodium hydroxide (99.99%), sulphuric acid (>95%), sodium sulphate (99%), cetyl trimethyl ammonium bromide (98%), silver nitrate (98%) and L-ascorbic acid (98%) were received from Sigma-Aldrich. Tetraoctylammonium bromide (98%) was purchased from Fluka. 4-(N, N'-dimethylamino) pyridine (99%) was obtained from Fluka Analytical. All the reagents were used as received. The aqueous solutions were prepared from Milli-Q reagent water (Millipore Corp.,), 18 MΩ cm.

3.2.2. Gold Nanoparticles

The DMAP-protected gold nanoparticles were synthesised by the phase transfer protocol developed by Gittins and Caruso[6] and the influence of the synthetic conditions on the gold nanoparticle size was systematically analysed.

3.2.2.1. Synthesis of Gold Nanoparticle

Aqueous solution of gold (III) chloride trihydrate ($HAuCl_4$. $3H_2O$) (30 mM, 30 cm^3) was added to tetraoctylammonium bromide (TOAB) (25 mM, 80 cm^3) in toluene. Then, aqueous sodium borohydride ($NaBH_4$) (0.1 to 0.4 M, 25 cm^3) were added to the mixture with stirring causing an immediate reduction to occur. After 30 min, the toluene phase turned dark pink due to the reduction of gold into nanoparticles. The two phases were allowed to separate and the toluene phase was subsequently washed with 0.1 M H_2SO_4, 0.1 M NaOH, and H_2O (three times), and then dried over anhydrous Na_2SO_4.

3.2.2.2. Phase Transfer

An aqueous 4-(N, N'-dimethylamino) pyridine (DMAP) solution (0.1 M, 80 cm^3) was added to the as-prepared nanoparticle mixtures. This concentration of DMAP was found to be sufficient to affect the complete and spontaneous phase transfer of

the nanoparticles. Direct phase transfer across the organic/aqueous boundary was completed within 1 h, with no stirring or agitation required. Solid DMAP could also be added directly to the toluene solution to precipitate the particles, which could then be resuspended in water. The phase transfer was clearly visible as the dark pink coloured solution transfers from toluene to water due to the addition of the DMAP.

3.2.3. Gold Nanorods

Gold Nanorods were synthesised by following the seed-mediated growth technique developed by Murphy *et al*.[21] It has been shown that the kinetics of reduction of gold ions to atomic gold can be controlled by the addition of silver nitrate.[22] Therefore, by controlling the kinetics of the growth step, the percentage of yield of nanorods can be improved. An attempt was made to increase the yield of nanorods by changing the silver nitrate concentration in the growth solution.

3.2.3.1. Synthesis of Gold seeds

In a typical procedure, an aqueous solution of $HAuCl_4.3H_2O$ (0.01 M, 0.250 cm^3) was added to cetyltrimethyl ammonium bromide ($C_{16}TAB$) solution (0.1 M, 7.5 cm^3) in a plastic tube. The solutions were gently mixed by inversion. The colour of the solution was bright brown-yellow. Then, a freshly prepared aqueous solution of ice cold $NaBH_4$ (0.1 M, 0.600 cm^3) was added all at once, followed by rapid inversion mixing for 2 minutes. The solution colour changed to pale brown-yellow. Then the test tube was kept undisturbed at 25° C for future use. This seed solution was used after 2 hours of preparation.

3.2.3.2. Gold Nanorod growth

For the growth of gold nanorods, $C_{16}TAB$ (0.1 M, 4.75 cm^3), $HAuCl_4.3H_2O$ (0.200 cm^3) and $AgNO_3$ (0.01 M, 0.030 cm^3) were added sequentially, followed by gentle mixing by inversion. The solution at this stage appeared bright brown-yellow. Then, ascorbic acid (AA, 0.1 M, 0.032 cm^3) was added and mixed by gentle inversion. The solution turned colourless and 0.010 cm^3 of the seed solution described in Section 3.2.3.1 was added. The resultant solution was gently mixed by inversion for 30

seconds and left undisturbed for at least 3 hours. The amount of silver nitrate in the growth solution was varied systematically from 60 μM to 300 μM, in order to achieve a higher yield of gold nanorods.

3.2.4. Apparatus and Procedures

Absorbance measurements for all the samples were recorded with a Shimadzu UV-240 spectrophotometer using a 1-cm optical path length quartz cuvette, which allows measurement in the spectral range from 300 to 1100 nm with 1 nm resolution. Transmission Electron Microscopy (TEM) was conducted using a JEOL JEM-2011 electron microscope operated at an accelerating voltage of 200 kV. Images were recorded using a Gatan DualVision 600t CCD camera attached to the microscope and were analysed using Gatan Digital Micrograph Software Version 3.11.1. The TEM was calibrated for diffraction and imaging mode using standard samples.

Energy dispersive X-ray analysis was undertaken with a Princeton Gamma Tech Prism 1G system with a 10-mm^2-silicon detector attached to the TEM and the peaks were analysed with Imix 10.594 software. The resolution of the system was calibrated with manganese (Mn). The samples were prepared by the standard method in which the colloidal solution was drop-cast onto a carbon coated copper grid and the solvent evaporated. The particle size of approximately ~400 individual nanoparticles was used to determine the particle size distribution.

Field Emission Scanning Electron Microscopic (FE-SEM) images were taken using a Hitachi S5500 in-lens field emission scanning electron microscope. SE, LA-BSE or HA-BSE type detector was used for FE-SEM imaging. The samples were prepared by drop casting the gold nanorod solutions on a clean silicon wafer and the solvent was evaporated to dryness. Prior to sample preparation, the silicon wafers were cleaned by sonicating in acetone, ethanol and water for 15 minutes. Each sample was mounted on a type 2 high purity aluminium stub using either silver DAG conductive glue or conductive carbon tape.

The aspect ratio of the gold nanorods was calculated by measuring the length and width of approximately ~200 individual nanorods that was used to determine the

particle size distribution. The zeta potentials for DMAP-protected gold nanoparticles and C_{16}TAB-protected gold nanorods were measured in water using a Malvern Zetasizer Nano. Standard disposable capillary cells integrated with gold electrode were used for measuring the zeta potential. These cuvettes were manufactured from clear polycarbonate material, which made it possible to use in both aqueous and non-aqueous medium.

3.3. Results and Discussion

3.3.1. Gold Nanoparticles

3.3.1.1. Transmission Electron Microscopy

4-(N,N'-dimethylamino) pyridine protected gold nanoparticles were synthesised by following the modified procedure developed by Gittins and Caruso.[6] Size control in the synthesis of nanoparticles is a kinetically driven process, where the ratio between the rates of nucleation and growth is responsible for the final nanoparticle size. It is known from the literature that varying concentration of the reducing agent [23] and the reduction rate[24] employed in the synthesis enables the nanoparticle size to be controlled. Hence, in order to tune the gold nanoparticle size, molar ratio of initial gold salt concentration to the concentration of reducing agent was changed.

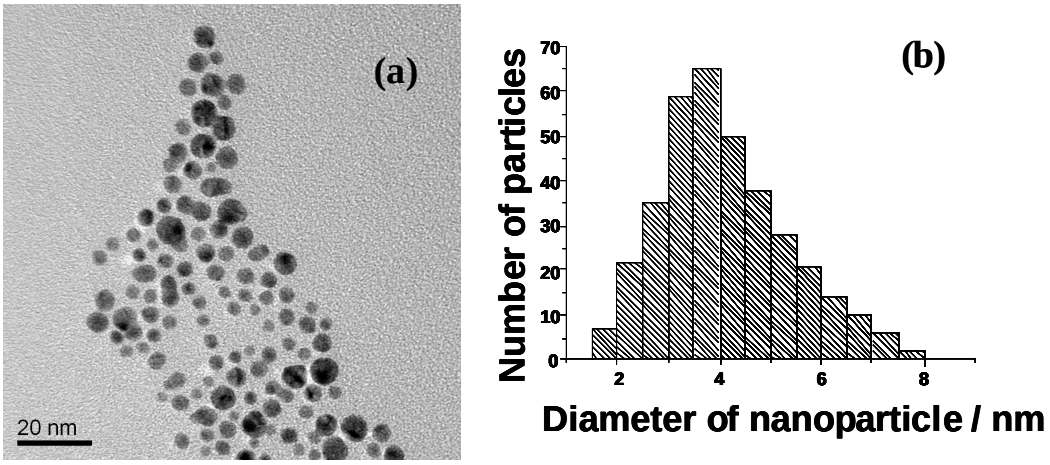

Figure 3.1: (a) Transmission electron microscopic image of 4 nm DMAP-protected gold nanoparticles. Figure (b) shows the size distribution of the nanoparticles calculated from multiple areas of TEM grid. The average particle size was calculated by measuring nearly 400 individual particles from different grids.

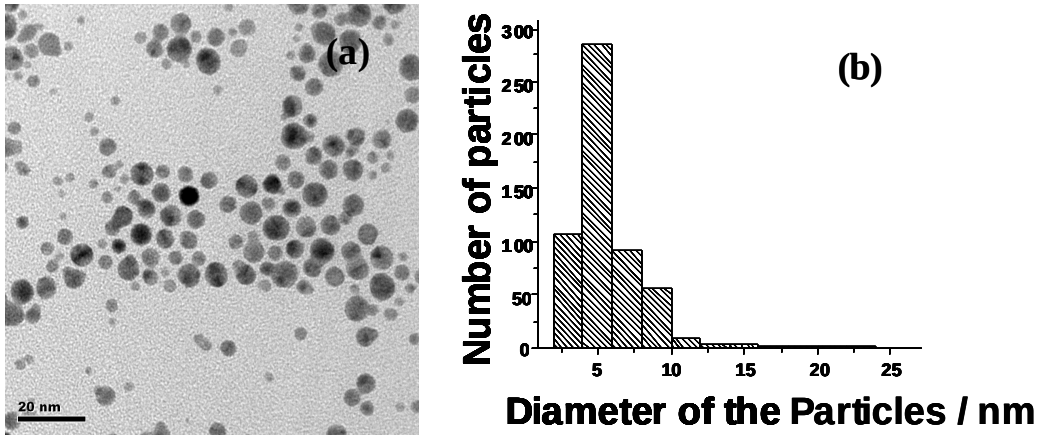

Figure 3.2: (a) Transmission electron microscopic image of 5 nm DMAP-protected gold nanoparticles. The figure (b) shows the size distribution of the nanoparticles calculated from multiple areas of TEM grid.

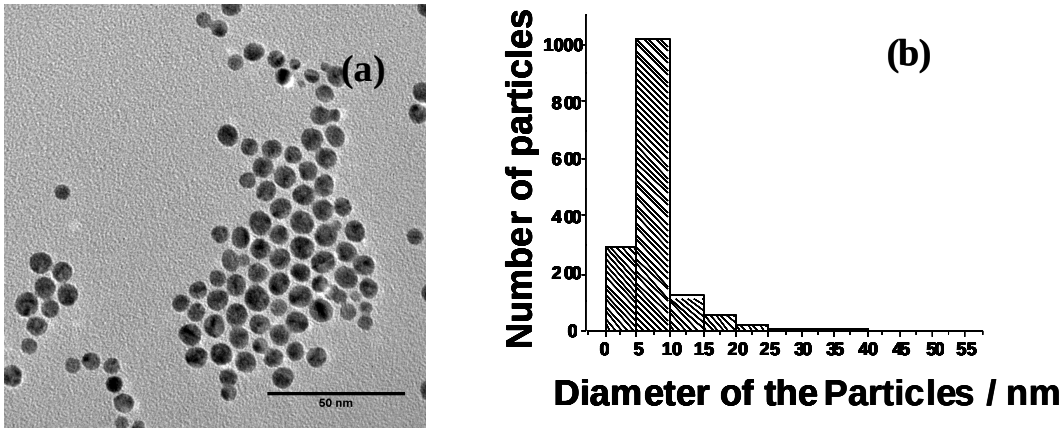

Figure 3.3: (a) Transmission electron microscopic image of 7.5 nm DMAP-protected gold nanoparticles. The figure (b) shows the histogram for the size distribution of the nanoparticles calculated from multiple areas of TEM grid.

The structural analysis for DMAP-protected gold nanoparticles was carried out using transmission electron microscopy (TEM). Figures 3.1 to 3.4 show the TEM images of DMAP-protected gold nanoparticles with mean diameters of 4 ± 0.5, 5 ± 0.5, 7.5 ± 1 and 12.5 ± 2 nm. The TEM images were recorded by drop-casting the nanoparticle solution on the carbon coated copper grid and the solvent was evaporated to dryness.

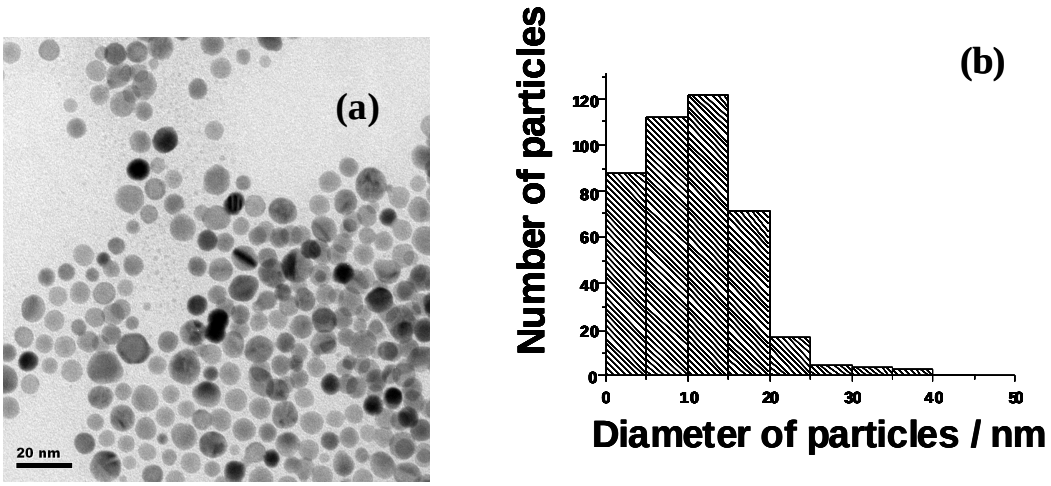

Figure 3.4: (a) Transmission electron microscope image of 12.5 nm DMAP-protected gold nanoparticles. The figure (b) shows the size distribution of the nanoparticles calculated from multiple areas of TEM grid.

The size analysis of the gold nanoparticles was made using a public domain java image processing and analysis program called ImageJ. The size of the particles was calculated by following a standard procedure.[25] Figure 3.5 shows the screen shot image obtained for 7.5 nm DMAP-protected gold nanoparticle during the process of particle counting. The green outlines show the particles that are taken into account for obtaining the size of the nanoparticles. The area of each particle was obtained from the ImageJ software analysis. The effective diameter of the particles was calculated from the area of the particles. The average size distribution of the gold nanoparticles was measured from different regions of the TEM imaging grids.

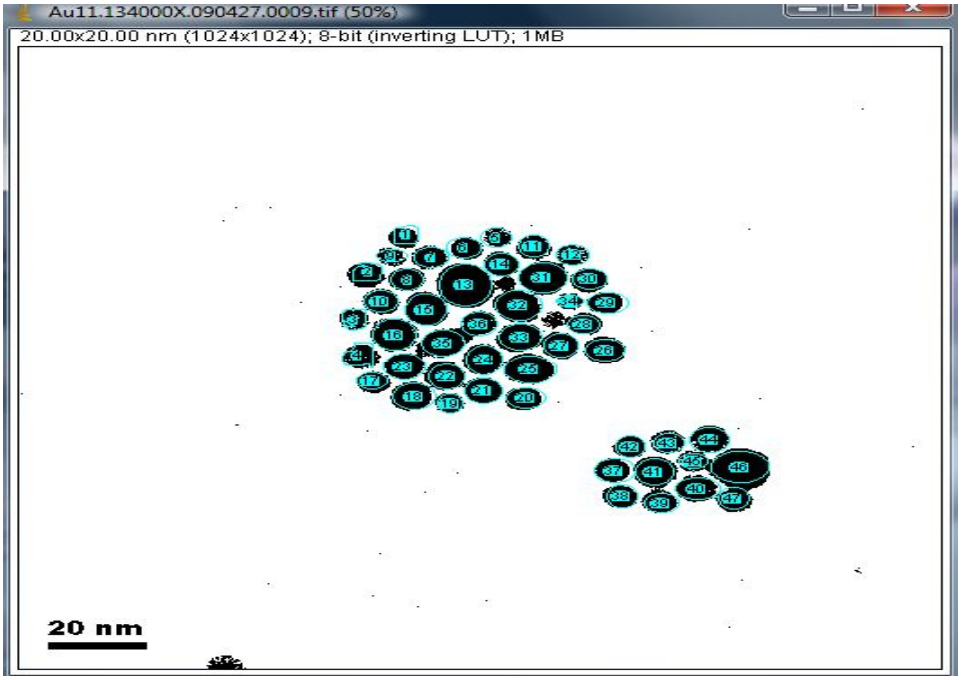

Figure 3.5: Screen shot of the TEM image of 7.5 nm DMAP-protected gold nanoparticle showing the particle counting process. The size distribution was obtained from the ImageJ software.

Quantitative analysis of the size distribution for each nanoparticle system was performed by measuring the mean diameter of over hundreds of individual nanoparticles from multiple micrographs, imaged from several areas of the sample grid to ensure statistical relevance. The particle size distribution is shown as Figure (b) of the respective TEM images. All the images obtained from TEM analysis support the formation of monodisperse DMAP-protected gold nanoparticles. The DMAP-protected gold nanoparticles were well separated from each other at least by 1.5 nm. This might be because of the presence of a monolayer of DMAP molecules on the surface of the gold nanoparticles.[26]

Energy dispersive spectrum (EDS) of the gold nanoparticles illustrates that the gold nanoparticles are of high purity as it shows the peaks corresponding to Au whereas the Ni and Cu peaks originate from the TEM grid. Figure 3.6 shows the EDS spectrum for DMAP-protected gold nanoparticles obtained from the EDS analysis.

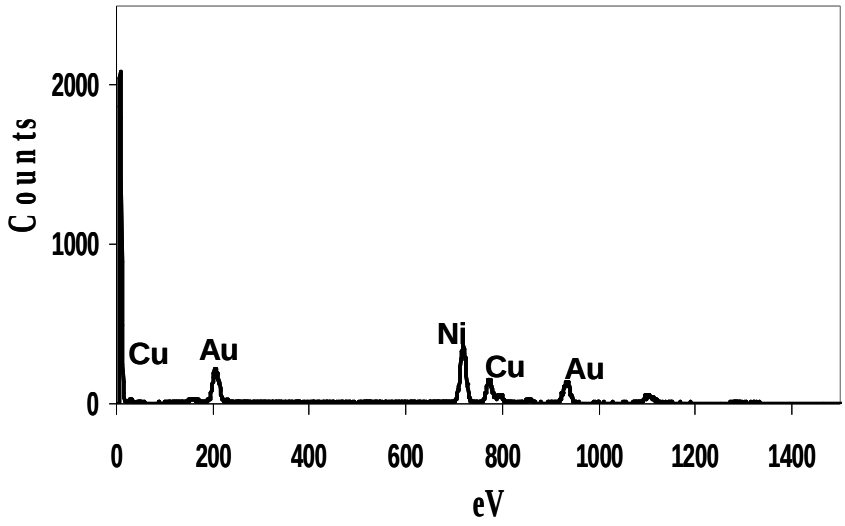

Figure 3.6: Energy Dispersive Spectra (EDS) for the DMAP-protected gold nanoparticles. The samples were prepared by drop casting the nanoparticle solution on the carbon-coated grids.

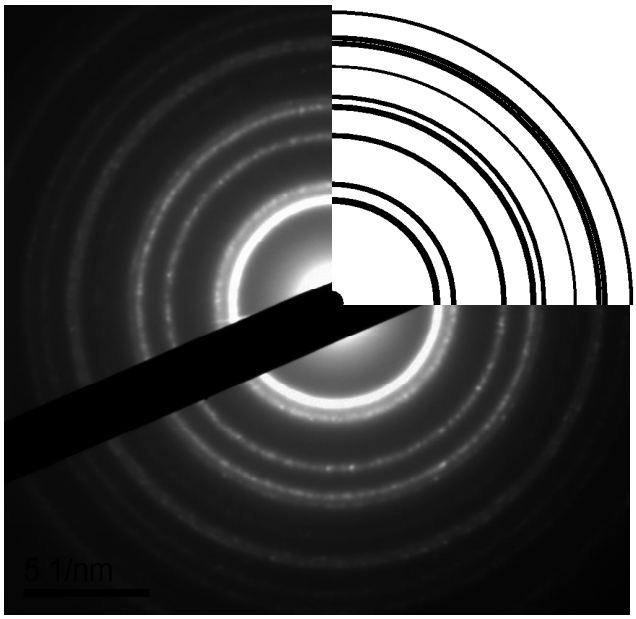

Figure 3.7: Diffraction pattern obtained for 4 nm DMAP-protected gold nanoparticles synthesised using phase transfer protocol. The inset (white background) shows the theoretically simulated diffraction pattern corresponding to the polycrystalline gold.

Figure 3.7 shows the diffraction patterns obtained for 4 nm DMAP-protected gold nanoparticles. The inset in Figure 3.7 shows the theoretically simulated diffraction pattern corresponding to polycrystalline gold. The experimental diffraction pattern was matched with that of the theoretically simulated (with white background in Figure 3.7) corresponding to polycrystalline gold (FORTRAN program was developed by Prof Shohei Nakahara, University of Limerick).

Figure 3.8 shows the variation of the diameter of gold nanoparticles with the molar ratio of initial gold salt concentration to the concentration of the reducing agent. At higher concentration of the reducing agent, the population of the available nucleation sites is very large leaving a low concentration of unreduced gold salt around the nucleation sites for further growth. Hence, the growth of the nanoparticle is arrested due to the lack of gold salt in immediate vicinity region. This results in the production of small sized gold nanoparticles at higher reducing agent concentration. Whereas, gold nanoparticles with larger diameter are produced at lower reducing agent concentration, which is attributed to the lower nucleation density.

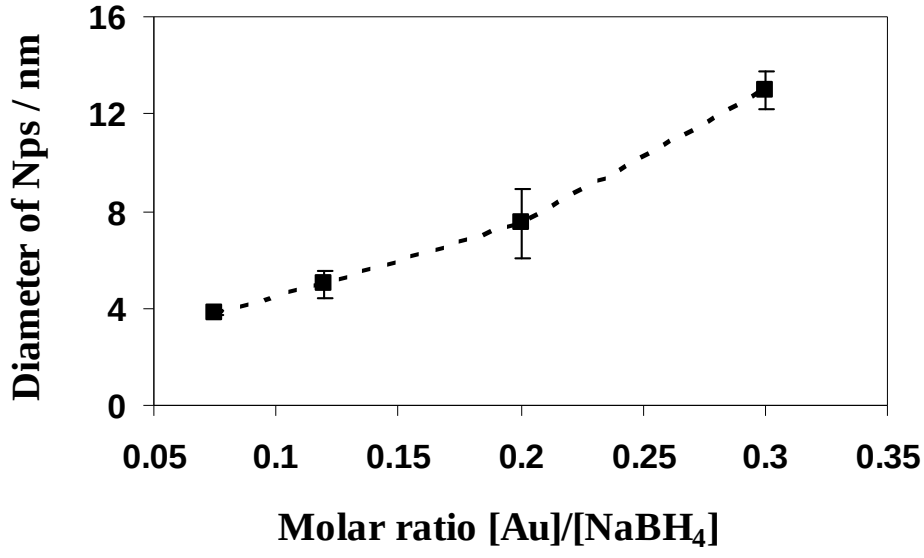

Figure 3.8: The diameter of the DMAP-protected gold nanoparticles plotted against the molar ratio of gold to sodium borohydride concentration at 25 mM concentration of TOAB.

It is also clear from the graph (Figure 3.8) that the particle diameter increases as the concentration of the reducing agent decreases, since the concentration of the initial gold salt is maintained constant. Yet, it is important to maintain the optimum molar ratio of [Au]/[$NaBH_4$] as the stability of the bigger nanoparticles (~ 50 nm) obtained by this synthetic protocol is poor. A very high concentration (> 0.5 M) of the reducing agent results a very low yield. However, a very low concentration (< 0.05M) does not reduce the gold salt.

3.3.1.2. Concentration Analysis

Determining the nanoparticles concentration is essential if the impact of the loading of the DMAP-protected gold nanoparticles is to be probed successfully. The use of very strong reducing agent such as sodium borohydrate ($NaBH_4$) for the synthesis of smaller spherical gold nanoparticles results in complete reduction of the gold salt. The concentrations of the as-prepared DMAP-protected gold nanoparticles with four different diameters were calculated using the following expressions. Assuming 100% efficient reduction of the gold chloride and no losses during transfer and washing methods, the number of gold atoms per single nanoparticle (N_{atoms}) can be obtained using the effective radius of the gold atom (r_{Au}) as 1.62 Å, which includes the atomic packing conditions.

The number of moles of gold (N_{moles}) in the reaction mixture can be calculated from:

$$N_{moles} = \frac{X}{MW} \quad \text{.....(3.1)}$$

where X is the initial amount of gold in the salt used in the synthesis, MW is the molecular weight of gold (196.97 g/mol). The number of moles of gold nanoparticles in the reaction mixture can be obtained from the ratio of number of moles of gold (N_{moles}) to the number of gold atoms per single nanoparticle (N_{atoms}).

$$N_{Au} = \frac{X/MW}{\left(r_{NP}/r_{Au}\right)^3} \quad \text{.....(3.2)}$$

The total concentration of gold nanoparticles (NP_{CONC}) can be calculated by dividing the moles of gold nanoparticle (N_{Au}) in the reaction mixture by the total volume of the reaction mixture (V).[26]

$$NP_{CONC} = \frac{X}{MW \cdot V}\left(\frac{r_{Au}}{r_{NP}}\right)^3 \quad \text{.....(3.3)}$$

where V is the total volume of the reaction solution (ml).

Table 3.1: Change in the concentration of the as prepared DMAP-protected gold nanoparticles with different diameters achieved by varying the concentration of the reducing agent.

Diameter of DMAP-Au NPs (nm)	Volume of DMAP-Au NPs ($Å^3$)	Number of Au atoms per nanoparticle	Number of moles of DMAP-Au NPs (Moles)	Concentration of DMAP-Au NPs
4	33510	1881	8.26×10^{-7}	3.30×10^{-6}
5	65416	3675	1.63×10^{-7}	5.44×10^{-6}
7.5	220781	12403	4.84×10^{-8}	$1.61\times^{-6}$
12.5	1022135	57424	1.045×10^{-8}	3.48×10^{-7}

Table 3.1 shows the changes in the concentration of the DMAP-protected gold nanoparticles *vs* diameter of the nanoparticles. The number of gold atoms increases with the size of the gold nanoparticles. The number of moles of nanoparticles decreases as the diameter of the nanoparticles increases, due to the increase in the number of atoms present in each particle as the diameter increases. As the initial amount of gold salt is maintained constant, the concentration of nanoparticles decreases as the size increases.

3.3.1.3. UV-Vis-NIR Spectroscopy

Colloidal solutions of gold nanoparticles have a very distinctive red colour[27] and show an intense absorption peak from 500-550 nm[28] arising from the localised surface plasmon resonance (LSPR).[29] The plasmon band is sensitive to the surrounding environment, e.g., dielectric changes and binding to the surface. However, smaller nanoparticles (dimensions, < 1-2 nm) do not display this phenomenon, as their electrons exist in discrete energy levels. Figure 3.9 shows the plasmon absorption band for the DMAP-protected gold nanoparticles in water with different mean diameters (4 to 12.5 nm) synthesised by the phase transfer protocol.

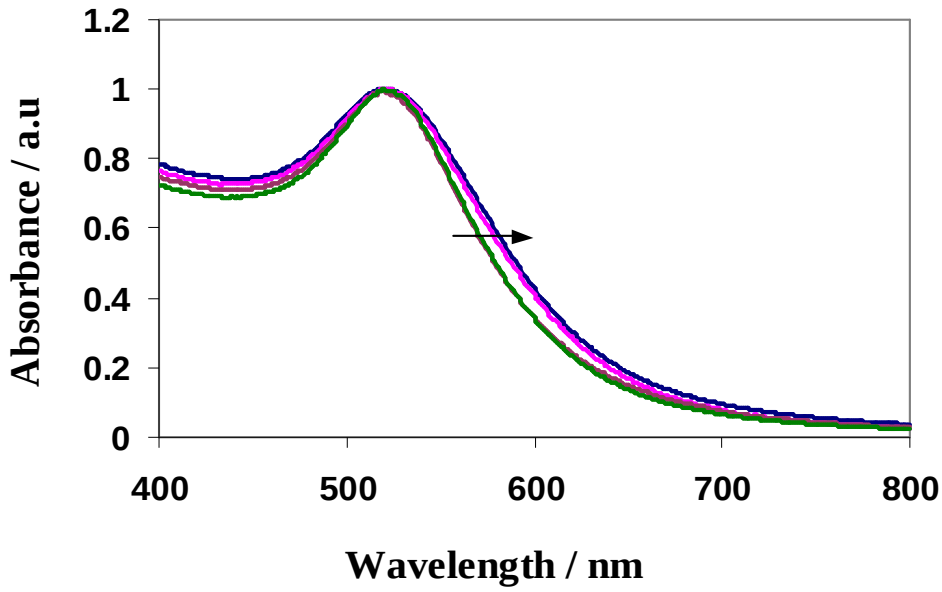

Figure 3.9: **N**ormalised SPR absorption band for the DMAP-protected gold nanoparticles in water with diameters of 4 (—- green line), 5 (—- purple line), 7.5 (—- pink line) and 12.5 nm (—- blue line). The arrow shows the broadening of the spectra as the size increases from 4 nm to 12.5 nm.

The maximum intensity of surface plasmon band was normalised to unity for comparative purpose. The surface plasmon resonance maximum at 524 nm for gold nanoparticles does not shift dramatically when the particle diameter changes from 4 to 12.5 nm, but some broadening in the SPR band of the gold nanoparticles is observed. Scaffardi *et al* has reported that the broadening of the absorption peak and

shifting to longer wavelength region occurs only for the larger nanoparticles (radius > 10 nm). The nanoparticles with radius ranging from 2.6 nm and 10 nm will exhibit a peak near 520 nm, which is independent of their size.[30]

3.3.1.4. Molar extinction coefficients

In a spectrophotometer, monochromatic plane-parallel light enters the samples at right angles to the plane surface of the sample. Under these conditions, the transmittance and absorbance of a sample is proportional to the concentration of the sample (C), path length in centimetres (b) and the molar absorptivity (ε). Beer's Law states that the molar absorptivity, which is commonly known as *molar extinction coefficient*, is a constant. The determination of the molar molar extinction coefficient relies on the Beer-Lambert Law:

$$A = \varepsilon bC \quad \text{.....(3.4)}$$

where A is the absorbance (a.u), b is the path length (cm) and C is the concentration (M) of the nanoparticles.

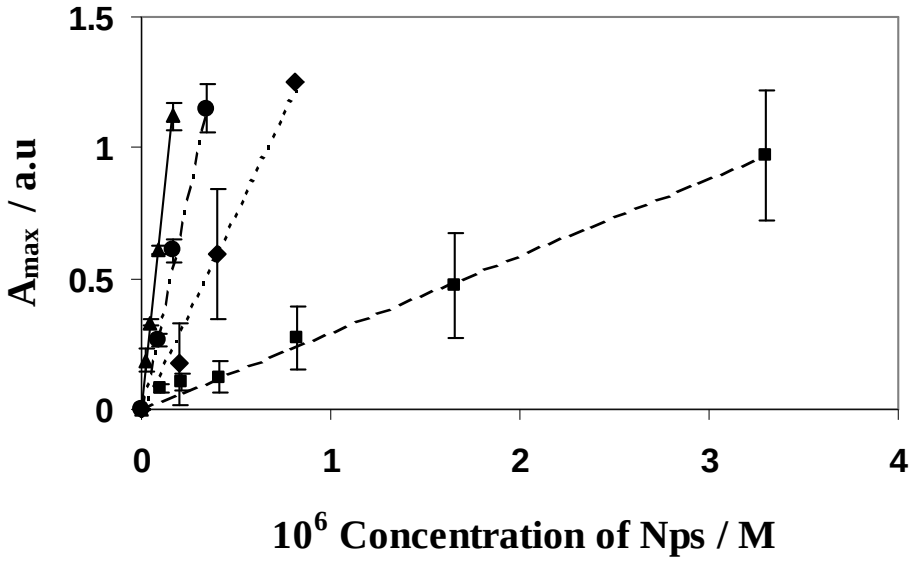

Figure 3.10: Linear dependence of maximum absorption of the SPR band at 524 nm on different concentrations of gold nanoparticle solutions with mean diameter of 4(■), 5(♦), 7.5(•) and 12.5(▲) nm, respectively. The R^2 value is greater than 0.99 for all the samples.

In order to determine the molar extinction coefficient, it is important to define a wavelength of maximum absorbance. Indeed, for gold nanoparticles the surface plasmon resonance wavelength is considered as the wavelength of maximum absorbance. The absorption spectra for the DMAP-protected gold nanoparticles were recorded at different concentrations. A graph between the maximum absorption at the SPR wavelength (524 nm) of DMAP-protected gold nanoparticles was plotted against the concentration of gold nanoparticles. Figure 3.10 shows the plot of maximum absorption *versus* the concentration of the nanoparticles of diameter 4(■), 5(♦), 7.5(●) and 12.5(▲) nm respectively.

A linear relationship between the absorbance and the concentration was observed for all the gold nanoparticles prepared at different concentrations with the correlation coefficient nearly 0.99 ± 0.002. This result confirms that the Beer-Lambert Law is applicable. The slopes of these linear graphs give the molar extinction coefficient of the individual nanoparticles.[31]

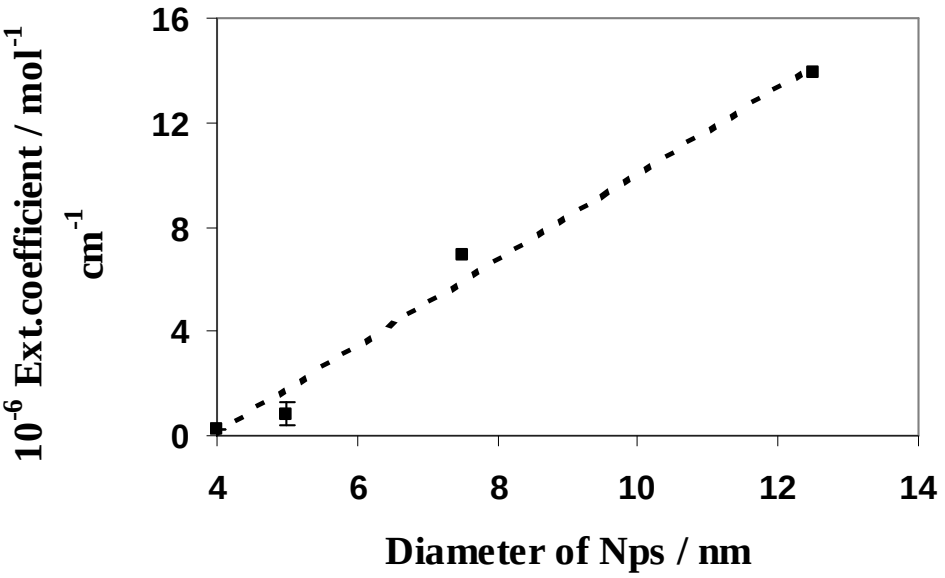

Figure 3.11: The dependence of the molar extinction coefficient of gold nanoparticles on the mean diameter prepared by varying the reducing agent concentration.

Figure 3.11 shows the variation in the molar extinction coefficient of DMAP-protected gold nanoparticles with the diameter of the nanoparticles. A linear dependency was observed for the molar extinction coefficient on the diameter of the nanoparticles between 4 and 12.5 nm diameter. Yet, the number of data points presented here is not sufficient for the complete understanding of the molar extinction coefficient dependence on the diameter of the nanoparticles. Mulvaney *et al* reported the dependence of molar extinction coefficient on the diameter of nanoparticles based on theoretical predictions using Mie theory.[32]

The molar extinction coefficient was found to vary between 0.25×10^{6} $M^{-1}cm^{-1}$ and 13.9×10^{6} $M^{-1}cm^{-1}$ for the DMAP-protected gold nanoparticles of diameter 4 and 12.5 nm, respectively. Murray *et al* has reported that the molar extinction coefficient of gold nanoparticles of 4.4 nm diameter as 6.2×10^{6} M^{-1} cm^{-1} at 518 nm.[33,34] Similarly, Huo *et al* has also reported that gold nanoparticles with mean diameter of 5 nm exhibit an molar extinction coefficient of around 3.6×10^{6} M^{-1} cm^{-1} which is also found to increase with the diameter of the nanoparticles.[31] Thus, our experimental results are in good agreement with the reported values.

3.3.1.5. Zeta Potential

Nanoparticles with unmodified surfaces tend to form aggregates that will disturb their stability. Hence, a monolayer of charged species are attached to the surface of the nanoparticles will prevent aggregation, by columbic repulsion.[35] Zeta potential measurements are used in order to find out the charge on the nanoparticles. The adsorption of pyridine molecules on monocrystalline and polycrystalline gold has been studied by Stolberg in great detail using electrochemical techniques.[36] Pyridine molecules are adsorbed parallel to a negatively charged surface and bind through the π-orbitals of the aromatic ring. When the gold surface is positive of the point of zero charge (PZC), the pyridine molecules re-orient to adopt a vertical position and bind through the free electron pair of the nitrogen atom.[26]

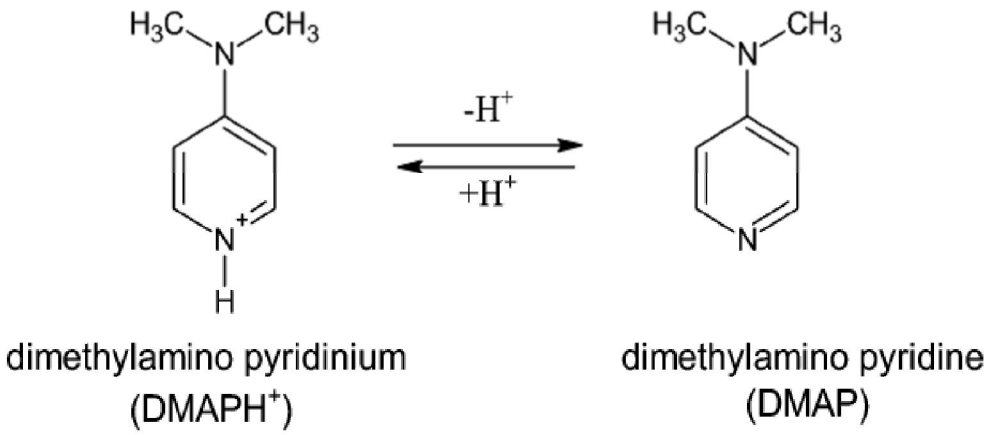

Figure 3.12: The chemical structures of $DMAPH^+$ and DMAP. The primary pK_a is +9.7. Adapted from Burke Barlow and Ian Burgess, *Electrochemical Evaluation of 4-(Dimethylamino) pyridine Adsorption on Polycrystalline Gold*, Langmuir, **2007**, 23, 1555.

The orientation of 4-(dimethylamino) pyridine molecules on polycrystalline gold can also be studied using electrochemical desorption techniques. Burgess and co workers[37] has reported that at higher pH (above the pK_a), the adsorbed species is DMAP and orients vertically on the surface *via* the lone pair of electrons on the pyridine ring nitrogen atom. The adsorbed species at lower pH is $DMAPH^+$, which is the protonated form of DMAP that can be easily desorbed from the surface. Figure

3.12 shows the possible orientation for binding of 4-(N,N' dimethylamino)pyridine groups to the gold surface. DMAP-protected gold nanoparticles are stable in basic aqueous solutions and only exhibit signs of aggregation when the pH of the solution was made significantly acidic (~ pH 3) because of the pK_a of DMAP (the pK_a values of the endocyclic[38] and exocyclic[39] DMAP nitrogens are +9.97 and approximately -4.4 respectively).

The zeta potential for the DMAP-protected gold nanoparticles was measured using Malvern Zetasizer instrument. The nanoparticles were dispersed in water and all the measurements were carried at room temperature (25 ± 0.1 °C). The Zeta potential and the electrophoretic mobility obtained for the mono dispersed DMAP-protected gold nanoparticles with different sizes showed a Zeta potential value between +17 and +19 at a pH 9. The positive magnitude of the Zeta potential obtained for different sized nanoparticles is in agreement with the possibility of binding through the endocyclic[26] nitrogen lone pair with the gold surface.

3.3.2. Gold Nanorods

3.3.2.1. Field Emission Scanning Electron Microscopy

Gold nanorods were synthesised using a seed-mediated growth technique.[21] Cetyltrimethyl ammoniumbromide (C_{16}TAB) is used as the growth-directing agent in the seed-mediated growth technique to prepare gold nanorods of uniform morphology. It has been reported that the C_{16}TAB forms a bilayer on the gold surface *via* the hydrocarbon tails ue to electrostatic interaction. The free energy of bilayer stabilisation between C_{16}TAB surfactant is found to be approximately 6 KJ/mol per two methylene groups. As a consequence, dynamic formation of a bilayer on the gold surfaces may stabilise the nanoparticles during the growth phase.[40] Thus, C_{16}TAB acts as a growth-directing agent in the nanorod synthesis.

The aspect ratio of the gold nanorods and the yield of the gold nanorods can be controlled by using the appropriate synthetic parameters. Though the role of silver nitrate on nanorod growth is not completely understood, it has also been shown in literature that the presence of silver nitrate in the growth solution improves the yield of nanorods.[22] As the bromide tends to chemisorb on gold surfaces,[41,42] the presence of silver nitrate might result in the formation of silver bromide that could control the yield of gold nanorods in the seed-mediated synthesis.

One source of bromide is cetyltrimethyl ammonium bromide (C_{16}TAB). As the concentration of C_{16}TAB employed in the seed-mediated growth (0.1 M) is sufficient to direct the nanorod growth, an attempt was made to introduce silver nitrate to control the yield of gold nanorods. Hence, the concentration of silver nitrate ($AgNO_3$) in the growth solution was altered. The aspect ratio and the yield of gold nanorods were calculated using scanning electron microscopy. The aspect ratio of the gold nanorods was calculated by measuring the length and width of each nanorods obtained at various synthesis conditions.

The yield of gold nanorods is calculated by counting the number of rods from various images. The yield is given by equation 3.5:

$$Yield = \frac{N_{rods}}{N_{Total}} \times 100 \quad \text{.....(3.5)}$$

where N_{rods} is the number of gold nanorods and N_{Total} is the total number of particles calculated from the FE-SEM images. Figures 3.13 and 3.14 shows the scanning electron microscopic images of the gold nanorods prepared with 60, 120, 240 and 300 μM of the silver nitrate solution concentration in the growth solution respectively.

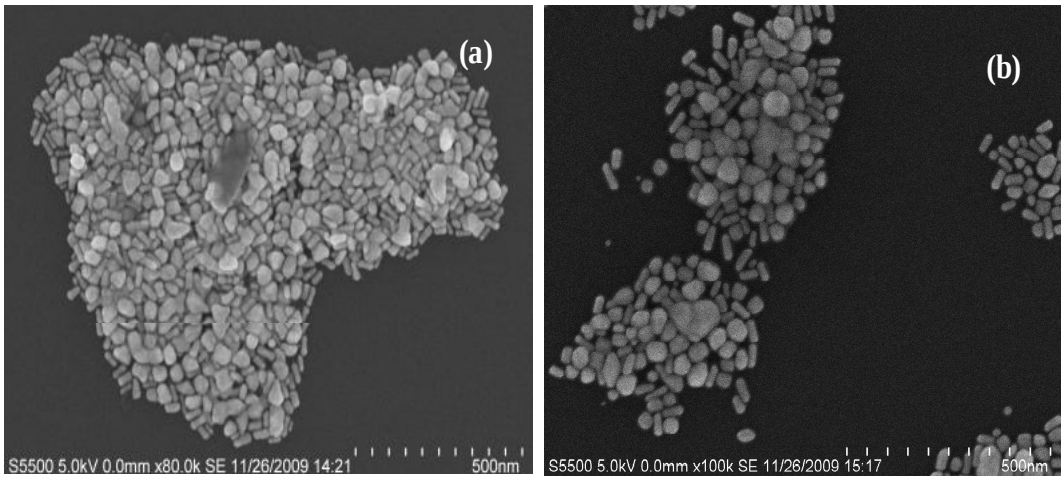

Figure 3.13: (a) and (b) shows the SEM image of gold nanostructures prepared with 60 μM and 120 μM of $AgNO_3$ solution in the growth solution respectively. The samples were prepared by drop-casting 100 μl of the nanorod solution on a clean silicon wafer and the solvent was evaporated to dryness.

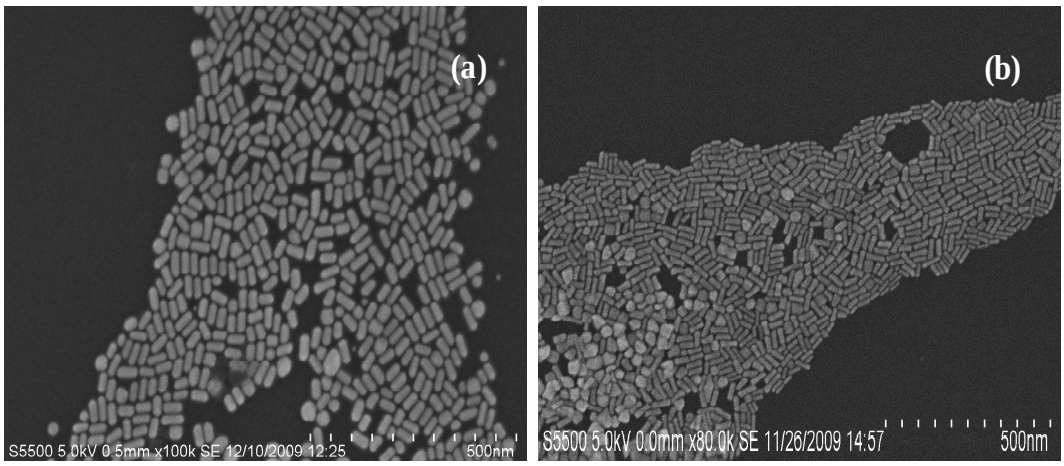

Figure 3.14: (a) and (b) shows the FE-SEM images of gold nanorods prepared with 240 μM and 300 μM of silver nitrate ($AgNO_3$) solution in the growth solution. The samples were prepared by drop-casting 100 μl solution on a clean silicon wafer and the solvent was evaporated to dryness.

The FE-SEM images show that the presence of silver nitrate in the growth solution greatly increases the formation of gold nanorods. This could be attributed to the catalytic nature of silver, which enhances the growth of gold nanorods. Hence, low concentration of silver nitrate in the growth solution (Figure 3.14 (a) and (b)) produced a significant fraction of non-rod structures. The FE-SEM images confirm the existence of a mixture of rods and particles. In striking contrast, higher silver nitrate content in the growth solution results in large number of nanorods. Gold nanorods with a uniform aspect ratio of 3.6 were obtained at the higher concentration of the silver nitrate (Figure 3.14 (b)). This shows that the presence of silver nitrate has a remarkable influence on the production of short gold nanorods with very high yield.

The yield of gold nanorods prepared with various amounts of silver nitrate in the growth solution was calculated from different micrographs obtained from scanning electron microscopy image. Table 3.2 shows the summarised information on the dependence of yield of gold nanorods on silver nitrate content in the growth solution.

Table 3.2: Influence of the concentration of silver nitrate in the growth solution on the yield of gold nanorods.

Concentration of $AgNO_3$ (μM)	Gold Nanostructures (N_{Total})	Gold nanorods (N_{Rods})	Yield (%)
60	633	197	31.2±0.7
120	519	173	33.4±1.8
240	1100	530	48.18±4
300	756	664	87.8±1.2

The percentage yield of gold nanorods (Table 3.2) increases drastically from 31% to 87% with 5-fold increase in the concentration of silver nitrate in the growth solution. It is useful to analyse the role of silver nitrate in controlling the yield of gold nanorods. Earlier reports show that silver nitrate can only be reduced at basic pH using the weak ascorbic acid as the reducing agent.[43] The pH of the growth solution was found to be somewhat acidic (~pH=5). Hence, the presence of Ag^0 is less likely than Ag^+ because of the presence of weak reducing agent (ascorbic acid).

Under these conditions, there is the possibility of forming silver bromide from $AgNO_3$ in the presence of C_{16}TAB. The silver bromide that has been precipitated in the growth solution could be adsorbed to the facets of growing gold nanorods in an epitaxial fashion[21] and therefore restricting the over growth of nanorods on the other facets. Thus, silver nitrate helps in stabilising the gold nanorods and hence results in a very high yield of rod shaped particles at higher silver nitrate concentrations.

3.3.2.2. UV-Vis-NIR Spectroscopy

The spectral properties of gold nanorods have received considerable attention due to the presence of two distinct localised surface plasmon resonance bands in the UV-Vis-NIR region. Figure 3.15 shows the normalised UV-Vis spectra obtained for the gold nanorods synthesised by using various amounts of silver nitrate in the growth solution. The presence of silver nitrate in the growth solution is found to increase both the percentage yield and length of the nanorods as seen using scanning electron microscopy.

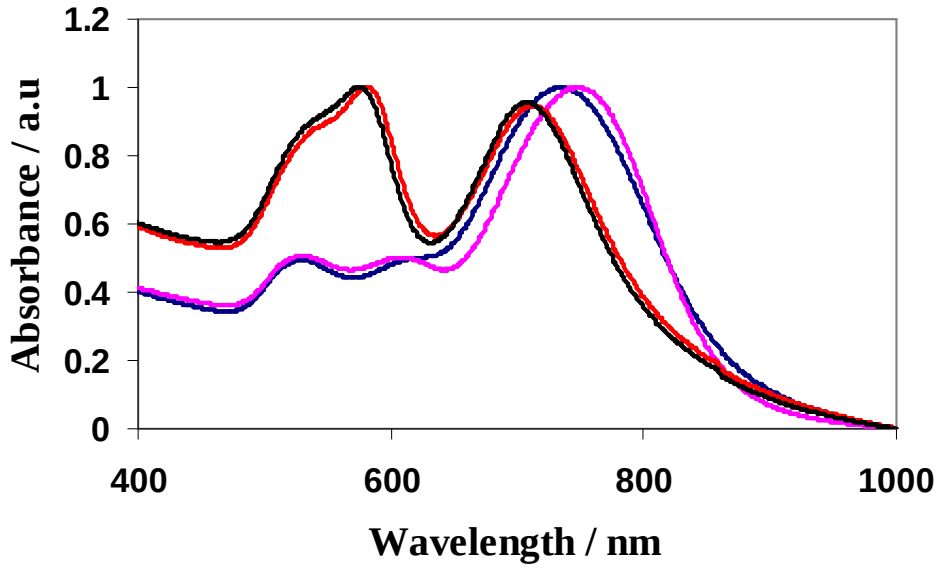

Figure 3.15: UV-Vis-NIR spectra recorded for the gold nanorods prepared with different concentrations of silver nitrate ranging from 60 (— - black line), 120 (— - red line), 240 (— - blue line) and 300×10^{-6} M (— - pink line) in the growth solution.

Figure 3.15 also shows a red shift in the longitudinal plasmon band of the gold nanorods with an increasing concentration of silver nitrate in the growth solution. It is well known that the increase in the length of the gold nanorods results in shift in the longitudinal absorption band towards longer wavelength. Also, the transverse absorption peak intensity decreases with the silver nitrate concentration. This most likely arises because of the increased yield of the rod shaped nanoparticles suggested by TEM.

3.3.2.3. Molar extinction coefficients

There has been significant interest in gold nanorods because of the strong absorption band in the visible-NIR spectrum. For example, El-Sayed *et al* have reported the molar extinction coefficient for the longitudinal plasmon band of electrochemically prepared gold nanorods to be $1.9\pm0.4\times10^{9}$ $M^{-1}cm^{-1}$ at 695 nm determined by Inductive coupled plasma (ICP) atomic absorption spectroscopy.[44]

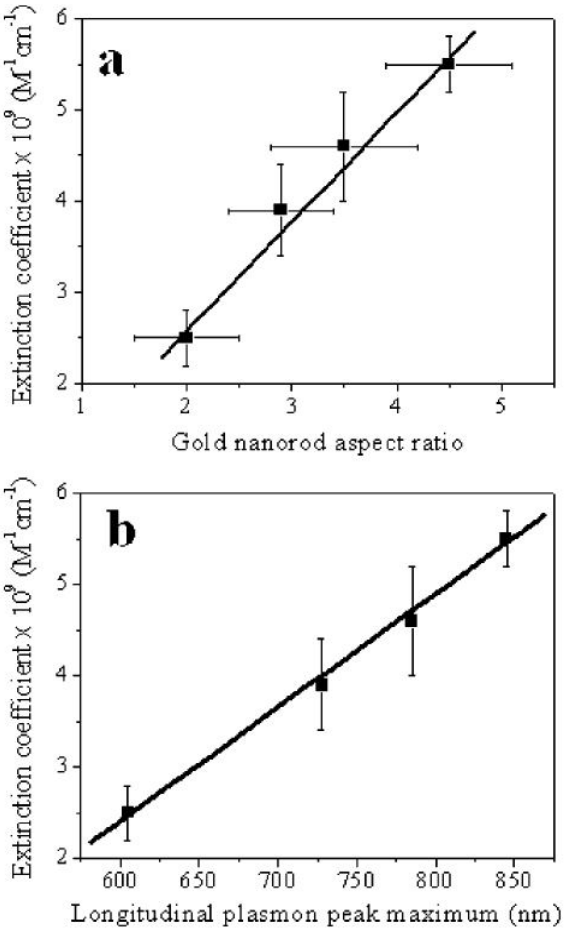

Figure 3.16: (a) Plot of molar extinction coefficient versus aspect ratio for gold nanorods with aspect ratios from 2.0 to 4.5. The *y*-axis error bars correspond to error in the ICP measurement, and the *x*-axis error bars correspond to the error in the measured dimensions of nanorods by TEM. (b) Plot of molar extinction coefficient versus longitudinal plasmon peak maximum for gold nanorods with aspect ratios from 2.0 to 4.5. Adapted from Christopher Orendorf and Catherine J. Murphy, *Quantitation of Metal content in the Silver-Assisted Growth of Gold Nanorods,* J. Phys.Chem. B, **2006**, 110, 3990.

Moreover, Murphy *et al* have also reported the dependence of the molar exinction coefficient on the longitudinal absorption maxima on the aspect ratio. Figure 3.16 (a) shows the plot of the molar extinction coefficient versus the aspect ratio of the gold nanorods. Figure 3.16 (b) shows the variation of the extinction coefficient with the longitudinal plasmon band maximum. It has been reported[45] that the molar extinction coefficient for the longitudinal plasmon band increases from 2.5×10^{9} $M^{-1}cm^{-1}$ to 5.5×10^{9} $M^{-1}cm^{-1}$ with increasing the aspect ratio from 2.0 to 4.5. Thus, the linear dependence of the molar extinction coefficient on the longitudinal plasmon band was used as the reference to calculate the molar extinction coefficient of the gold nanorods that has been prepared here.

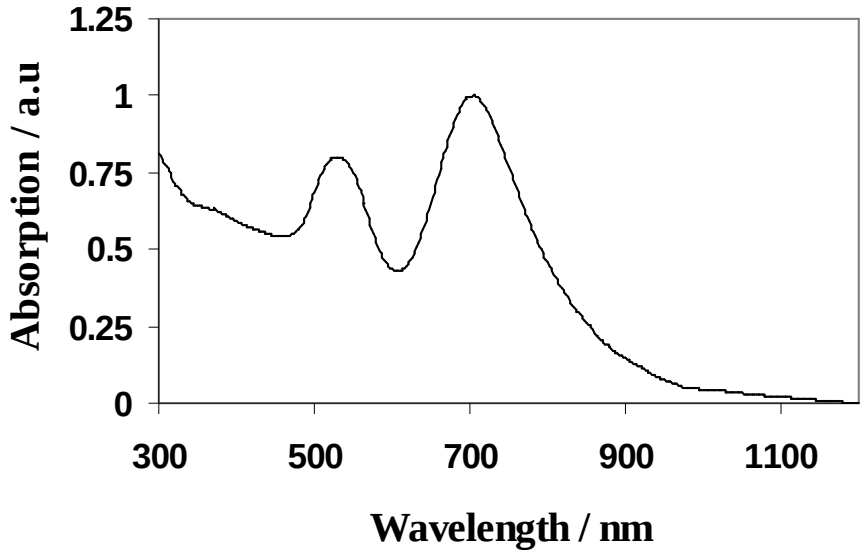

Figure 3.17: Normalised UV-Vis-NIR spectra for gold nanorod prepared using seed-mediated growth technique. The gold nanorods were dispersed in water. The longitudinal absorption maximum was found to be around 700 nm.

Figure 3.17 shows the normalised extinction spectrum obtained for the gold nanorods synthesised using seed-mediated growth. The gold nanorods with an aspect ratio of 3.6 has the longitudinal absorption band around 700 nm. The maximum yield of the gold nanorods was achieved for the nanorods with aspect ratio 3.6. Also, the presence of longitudinal absorption band around 700 nm is attractive for the development of the osmium metallopolymer-gold nanocomposite. This is because of

the possibility of achieving a good spectral overlap of nanorod plasmon resonance band with the emission of the $[Os(bpy)_2PVP_{10}]^{2+}$ metallopolymer. The molar extinction coefficient for the gold nanorods with an aspect ratio 3.6 (Figure 3.14(b)) was calculated to be 3.5×10^9 M^{-1} cm^{-1} using the longitudinal absorption band at 700 nm.

3.3.2.4. Concentration Analysis

Quantifying the gold nanorod concentration in the as-prepared solution is important when trying to create metallopolymer-gold nanorod composites of defined composition. In the conventional synthesis of spherical gold nanoparticles *via* chemical reduction, a strong reducing agent is used to reduce Au^{3+} or Au^{+} to Au^{0}. In such cases, it is fair to assume 100% reduction of the initial gold salt. Thus, by analysing the size of the gold nanoparticles using electron microscopy, it is easy to theoretically calculate the concentration of spherical gold nanoparticles. But in the case of anisotropic gold nanoparticles such as nanorods, weak reducing agents like ascorbic acid are used to reduce the initial gold salt and hence 100% reduction may not occur.[46] Therefore, quantifying the concentration of the gold nanorods is critical.

Since gold nanorods have a strong absorption band in the visible region, their molar extinction coefficient can be used to determine the concentration of the gold nanorods. Murphy *et al* has calculated the gold nanorod concentration in the as-prepared solution using a Liberty II Axial inductively coupled plasma (ICP) atomic emission spectroscopy.[45] The gold nanorods were separated using a centrifuge and dissolved in aqua regia. The gold concentration was calculated using ICP and the results showed that 95% of the initial gold was completely reduced when a strong reducing agent is used in the case of spherical gold nanoparticles, whilst in the case of gold nanorods, only 15% of the initial gold in the growth solution is reduced. The concentration of the gold nanorods was calculated using Beer-Lambert's law (Equation 3.5). The maximum absorption intensity for the gold nanorods with a longitudinal SPR band at 700 nm was found to be 1.311. The molar extinction coefficient for the corresponding gold nanorod was found to be 3.5×10^{9} M^{-1} cm^{-1}. Thus the concentration of the gold nanorods was evaluated to be 0.37×10^{-9} M.

3.3.2.5. Zeta Potential

Gold nanorods were synthesised in the presence of C_{16}TAB using the seed-mediated growth technique. The C_{16}TAB in the growth solution acts as the directional agent that results in the growth of rod shaped particles in aqueous solutions. In addition, the C_{16}TAB molecules also act as the surface capping ligands. The binding of C_{16}TAB on the surface of gold is interesting because of the possibility of forming bilayer.[47] Figure 3.18 (a) shows a chemical structure of C_{16}TAB. Figure 3.18 (b) shows the schematic representation of the formation of a bilayer of C_{16}TAB surfactant on a gold nanorod. The C_{16}TAB molecule has a quartenary ammonium head group (blue circles) with a long hydrocarbon chain (orange zigzag). The length of the hydrocarbon chain also plays a significant role in controlling the aspect ratio of the resultant gold nanorod.

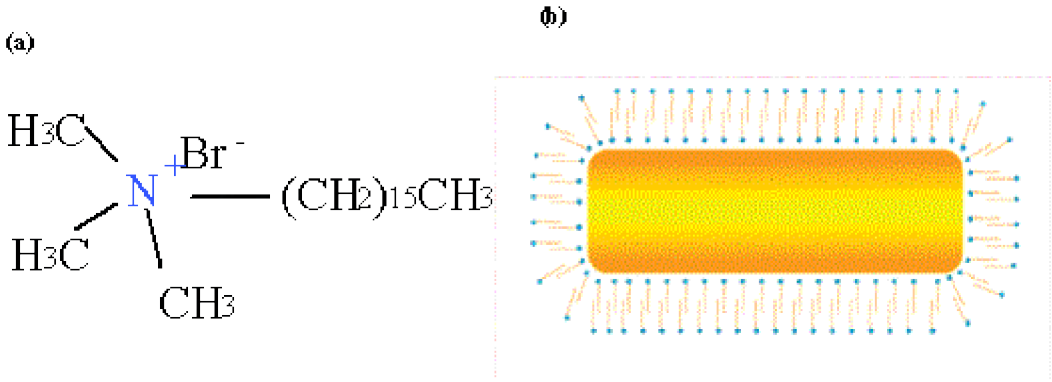

Figure 3.18: (a) Structure of hexadecylcetyltrimethyl ammonium bromide (C_{16}TAB) and (b) Formation of bilayer of C_{16}TAB on gold nanorods. The blue circles represent the ammonium head groups whereas the orange zigzags are the hydrocarbon tails of C_{16}TAB.

The zeta potential measurements were used to study the charge on the surface of the gold nanorods. The zeta potential value gives the idea of the orientation of the surface capping ligands and also gives the stability of the gold nanorods. Table 3.3 shows the consolidated zeta potential values obtained for gold nanorods synthesised with various amounts of silver nitrate content.

Table 3.3: Zeta Potential values obtained from electrophoretic mobility measurements for gold nanorods synthesised with various amounts of silver nitrate in the growth solution.

Concentration of $AgNO_3$ (μM)	Temperature °C	Zeta potential (mV)	Mobility (μm cm/Vs)	Conductivity (S/m)
60	25	+44.2	3.468	0.0878
120	25	+42.1	3.297	0.0452
240	25	+31.6	2.475	0.0108
300	25	+34.4	2.695	0.0863

The zeta potential measurements show that the gold nanorods have a positive potential on the surface. This might be because of the presence of ammonium head groups that extend away from the surface of the gold nanorods, which has been formed due to the bilayer formation. The magnitude of the zeta potential value (~+45 mV) of the gold nanorods is comparatively high. The net positive charge present in the surface of the gold nanorods gives columbic repulsion to the colloidal suspension and thus prevents the aggregation of the gold nanorods. This provides very good stability to the gold nanorods in aqueous solution over several months.

3.4. Conclusion

Spherical and rod shaped gold nanoparticles have been synthesised using a phase transfer protocol and a seed-mediated growth technique, respectively. The mono dispersity and the morphology of the nanoparticles were analysed using electron microscopy techniques. Changing the concentration of the reducing agent controlled the diameter of DMAP-protected spherical gold nanoparticles. The dependence of concentration and the molar extinction coefficient of the spherical gold nanopartices on diameter were explored. As the yield of gold nanorods was initially low, an attempt was made to improve the yield. The addition of silver nitrate in the growth solution increased the percentage yield of rod shaped particles. The orientation of the capping ligands was analysed using zeta potential measurements.

3.5. Reference

1 Anker, F. N.; Hall, W. P.; Lyandres, O.; Shah, N. C.; Zhao, J.; Van Duyne, R. P., *Nature Mater*, **2008**, 7, 442.

2 Caseri, W. *Macromol. Rapid Commun*. **2000**, 21, 705.

3 Crosby, A. J.; Lee, J-Y. *Polymer Rev.*, **2007**, 47, 217.

4 Sau, T. K.; Murphy, C. J. *J. Am. Chem. Soc*, **2004**, 126, 8648.

5 Sastry, M. *Current science*, **2003**, 85, 1735.

6 Gittins, D. I.; Caruso, F. *Angew. Chem. Int. Ed*. **2001**, 40,16, 3001

7 Wilcoxon, J. P.; Williamson, R. L.; Baughman, R. *J. Chem. Phys*. **1993**, 98, 9933.

8 Han, M. Y.; Quek, C. H. *Langmuir*, **2000**, 16, 362.

9 Turkevich, J.; Stevenson, P.; Hillier, J. *J. Am. Chem. Soc*. **1951**, 11, 55.

10 Jolivet, J.-P. *Metal Oxide Chemistry and Synthesis - From Solution to Solid State***,** John Wiley & Sons, Chichester, **2003**.

11 Oskam, G. *J. Sol-Gel Sci Techn*. **2006**, 37, 161.

12 Iwamoto, M.; Kuroda, K.; Kanzow, J.; Hayashi, S.; Faupel, F. *Adv. Powder Technol*,. **2005**, 16, 137.

13 Tam, F.; Goodrich, G. P.; Johnson, B. R.; Halas, N. J., *Nano Lett*, **2007**, 7, 496.

14 Weimer, W. A.; Dyer, M. J., *Appl. Phys. Lett*, **2001**, 79, 3164.

15 Chan, G. H.; Zhao, J.; Hicks, E. M.; Schatz, G. C.; Duyne, R. P. V., *Nano Lett*., **2007**, 7, 1947.

16 Link, S.; Mohamed, M. B.; El-Sayed, M. A. *J. Phys. Chem. B.* **1999**, 103, 3073.

17 Esumi, K.; Matsuhisa, K.; Torigoe, K., *Langmuir*, **1995**, 11, 3285.

18 Govindaraj, A.; Satishkumar, B. C.; Nath, M.; Rao, C. N. R., *Chem. Mater*, **2000**, 12, 202.

19 Gole, A.; Murphy, C. J., *Chem. Mater*, **2004**, 16, 3633.

20 Jana, N. R.; Gearheart, L.; Murphy, C. J. *J. Phys. Chem. B*, **2001**, 105, 4065

21 Sau, T. K.; Murphy, C. J. *Langmuir*, **2004**, 20, 6414.

22 Rao, P.; Doremus, R. *J. Non-cryst. Solids*, **1996**, 203, 202.

23 Hostetler, M.J. *Langmuir*, **1998**, 14, 17.

24 Iwamoto, M.; kuroda, K.; Kanzow, J.; Hayashi, S; Faupel, F. *Adv. Powder Technol*., **2005**, 16, 2, 137.

25 http://rsbweb.nih.gov/ij/index.html

26 Gandubert, V.J.; Lennox, B. *Langmuir*, **2005**, 21, 6532.

27 Mulvaney, P. *Langmuir*, **1996**. 12, 788.

28 Jain. P. K.; Lee. K. S.; El-Sayed. I. H.; El-Sayed, M.A. *J. Phys. Chem. B*. **2006**, 110, 7238.

29 Eustis, S.; El-Sayed, M. A. *Chem. Soc. Rev*. **2006**, 35, 209.

30 Scaffardi, L. B.; Pellegri, N.; Sanctis, O.; Tocho, J. O. *Nanotechnology*, **2005**, 16, 158.

31 Liu, X.; Atwater, M.; Wang, J.; Huo, Q. *Colloid Surface B*, **2007**, 58, 3.

32 Mulvaney, P. *Langmuir*, **1996**, 12, 788.

33 Hostetler, M.J.; Wingate, J. E.; Murray, R. W. *Langmuir*, **1998**, 14, 17.

34 Nerambourg, N.; Werts, M. H. V.; Charlot, M. Blanchard-Desce, M. *Langmuir*, **2007**, 23, 5563.

35 Hunter, R. J. *Zeta potential in colloid science*, Academic, London, **1981**.

36 Stolberg, L.; Richer, J.; Lipkowski, J.; Irish, D. E. *J. Electroanal. Chem*. **1986**, 207, 213

37 Barlow, C. B.; Burgess, I. J., *Langmuir*, **2007**, 23, 1555.

38 Dean, J. A. Lange's *Handbook of Chemistry*, 15th ed: McGraw-Hill: New York,

1999.

39 Forsythe, P.; Frampton, R; Johnson, C. C; Katritziky, A. R. *J. Chem. Soc., Perkin Trans.* **1972**, 2, 671.

40 Murphy, C. J.; Sau, T. K.; Gole, A. M.; Orendorff, C. J.; Gou, L.; Hunyadi, S. E.; Li, T., *J. Phys. Chem. B*, **2005**, 109, 13857.

41 Wang, J. X.; Marinkovic, N. S.; Adzic, R. R. *Colloid Surface. A*, **1998**, 134, 165.

42 Magnussen, O. M.; Ocko, B. M.; Wang, J. X.; Adzic, R. R. *J. Phys. Chem*. **1996**, 100, 5500.

43 Pal, T.; De, S.; Jana, N. R.; Pradhan, N.; Mandal, R.; Pal, A.; Beezer, A. E.; Mitchell, J. C., *Langmuir*, **1998**, 14, 4724.

44 Nokoobakht, B.; Wang, J.; El-Sayed, M. A. *Chem. Phys. Lett*, **2002**, 366, 17.

45 Orendorff, J. C.; Murphy, C. J. *J. Phys. Chem. B*, **2006**, 110, 3990.

46 Gou, L.; Murphy, C. J. *Chem. Mater*. **2005**, 17, 3668.

47 Smith, D. K.; Korgel, B. A., *Langmuir*, **2008**, 24, 644.

Chapter 4

Metallopolymer-Gold Nanoparticle Composites

4.1. Introduction

Composite materials, formed by combining metal nanoparticles and polymers that incorporate coordinated metal complexes, ought to lead to materials with interesting electrochemical and photonics properties. For example, the statistical separation between adjacent metal complexes, as well as between metal complexes and nanoparticles, can be systematically varied to control the nanoparticle-luminophore separation. Moreover, by tuning nanoparticle's plasmon,[1,2,3,4] resonance can also be achieved between the metallopolymer absorbance or emission. In this way, metal enhanced fluorescence or surface enhanced resonance Raman may be observed. These properties are attractive for biological optical imaging,[5,6] sensing[7] and optoelectronic nanodevices.[8]

Poly (4-vinylpyridine) (PVP) based polymers incorporating coordinated metal centres, e.g., $[M(bpy)_2PVP\ L]^{2+}$, where M is osmium or ruthenium and L is a monodentate ligand, are an attractive class of materials for forming nanocomposites[9] because of their electrochemical[10,11,12] and photonics properties.[13,14] Moreover, the unlabelled pyridine groups in polyvinyl pyridine backbone are capable of stabilising the metal nanoparticles. Electrochemiluminescence represents an important transduction methodology for ECL based assays,[15,16] especially for the detection of molecules and metabolites of biological relevance.[17,18] For example, it has been previously demonstrated that nanoparticles free metallopolymers generate ECL directly from the reaction of guanine bases in oligonucleotides in the ultra thin films without using a sacrificial reductant.[19]

Recently, several authors reported on composites of gold nanoparticles and *monomeric* metal complexes such as AuNP-$[Ru(bpy)_3]^{2+}$ for the ECL detection of nicotinamide adenine dinucleotide (NADH)[20] and thrombin.[21] AuNP-CdS:Mn nanocrystal films were developed for DNA ECL biosensor.[22] However, there are particular challenges when using immobilised monomeric luminophores, e.g., the

rate of Ru^{3+} production as dictated by the rate of homogeneous charge transport through thin films may be slow, and the fact that less than a few nanomoles of luminophore are typically immobilised on the electrode surface may limit the sensitivity of the ECL assay. Moreover, these systems do not lend themselves easily to thin film formation and it is challenging to control luminophore/gold nanoparticle ratios and physical separations. This is an important objective since the metallic surfaces strongly influence the emission characteristics of luminophores depending on the absorbance and emission characteristics of both nanoparticles and luminophores. Therefore, depending on their physical separation, the emission may be enhanced[23] or quenched.[24]

Controlling the separation between nanoparticles and ruthenium metal centres in a nanocomposite system involving polymeric structures is even more challenging because of the complex nature of the polymer structures. Controlled loading is a convenient alternative by which the molar ratio between the ruthenium metal centres and the gold nanoparticles can be varied, which could also change the separation between the nanoparticles and metal centres. Specifically, the dispersion of the gold nanoparticles within the ruthenium metallopolymer matrix ought to improve both the conductivity of the polymer and hence the number of Ru^{3+} centres available per unit time for light production. Moreover, the gold nanoparticles potentially can enhance the emission intensity by perturbing radiative and non-radiative decay paths.

In this chapter, modulations in the electrochemical, luminescence, and charge transport properties of $[Ru(bpy)_2PVP_{10}]^{2+}$ metallopolymer - DMAP-protected gold nanoparticle composites of defined Au NP:Ru ratios have been investigated. Incorporating the nanoparticles enhances the conductivity of the metallopolymer for certain loadings. Besides, the influence of size of the nanoparticles on the luminescence and electrochemiluminescence has also been investigated and reported. Significantly, the behaviour of the metallopolymer in the presence of DMAP-protected gold nanoparticles is different for the photo and electrochemiluminescence methods, which is believed to provide significant new insights into the design of advanced sensors.

4.2. Experimental

4.2.1. Materials

The synthesis and characterisation of $[Ru(bpy)_2PVP_{10}]^{2+}$ metallopolymer and DMAP-protected gold nanoparticles with four different mean mean diameters (4, 5, 7.5 and 12.5 nm) have already been discussed in Chapters 2 and 3, respectively. Alumina polishing powder (0.3 μm and 0.05 μm) was received from Buehler. Dimethylformamide (>97%) was received from Sigma-Aldrich. All the chemicals were used as received. The aqueous solutions were prepared from Milli-Q reagent water (Millipore Corp.,), 18 MΩ cm.

4.2.2. Metallopolymer-gold Nanocomposite

The ruthenium metallopolymer-gold nanoparticle composite was formed by mixing. To prepare micro molar aqueous solutions of ruthenium metallopolymer, a concentrated solution was first prepared in dimethylformamide (DMF) and diluted to the required concentration such that the DMF content was less than 1%. The concentration of the metallopolymer in the composite was maintained at 20 μM in all cases. Hence, by changing the concentration of DMAP-protected gold nanoparticles, the molar ratio of ruthenium metal centres to gold nanoparticles was systematically varied. Nanoparticles with different mean diameters (4, 5, 7.5 and 12.5 nm) were also used to develop the nanocomposite so as to probe the influence of the nanoparticle diameter on ruthenium metallopolymer properties.

4.3. Results and Discussion

4.3.1. Transmission Electron Microscopy

Transmission electron microscopy was used to investigate the distribution of the DMAP-protected gold nanoparticles within the $[Ru(bpy)_2PVP_{10}]^{2+}$ metallopolymer matrix. The metallopolymer-gold nanoparticle solution was prepared by mixing the separate solutions of metallopolymer and nanoparticle in the required molar ratio. The samples for the TEM analysis were prepared by drop-casting the nanocomposite solution on the TEM grids and the solvent was evaporated to dryness.

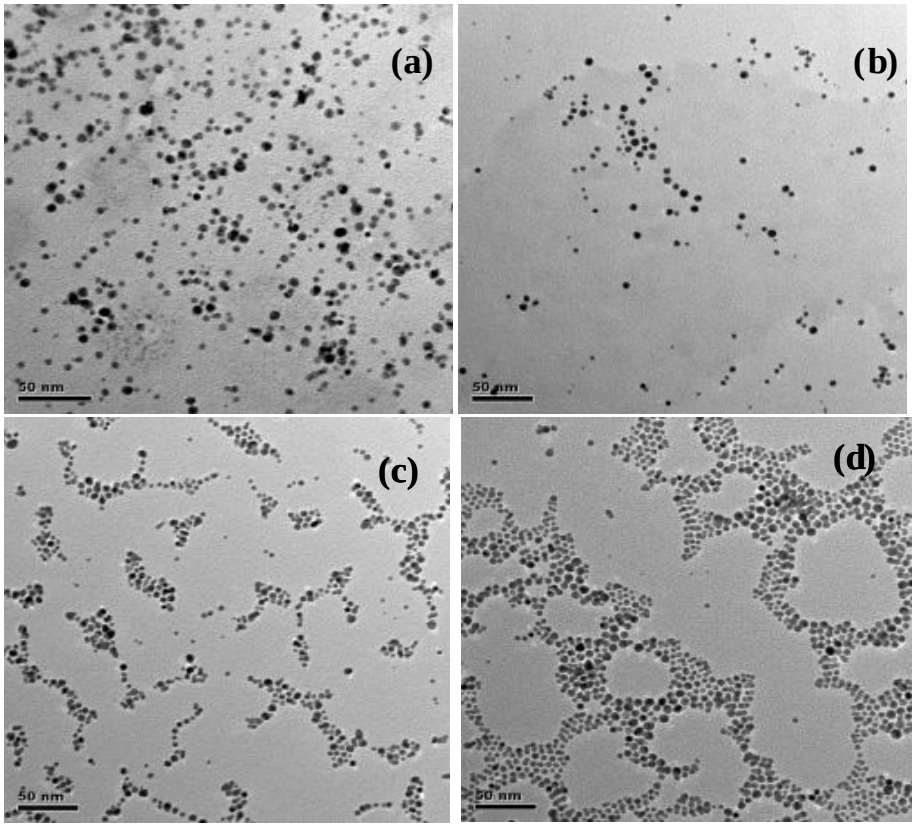

Figure 4.1: TEM image of $[Ru(bpy)_2PVP_{10}]^{2+}$ metallopolymer nanocomposites formed by incorporating (a) 4 nm, (b) 5 nm, (c) 7.5 nm and (d) 12.5 nm sized DMAP-protected gold nanoparticles, respectively.

Figure 4.1(a) to (d) shows the TEM images obtained from ruthenium metallopolymer-gold nanocomposites formed by incorporating 4, 5, 7.5 and 12.5 nm DMAP-protected gold nanoparticles, respectively. It is observed from the TEM

images that the gold nanoparticles are very well dispersed in the metallopolymer matrix. No noticeable aggregation of gold nanoparticles was observed in the nanocomposite systems.

4.3.2. UV-Vis-NIR Spectroscopy

The metallopolymer-gold nanocomposite was formed by mixing solutions of $[Ru(bpy)_2PVP_{10}]^{2+}$ with different amounts of DMAP-protected gold nanoparticles to achieve the required molar ratio. The solution phase UV-Vis absorption spectra were recorded between 300-900 nm. Ruthenium metallopolymer has its absorption maximum at 460 nm due to the metal-to-ligand charge transfer (MLCT) and around 350 nm due to the ligand centred transitions. The strong localised surface plasmon resonance (LSPR) band for the DMAP-protected gold nanoparticles is observed at 524 nm in water.

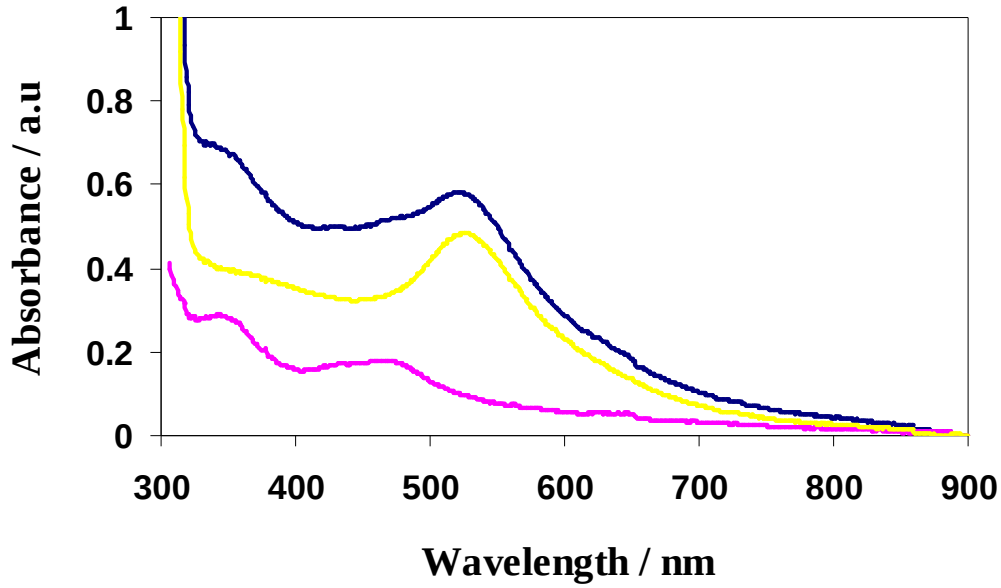

Figure 4.2: Absorbance spectrum corresponding to pure 20 μM ruthenium metallopolymer (—-pink line) and 2.97 μM DMAP-protected gold nanoparticles (—-yellow line). The blue line (—-blue line) shows the resultant absorption spectrum of the nanocomposite solution obtained by mixing the separate solutions of metallopolymer and nanoparticles. The mean diameter of the DMAP-protected gold nanoparticle is 4 nm.

Figure 4.2 shows the absorbance spectrum corresponding to the absorption of ruthenium metallopolymer (—-pink line) and 4 nm DMAP-protected gold nanoparticles (—-yellow line), respectively. The concentration of ruthenium

metallopolymer and DMAP-protected gold nanoparticle solutions are 20 μM and 2.97 μM, respectively. The blue line in Figure 4.2 shows the absorption spectrum corresponding to the metallopolymer-nanocomposite at Au NP:Ru molar ratio of 14.85×10^{-2}, which is obtained by mixing separate solutions of pure metallopolymer and 4 nm DMAP-protected gold nanoparticles.

The nanocomposites absorption spectrum shows the absorption peaks corresponding to both the metallopolymer and nanoparticles. The small peak observed at 350 nm and 460 nm in the composite solution resembles the electronic transitions that are observed in nanoparticle free metallopolymer solutions (Figure 4.2, pink line). The UV-Visible spectrum can also be used to study the extent of dispersion of the gold nanoparticles in the polymer matrix as the broadening and red shift of the spectral peaks indicates the chances of formation of aggregates. No peak shift or broadening was observed in the absorbance spectrum (Figure 4.2) of the metallopolymer-gold nanocomposite. This shows that the nature of the individual components of the composite remains unaffected even after the formation of a composite system.

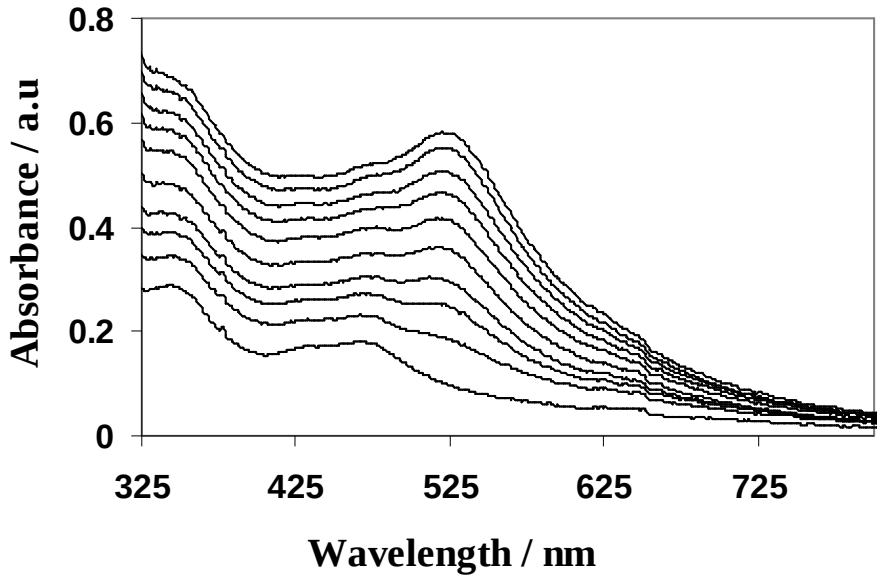

Figure 4.3: UV-Visible absorption spectra of 20 μM of Ru metallopolymer in presence of 4 nm DMAP-protected gold nanoparticles, with concentrations from 0 to 2.97 μM (from bottom to top) with an increment of 0.33 μM.

The UV-Visible absorption spectrum was recorded for the nanocomposites incorporating various amounts of DMAP-protected gold nanoparticles. Figure 4.3 shows the absorbance spectra for a Ru metallopolymer-gold nanocomposite at different molar ratios of DMAP-protected gold nanoparticles recorded between 300 nm and 800 nm. Here, the concentrations of 4 nm DMAP-protected gold nanoparticles were changed systematically from 0.33 μM to 2.97 μM so as to study the influence of the gold nanoparticles loading at different molar ratios.

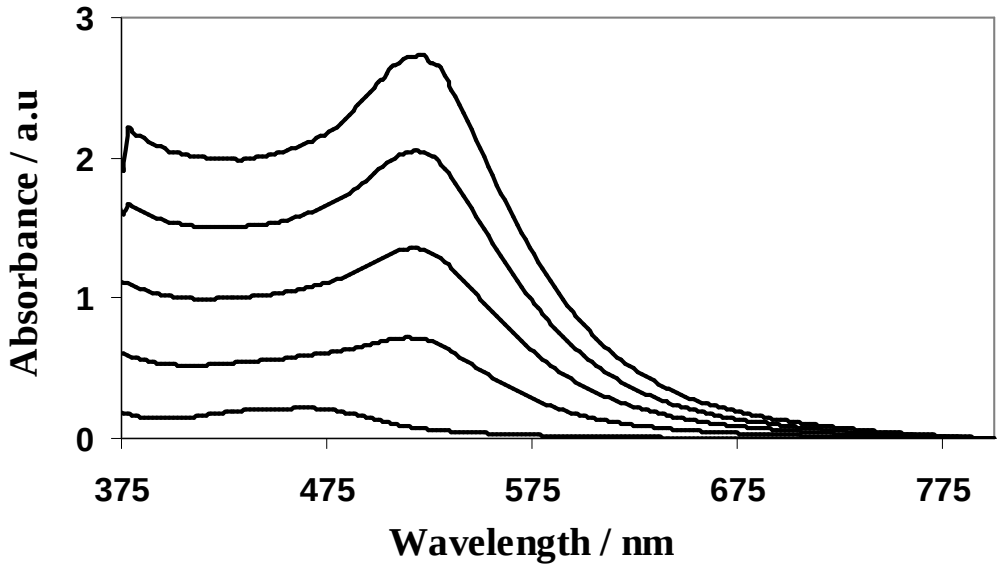

Figure 4.4: UV-Vis spectra for the metallopolymer-gold nanocomposite formed using 5 nm DMAP-protected gold nanoparticles with concentrations ranging from 0, 16.3, 32.6, 48.9 and 65 nM (from bottom to top). The concentration of metallopolymer was 20 μM, which is maintained constant.

Figure 4.4 shows the UV-Vis spectra for the metallopolymer-gold nanocomposite incorporating DMAP-protected gold nanoparticles with mean size 5 nm. The UV-absorption spectra for the nanocomposites with 7.5 nm diameters are shown in Figure 4.5. Figure 4.6 shows the UV-spectra for the composites made of ruthenium metallopolymer and 12.5 nm DMAP-protected gold nanoparticles. The concentration of ruthenium metallopolymer was 20 μM, which is maintained constant in all cases.

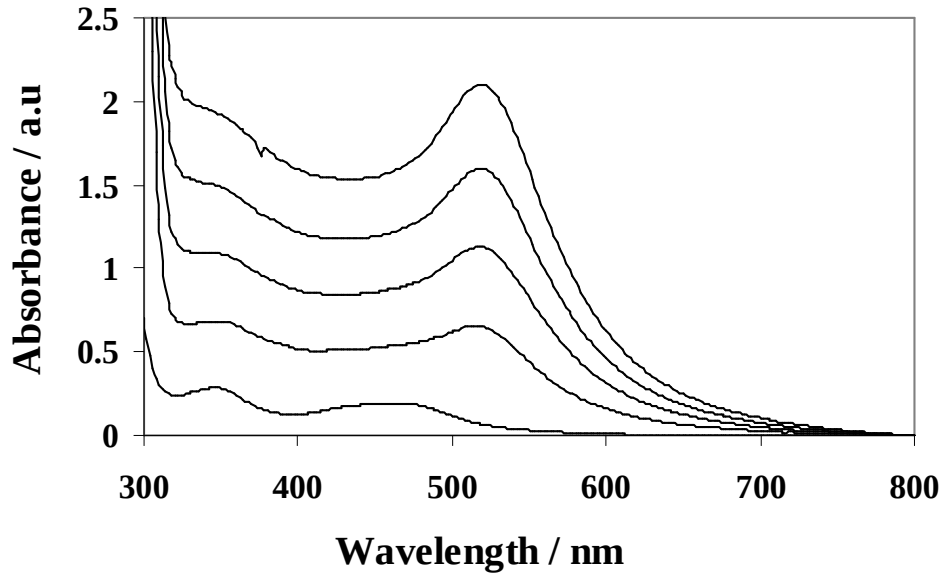

Figure 4.5: UV spectra for the metallopolymer-gold nanocomposite with 7.5 nm DMAP-protected gold nanoparticles with concentrations 0, 4.8, 9.6, 14.5, 19.3, 24.2 and 29 nM (from bottom to top).

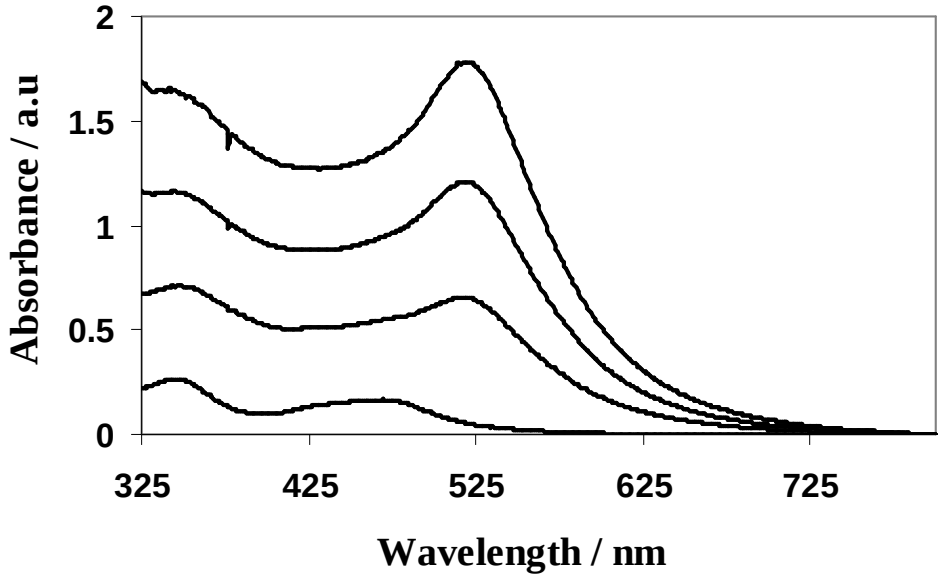

Figure 4.6: UV spectra for the nanocomposite developed with 12.5 nm DMAP-AuNPs with the concentration 0, 16.3, 32.6, 48.9, 65, 81.6 and 98 nM (bottom to top), respectively.

No evidence of broadening of the localised surface plasmon band of the gold nanoparticles and also in the ruthenium metallopolymer absorption is observed from the UV-Vis spectra of metallopolymer-gold nanocomposite solutions loaded with different sized gold nanoparticles. This shows that the spectral properties of individual components are not affected by the formation of the nanocomposites.

4.3.3. Förster Distance

Fluorescence or Förster resonance energy transfer (FRET) between donor luminophores and acceptor nanoparticles can occur when the donor emission and acceptor/quencher absorbance overlap.[25] Depending on the distance d, separating a luminophore and a metal surface, either quenching (d < 10 nm) or metal enhanced emission (20<d<50 nm), is possible.[26] The Förster integral quantifies the spectral overlap between luminophore emission and surface plasmon resonance of the nanoparticles. As illustrated in Figure 4.7, the DMAP-protected gold nanoparticles absorbance and the metallopolymer emission spectra overlap (shaded region) in the region between 550 and 750 nm making energy transfer thermodynamically feasible.

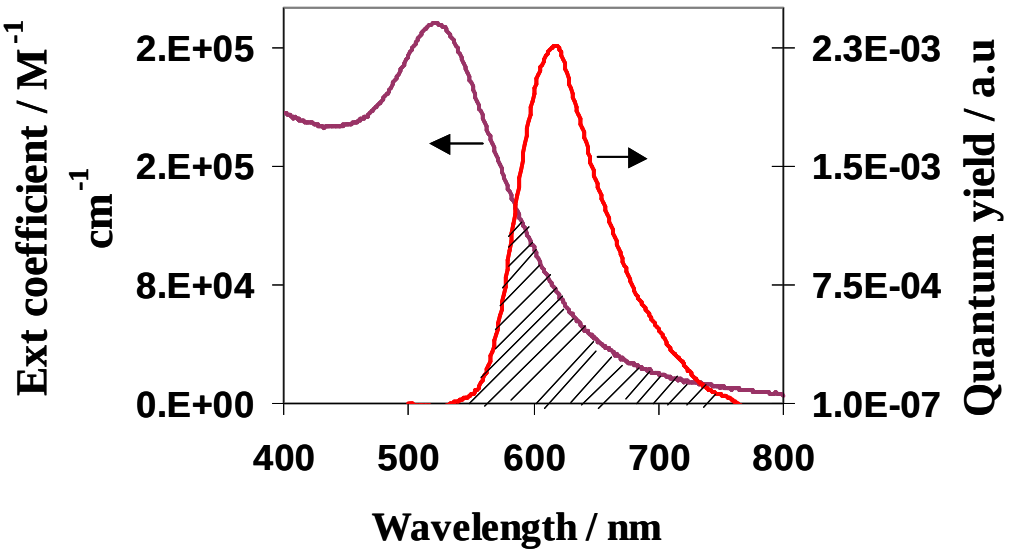

Figure 4.7: Spectral (shaded region) overlap between the normalised absorption spectrum (—-plum coloured line) of pure DMAP-protected gold nanoparticles dispersed in water and emission spectrum of $[Ru(bpy)_2PVP_{10}]^{2+}$ metallopolymer (—-red line) dissolved in DMF/ethanol mixture. The emission spectrum was recorded by exciting at 460 nm.

Figure 4.7 shows the electronic transitions, where the relative intensities of absorption and emission of DMAP-protected gold nanoparticles (—-plum coloured line) and ruthenium metallopolymer (—-red line) are plotted versus the wavelength,

respectively. Both the intensities of the absorption and emission spectra are normalised to unity. The efficiency of absorption can be expressed in terms of molar extinction coefficient, whereas the emission efficiency is denoted as quantum efficiency. Hence, the absorbance is plotted in terms of molar extinction coefficients, which can be expressed as M^{-1} cm^{-1}, whereas the emission spectrum is plotted in terms of the quantum yield of the metallopolymer. The amount of luminescence enhancement or quenching will depend on the amount of spectral overlap between the luminophore and plasmon band of the nanoparticle.[27]

Table 4.1: Förster distance changes with diameter of the DMAP-protected gold nanoparticles.

Diameter of gold nanoparticles (nm)	Spectral overlap integral $\int_0^\infty F_D(\lambda)\varepsilon_A(\lambda)\lambda^4 d\lambda$	Förster Distance (Å)
4	1.46×10^{-12}	26.46
5	1.08×10^{-12}	27.07
7.5	1.58×10^{-12}	28.84
12.5	9.63×10^{-12}	38.98

The Förster integral quantifies the spectral overlap between the luminophore emission and the surface plasmon resonance of the nanoparticles. The Förster distance between the gold nanoparticles synthesised with various mean diameters and the ruthenium metal centre was calculated using the Equation 1.10 in Section 1.7.3.[28] The spectral overlap was calculated from the spectral data of $[Ru(bpy)_2PVP_{10}]^{2+}$ emission and DMAP-protected gold nanoparticles absorbance.

Table 4.1 shows the spectral overlap integral and the Förster distance calculated for the metallopolymer-gold nanoparticle composite developed by loading nanoparticles with four different mean diameters. Figure 4.8 shows the dependence of Förster distance on the diameter of the DMAP-protected gold nanoparticles.

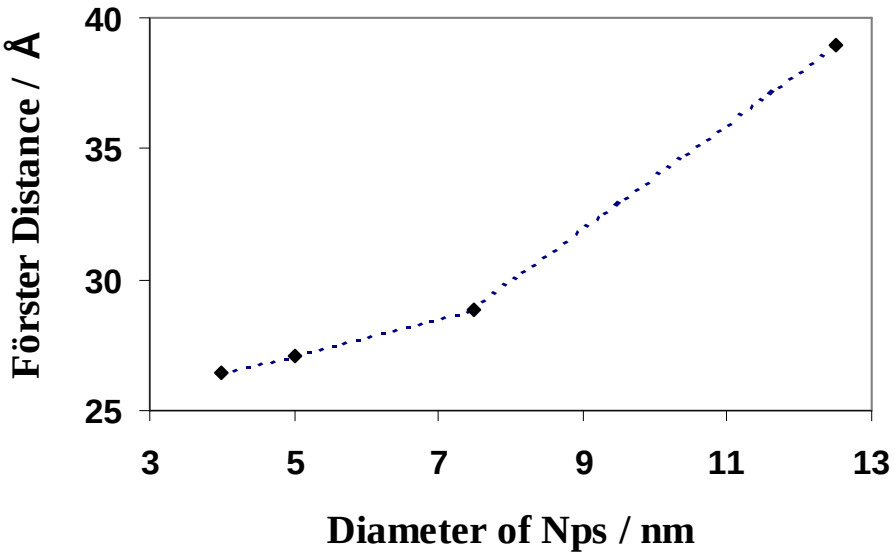

Figure 4.8: Dependence of Förster distance on the diameter of DMAP-protected gold nanoparticles.

The Förster distance between the ruthenium metal centre and the DMAP-protected gold nanoparticles with four different mean diameters is found to vary between 26Å to 40Å, which makes the nanocomposite system convenient to facilitate energy transfer. The Förster distance increases with increasing nanoparticle size, which can be ascribed to the broadening of the surface plasmon resonance band of the nanoparticles.

4.3.4. Luminescence Quenching

The plasmon band of the DMAP-protected gold nanoparticle overlaps with the emission spectra of the ruthenium metallopolymer between 550-750 nm (Figure 4.7). The Förster distance between the ruthenium metal centres and gold nanoparticles is found to increase from 25 to 40 Å with increasing nanoparticle diameter. Since the Förster distance is less than 100 Å, the gold nanoparticles are expected to enhance the luminescence intensity of the ruthenium metallopolymer *via* Förster resonance energy transfer (FRET) phenomenon. The Ru metallopolymer emits at 610 nm. Hence, the luminescence spectra for the metallopolymer-gold nanocomposites were recorded over the region from 500-800 nm upon exciting the luminophore at 460 nm. Figure 4.9 show that the ruthenium emission at 610 nm decreases with increasing concentration of the 4 nm DMAP-protected gold nanoparticles.

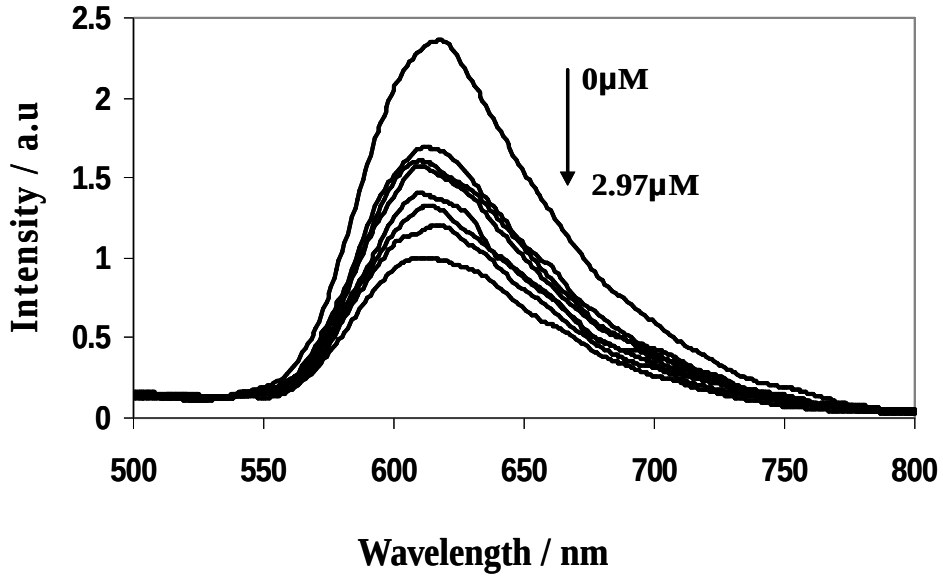

Figure 4.9: Luminescence spectra of Ru metallopolymer (20 µM) in presence of 4 nm DMAP-protected gold nanoparticles, with concentrations of 0, 0.33, 0.66, 0.99, 1.32, 1.65, 1.98, 2.31, 2.64 and 2.97 µM (from top to bottom).

The luminescence intensities of the metallopolymer-gold nanocomposites were recorded with various loadings of DMAP-protected gold nanoparticles. The concentration of ruthenium metal centres in all nanocomposite solutions was

maintained constant (20 μM). Incorporation of 4 nm DMAP-protected gold nanoparticles partially quenches the luminescence intensity of the ruthenium metallopolymer. In the presence of 4 nm DMAP-protected gold nanoparticles (Figure 4.9), the luminescence spectrum shows a shoulder on the low energy side, especially when the AuNPs:Ru molar ratio is high. This behaviour is reminiscent of the behaviour observed in solid solution, e.g., nitrile glass at 77 K suggesting a significant interaction between the polymer and the surface of the gold nanoparticles leading to a more rigid microenvironment around the luminophore.

A similar kind of quenched emission was observed for the nanocomposite systems developed with the DMAP-protected gold nanoparticles with mean diameters of 5, 7.5 and 12.5 nm, respectively. The presence of the gold nanoparticles in the nanocomposite clearly shows quenching of the luminescence of the metallopolymer. Despite the spectral overlap, it is clear from the luminescence measurements that metal enhanced fluorescence due to FRET might not be applicable to this nanocomposite system.

Bimolecular luminescence quenching can occur by two different mechanisms, i.e., dynamic quenching (collisional quenching) or static quenching (complex formation).[28] Where dynamic quenching is the dominant mechanism, the dependence of the emission intensity and lifetime on the quencher concentration is similar. When the lifetime remains unchanged with the concentration of the quencher, then static quenching is occurring. These measurements can assess if the nanoparticles are mobile within the excited state lifetime of the ruthenium complex or remain statically bound to the polymer backbone, e.g., through the available pyridine groups.

Luminescence enhancement of luminophores near the metal nanoparticles surface might arise from two different conditions. First, by concentrating incident light into local electromagnetic “hot spots”; nanostructured materials might lead to increased absorption of the incident light by luminophores. Second, metal nanostructures can alter the radiative and non-radiative decay rates of the nearby luminophores, changing both the lifetime and quantum yield.[27] Hence, luminescence lifetime measurements were carried out with the time-correlated single photon counting

technique (TCSPC). The excited state lifetimes were calculated for both pure metallopolymer and for the metallopolymer-gold nanocomposites with various nanoparticle mean diameters in solution at different nanoparticle loading.

Table 4.2: Lifetimes for 20 μM $[Ru(bpy)_2PVP_{10}]^{2+}$ metallopolymer with different amounts of DMAP-protected gold nanoparticles with 4 and 5 nm mean diameter. The maximum count for all the measurements was 10,000.

Amount of Nanoparticles μl	Life times (τ ns)			
	DMAP-AuNPs (4 nm)		DMAP-AuNPs (5 nm)	
	τ_1	τ_2	τ_1	τ_2
100	36±2	196±18	67.4±1	250±20
300	34±0.7	157±11	61.8±1	270
500	41±9	116±15	70±1.2	240±10
700	35±0.5	137±7	73.4±3.5	253±5

As discussed already in section 2.3.4, Figure 2.13 shows that the lifetimes for the ruthenium metallopolymer is a bi-exponential decay. Tables 4.2 and 4.3 show the lifetimes observed for Ru metallopolymer at different molar ratio of various sized DMAP-protected gold nanoparticles to the Ru metal centre. The lifetime measurements carried out for pure metallopolymer and metallopolymer-gold nanoparticle composite solution suggest that the loading of the nanoparticles does not affect the excited state properties of the ruthenium metal centres. The lifetime measurements do not show any considerable change greater than ±15%. However, the excited state lifetimes of ruthenium metallopolymer-nanocomposite changes slightly with the diameter of the dispersed nanoparticles. This suggests that in a nanocomposites solution, only the luminophores that are present in close proximity to the nanoparticles undergo quenched emission, whereas the luminophores that are unavailable to the nanoparticles exhibit lifetimes similar to those of the pure metallopolymer.

Table 4.3: Lifetimes for 20 μM $[Ru(bpy)_2PVP_{10}]^{2+}$ metallopolymer with different amounts of DMAP-protected gold nanoparticles with 7.5 and 12.5 nm mean diameter. The counts collected for all the measurements were maintained at 10,000.

Amount of DMAP-AuNPs μl	Life times (τ ns)			
	DMAP-AuNPs (7.5 nm)		DMAP-AuNPs (12.5 nm)	
	τ_1	τ_2	τ_1	τ_2
100	46.1±1.2	149±6	88	18±2
300	54.7±2	156±12	52.9±4	25
500	61.8±1	126±2	88	25.6
700	59.6±3	175±15	88.3	25

The decay measurements show that the lifetimes are unaffected by the gold nanoparticle loading in the ruthenium polymer matrix. Hence, the luminescence quenching may be ascribed to the static quenching mechanism. The term static quenching implies either the existence of a sphere of effective quenching or the formation of a ground state non-fluorescent complex.

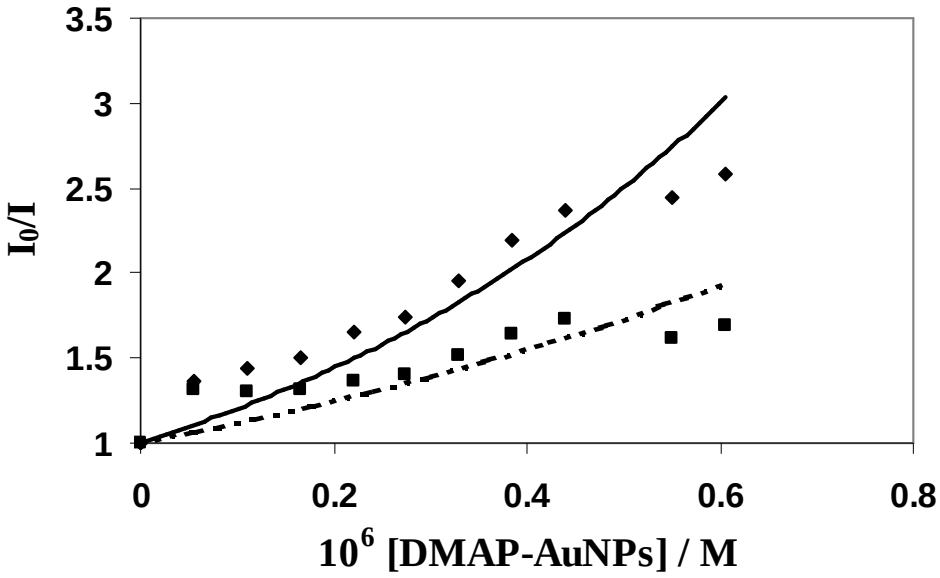

Figure 4.10: Stern-Volmer plot for the luminescence-quenching phenomenon observed for metallopolymer-4 nm DMAP protected gold nanoparticle (♦) composite.

The association constant for the nanoparticles and the luminophore can be estimated from the Stern-Volmer constant, which can be calculated using the following equation [28]:

$$\frac{I_0}{I} = 1 + K_{SV}[Q] \qquad \text{.....(4.1)}$$

where I_0 and I are the luminescence intensities of the metallopolymer before and after quenching respectively, K_{SV} is the Stern-Volmer constant and [Q] is the concentration of the quencher.

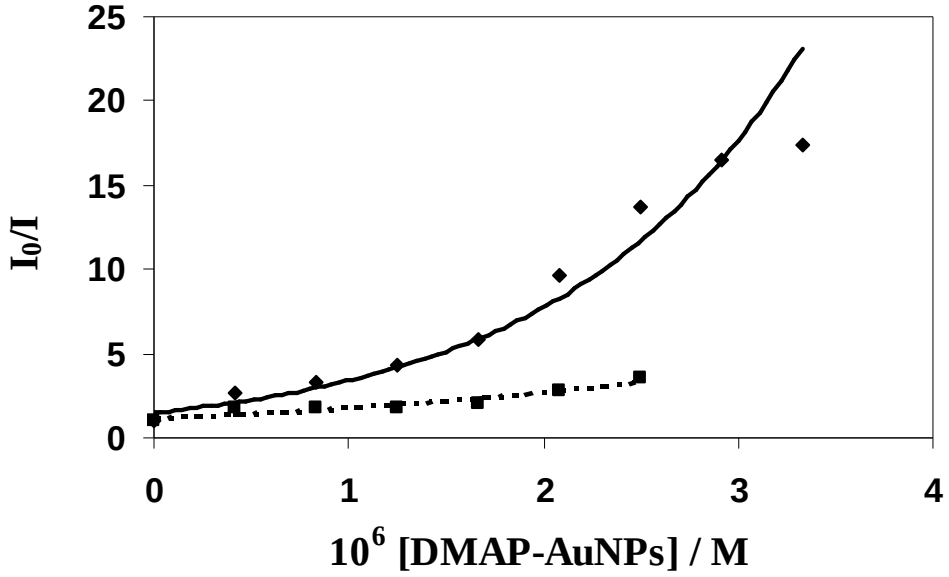

Figure 4.11: Stern-Volmer plot for the luminescence-quenching phenomenon observed for metallopolymer-5 nm DMAP protected gold nanoparticle composite before (♦) and after (■) correcting for self-absorption of nanoparticles.

Figures 4.10, 4.11, 4.12 and 4.13 show the Stern-Volmer plots of I_0/I *vs.* quencher concentration for the nanocomposite systems formed by loading 4, 5, 7.5 and 12.5 nm DMAP-protected gold nanoparticles, respectively. In the case of quenching due to the formation of a ground state non-fluorescent complex, the lifetime of the uncomplexed luminophore remains unaffected. Also, the ratio of the luminescence

intensities (I_0/I) of the luminophores should show a linear dependence on quencher concentration ([Q]).[29]

However, the lifetime of ruthenium metal centres in nanocomposite systems changes with the diameter of DMAP-protected gold nanoparticles. Moreover, Figures 4.10 to 4.13 show an approximately exponential dependence of I_0/I on quencher concentration ([Q]), DMAP-protected gold nanoparticles, irrespective of their diameters. Also, no evidence of formation of a complex (e.g., broadening or red shift) was observed from the absorption spectra of metallopolymer-gold nanocomposites. Thus the interaction is more likely to be non-specific and the Perrin model of an effective sphere of quenching is likely to be more appropriate.

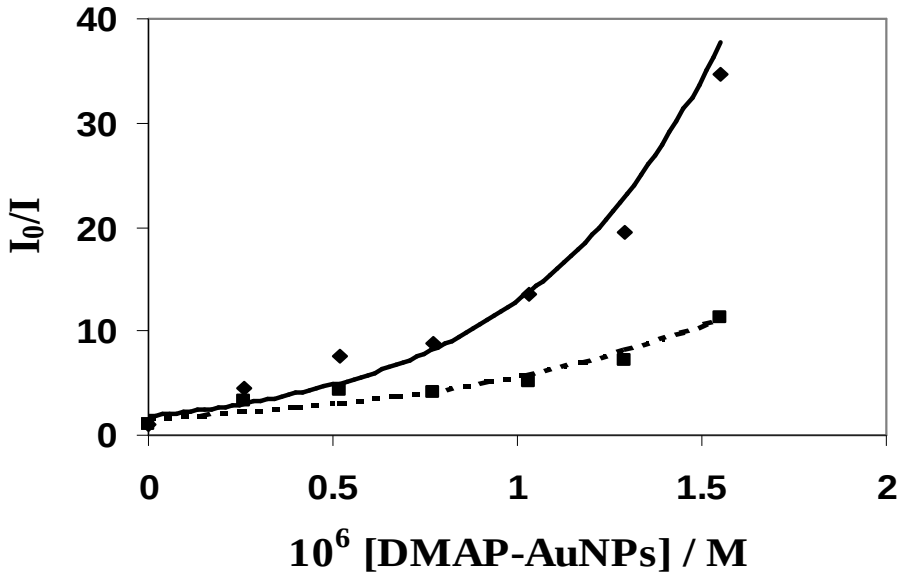

Figure 4.12: Stern-Volmer plot for the luminescence-quenching phenomenon observed for metallopolymer-7.5 nm DMAP protected gold nanoparticle composite before (♦) and after (■) correcting for self-absorption of nanoparticles.

However, given the large molar extinction coefficient of the nanoparticles at the excitation wavelength, it is important to consider the impact of increased absorbance of the DMAP-protected gold nanoparticles when their concentration is high. The higher concentrations of the nanoparticles might result in the possible absorption of

most of the excitation light by nanoparticles instead of the ruthenium metal centres. Due to this, the number of photons available to excite the luminophore is reduced.

In order to separate the effects of quenching and dilution from those due to absorption/scattering by the gold nanoparticles, the emission intensity was corrected by using the following equation:[30]

$$\left(\frac{I_0}{I}\right)_{Corr} = \left(\frac{I_0}{I}\right)_{app}\left[\frac{1-10^{-(A_D+A_Q)}}{1-10^{-A_D}}\right]\frac{A_D}{(A_D+A_Q)} \quad \text{.....(4.2)}$$

where $(I_0/I)_{app}$ is the observed ratio of the emission intensity from the unquenched sample to that of the quenched one, and A_D and A_Q are the absorbances of donor and quencher, respectively, at the excitation wavelength (460nm).

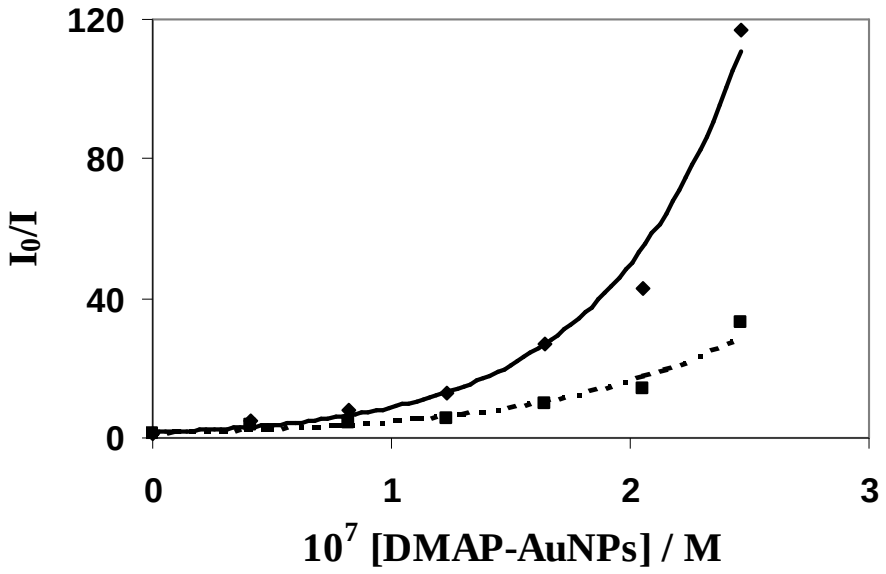

Figure 4.13: Stern-Volmer plot for the luminescence-quenching phenomenon observed for metallopolymer- 12.5 nm DMAP protected gold nanoparticle composite in water before (♦) and after (■) correcting for inner filter effects.

Figures 4.10 to 4.13 show the decrease in the ratio of I_0/I in the Stern-Volmer plots after (■) correcting for the self-absorption of the nanoparticles at the excitation wavelength. The correction for the self-absorption of the DMAP-protected gold

nanoparticles is found to be less than 30% for all the nanocomposite systems. The luminescence-quenching phenomenon due to a sphere of effective quenching can be described by the Perrin's model as described in Section 1.7.2.

According to this Perrin model, the quenching of the luminophore is assumed to be complete if a quencher molecule Q is located inside the active sphere (sphere of effective quenching) of volume V_q surrounding the luminophore. Hence, the luminescence intensity decreases with increasing quencher concentration, but the luminescence decay remains unaffected. A plot of ln (I_0/I) *versus* [Q] gives the volume of the sphere of effective quenching and hence the radius was calculated from this volume using Equation 1.7. Table 4.4 shows the calculated value for the radius of sphere of effective quenching. Its value was 75 ±5 Å, and this was unaffected by the diameter of the DMAP-protected gold nanoparticles.

Table 4.4. The radius of the quenching sphere and the quenching efficiency obtained for metallopolymer-gold nanocomposites prepared with different sized DMAP-protected gold nanoparticles before and after correcting for inner filter effects.

Diameter of DMAP-Au Nanoparticles (nm)	Before correcting for Inner filter effects		After correcting for Inner filter effects	
	Radius of Quenching Sphere (Å)	Quenching Efficiency (%)	Radius of Quenching Sphere (Å)	Quenching Efficiency (%)
4	90	59	80	38
5	70	92.7	50	71.8
7.5	90	97.2	80	91.2
12.5	80	97.7	70	92.9

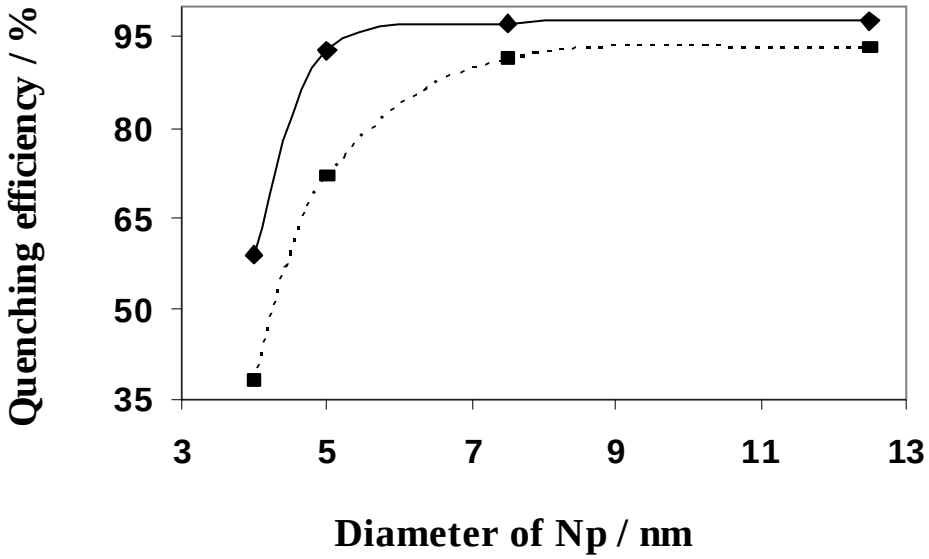

Figure 4.14: Dependence of the luminescence quenching efficiency on mean diameter of the DMAP-protected gold nanoparticle filler calculated before (♦) and after (■) performing correction for inner filter effects.

The luminescence quenching efficiency can be calculated from the decrease in the donor emission using Equation 1.13 as already described in Section 1.7.3. Figure 4.14 shows the variation in the quenching efficiencies with respect to the diameter of the DMAP-protected gold nanoparticles calculated before (♦) and after (■) performing corrections for inner filter effects. The quenching efficiency increases with increasing nanoparticle diameter. The quenching efficiency increases from 38% to 93% with the size of the nanoparticles at a 1:1 volume ratio of Au NP:Ru. The increase in the quenching efficiency is consistent with the increase in Förster distance. Significantly, for the $[Ru(bpy)_2PVP_{10}]^{2+}$ metallopolymer used here, the ruthenium centres are separated by approximately 30 Å making it likely that the 12.5 nm diameter nanoparticle can quench more than one ruthenium centre.

4.3.5. Charge Transfer Characteristics

A key objective of incorporating metallic nanoparticles within the metallopolymer matrix is to increase the rate at which the oxidation of the ruthenium centres proceeds. Nanocomposites containing Au NP with four different mean diameters i.e., 4, 5, 7.5 and 12.5 nm, were formed at different reactant molar ratios. Figure 4.15 shows the electrochemical response of the metallopolymer-gold nanocomposites at AuNP:Ru molar ratio of $4.5x10^{-2}$ formed by incorporating nanoparticles with mean diameters of 4 nm (orange line), 7.5 nm (pink line) and 12.5 nm (blue line) recorded at a scan rate of 100 mV s^{-1} with 0.5 M H_2SO_4.

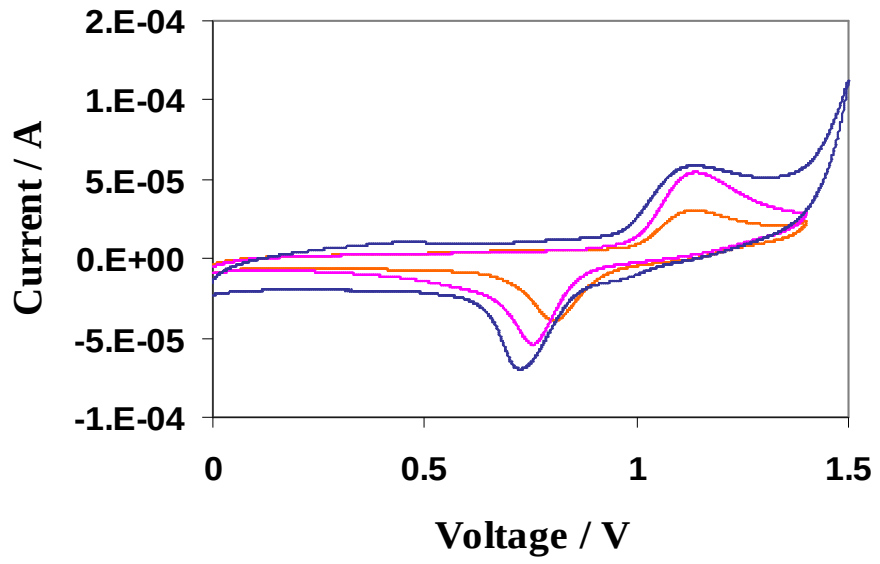

Figure 4.15: (a) Cyclic voltammetric response of $[Ru(bpy)_2PVP_{10}]^{2+}$ metallopolymer-gold nanocomposite films with mean diameters of 4 (orange line), 7.5 (pink line) and 12.5 nm (blue line) at a AuNP:Ru volume ratio of 1:1 recorded at a scan rate of 100 mV s^{-1}. The supporting electrolyte is 0.5M H_2SO_4.

The redox peaks are attributed to the oxidation and subsequent reduction of the metallopolymer-gold nanocomposites, which includes the charge associated with both Ru and gold.[31] The reduction potential of gold becomes slightly negative when the diameter of the incorporated gold nanoparticles increases. This could be due to

the increased electron transfer rates between the nanoparticle and the electrode with an increase in the nanoparticle size.

Figure 4.16 shows the electrochemical response of a AuNP:Ru molar ratio of $9.9x10^{-2}$ composite film at a scan rate (from top to bottom) of 500, 400, 300, 200 and 100 mVs^{-1}. Inset in Figure 4.16 shows that the peak current (i_p) varies linearly with the square root of scan rate ($\upsilon^{1/2}$) for the nanocomposite system. Thus, the charge transfer characteristics of metallopolymer-gold nanoparticle composite system are semi-infinite linear diffusion controlled and hence the Randles-Sevcik equation can be applied to find out the rate of charge transport through the films.

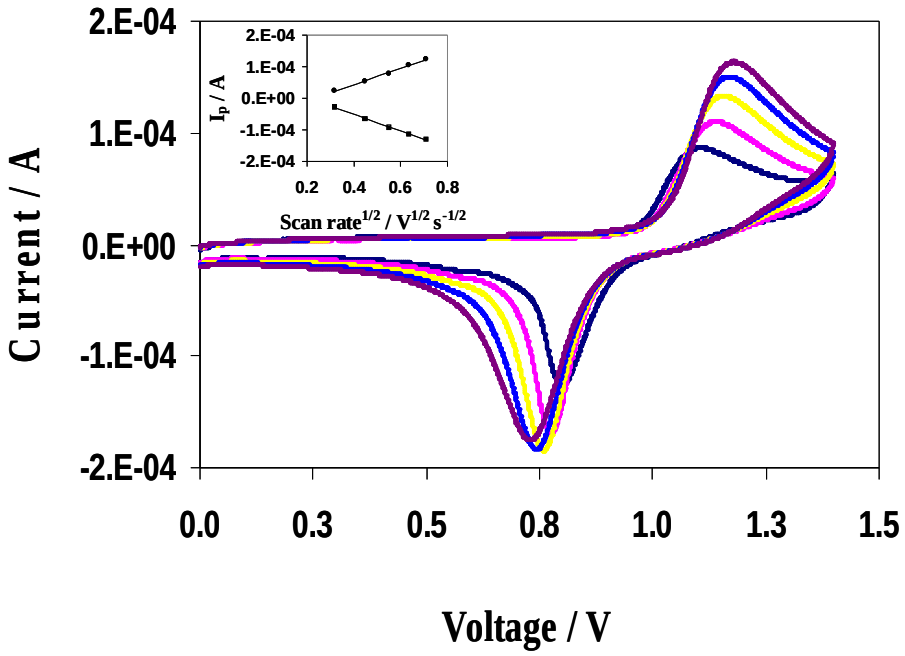

Figure 4.16: The electrochemical behaviour of metallopolymer-gold nanocomposite with 5 nm DMAP-Au NPs at the molar ratio $9.9x10^{-2}$ at a scan rate of 500 (plum), 400 (blue), 300 (yellow), 200 (pink) and 100 (dark blue) mV s^{-1}. Aqueous solution of 0.5 M H_2SO_4 was used as supporting electrolyte. The inset shows the linear dependence of i_p versus $\upsilon^{1/2}$.

The electronic communication between the nanoparticles and the polymer backbone can be evaluated from the rate of homogeneous charge transfer with the nanoparticle

loading. The homogeneous charge transfer diffusion coefficient, D_{CT}, can be determined using Randles- Sevcik Equation 1.18[32]:

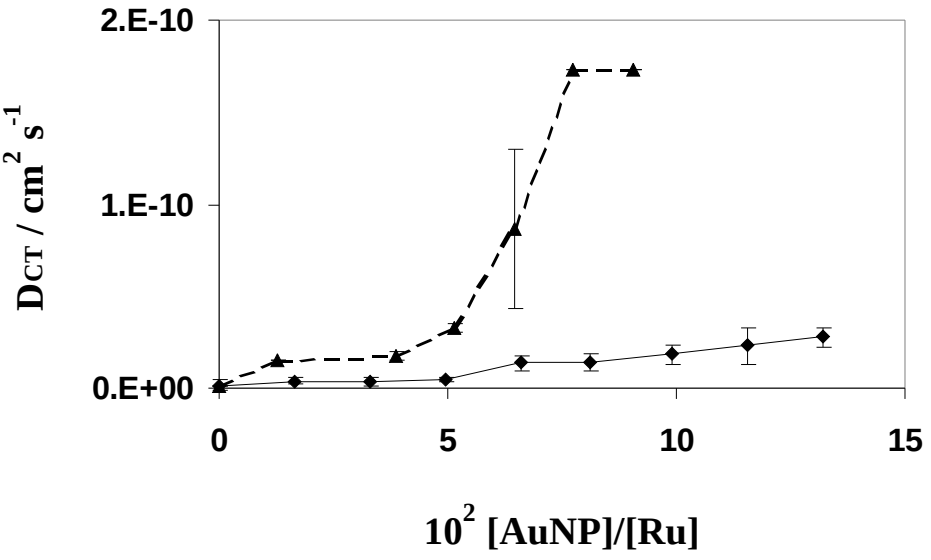

Figure 4.17: Charge transfer diffusion coefficient of $[Ru(bpy)_2PVP_{10}]^{2+}$ metallopolymer-gold nanocomposite films at different Au NP:Ru molar ratios formed by incorporating DMAP-protected gold nanoparticles with mean diameter 4 nm (♦) and 5 nm (▲) respectively.

For all the four systems formed by incorporating DMAP-protected gold nanoparticles of different sizes, addition of different amounts of the DMAP-protected gold nanoparticles systematically varied the ratio of the number of ruthenium centres per nanoparticle (molar ratio). Figure 4.17 shows the homogeneous charge transfer diffusion coefficient (D_{CT}) of the Ru metallopolymer at different molar ratio of Au NP:Ru metal centres for nanoparticles with mean diameter 4 (♦) and 5 (■) nm. Figure 4.18 shows the rate of homogeneous charge transport through metallopolymer-gold nanocomposites films formed by incorporating 7.5 nm DMAP-protected gold nanoparticles. The inset to Figure 4.18 shows the rate of charge transport for the composite with 12.5 nm particles. The nanoparticle loading required for enhanced charge transport varies with the nanoparticle diameter.

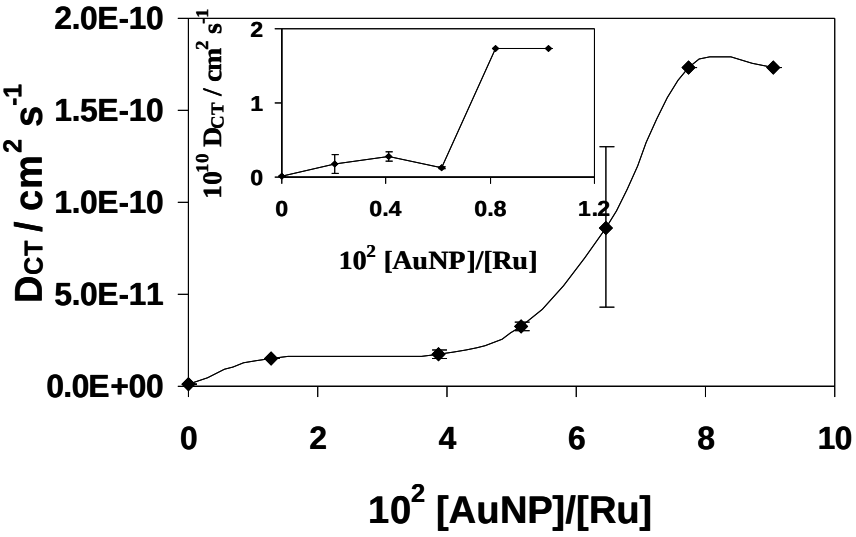

Figure 4.18: Charge transfer diffusion coefficient of $[Ru(bpy)_2PVP_{10}]^{2+}$ metallopolymer-gold nanocomposite films at different Au NP:Ru molar ratio developed by incorporating DMAP-protected gold nanoparticles with mean diameter 7.5 nm (♦) nm. The inset shows the dependency of charger transfer diffusion coefficient on the Au NP:Ru molar ratio for the nanocomposites developed with 12.5 nm nanoparticles.

Enhanced homogeneous charge transfer rate is achieved for the metallopolymer-gold nanocomposite after reaching the molar ratio $4.5x10^{-2}$ by loading 4, 5 and 7.5 nm nanoparticles respectively whereas for 12.5 nm the molar ratio is $4.1x10^{-3}$. The incorporation of nanoparticles with higher diameter (7.5 and 12.5 nm) increases D_{CT} from $1.7x10^{-11}$ cm^2s^{-1} to the maximum of about $1.73x10^{-10}$ cm^2s^{-1}. In all the nanocomposite system, the diffusion coefficient is insensitive to the incorporation of DMAP-protected gold nanoparticles until reaching a particular loading called the percolation threshold, after which D_{CT} increases significantly.

However, since the gold oxide formation and its reduction is convoluted with he ruthenium response, it is difficult to separate their contribution to the charge observed in the nanocomposite systems. This arises due to the similarity in the oxidation potential of both Ru and Au. Thus, the knowledge on the electrochemically active area of gold nanoparticles is significant to analyse the contribution of gold towards the charge transfer diffusion coefficients. It has been

reported that the charge density associated with the reduction of the oxide layer on gold nanoparticles is similar to that of a bulk gold electrode.[33] The charge associated with the reduction of a gold oxide monolayer is 386 μCcm^{-2}.[34] Thus, the available surface of the colloidal gold nanoparticles involved in the electrochemical process can be determined by measuring the charge associated with the cathodic peak in the cyclic voltammogram.

For the metallopolymer-gold nanocomposite systems, it is important to determine the extent to which the electrochemical communication between nanoparticles changes as a function of loading, e.g., there could be electrochemically isolated nanoparticles at low loadings that become connected at higher loadings. The total surface area of the electrochemically active gold nanoparticles in the composite was calculated from the charge passed under the oxide reduction peak. The electrochemical surface area is given by:

$$A_{ec} = \frac{Q_{ad}}{Q_m} \quad \text{.....(4.3)}$$

where Q_{ad} is the charge associated with monolayer coverage of the gold and Q_m is the absorption charge associated with standard polycrystalline gold, 386 μC cm^{-2}.[35]

Figure 4.19 shows the dependence of the electrochemically active area, A_{ec}, of the gold nanoparticles with diameters 4, 7.5 and 12.5 nm respectively, for different molar ratios of nanoparticles to ruthenium centres. For all the nanocomposite systems, A_{ec}, increase linearly with increasing nanoparticle loading. Yet, the magnitude of increase is not great at low nanoparticle loadings. This result is interesting, since it suggests that the ruthenium centres do not efficiently mediate the electron transfer to the gold nanoparticles despite the similarity of their oxidation potentials.

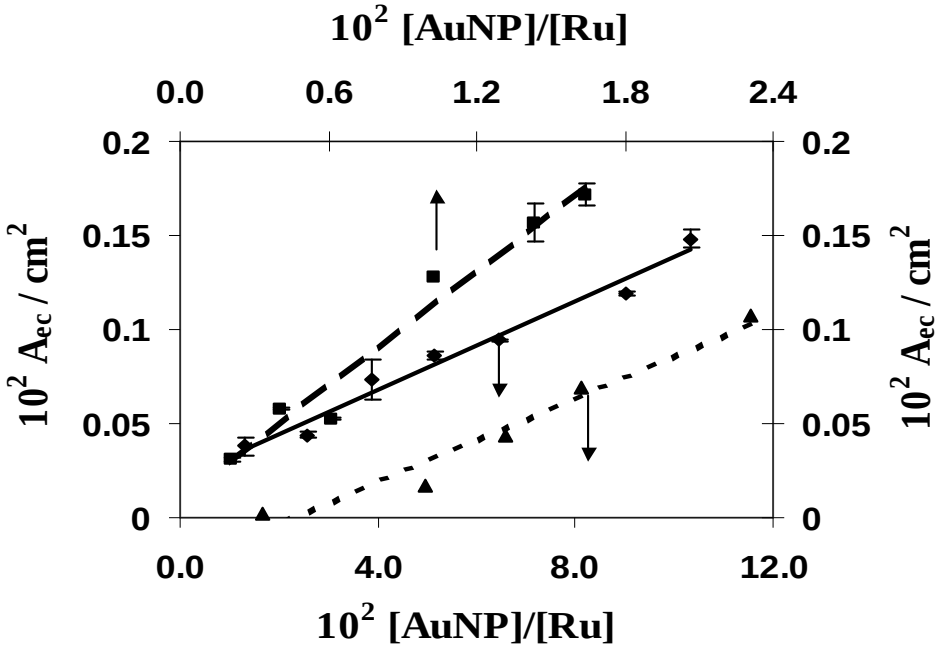

Figure 4.19: Electrochemically active surface area of the gold nanoparticles with mean diameter 4 nm (▲), 7.5 nm (♦) and 12.5 nm (■) as a function of AuNP:Ru molar ratio measured at a scan rate of 5 mV s^{-1} on a 3 mm glassy carbon electrode.

More interestingly, the metallopolymer-gold nanocomposites formed by incorporating gold nanoparticles show a linear increase in the electrochemically active area with the nanoparticle loading. However, as the loading increases, A_{ec} increases at a rate that exceeds that expected on the basis of the number of additional nanoparticles incorporated. This result indicates that nanoparticles, which were previously isolated can undergo oxide monolayer formation at the higher loadings. This suggests that the larger gold nanoparticles might be very well dispersed in the polymer matrix that makes the nanoparticles available for the electrochemical activity.

Though the charge observed at 1.2 V might include the contribution from gold oxide formation, the linear dependency of A_{ec} (Figure 4.19) on nanoparticle loading shows that the contribution of AuO formation might not be drastic after the percolation threshold. Thus, the increase in the charge transport diffusion coefficient might be due to the possibility of formation of a network of communicating particles that enhances the conductivity of the composite.

The study of electronic conductivity through metallopolymer nanocomposites might provide significant information on the charge transport mechanism. Wrighton and co-workers have demonstrated a useful way to estimate the film conductivity from slope $\partial i/\partial E$ obtained from the conductivity measurements.[36,37,38] The electronic conductivity of the metallopolymer-gold nanocomposite films incorporating 4 nm DMAP-protected gold nanoparticles was measured using IDA electrodes at different Au NP:Ru molar ratios to study the influence of conductivity on the ECL properties.

The film conductivity was measured using Equation 4.4:

$$\sigma = \frac{d_G}{A_{Total}} \cdot \frac{\partial i}{\partial E} \qquad \text{.....(4.4)}$$

where σ is the conductivity and (d_G / A_{Total}) is Zaretsky cell constant (0.04 cm^{-1}). $\partial i/\partial E$ was obtained from the slope of the linear plots of current versus voltage.

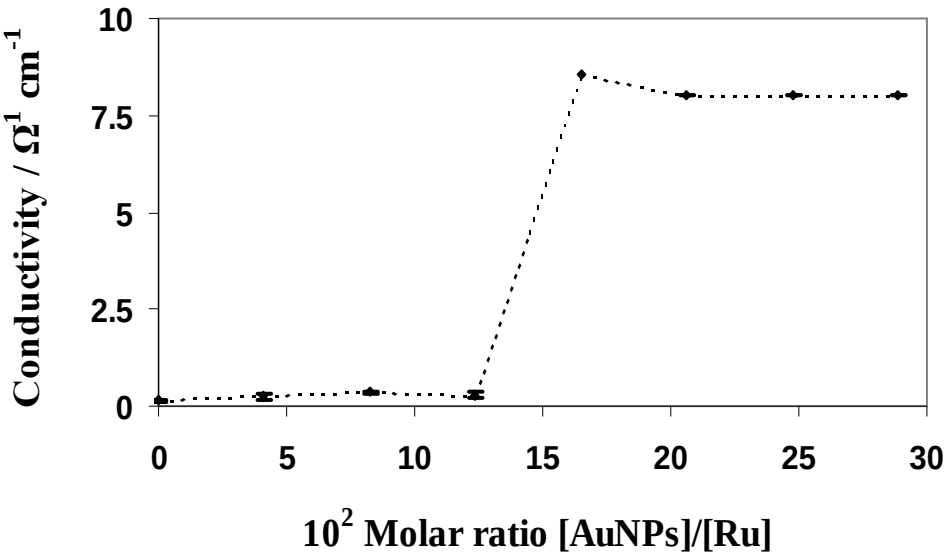

Figure 4.20: Dependence of the conductivity on the Au NP:Ru molar ratio for a metallopolymer nanocomposite incorporating 4 nm DMAP-protected gold nanoparticles. 20 μM metallopolymer was used in the analysis.

Figure 4.20 shows the dependence of the conductivity of the nanocomposite films on the Au NP:Ru molar ratio. This Figure reveals that the conductivity of the

nanocomposite is independent of the nanoparticle loading until reaching a particular loading (percolation threshold), approximately 5×10^{-2}, after which the conductivity increases significantly before again becoming independent of the nanoparticle loading. The conductivity for the pure metallopolymer was found to be 0.14×10^{-10} Ω^{-1} cm^{-1}, whereas the conductivity increased to 8×10^{-10} Ω^{-1} cm^{-1} after reaching the percolation threshold (molar ratio 4.95×10^{-2}). This enhanced conductivity is attractive for electrochemiluminescence since it could increase the rate of luminophore production.

When electron hopping represents the overall charge transport through the film, the Dahms-Ruff equation can be applied to calculate the electron self-exchange rate constant, k_{SE}, from the value of D_{CT} using the following equation:[39]

$$D_{CT} = D_{Phys} + \frac{1}{6} k_{SE} \delta^2 C \quad \text{.....(4.5)}$$

where C is the concentration of ruthenium centres within the film, δ is the intersite separation between adjacent ruthenium centres and D_{phys} describes the physical diffusion in the absence of elctron hopping. Here D_{phys} is assumed to be zero, because Ru centres are bound to the polymer. Therefore, the above equation can be rewritten as:[39]

$$D_{CT} = \frac{1}{6} k_{SE} \delta^2 C \quad \text{.....(4.6)}$$

Thus, for a pure metallopolymer film, the calculated electron self-exchange rate constant was 3.6×10^{5} M^{-1} s^{-1}. For the metallopolymer-gold nanocomposite, the k_{SE} after reaching the percolation threshold was 1.7×10^{8} M^{-1} s^{-1}. The charge transfer diffusion coefficient for dry films can be evaluated from the electron self-exchange rate constant. The electron self-exchange rate constant can also be expressed as follows:[39]

$$k_{SE} = \frac{6RT\sigma}{10^{-3} F^2 \delta^2 [Ru]^{2+} [Ru]^{3+}} \quad \text{.....(4.7)}$$

where R is the gas constant, σ is the conductivity at temperature T, F is Faraday's constant and δ is the intersite separation between adjacent ruthenium centres.

From equations (4.6) and (4.7), we have:

$$D_{CT} = \frac{RT\sigma}{10^{-3}F^2C} \quad \text{.....(4.8)}$$

It has been found that the D_{CT} for dry ruthenium metallopolymer (4.6×10^{-12} cm^2 s^{-1}) and metallopolymer-nanocomposite films (2.6×10^{-10} cm^2 s^{-1}) are consistent with the D_{CT} values obtained for the solvent equilibrated metallopolymer and metallopolymer-nanocomposite films using cyclic voltammetry. Thus, the enhancement in the charge transfer diffusion coefficient is mainly due to the increasing conductivity through the metallopolymer films. However, incorporating gold nanoparticles also causes quenching of the emission. Therefore, a central objective is to investigate the ECL properties of the nanocomposites.

4.3.6. Electrochemiluminescence

Nanocomposites offer potential advantages in the context of electrochemiluminescence. For example, the enhanced rate of homogeneous charge transport ought to lead to generation of more photons per unit time. Also if the photonics properties and separation of the nanoparticles and luminophores are appropriately engineered, it ought to be possible to achieve metal enhanced luminescence. The electrochemiluminescence for the metallopolymer-gold nanocomposite thin films was measured at different molar ratios of DMAP-protected gold nanoparticles to that of the ruthenium metal centre. Figure 4.21 shows the normalised ECL intensities of the ruthenium metallopolymer in the presence (blue line) and absence (pink line) of 4 nm DMAP-protected gold nanoparticles versus applied potential. 0.1 M tripropylamine was used as the co-reactant.

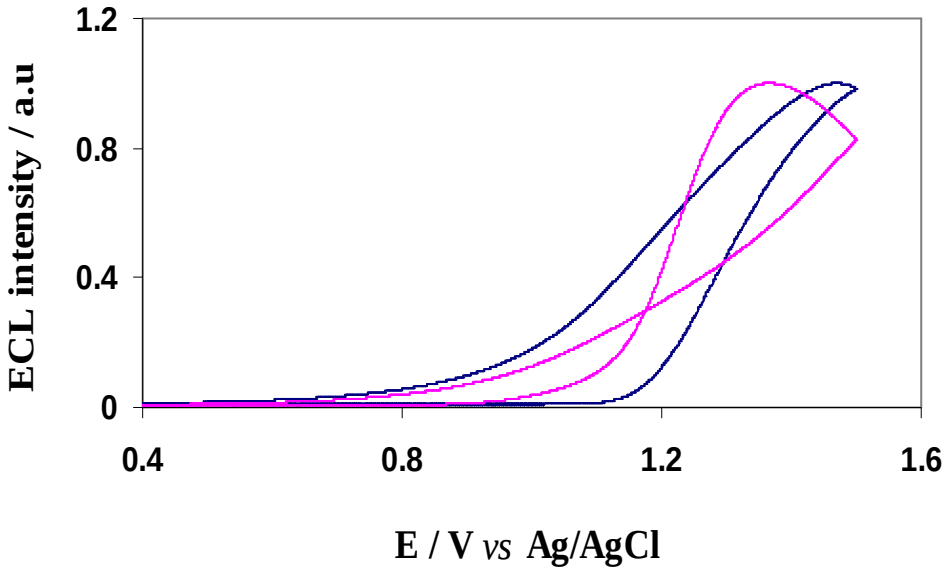

Figure 4.21: ECL emission intensity for pure $[Ru(bpy)_2PVP_{10}]^{2+}$ metallopolymer (blue line) and metallopolymer-gold nanocomposite (pink line) film at a molar ratio of 1.65×10^{-2}. 0.1 M tri propylamine (TPrA) was used as the co-reactant. Surface coverage was 6×10^{-9} mol/cm^2. The ECL intensities were normalised to unity.

Figure 4.21 shows that the ECL emission corresponding to the oxidation of Ru^{2+} for both the parent metallopolymer and metallopolymer nanocomposite that occurs at

+1.2 V irrespective of the presence of nanoparticles. No ECL emission was observed from the DMAP-protected gold nanoparticles alone. Interestingly, it is observed from the spectra that the ECL potentials are independent of the nanoparticle loading. This shows that the presence of gold nanoparticles has no effect on the nature of the excited state but effectively promote only the switching of $Ru^{2+/3+}$ states and hence the nature of ECL emission remains unaffected by the gold nanoparticles loading.

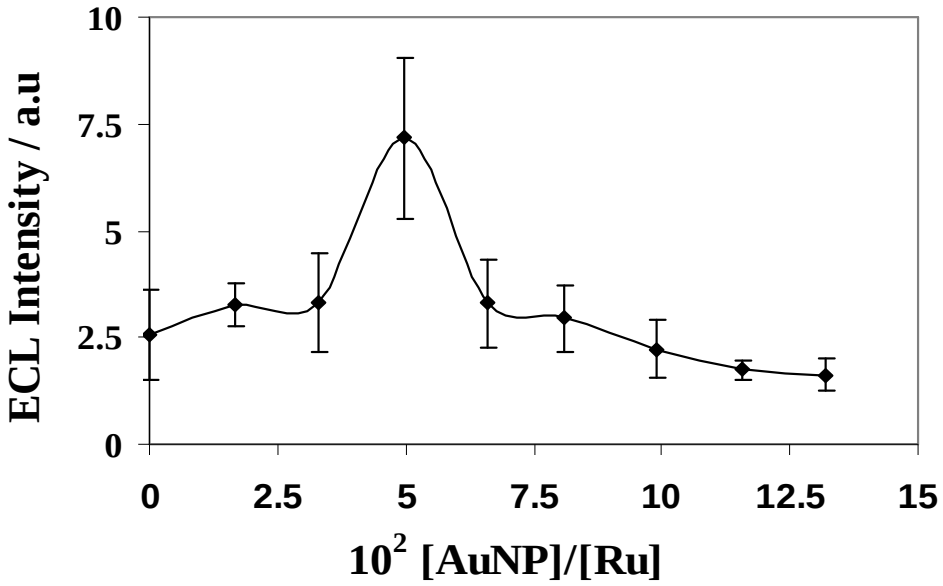

Figure 4.22: Dependency of ECL intensity of $[Ru(bpy)_2PVP_{10}]^{2+}$ films on the Au NP:Ru molar ratio obtained by incorporating 4 nm DMAP-protected gold nanoparticles. 0.1 M TPA was used as the co-reactant and the electrode was poised at 1.2 V.

The ECL intensity of ruthenium metallopolymer and metallopolymer-gold nanoparticle composite was measured with different nanoparticle loadings. Figure 4.22 shows the variation of ECL intensity of $[Ru(bpy)_2PVP_{10}]^{2+}$ based on the loading of DMAP-protected gold nanoparticles. 0.1 M TPA was used as the co-reactant. While the precision is somewhat low, the ECL intensity of $[Ru(bpy)_2PVP_{10}]^{2+}$ film is enhanced by a factor of approximately 3 at a molar ratio of AuNP:Ru of $4.95x10^{-2}$ when compared to the pure metallopolymer. This concentration corresponds to ~20 ruthenium centres per Au nanoparticle. This enhancement is consistent with the

higher rate of charge transport through the layer once the nanoparticle concentration is above the percolation limit.

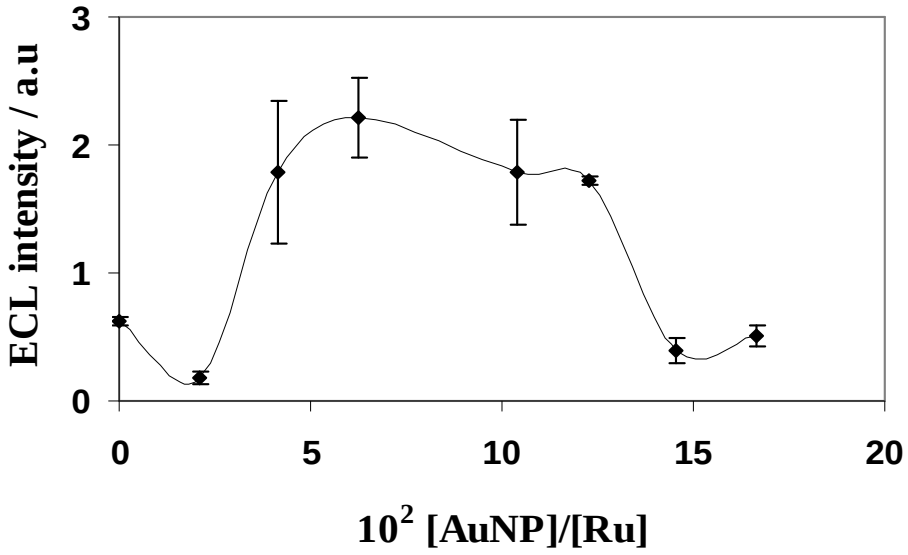

Figure 4.23: Electrochemiluminescence behaviour of the metallopolymer nanocomposite with 5 nm DMAP-protected gold nanoparticles. 0.1 M TPrA was used as the co-reactant. The ECL intensity was plotted *versus* the molar ratio of concentration of gold nanoparticles to ruthenium metal centre in the nanocomposite.

The influence of the nanoparticle diameter on the ECL emission intensity of the pure metallopolymer was investigated for different molar ratio using DMAP-protected gold nanoparticles with different diameters. Figures 4.23, 4.24 and 4.25 show the electrochemiluminescence behaviour of $[Ru(bpy)_2PVP_{10}]^{2+}$ metallopolymer-gold nanocomposite formed by incorporating 5, 7.5 and 12.5 nm DMAP-protected gold nanoparticles at different molar ratios, respectively. The films were obtained by drop-casting the solutions on 3mm glassy carbon electrode and were scanned at a rate of $100mVs^{-1}$.

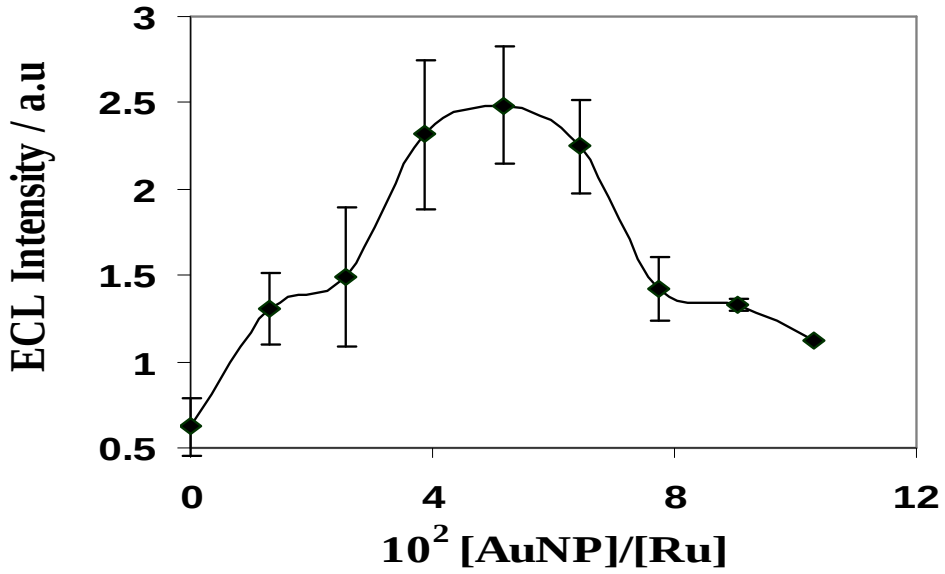

Figure 4.24: Electrochemiluminescence behaviour of the metallopolymer nanocomposite film with 7.5 nm DMAP-protected gold nanoparticles. The ECL emission intensity is plotted *versus* the molar ratio of gold nanoparticles to that of the ruthenium metal centres. 0.1 M TPrA was used as the co-reactant.

Surprisingly, the maximum ECL emission intensity was observed at the intermediate loading for all the nanocomposite systems. As the gold nanoparticles can quench the ruthenium-based emission, there is a trade off between enhanced emission in films due to increased conductivity and increased quenching at higher nanoparticle concentrations. Thus, for the highest nanoparticle loadings investigated the ECL intensity decreases relative to the value observed for intermediate values. The optimum Au NP:Ru molar ratio for the metallopolymer-gold nanocomposite systems with different nanoparticle diameters was 5.2×10^{-2} for 4, 5 and 7.5 nm whereas for 12.5 nm particles it was 6×10^{-3}.

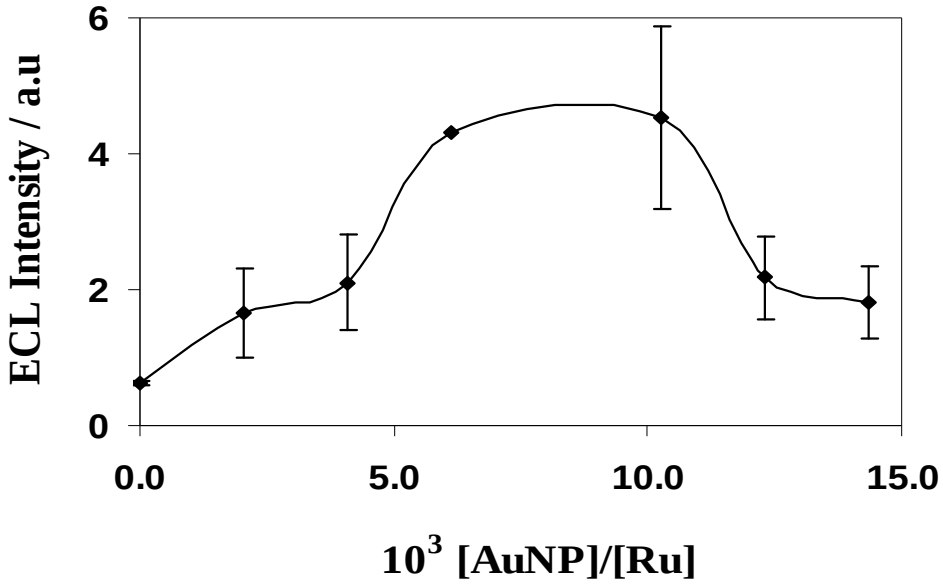

Figure 4.25: Electrochemiluminescence behaviour of the metallopolymer nanocomposite with 12.5 nm DMAP-protected gold nanoparticles**.** 0.1 M TPrA was used as the co-reactant. The concetration of ruthenium is found to be 6×10^{-9} mol/cm^2.

Figure 4.26 shows the increase in the electrochemiluminescence obtained for the thin films of nanoparticle free metallopolymer (— - green line) and the nanocomposite systems at the optimal Au NP:Ru molar ratio with mean diameters (b) 4, (c) 5, and (d) 7.5 nm. The inset of Figure 4.26 shows the ECL emission obtained for the composite prepared with 12.5 nm nanoparticles. The electrochemiluminescence intensity of $[Ru(bpy)_2PVP_{10}]^{2+}$ metallopolymer film increases with increasing diameter of the incorporated DMAP-protected gold nanoparticles at the optimised molar ratio.

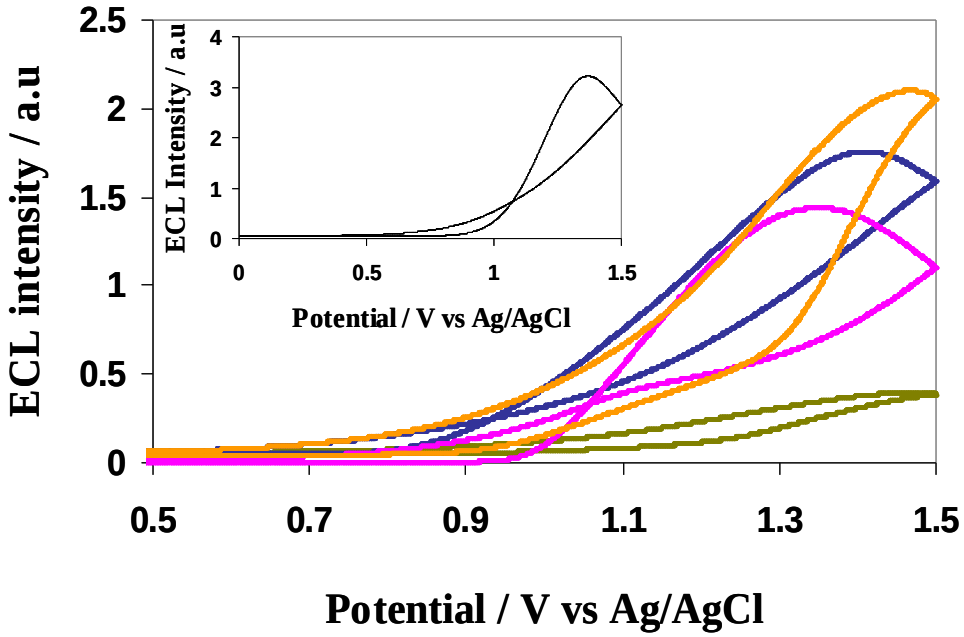

Figure 4.26: The electrochemiluminescence spectra obtained from nanoparticle free metallopolymer (— - green line) and the metallopolymer-gold nanocomposite films developed at the optimal AuNP:Ru molar ratio by incorporating 4 nm (— - pink line), 5 nm (— - blue line) and 7.5 nm (— - orange line) respectively. The inset shows the ECL spectra corresponding to the nanocomposite formed by incorporating 12.5 nm DMAP-protected gold nanoparticles. 0.1 M TPrA was used as the co-reactant and the electrodes were poised at 1.2V.

The maximum enhancement for the nanocomposite incorporating 4, 5 and 7.5 nm particles was obtained at a molar ratio corresponding to nearly 20 ruthenium metal centres per nanoparticle. For the 12.5 nm DMAP-protected gold nanoparticles (Au NP:Ru molar ratio of 6.15×10^{-3}), the electrochemiluminescence intensity of the metallopolymer film is nearly seven times higher than the parent metallopolymer. These enhanced ECL intensities indicate that the increased rate of luminophore production due to the higher conductivity of the nanocomposites overcomes the nanoparticle quenching effects.

4.4. Conclusion

Nanocomposites formed by dispersing DMAP-protected gold nanoparticles within a ruthenium containing metallopolymer exhibit interesting size dependent luminescene properties. Gold nanoparticles quench the ruthenium emission while the quenching efficiency increases with increasing nanoparticle size. Electrochemical measurements demonstrated the ability of the gold nanoparticles to enhance the rate of charge transport through the metallopolymer. The electronic conductivity and the electrochemiluminescence intensity are enhanced by loading with DMAP-protected gold nanoparticles.

The maximum ECL emission enhancement is found at intermediate nanoparticle loadings. The trade off between increasing film conductivity and quenching with increasing nanoparticle loading results in the electrochemiluminescence intensity being enhanced at intermediate loadings. The ECL intensity decreases at higher DMAP-protected gold nanoparticle concentrations predominantly due to enhanced quenching. The enhancement factor increases with the size of the nanoparticles. This result has significant implications for the design of ECL based sensors since metal nanoparticles can be easily incorporated into the metallopolymer but do not promote an enhanced ECL response at all molar ratios.

4.5. References

1 Chen, S.; Liu, Y.; Wu, G. *Nanotechnology*, **2005**, 16, 2360.

2 Hu, M.; Chen, J.; Li, Z. Y.; Au, L.; Hartland, G. V.; Li, X.; Marqueze, M.; Xia, Y.; *Chem. Soc. Rev*. **2006**, 35, 1084.

3 Yuan, H.; Ma, W.; Chen, H.; Zhao, J.; Liu, J.; Zhu, H.; Gao, X. *Chem. Mater*, **2007**, 19, 1592.

4 Murphy, C. J.; Sau, T. K.; Gole, A. M.; Orendorff, C. J.; Gao, J.; Gou, L.; Hunyadi, S.E.; Li, T. *J. Phys. Chem. B*, **2005**, 109, 13857.

5 Schultz, D. A. *Curr. Opin. Biotechnol.* **2003**, 14, 13.

6 Hashmi, A. S. K. *Chem. Rev*, **2007**, 107, 3180.

7 Yu, A.; Liang, Z.; Cho, J.; Caruso, F. *Nano. Lett.* **2003**, 3, 1203.

8 Niemeyer, C. M. *Angew. Chem. Int. Ed.* **2001**, 40, 4128.

9 Forster, R. J.; Keane, L. *J. Electroanal. Chem*. **2003**, 554-555, 345.

10 Dennany, L.; Innis, P. C.; Wallace, G. C.; Forster, R. J. *J. Phys. Chem. B*, **2008**, 112, 12907.

11 Pellegrin, Y.; Forster, R. J.; Keyes, T. E. *Inorg. Chim. Acta.* **2009**, 362, 1715.

12 Dennany, L.; Hogan, C. F.; Keyes, T. E.; Forster, R. J. *Anal. Chem*. **2006**, 78, 1412.

13 Spehar-Délèze, A.-M.; Pellegrin, Y.; Keyes, T. E.; Forster, R. J. *Electrochem. Comm*. **2008**, 10, 984.

14 Dennany, L.; Keyes, T. E.; Forster, R. J. *Analyst*, **2008**, 133, 753.

15 Haddad, P. R. *Anal. Lett.* **1999**, 32, 2909.

16 Qiu, H.; Yan, J.; Sun, X.; Liu, J.; Cao, W.; Yang, X.; Wang, E. *Anal. Chem*. **2003**, 75, 5435.

17 Forster, R. J.; Bertoncello, P.; Keyes, T. E. *Annu. Rev. Anal. Chem*. **2009**, 2,

359.

18 Bertoncello, P.; Forster, R. J. *Biosens. Bioelectron*. **2009**, 24, 3191.

19 Dennany, L.; Forster, R. J.; Rusling, J. F. *J. Am. Chem. Soc.*, **2003**, 125, 5213.

20 Deng, L.; Zhang, L.; Shang, L.; Guo, S.; Wen, D.; Wang, F.; Dong, S, *Biosens. Bioelectron.* **2009**, 2273.

21 Wang, X.; Dong, P.; Yun, W.; Xu, Y.; He, P.; Fang, Y. *Biosens. Bioelectron.* **2009**, 24, 3288.

22 Shan, Y.; Xu, J-J.; Chen, H-Y.; *Chem. Comm*. **2009**, 905.

23 Thomas, K. G.; Kamat, P. V. *J. Am. Chem. Soc.* **2000**, 122, 2655.

24 Ipe, B. I.; Thomas, K. G.; Barazzouk, S.; Hotchandani, S.; Kamat, P. V. *J.Phys. Chem. B.* **2002**, 106, 18.

25 Jennings, T. L.; Singh, M. P.; Strouse, G.F. *J. Am. Chem. Soc.* **2006**, 128, 5462.

26 Eustis, S.; El-Sayed, M. A. *Chem. Soc. Rev*. **2006**, 35, 209

27 Chen, Y.; Munechika, K.; Ginger, D. S. *Nano. Letters*, **2007**, 7, 690.

28 Lakowicz, J. R. *Principles of Fluorescence Spectroscopy*, Kluwer Academic Plenum Press, New York, **1999.**

29 Valeur, B. *Molecular Fluorescence- Principles and Applications*, Wiley, Weinheim, **2002**.

30 Navon, G.; Sutin, N. *Inorg. Chem*., **1974**, 13, 2159.

31 Burke, L. D.; Nugent, P. F. *Gold Bull*. **1998**, 31, 39.

32 Bard, A.J.; Faulkner, L.R. *Electrochemical Methods: Fundamental and Applications*, Wiley, 2nd ed. New York, **2001**.

33 Finot, M.O.; Braybrook, G.D.; McDermott, M.T.; *J. Electroanal. Chem*., **1999**, 466, 234.

34 Rand, D. A. J.; Woods, R. *J. Electroanal.Chem,* **1971**, 31, 29.

35 Trasatti, S.; Petriii, O. A. *J. Electroanal. Chem*. **1992**, 327, 353.

36 Paul, E. W.; Ricco, A. J.; Wrighton, M. S.; *J. Phys. Chem*. **1985**, 89, 1441.

37 Thackeray, J. W.; White, H. S.; Wrighton, M. S.; *J. Phys. Chem*. **1985**, 89, 5133.

38 Ofer. D.; Crooks, R. M.; Wrighton, M. S. *J. Am. Chem. Soc*. **1990**, 112, 7869.

39 Zeng, Q.; McNally, A.; Keyes, T. E.; Forster, R. J. *Electrochimical Acta,* **2008**, 53, 7033.

Chapter 5

Metallopolymer-Gold Nanorod Composites

5.1. Introduction

Metallopolymers containing redox centres attached to the polymer backbone represent a novel class of materials that exhibits interesting photo physical and electrochemical properties.[1,2] The redox potentials and the luminescence characteristics of such polymers can be tuned by selecting the appropriate metal centres attached to the polymer backbone.[3] Among them, metallopolymers of the type $[M(bpy)_2PVP_{10}]^{2+}$, where M is a transition metal, bpy is 2,2'-bipyridyl, PVP is poly (4-vinylpyridine), is widely used in electrochemiluminescence (ECL) based biomolecule detection due to their excellent electrochemiluminescence properties. For example, metallopolymers containing ruthenium and osmium have been used in the study of DNA hybridisation.[4] The ECL produced from such metallopolymers is sensitive to the chemical damage and base pair mismatching in ss-DNA.[5,6]

Changing the metal centres that are attached to the polymeric backbone from ruthenium to osmium changes the electrochemical and photo physical properties. For example, the redox potential of the osmium metallopolymer of the form $[Os(bpy)_2PVP_{10}]^{2+}$ is approximately 600 mV less positive than the ruthenium analogue.[3] Osmium metallopolymers show much higher photo stability than ruthenium based polypyridyl complexes[7] and the luminescence occurs at a longer wavelength. This could be an attractive feature in the field of biosensors that use whole blood samples, as there may be less spectral overlap with the absorption spectrum of whole blood.[8] However, there are some limitations for the ECL emission of osmium metallopolymers. Firstly, shorter excited state lifetimes and weaker ECL emission of some osmium complexes like $[Os(bpy)_2PVP_{10}](ClO_4)_2$ occur due to spin-orbit coupling.[9] Hence, it is important to enhance the ECL emission properties to achieve lower limits of detection. Secondly, the rate of homogeneous charge transport is generally rather slow.[10]

More interestingly, by achieving resonance between the absorption bands of gold nanorods with the emission bands of osmium metallopolymer, metal enhanced fluorescence effects might be achieved. Recent works has demonstrated the influence of gold nanoparticles on ECL emission properties of various systems including luminol[11] and *monomeric* tris (2,2'-bipyridyl) ruthenium (II) complex ($Ru(bpy)_3^{2+}$).[12,13,14] It has been reported in Chapter 4 that the presence of DMAP-protected gold nanoparticles enhances the ECL production of ruthenium-based metallopolymers of the form $[Ru(bpy)_2PVP_{10}]^{2+}$, by enhancing the electronic conductivity of the polymer.

Gold nanorods are attractive due to their spectral properties, which arise from the transverse and longitudinal plasmons.[15] The gold nanorods were produced using surfactant assisted seed-mediated growth technique, in which cetyltrimethyl ammonium bromide ($C_{16}TAB$) acts as the surface-capping agent, which provides the stability to the gold nanorods through electrostatic repulsion.[16] Resonance can be achieved between the osmium metallopolymer emission (760 nm) and longitudinal plasmon band of the gold nanorods. A well-defined spectral overlap was observed between 650-950 nm making the nanocomposite system suitable for studying energy transfer or quenched luminescence.

Indeed, the presence of a weakly bound bilayer of surfactant molecules on the surface of the gold nanorods might result in an interesting interaction between polymer and the surfactant molecules. This could be possible as the pyridine units in the poly (4-vinylpyridine) backbone have a stronger affinity towards metallic surfaces. It has been already demonstrated that the unbound pyridine units of $[Os(bpy)_2PVP_{10}Cl]^+$ can be used as the capping ligand for producing gold nanoparticles *via* chemical reduction.[17] Tam *et al* has described the formation of polymer-surfactant complex by simply mixing the anionic surfactant with the polymer chains.[18]

In this chapter, the luminescence and charge transport properties of osmium metallopolymer-gold nanorod composites are reported. The interaction between the surface capping ligands of gold nanorods with poly (4-vinylpyridine) backbone was investigated and addressed. The charge transport properties and ECL characteristics

of the metallopolymer were determined both in the presence and absence of gold nanorods and are discussed in detail.

5.2. Experimental

5.2.1. Materials

The synthesis and characterisation of $[Os(bpy)_2PVP_{10}]^{2+}$ metallopolymer and cetyltrimethyl ammonium bromide ($C_{16}TAB$)-protected gold nanorods has already been discussed in detail in Chapters 2 and 3. Alumina powder (0.3 μm and 0.05 μm) was from Buehler and was used as received. Dimethylformamide (>97%) was from Sigma-Aldrich. The aqueous solutions were prepared from Milli-Q reagent water (Millipore Corp.,), 18 MΩ cm.

5.2.2. Metallopolymer-gold Nanocomposite

The osmium metallopolymer-gold nanorod composite solutions were prepared by mixing the solutions of osmium metallopolymer and gold nanorods at the required molar ratio. To prepare micro molar aqueous solutions of $[Os(bpy)_2PVP_{10}]^{2+}$ metallopolymer, a concentrated solution was first prepared in dimethylformamide (DMF) and diluted to the required concentration such that the DMF content was less than 1% in the final solution. The concentration of metallopolymer in the nanocomposite was 20 μM in all cases. Hence, by changing the concentration of $C_{16}TAB$-protected gold nanorods, the molar ratio of osmium metal centres to gold nanorods was easily varied from 0 to 1.5×10^{-3}.

5.3. Results and Discussion

5.3.1. Transmission Electron Microscopy

Metallopolymer-gold nanorod composites were formed by mixing the respective solutions of $[Os(bpy)_2PVP_{10}]^{2+}$ metallopolymer and gold nanorods as described in Section 5.2.2. The gold nanoparticles protected with cetyltrimethyl ammonium bromide were prepared using seed-mediated growth technique as described in Section 3.2.3. Transmission electron microscopy (TEM) was used to analyse the distribution of the gold nanorods within the osmium metallopolymer matrix. The samples were prepared by drop-casting the respective nanocomposite solution with different molar ratios of Au NRs:Os on the carbon coated TEM grid and the solvent was evaporated. Figures 5.1 and 5.2 show TEM images of the metallopolymer-gold nanorod composite prepared at different Au NR:Os molar ratios of 0, 0.37×10^{-4}, 0.075×10^{-3} and 0.11×10^{-3} by dispersing gold nanorods in a 20 μM $[Os(bpy)_2PVP_{10}]^{2+}$ metallopolymer solution.

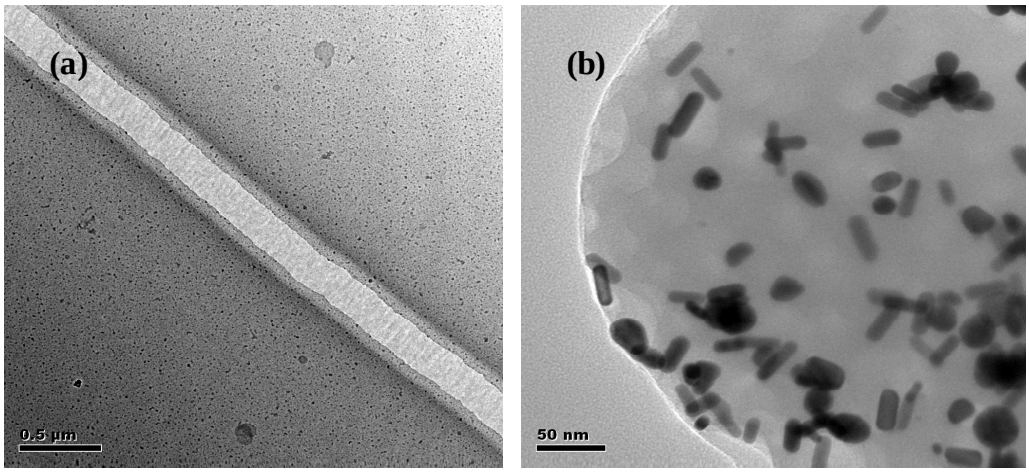

Figure 5.1: TEM images of (a) nanoparticle free $[Os(bpy)_2PVP_{10}]^{2+}$ metallopolymer and (b) metallopolymer-gold nanorod composite at Au NR: Os molar ratio of 0.37×10^{-4}.

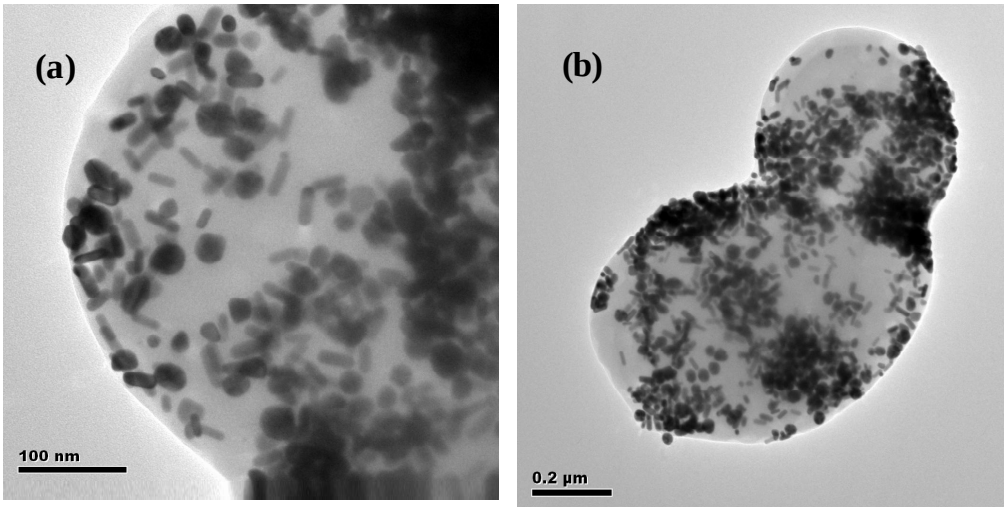

Figure 5.2: TEM images of Os metallopolymer-gold nanorod composites prepared at Au NR:Os molar ratios of (a) 0.075×10^{-3} and (b) 0.11×10^{-3}.

Aggregates of gold nanorods were observed from the TEM images perhaps suggesting that the gold nanorods interact with the pyridine groups of the polymer backbone displacing the surface capping cetyltrimethyl ammonium bromide (C_{16}TAB) ligands on the gold nanorods. The degree of aggregation in the nanocomposites increased with increasing Au NR:Os molar ratio. This could possibly be due to the availability of a greater concentration of gold nanorods in the nanocomposite system.

It is well known that pyridine in its neutral form binds strongly to metal surfaces[19] *via* formation of covalent bond through donation of the lone pair of electrons of the nitrogen atom. Forster *et al* has demonstrated the chemical reduction of gold nanoparticles in the poly (4-vinylpyridine) backbone of $[Os(bpy)_2PVP_{10}Cl]^+$ metallopolymer. Oyama *et al* also reported the growth of gold nanoplates using PVP as the reducing, as well as the surface-capping, agent.[20] Thus, the C_{16}TAB protecting layer might be partially/completely displaced by the pyridine group from the polymer backbone that could result in the formation of gold nanorod aggregates.

Surface Enhanced Raman Spectroscopy (SERS) was used to study the interaction of gold nanorods with the pyridine groups of the PVP polymer backbone. The films were formed by typically drop-casting 100 µl of metallopolymer and metallopolymer-nanorod composite solution with different molar ratios on a

microscopic slide and the solvent was evaporated. The Raman signals were recorded upon exciting the film using 633 nm excitation. Figure 5.3 shows the Raman spectra obtained for gold nanorod free 20 μM Os metallopolymer (—-pink line) and metallopolymer-gold nanorod composite (—-black line) at a Au NR:Os molar ratio of 0.11×10^{-3}. It is clear from the Raman spectra that no significant Raman signal was observed from pure osmium metallopolymer.

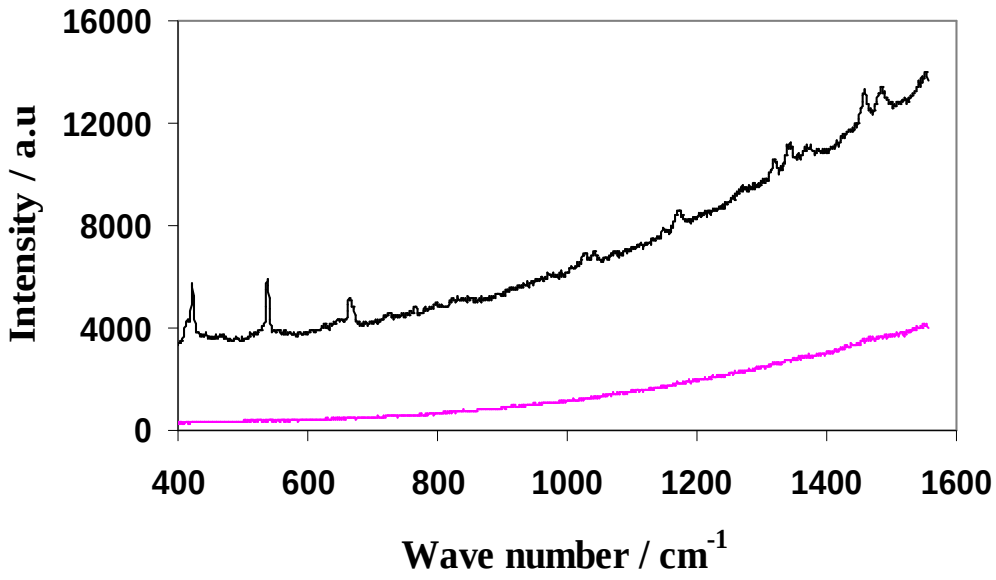

Figure 5.3: SERS observed from Os metallopolymer-gold nanorod composite (—-black line) due to the interaction of gold nanorods with the pyridine groups of poly (4-vinylpyridine) backbone. The pink line (—-pink line) shows the Raman spectra obtained for pure 20 μM osmium metallopolymer. Laser wavelength is 633 nm.

The metallopolymer-gold nanorod composite shows well-defined Raman peaks that have been enhanced due to the presence of gold nanorods. Lippert and co-workers have demonstrated SERS obtained for poly (2-vinylpyridine) adsorbed on silver electrode.[21] Thus, the enhanced Raman peaks observed in osmium metallopolymer-gold nanorod composite films correspond predominently to pyridine from the poly (4-vinylpyridine) backbone. This strongly suggests that there exists a strong interaction between the gold nanorod surface and the pyridine groups from the PVP backbone, which could be attributed to at least a partial replacement of the C_{16}TAB layer by pyridine.

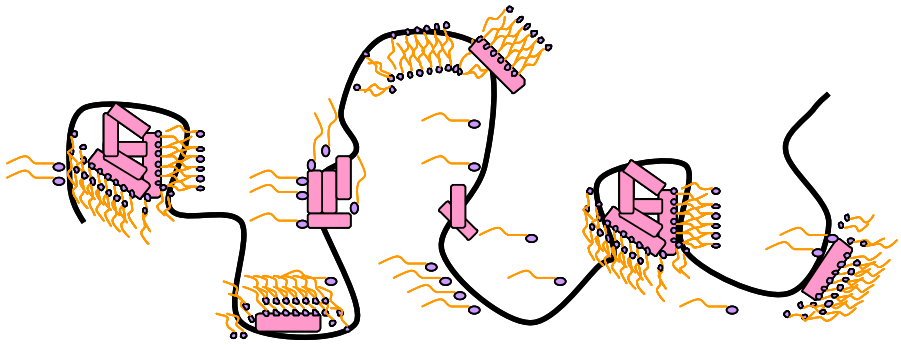

Figure 5.4: Schematic representation of aggregation of gold nanorods formed due to the partial replacement of C_{16}TAB surface layer on the nanorods in osmium metallopolymer-gold nanoparticle composite. The figure shows poly (4-vinylpyridine) backbone (—-thick black curves), gold nanorods (▭-pink rods), and ammonium head group (○-violet circles) and hydrocarbon chain (—-orange lines) of cetyltrimethyl ammonium bromide capping ligands, respectively.

Figure 5.4 shows the schematic representation of the formation of aggregates induced by the partial/complete replacement of the C_{16}TAB capping layer of the gold nanorods with pyridine group from the poly (4-vinylpyridine) backbone. It has been reported that the C_{16}TAB molecules form a bilayer on the surfaces of gold nanorods via chemisorbed bromide at the gold surface. This provides the electrostatic association for the cationic head groups of C_{16}TAB.[21] Murphy *et al* has reported that the C_{16}TAB bilayer is dynamic in nature, which might result in the desorption of the surfactant. Moreover, desorption of surfactant from the bilayer might result in decreased stability of the rods.[22,23]

However, due to the greater affinity of pyridine groups towards metallic gold,[24] the probability of displacement of C_{16}TAB layer is greater in the metallopolymer nanocomposite system. Indeed, the removal of C_{16}TAB layer might affect the stability of the gold nanorods due to the higher surface energy of the nanorods. It is found from the TEM images that the gold nanorods are clearly entrapped inside the metallopolymer matrix. Nanocomposites prepared with low concentrations (Figure 5.1b) of gold nanorods shows co-localisation of gold nanorods inside the polymer matrix. However, at higher loadings (5.2b), the nanorods are fused together inside the metallopolymer matrix and hence making the aggregation irreversible.

5.3.2. UV-Vis-NIR Absorption

The electronic transitions of metallopolymer-gold nanorod composites were studied using UV-Vis-NIR absorption spectroscopy. The aspect ratio of C_{16}TAB-protected gold nanorods used for forming the nanocomposite is 3.6 (Figure 3.14 (b)). Figure 5.5 shows the UV-Vis-NIR absorption spectra obtained for 1.9 nM C_{16}TAB-protected gold nanorod (—-blue line) and 20 μM $[Os(bpy)_2PVP_{10}]^{2+}$ metallopolymer (—-orange line), respectively. The transverse vibrations of the conduction band electrons in gold nanorods are observed around 520 nm whereas the peak at 700 nm corresponds to the longitudinal vibrations of the electrons. The osmium metallopolymer shows a strong absoption around 350 nm that corresponds to metal to ligands charge transfer (MLCT).

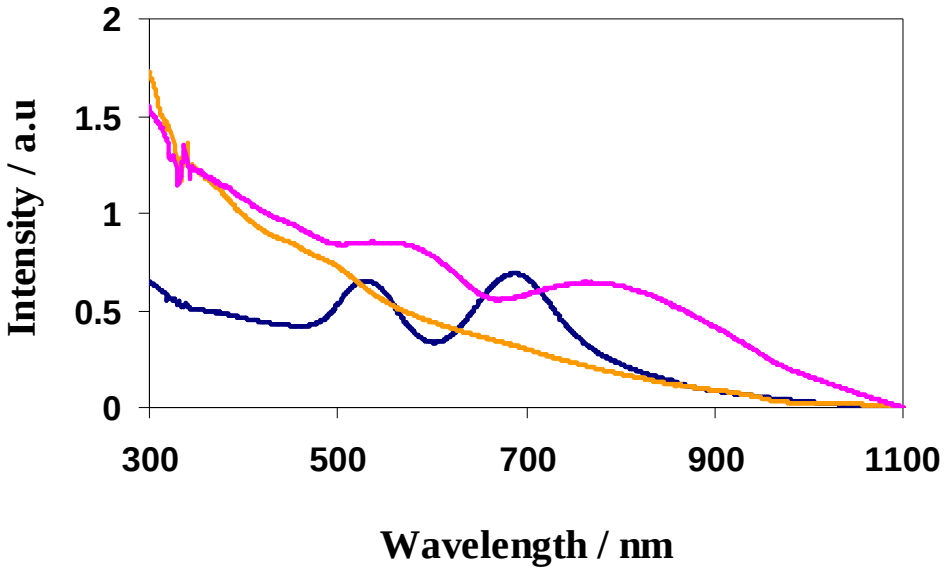

Figure 5.5: UV-Vis-NIR spectrum of 20 μM $[Os(bpy)_2PVP_{10}]^{2+}$ metallopolymer (—-orange line), 1.9 nM C_{16}TAB-protected gold nanorods (—-blue line) and the resultant metallopolymer-gold nanorod composite (—-pink line) formed by mixing the osmium polymer and C_{16}TAB-protected gold nanorods. All solutions are aqueous.

Figure 5.5 also shows the absorption spectrum corresponding to the osmium metallopolymer-gold nanorod composite (—-pink line) at a Au NR:Os molar ratio of

9.4×10^{-5}. The absorption bands shows broadening which indicates the possibility of aggregation of gold nanorods in the composite.

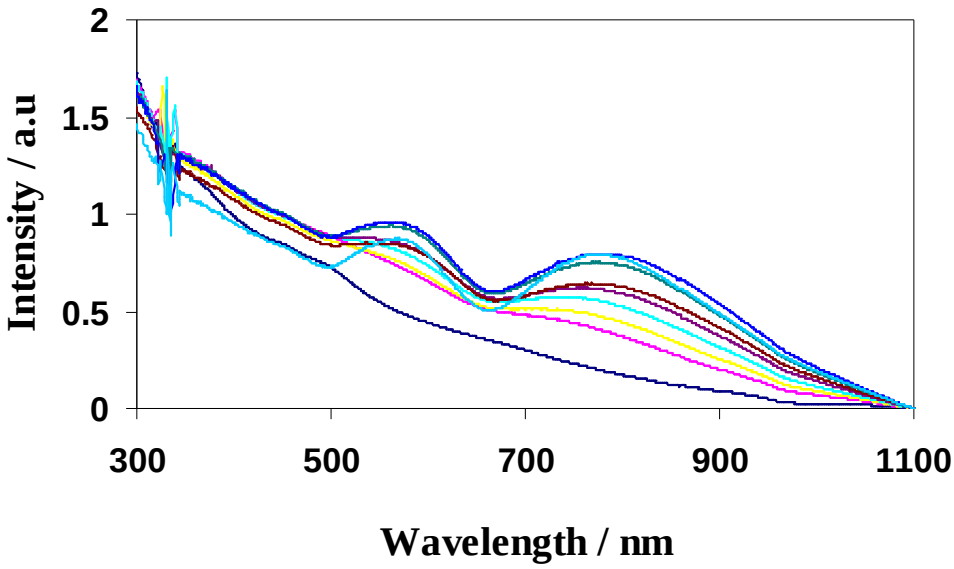

Figure 5.6: UV-Vis-NIR spectra of osmium metallopolymer-gold nanorod composite solution formed with different AuNR:Os molar ratios (0, 0.18×10^{-5}, 0.37×10^{-4}, 0.5×10^{-4}, 0.75×10^{-4}, 0.9×10^{-4}, 1.1×10^{-3}, 1.3×10^{-3} and 1.5×10^{-3} (bottom to top) by mixing aqueous solution of C_{16}TAB-protected gold nanorods with 20 μM osmium metallopolymer.

Figure 5.6 shows the absorption spectra of the metallopolymer-gold nanorod composite formed by loading various amounts of gold nanorods. The MLCT peak corresponding to osmium metallopolymer is barely visible because of the lower concentration of the polymer. Significantly, there is nearly a 100 nm shift in the absorption peaks corresponding to the longitudinal vibrations of gold nanorods from 700 to 800 nm when the nanorods are incorporated within the metallopolymer matrix.

Significantly, the nanocomposite absorption spectra obtained by loading various amounts of C_{16}TAB-protected gold nanorods shows broadening. Similar kind of broadening and red shift is observed in the core/shell nanohybrid formed with gold nanorod and polymerised N-polyacrylamide (PNIPAAm) due to the formation of aggregated nano islands.[25] Similarly, in our case the broadening and red shift in the

absorption spectra might have resulted because of the formation of nanorod aggregates is in agreement with the TEM images.

5.3.3. Luminescence Quenching

Figure 5.7 shows the spectral overlap between the luminescence of $[Os(bpy)_2PVP_{10}]^{2+}$ metallopolymer solution with the plasmon band of the C_{16}TAB-protected gold nanorods. Both emission intensity at 760 nm and the longitudinal absorption maximum at 700 nm are normalised to unity for better understanding the spectral overlap. The luminescence was observed upon excitation of the MLCT band at 355 nm. The extent of interaction between the osmium metal centres and the gold nanorods can be obtained from the spectral overlap. Figure 5.7 shows a spectral overlap illustrating that nearly 95% of the osmium metallopolymer emission overlaps with the plasmon band of the gold nanorods.

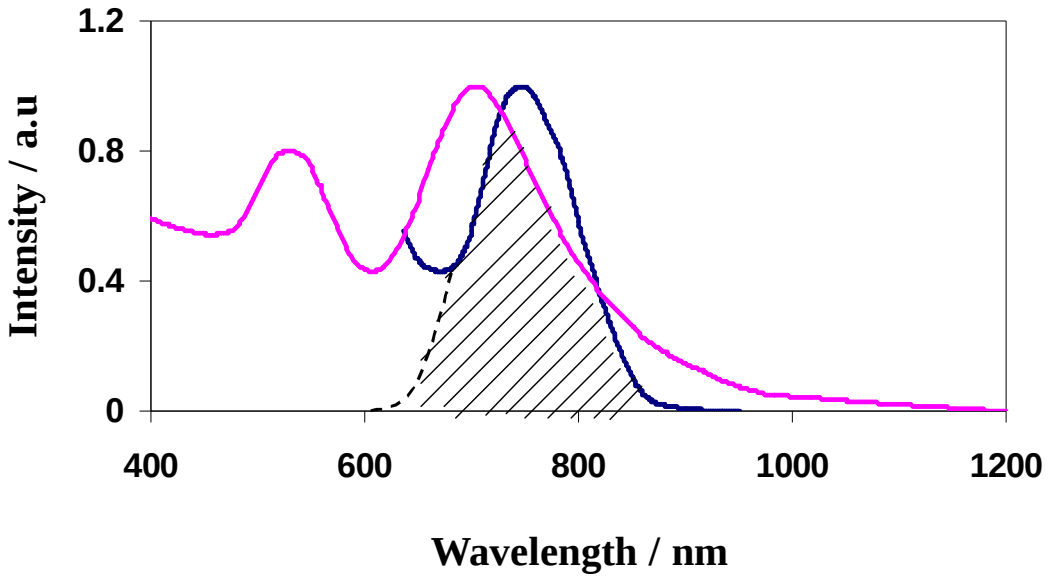

Figure 5.7: The spectral overlap (shaded region) between the normalised emission and absorbance of 20 μM osmium metallopolymer (—-blue line) and 0.38 nM C_{16}TAB-protected gold nanorods (—-pink line), respectively.

The spectral overlap between the luminescence of the osmium metallopolymer with the plasmon band of the C_{16}TAB-protected gold nanorods is significant. Due to this, either metal enhanced fluorescence effects or luminescence quenching might be possible depending on the distance between the nanorods and the osmium metal

centres.[26,27] Quenched luminescence was observed with an addition of gold nanorods, rather than metal enhanced fluorescence effects as shown in Figure 5.8.

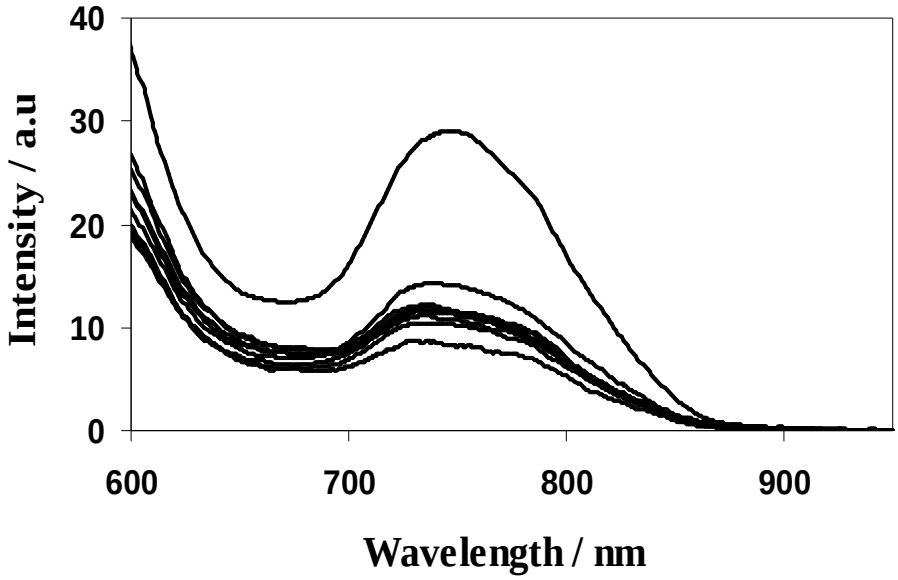

Figure 5.8: Luminescence of a 20 μM solution of osmium metallopolymer-gold nanorod composite formed with different Au NR:Os molar ratios (0, 0.18×10^{-5}, 0.37×10^{-4}, 0.5×10^{-4}, 0.75×10^{-4}, 0.9×10^{-4}, 1.1×10^{-3}, 1.3×10^{-3} and 1.5×10^{-3} (top to bottom) achieved by loading aqueous solution of C_{16}TAB-protected gold nanorods.

The extent of quenching increases with gold nanorods loading. This behaviour clearly suggests that the gold nanorods act as the luminescence quenchers. However, due to the large molar extinction coefficient of the gold nanorods, there is a possibility that the gold nanorods absorb at the excitation wavelength decreasing the excitation intensity.[7] This might lead to the generation of fewer excited state populations, which will result in reduced luminescence. Thus, it is important to correct the luminescence intensities for the self-absorption (Inner filter effect) of the C_{16}TAB-protected gold nanorods at the MLCT wavelength of osmium.

Sutin and Navan *et al* have proposed a new method to correct for the inner filter effects.[28] The emission intensities of the metallopolymer-gold nanocomposites were corrected to separate the effects of quenching from those due to the absorption of the

gold nanorods using Equation 4.2. Figure 5.9 shows the dependence of luminescence intensities I_0/I *versus* the concentration of the quencher gold nanorods.

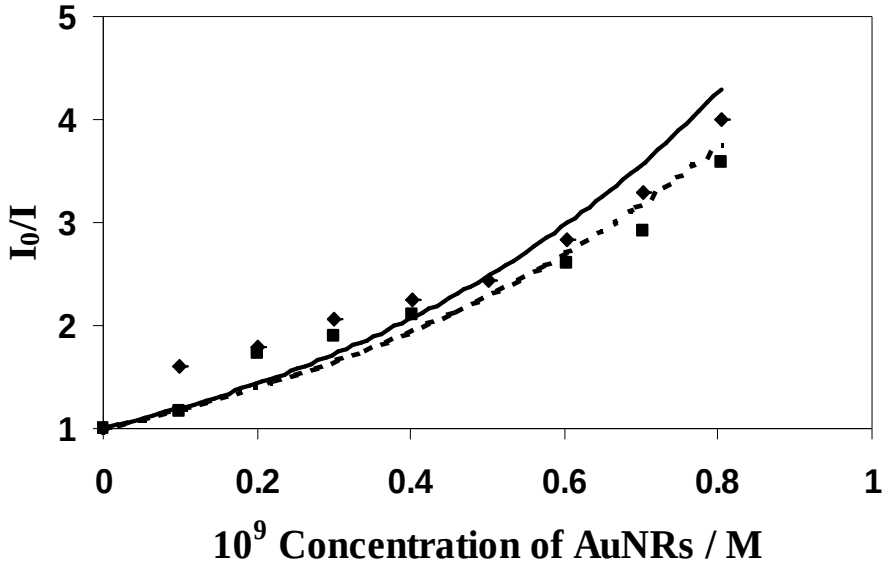

Figure 5.9: Dependence of luminescence intensities I_0/I *versus* the concentration of C_{16}TAB-protected gold nanorods before (♦) and after (■) correcting for the effects due to the self-absorption of gold nanorods at the excitation wavelength. The solid line and dotted line shows the approximately exponential fit.

It is observed from Figure 5.9 that the effect of self-absorption of gold nanorods on the luminescence of osmium metal centres is minor. As mentioned already in Section 4.3.5, the quenching of the excited state of luminophores can occur via static quenching or dynamic quenching mechanism. An insight into the nature of the quenching mechanism can be obtained from the dependence of luminescence intensities I_0/I on the quencher concentration. Figure 5.9 shows the approximately exponential dependence of I_0/I on the concentration of the gold nanorods. Significantly, no change is observed in the lifetimes of the metallopolymer-gold nanocomposites even at higher gold nanorod loading. Thus, the observed quenching mechanism can be explained by the static quenching Perrin model.

According to the Perrin model, the quencher particles that are present inside the quenching sphere influence the luminescence of the luminophore, whereas quencher

particles that are outside the sphere do not influence the emission properties of the luminophore. Thus, the lifetimes of such systems remain unaffected by the quencher particle loading. The Perrin model pedicts an exponential dependence of I_0/I on quencher concentration. The volume of the quenching sphere can be calculated from the slope of the linear plot of ln (I_0/I) *versus* the concentration of gold nanorods using Equation 1.7. The slope of the linear plot is equivalent to the product of volume of quenching sphere (V_q) and Avogadro's constant (N_a). Thus, the volume and the radius of the quenching sphere were calculated and are tabulated in Table 5.1. The radius of the quenching sphere is found to be around 86Å.

Table 5.1: Summary of the quenching sphere dimensions and quenching efficiency before and after correcting for inner filter effects.

Quenching Sphere	Correction for Inner Filter Effects	
	Before	After
Volume	0.3×10^{-23} (m^3)	0.27×10^{-23} (m^3)
Radius	8.96 (nm)	8.68 (nm)
Quenching Efficiency	75%	72%

The luminescence quenching efficiency for osmium metallopolymer-gold nanorod composite (AuNR:Os molar ratio=1.5×10^{-3}) can be calculated using Equation 1.13. The luminescence quenching efficiency of the gold nanorods in metallopolymer-gold nanocomposite at Au NR:Os molar ratio of 1.5×10^{-3} is found to be around 75% before correcting the luminescence intensities for the self-absorption of gold nanorods at the excitation wavelength. The luminescence quenching efficiency decreased to 72% after correcting the emission intensities for inner filter effects. This clearly shows that the strong quenching nature of C_{16}TAB-protected gold nanorods on the luminescence of metallopolymer is dominant over possible metal enhancement effects.

5.3.4. Electrochemical Characterisation

The electronic properties of gold nanoparticles has been used to enhance the conductivity of various polymers.[29,30] The incorporation of the gold nanorods into the metallopolymer matrix ought to increase the electronic conductivity of the nanocomposite system. Figure 5.10 shows the cyclic voltammetric response of 0.37 nM C_{16}TAB-protected gold nanorod film on a 3 mm glassy carbon electrode scanned at a rate of 100-500 mV s^{-1}.

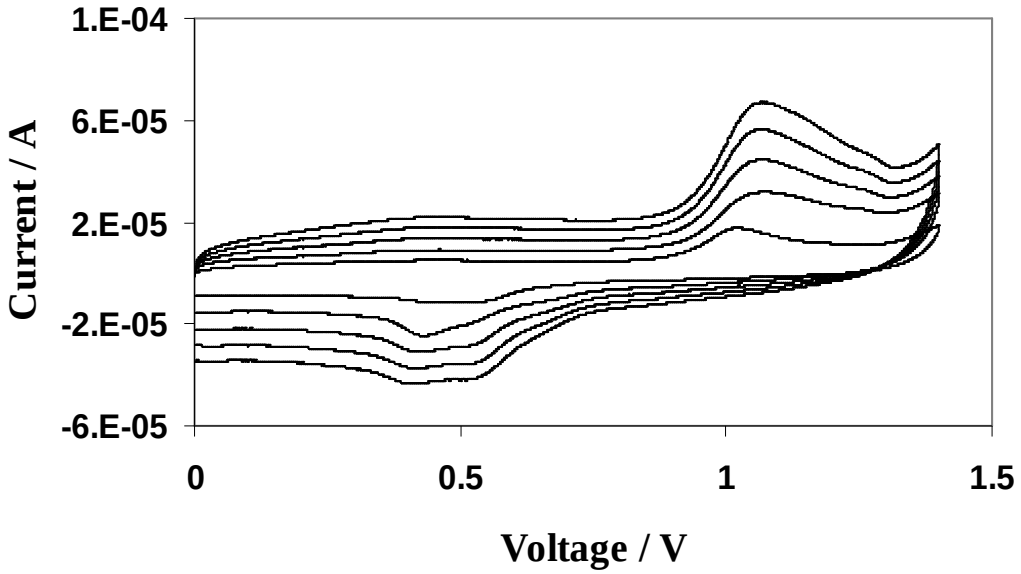

Figure 5.10: Cyclic voltammogram of a 0.37 nM C_{16}TAB-protected gold nanorod film on 3 mm glassy carbon electrode scanned at a rate of 500 - 100 mV s^{-1} (top to bottom) with 100 mVs^{-1} intervals. 0.5 M H_2SO_4 was used as the supporting electrolyte.

The gold nanorod films were formed by drop-casting 100 µl of 0.37 nM aqueous C_{16}TAB-protected gold nanorod solutions and the solvent was evaporated to dryness in dark overnight. 0.5 M sulphuric acid was used as the supporting electrolyte. The voltammogram shows well-defined peaks around +1.2 V and +0.5 V that corresponds to the formation and re-reduction of gold oxide layer, respectively. The peak potentials at +1.2 V and +0.5 V show that the oxidation and reduction of gold oxide is similar to that observed in bulk.

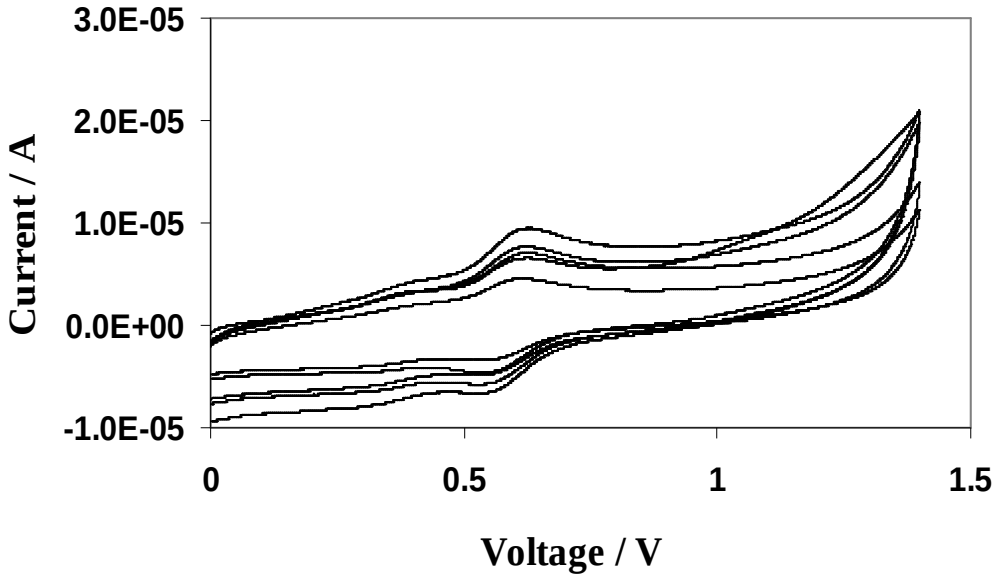

Figure 5.11: Voltammetric response of $[Os(bpy)_2PVP_{10}]^{2+}$ metallopolymer nanocomposites at Au NR:Os molar ratio of 0.9365×10^{-5}. The films were cycled at 500-100 mV s^{-1} scan rate (top to bottom) with 100 mVs^{-1} intervals. 0.5 M H_2SO_4 was used as the supporting electrolyte. The concentration of Os metal centres per square centimetre is 5×10^{-9} mol/cm^2.

The random dispersion of gold nanorods in metallopolymer nanocomposite ought to enhance the conductivity of the polymer and increase the rate of charge transfer through the metallopolymer films. Therefore, cyclic voltammograms were recorded for osmium metallopolymer-gold nanorod composites with different gold nanorod loadings in the presence of 0.5 M H_2SO_4 as the supporting electrolyte. Figure 5.11 shows the voltammetric response of $[Os(bpy)_2PVP_{10}]^{2+}$ metallopolymer nanocomposite film formed by incorporating 0.5 nM C_{16}TAB-protected gold nanorods. The nanocomposite film was formed by drop-cast and the molar ratio of Au NR:Os was 0.94×10^{-5}.

It is well known that the oxidation potential of osmium and gold occurs at approximately 0.65 and 1.25V, respectively in acidic electrolyte. Surprisingly, no trace of gold oxidation was found in the nanocomposite film irrespective of the gold nanorod loading. This result is consistent with complete encapsulation of the gold

nanorods in the polymer matrix so that no gold oxide forms in the nanocomposite films.

The influence of gold nanorod loading on the rate of charge transport through the metallopolymer films can be determined from the diffusion coefficients. The charge transport diffusion coefficient was determined for the osmium metallopolymer nanocomposite systems with various amounts of gold nanorods using the Randles-Sevcik Equation 1.18.[31]

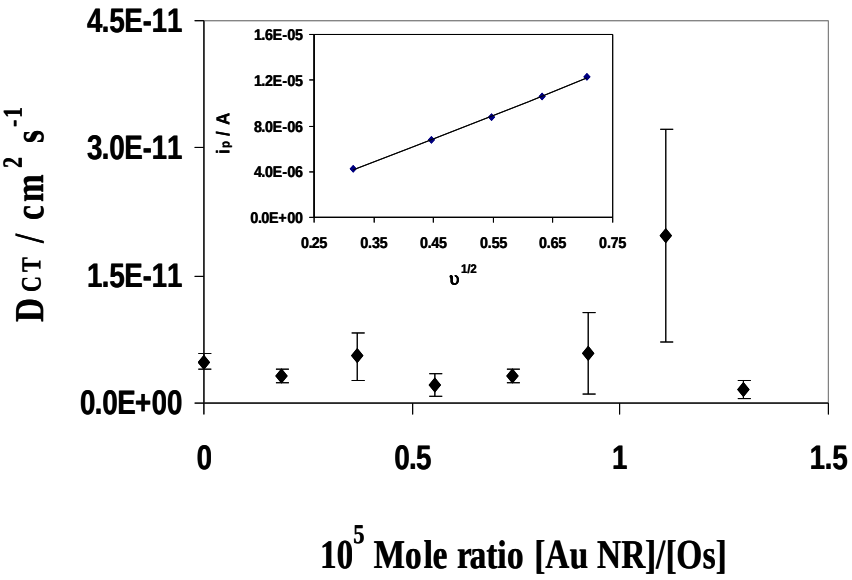

Figure 5.12: Dependence of charge transfer diffusion coefficient on gold nanorod loading in osmium metallopolymer nanocomposite films. Inset figure shows the plot of i_{pa} *vs.* $\upsilon^{1/2}$ obtained at a Au NR:Os molar ratio of 1×10^{-3}. Aqueous 0.5 M H_2SO_4 was used as the supporting electrolyte.

Figure 5.12 shows the dependence of the charge transport diffusion coefficient on the gold nanorod loading. The inset shows the plot of i_{pa} *vs.* $\upsilon^{1/2}$ are linear from 100-500 mV s^{-1}. Figure 5.12 shows that there are no significant changes in the charge transport diffusion coefficients irrespective of gold nanorod loading in the range studied. This shows that the switching rates of $Os^{2+/3+}$ at 650 mVs are not enhanced greately due to the lack of electrochemical activity of gold.

However, ruthenium metallopolymer-gold nanocomposite system shows that ruthenium centres mediate the electron transfer between the nanoparticles due to the existence of similar oxidation potential between Ru and gold. Moreover the fairly homogeneous dispersion of gold nanoparticles in the ruthenium metallopolymer matrix could also decrease the interparticle distance, which could enhance the electron transfer and hence the formation of oxide monolayer on gold nanoparticles.

These findings show that the switching rates of $M^{2+/3+}$ might increase only when a network of communicating particles is formed in the nanocomposite system. In addition, the interparticle separation also plays a vital role in modulating the charge transfer through the composite systems. Thus, by controlling fairly homogeneous dispersion of metal nanoparticles in the polymer matrix, enhanced charge transport can be achieved.

5.3.5. Electrochemiluminescence

It is clear from Section 5.3.4 that the loading of gold nanorods is not increasing the rate of charge transport through the nanocomposite film due to the aggregation of gold nanorods. The effect of gold nanorod aggregation on the ECL intensities of Os metallopolymer was analysed by the simultaneous detection of current and ECL intensity of metallopolymer-gold nanorod composite films with different molar ratios of Au NR:Os using 0.1 M tripropyl amine as the co-reactant. The working electrode was scanned at a rate of 100 mVs^{-1}.

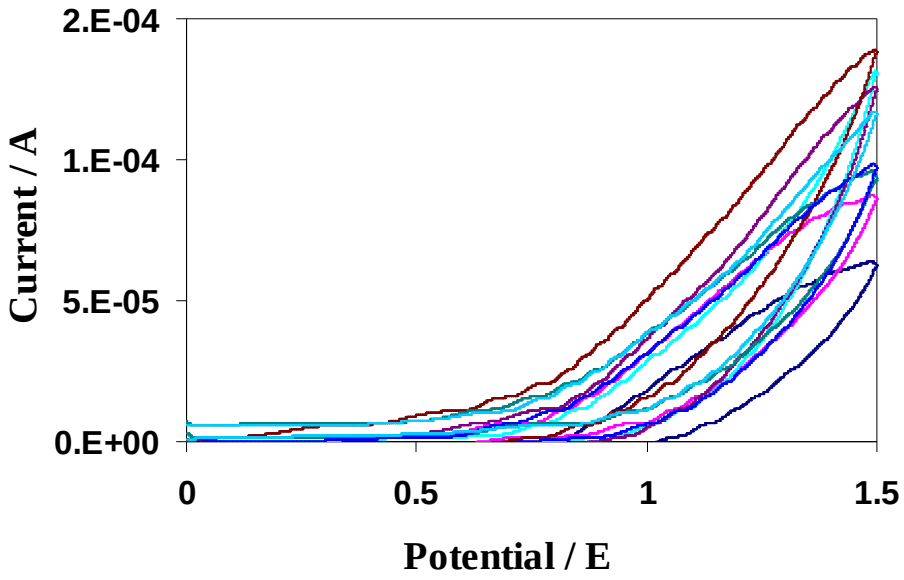

Figure 5.13: Voltammetric response of osmium metallopolymer-gold nanorod composite films on 3 mm glassy carbon electrode with various Au NR:Os molar ratios of 0 (—- dark blue line), 0.185×10^{-5} (—- pink line), 0.74×10^{-5} (—- violet line), 0.925×10^{-5} (—- brown line), 1.11×10^{-5} (—- turquoise line) and 1.295×10^{-5} (—- blue line), respectively. . The surface coverage of Os metal centres is 5×10^{-9} mol/cm^2.

Figure 5.13 shows the voltammogram obtained for the osmium metallopolymer-nanocomposite films at different molar ratio of Au NR:Os recorded at a scan rate of 100 mVs^{-1}. The voltammograms obtained at different molar ratios of Au NR:Os shows that no systematic change in the amount of current produced at the electrode is noticed irrespective of the loading on gold nanorods. Figure 5.14 shows the ECL

response obtained from the glassy carbon electrodes modified with osmium metallopolymer nanocomposite films at different molar ratios of Au NR:Os.

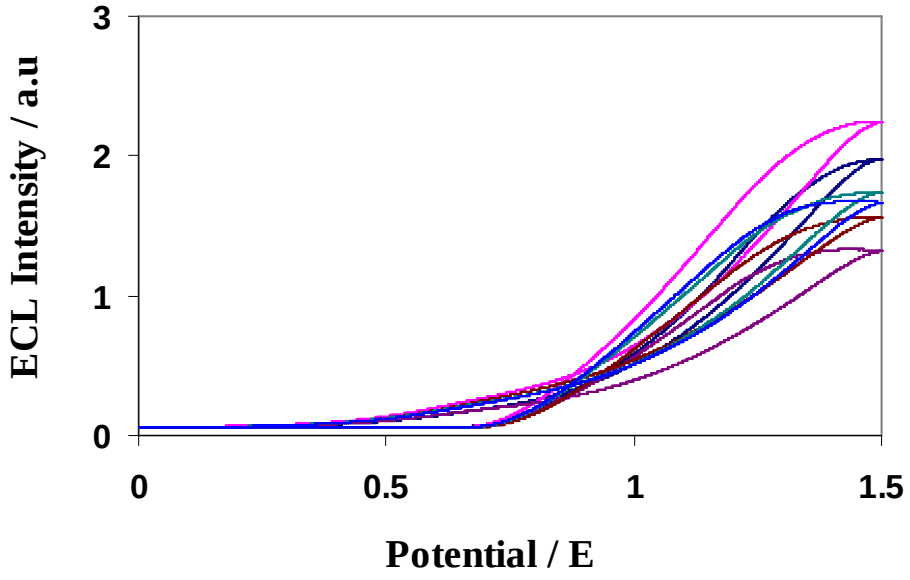

Figure 5.14: ECL emission intensity obtained from glassy carbon electrodes modified with osmium metallopolymer composite formed by loading various amounts of gold nanorods with Au NR:Os molar ratios of 0 (—- dark blue line), 0.185×10^{-5} (—- pink line), 0.74×10^{-5} (—- violet line), 0.925×10^{-5} (—- brown line), 1.11×10^{-5} (—- green line) and 1.295×10^{-5} (—- blue line), respectively.

Figure 5.14 shows the ECL intensity of 20 μM $[Os(bpy)_2PVP_{10}]^{2+}$ metallopolymer and metallopolymer gold nanorod composite at different Au NR:Os molar ratios formed by incorporating various amounts of C_{16}TAB-protected gold nanorods. The loading of gold nanorods is expected to result in two different processes in the nanocomposite films. A well-defined spectral matching between the absorption of gold nanorods and emission of osmium metallopolymer might result in metal enhanced fluorescence effect.

However, it is observed from the ECL response of osmium metallopolymer nanocomposite films that despite a small fluctuation at the initial loading of the nanorods, no considerable enhancement in the ECL generation were observed despite of the greater spectral overlap. This could be attributed to the lack of participation of

gold nanorods in the electrochemical process. Due to this, the percentage of electrochemically active surface area of gold is reduced greatly and hence no significant change is observed in the charge transport through the nanocomposite films even in the presence of gold nanorods and hence the ECL emission.

5.4. Conclusion

Metallopolymer-gold nanorod composites were formed by mixing the $[Os(bpy)_2PVP_{10}]^{2+}$ polymer with the C_{16}TAB-protected gold nanorods. The loading of C_{16}TAB-protected gold nanorods is found to quench the luminescence of the metallopolymer. The quenching efficiency is found to be 72% at a Au NR:Os molar ratio of 1.5×10^{-3}. No severe increase in the charge transport of the metallopolymer-gold nanorod composite due to the gold nanorod loading is observed and hence in the ECL emission intensities. It is found that the redox matching and /or the possibility of achieving a communication between the gold nanorods and the polymer backbone are essential for electrochemically activating the gold in the metallopolymer nanocomposite films for achieving enhanced ECL emission.

5.5. References

1 Dennany, L.; Keyes, T. E.; Forster, R. J. *Analyst*, **2008**, 133, 753.

2 Shen, L.; Li, X.; Qi, H.; Zhang, C.; *Luminescence*, **2008**, 23, 370.

3 Forster, R. J.; Vos, J. G.; *Macromolecules*, **1990**, 23, 4372.

4 Dennany, L.; Forster, R. J.; Rusling, J. F.; *J. Am. Chem. Soc*. **2003**, 125, 5213.

5 Wang, B.; Rusling, J. F.; *Anal. Chem.* **2003**, 75, 4229.

6 Dennany, L.; Forster, R. J.; White, B.; Smyth, M.; Rusling, J. F. *J. Am. Chem. Soc*. **2004**, 126, 8835

7 Lakowicz, J. R. *Principles of Fluorescence Spectroscopy*, Kluwer Academic/ Plenum Press, New York, **1999.**

8 Forster, R. J.; Bertoncello, P. Keyes, T. E. *Annu. Rev. Anal. Chem*. **2009**, 2, 359.

9 Creutz. C.; Chou. M.; Netzel. T.; Okumara. M.; Sutin. N. *J. Am. Chem. Soc.***1980**, 102:1309

10 Huang, T.; Murray, R. W. *Langmuir*. **2002**, 18, 7077.

11 Liu, X.; Niu, W.; Li, H.; Han, S.; Hu, L.; Xu, G. *Electrochem. Commun*, **2008,** 10, 1250.

12 Wang, J., Yang, Z.; Wang, X.; Yang, N. *Talanta*, **2008**, 76, 85.

13 Lv, B.; Ren, A.; Luo, Y.; Yuan, H.; Xiao, D. *Russ. J. Electrochem.*, **2008**, 44, 1047.

14 Chen, Z.; Zu, Y. *Langmuir*, **2007,** 23, 11387.

15 Guo, H.; Ruan, F.; Lu. L.; Hu, J.; Pan, J.; Yang, Z.; Ren, B. *J. Phys. Chem. C*. **2009**, 113, 10459.

16 Sau, T. K.; Murphy, C. J. *Langmuir*, **2004**, 20, 6414.

17 Forster, R. J.; Keane, L. *J. Electroanal. Chemistry*, **2003**, 554-555, 345

18 Tam, K. C.; Wyn-Jones, E. *Chem. Soc. Rev*, **2006**, 35, 693.

19 Gandubert, V. J.; Lennox, R. B. *Langmuir*, **2005**, 21, 6523.

20 Ali Omar, A.; Oyama, M. *Cryst. Growth. Des.* **2006**, 6, 818.

21 Lippert, J. L.; Brandt, E. S.; *Langmuir*, **1988**, 4, 127.

22 Alkilany, A. M.; Nagaria, P. K.; Hexel, C. R.; Shaw, T. J.; Murphy, C. J.; Wyatt, M. D. *Small*, **2009**, 5, 701.

23 Alkilany, A. K.; Nagaria, P. K.; Wyatt, M. D.; Murphy, C. J. *Langmuir*, **2010**, 26, 9328.

24 Gittins, D. I.; Caruso, F. *Angew. Chem. Int. Ed*. **2001**, 40, 3001.

25 Wei, Q.; Ji, J.; Shen, J. *Macromol. Rapid. Commun*. **2008**, 29, 645.

26 Sokolov, K.; Chumanov, G.; Cotton, T. M. *Anal. Chem*. **1998**, 70, 3898.

27 Lakowicz, J. R.; Malicka, J.; Gryczynski, I. *Anal. Biochem*. **2003**, 36, R240.

28 Navon, G.; Sutin, N. *Inorg. Chem.*, **1974**, 13, 2159.

29 Sharma, T. K.; Chowdury, D.; Paul, A.; Chattopadyay, A. *Chem. Comm*. **2002**, 1048

30 Breimer, M. A.; Yevgeny, G.; Sy, S.; Sadik, O. A. *Nano. Lett*. **2001**, 1, 305.

31 Bard, A.J.; Faulkner, L.R. *Electrochemical Methods: Fundamental and Applications*, 2nd ed.; Wiley, New York, **2001**.

Chapter 6

ECL biosensor for the detection of NADH

6.1. Introduction

Nicotinamide adenine dinucleotide is an essential co-enzyme that is found in every cell of living organisms and it plays a major role in respiratory and metabolic process.[1] The reduced and oxidised forms, NADH and NAD^+, are the key charge carriers in living cells. More than 300 enzymes are involved in cellular growth, differentiation and energy metabolism that depend on NADH.[2,3] Hence, it is important to develop a highly sensitive NADH sensor, which can provide information on numerous applications including clinical biology, food industry and bioprocess monitoring.

Electrochemical techniques are attractive for studying the redox reactions of the NADH/NAD^+ redox couple and their detection.[4] Amperometric techniques have been widely used for the detection of NADH[5] but these approaches are limited by the high overpotential for oxidising NADH and problems associated with electrode fouling.[6] Hence, considerable efforts have been devoted to reduce the overpotential for NADH oxidation by modifying the electrode surface with mediators.[7,8,9] Electrodes modified with mediators such as carbon nanotubes,[10,11] CdS nanoparticles[12] and nanostructured TiO_2[13] showed satisfactory improvement in NADH detection. It has been demonstrated that an electrode modified with a graphite/polymethylmethacrylate composite improved the electron transfer rates and hence a lower limit of detection of about 3.5 μM for NADH were achieved.[5]

Gold nanoparticles have been increasingly used to construct biosensors due to their ability to immobilise biomolecules while preserving the catalytic activity of those biomolecules. Moreover, ruthenium polypyridyl complexes can be used to re-oxidise NADH leading to ECL.[14] Through oxidative-reduction pathway process, ECL signals can be generated from ruthenium polypyridyl complexes using NADH as the co-reactant.[15] This process was explained earlier in detail in Chapter 1 (Figure 1.12).

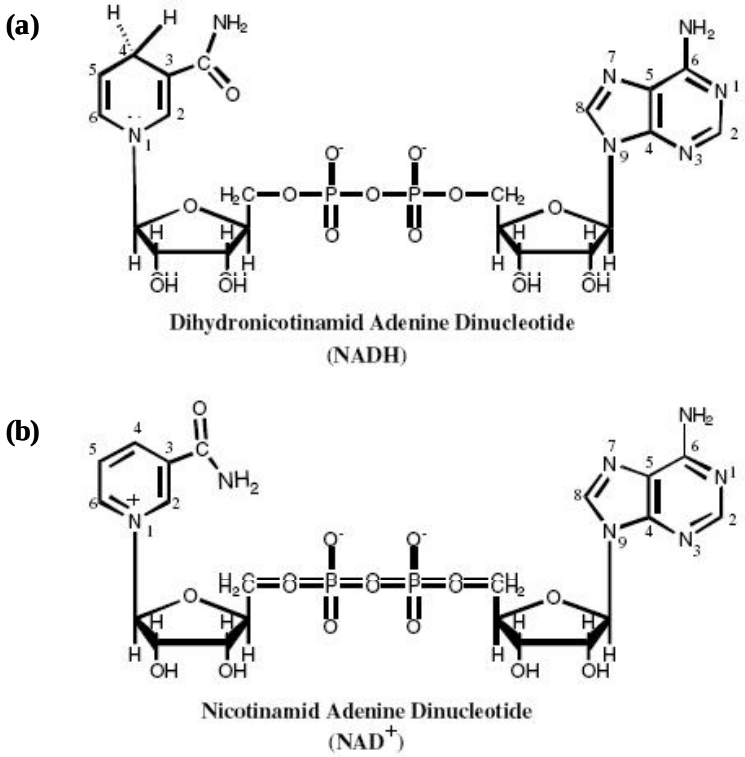

Figure 6.1: Chemical structure of reduced (NADH) and oxidised (NAD^+) form of Nicotinamide adenine dinucleotide. Adapted from *J. Photochem. & Photobiology B: Biology*, **2005**, 81, 76.

It has been reported that only the reduced form, NADH, initiates ECL reactions in ruthenium complexes. Figure 6.1 shows the chemical structure of the reduced (NADH) and oxidised (NAD^+) forms of nicotinamide adenine dinucleotide.[16] The aromaticity of the pyridine ring is lost in the reduced form and hence the aliphatic tertiary amine group undergoes ECL generation in presence of ruthenium complexes (Figure 6.1a). By contrast, the oxidised form of NADH does not interact with ruthenium complexes to generate ECL signals due to the presence of pyridine group (Figure 6.1b) in NAD^+.[17] Moreover, the oxidised form of the co-reactants is incapable of reducing Ru^{3+} to the excited state Ru^{2+*} so as to generate ECL.

The detection of NADH using ECL is attractive because lower limits of detection could be compared with other detection methods due to the higher sensitivity and lower signal to noise ratio of ECL detection methods. Enhancing the ECL characteristics of ruthenium metallopolymer lower detection limits can be achieved.

Figure 6.2 shows the scheme representing the ECL emission from Ru metallopolymer-gold nanoparticle composite using NADH as co-reactant.

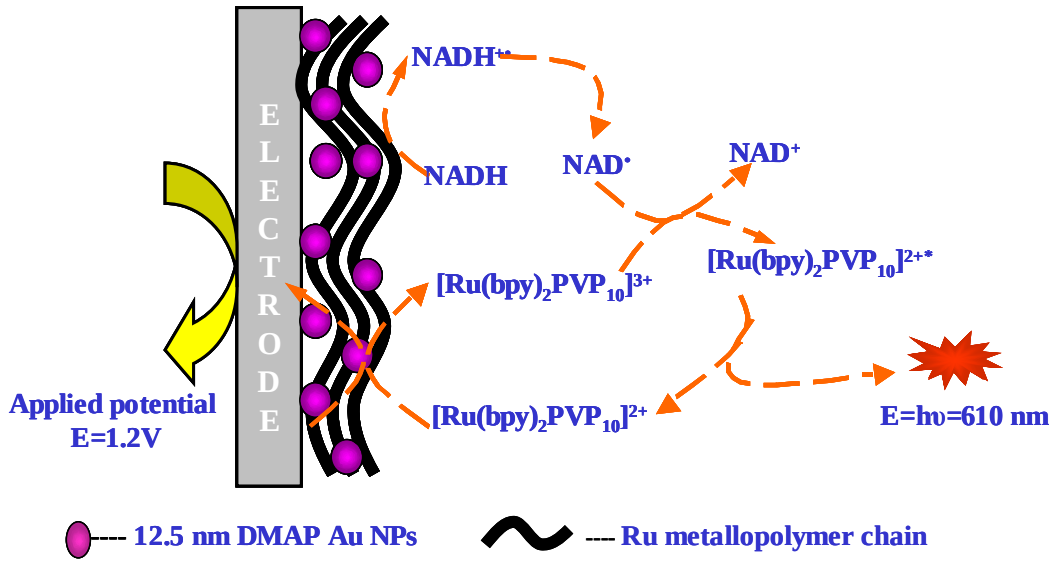

Figure 6.2: Scheme representing the ECL generation from a Ru metallopolymer-gold nanoparticle composite using NADH as co-reactant.

A major part of the work presented in this thesis has been devoted to studying the influence of gold nanoparticles on the charge transport and emission properties of ruthenium/osmium metallopolymers. It has been demonstrated in Chapter 4 that the presence of gold nanoparticles in a ruthenium metallopolymer $[Ru(bpy)_2PVP_{10}]^{2+}$, could enhance charge transport when the samples are prepared as thin films on glassy carbon electrode. It has also been demonstrated that incorporating 12.5 nm DMAP-protected gold nanoparticles within RuPVP at a molar ratio of 1.02×10^{-2} could enhance the ECL intensity by a factor of seven where the co-reactant is 0.1 M tripropyl amine (TPrA). Here, the possibility of exploiting these enhanced ECL properties to detect biomolecules has been explored.

In this chapter, the ECL emission intensities were monitored at different concentration of NADH ranging from 1 mM to 10 fM. The ECL response obtained from electrodes modified with pure ruthenium metallopolymer and metallopolymer-gold nanocomposite films were compared. Finally, the limits of detection and the sensitivity of this approach are presented.

6.2. Experimental

6.2.1. Materials

β-Nicotinamide adenine dinucleotide, reduced disodium hydrate (97%) was purchased from Sigma-Aldrich. $[Ru(bpy)_2PVP_{10}](ClO_4)_2$ and 12.5 nm DMAP-protected gold nanoparticles were synthesised and characterised as described in Chapters 2 and 3, respectively. 3 mm glassy carbon electrodes were purchased from IJ Cambria Scientific Ltd. Alumina powder (0.3 μm and 0.05 μm) was from Buehler. Dimethylformamide (99%) and sodium hydroxide (97%) were obtained from Sigma-Aldrich. All the chemicals were used as received. The aqueous solutions were prepared from Milli-Q reagent water (Millipore Corp.,), 18 MΩ cm.

6.2.2. Surface Modification of Electrodes

The solutions of ruthenium metallopolymer and gold nanoparticles were mixed to form the nanocomposite. Micromolar aqueous solutions of $[Ru(bpy)_2PVP_{10}]^{2+}$ metallopolymer and metallopolymer nanocomposites with different molar ratios ranging from 4.1×10^{-3} to 1.64×10^{-2} were formed by incorporating 12.5 nm DMAP-protected gold nanoparticles. The metallopolymer nanocomposites and the corresponding films were formed by the standard procedure as described in Chapter 4.

The ECL detection of NADH was carried out using the modified electrode with different molar ratios of ruthenium to gold nanoparticles. Since β-NADH solutions are susceptible to oxidation even at low temperatures, the solutions were prepared using 0.01 M NaOH (pH >9) and stored at 2-5° C when not in use. The concentration of β-NADH was varied from 1 mM to 10 fM to determine the limit of detection of the surface modified electrode at the optimal molar ratio between ruthenium metal centres and gold nanoparticles.

6.3. Results and Discussion

6.3.1. Absorption and Emission Spectroscopy

β-Nicotinamide adenine dinucleotide (β-NADH) exists in both the oxidised state (NAD^+) and reduced state (NADH) in cellular respiratory and metabolic processes.[18] Depending on its oxidation state, β-nicotinamide adenine dinucleotide shows two different transitions in the UV-Visible absorption spectrum. Figure 6.3 shows the absorption and emission spectrum of β-nicotinamide adenine dinucleotide.

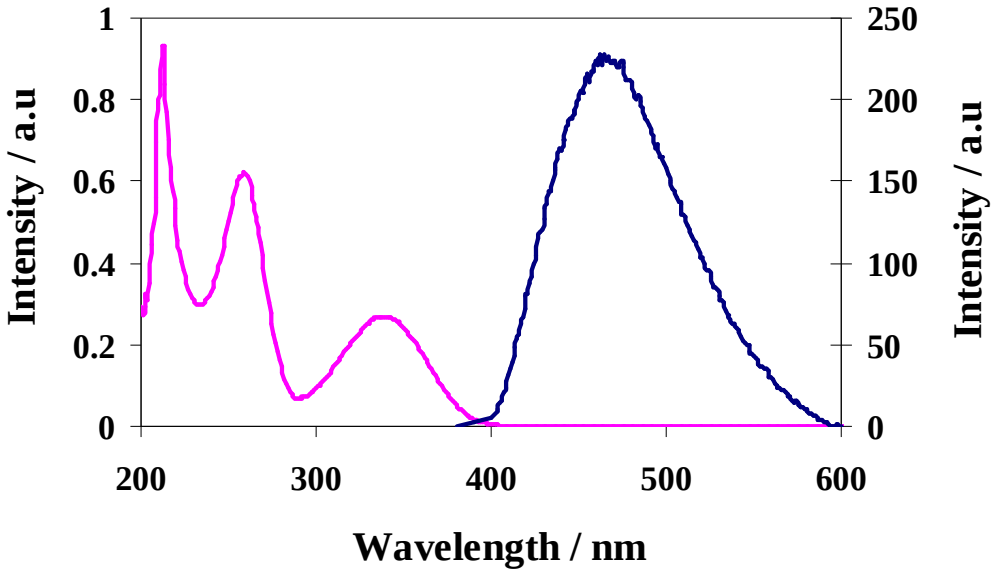

Figure 6.3: UV-Vis-NIR absorption (—-pink line) and luminescence (—-blue line) spectrum of β-nicotinamide adenine dinucleotide, reduced disodium salt in 0.01 M NaOH solution. The concentration of β-nicotinamide adenine dinucleotide is 120 μM.

It is well known that adenine bases absorb strongly in the ultra violet region. The electronic transitions of β-nicotinamide adenine dinucleotide show intense absorptions peaks at 259 nm and 340 nm.[19] The presence of absorption peak around at 340 nm is due to the presence of NADH state and that of 259 nm confirms the existence of oxidised form (NAD^+).[20] Thus, based on the increase (with the formation of reduced NADH) and decrease (with the formation of NAD^+) in the

absorption band intensity at 340 nm, enzymatic activities can be easily estimated.[18] The molar extinction coefficient of β-nicotinamide adenine dinucleotide at 340 nm and 259 nm is found to be around 6.22×10^3 M^{-1} cm^{-1} and 14.4×10^3 M^{-1} cm^{-1} (pH 9.5), respectively (Sigma Aldrich).

Figure 6.3 also shows the luminescence obtained for 120 μM β-nicotinamide adenine dinucleotide, reduced disodium solution in 0.01 M NaOH upon excitation at 340 nm. The luminescence observed around 460 nm upon excitation at 340 nm corresponds to the reduced form (NADH). However, exciting at 259 nm does not show any luminescence. This is in agreement with earlier reports on non-emissive nature of the oxidised form (NAD^+).[21]

6.3.2. Electrochemistry

The solution phase electrochemical properties of NADH were studied by cyclic voltammetry using a conventional three-electrode system. As the acidic solutions tend to decompose, a 1 mM solution was prepared by dissolving the estimated amount of β-NADH in 0.01 M NaOH. A 3 mm glassy carbon electrode was used as the working electrode, cleaned as described in Section 6.2.3. Figure 6.4 shows the cyclic voltammetric response of 1 mM β-NADH in 0.01 M NaOH.

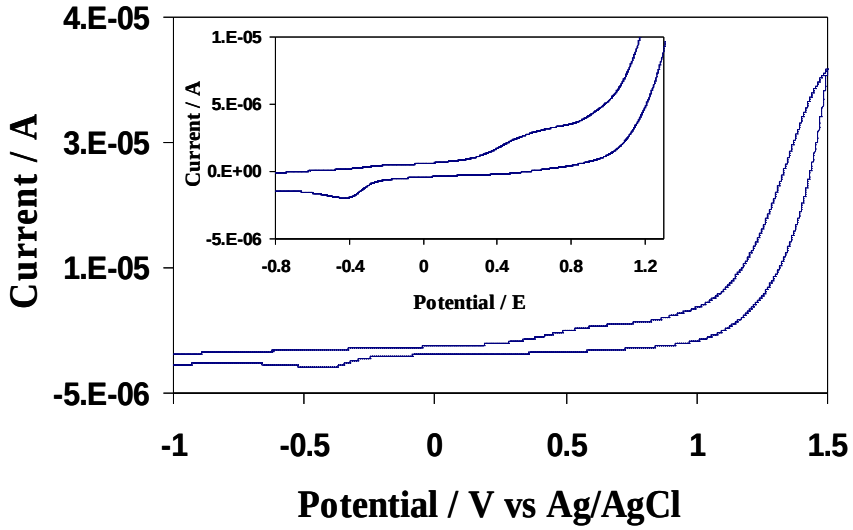

Figure 6.4: Voltammetric response of 1 mM β-nicotinamide adenine dinucleotide, disodium salt solution in 0.01 M NaOH. The inset shows an expanded view of NAD^+ reduction (-0.4 V) and oxidation of NADH (+0.7V). The electrode was scanned at a rate of 0.005 Vs^{-1}.

As the electrochemiluminescence of β-nicotinamide adenine dinucleotide greatly depends on the reduced state NADH, knowledge on the electro generation of $NADH/NAD^+$ is essential. Hence, an attempt was made to study the redox potentials of β-nicotinamide adenine dinucleotide, reduced disodium salt solution. The electrode was scanned between –1 V and +1.5 V. Gorton and co-workers have already demonstrated that both the oxidation of NADH and reduction of NAD^+ show pronounced irreversibility with overpotentials in the range of up to 1 V.[22] The

oxidation of NADH involves radical intermediates, electrode fouling and interfering background currents in the real sample and hence it is not likely to be regenerated.[23,24]

The voltammogram of 1 mM NADH (Figure 6.4) clearly shows two distinct peaks. The cyclic voltammogram shows that the anodic and cathodic peak potentials are widely separated, which confirms the irreversible nature of NAD^+/NADH redox couple.[22] The oxidation of NADH at the bare electrode appears to occur via two successive electron transfer steps. The overall reaction can be represented as follows:

$$NADH \rightarrow NAD^+ + H^+ + 2e^- \quad \text{……(6.1)}$$

The possible mechanism that corresponds to the oxidation of NADH redox reaction can be explained as follows.[25]

$$NADH \xrightarrow{-e^-} NADH^{\bullet +} \quad (E^0 = \sim 0.7\ V) \text{……(6.2)}$$

$$NADH^{\bullet +} \rightarrow NAD^{\bullet} + H^+ \quad \text{……(6.3)}$$

$$2NAD^{\bullet} \rightarrow NAD_2 \rightarrow 2NAD^+ + 2e^- \quad (E^0 = \sim -0.4\ V) \text{……(6.4)}$$

The possibility of oxidising NADH at 0.7 V is attractive in the case of ECL generation. Upon applying a potential, the oxidation of NADH resulted in an oxidised peak with an anodic potential of about 0.65 V *versus* Ag/AgCl. The peak that appears around –0.4 V corresponds to the re-reduction of NAD^+ to NADH.[26] It has been reported by Clark *et al* that the thermodynamic redox potential for NADH/NAD^+ redox couple was estimated to be –0.315 V vs NHE in neutral aqueous solution.[27] As the potential for NAD^+/NADH redox couple is relatively low (-0.3 V versus Ag/AgCl), the application of an applied potential below –0.4 V might result in interfering reactions like oxygen reduction, which would negatively impact on the reliability of a sensor system. Therefore, only the positive potential corresponding to the oxidation of NADH is further studied.

6.3.3. ECL detection of NADH

The electrochemiluminescence detection of NADH was carried out using modified glassy carbon electrodes. Electrochemiluminescence of ruthenium polypyridyl complexes in presence of NADH has been known for the past few decades.[14] Because of the presence of tertiary amine functional group in NADH, this can be used as a co-reactant for generating ECL in ruthenium polypyridyl complexes. The mechanism of ECL generation of ruthenium metallopolymer of the type $[M(bpy)_2PVP_{10}]^{2+}$, in the presence of NADH as the co-reactant occurs through oxidation-reduction[28] process that can be described as follows:

$$NADH \rightarrow NADH^{\bullet+} + e^{-} \quad \text{.....(6.5)}$$

$$[Ru(bpy)_2 PVP_{10}]^{2+} \rightarrow [Ru(bpy)_2 PVP_{10}]^{3+} + e^{-} \quad \text{.....(6.6)}$$

$$[Ru(bpy)_2 PVP_{10}]^{3+} + NADH \rightarrow [Ru(bpy)_2 PVP_{10}]^{2+} + NADH^{\bullet+} \quad \text{.....(6.7)}$$

$$NADH^{\bullet+} \rightarrow NAD^{\bullet} + H^{+} \quad \text{.....(6.8)}$$

$$[Ru(bpy)_2 PVP_{10}]^{3+} + NAD^{\bullet} \rightarrow [Ru(bpy)_2 PVP_{10}]^{2+*} + NAD^{+} \quad \text{.....(6.9)}$$

$$[Ru(bpy)_2 PVP_{10}]^{2+*} \rightarrow [Ru(bpy)_2 PVP_{10}]^{2+} + h\upsilon \quad \text{.....(6.10)}$$

As a preliminary test, electrodes were modified with different molar ratios of Au NPs:Ru, between 0 and 1.64×10^{-2}, by loading different amounts of 12.5 nm DMAP-protected gold nanoparticles. ECL emissions from ruthenium metallopolymer composites were recorded using 1 mM basic solution of β-NADH as the co-reactant. Figure 6.5 shows the ECL response of metallopolymer-gold nanocomposite modified electrodes with different Au NP:Ru molar ratios.

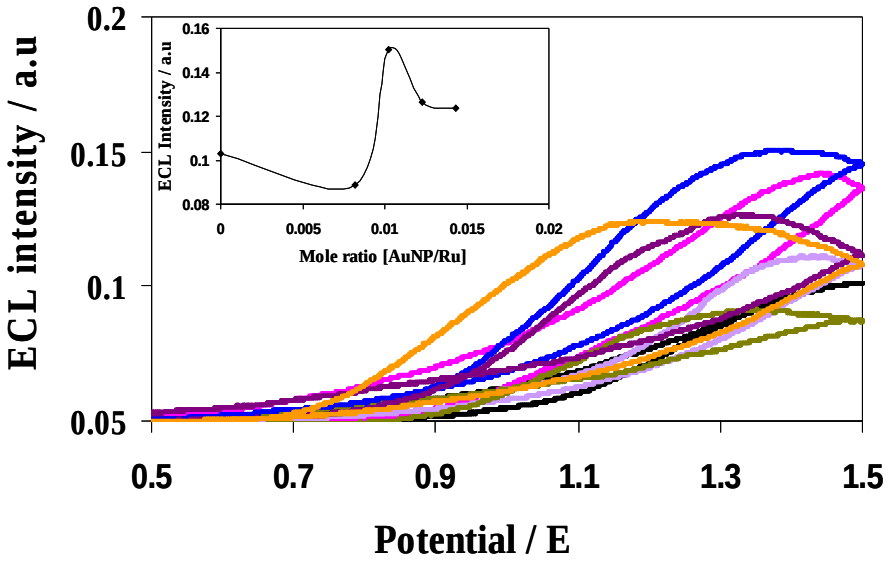

Figure 6.5: ECL emission response of 20 μM ruthenium metallopolymer (—-black line) and metallopolymer-gold nanocomposite films prepared at different molar ratios of gold nanoparticles to ruthenium metal centres from 4.1×10^{-3} (—-pink line), 8.2×10^{-3} (—-green line), 1.025×10^{-2} (—-blue line), 1.23×10^{-2} (—-purple line) and 1.435×10^{-2} (—-orange line), respectively. The ECL emission was recorded in the presence of 1 mM β-NADH as the co-reactant in 0.01 M NaOH solution. Inset shows the plot of ECL intensity *versus* molar ratios of Au NP:Ru.

It has been already reported that gold nanoparticle loading in a ruthenium metallopolymer matrix results in quenched luminescence (Section 4.3.4). In striking contrast, the increase in the charge transport rate through metallopolymer nanocomposite films enhanced the rate of electro-generation of $Ru^{2+/3+}$ moieties by enhancing the film conductivity, which resulted in brighter ECL emission (Section 4.3.6). This shows that the enhancement in the charge transport is dominating over the quenching nature of gold nanoparticles and hence brighter ECL emission is observed at intermediate Au loadings. It has been already shown that the nanocomposites developed using 12.5 nm DMAP-protected gold nanoparticles shows maximum enhancement in the ECL emission. Thus this nanocomposites were developed using 12.5 nm gold nanoparticles for detecting NADH.

Similarly in the ECL-based detection of NADH, it has been observed that the nanocomposite film prepared with an AuNP: Ru molar ratio of 1.025×10^{-2} shows the most intense ECL emission in the presence of 1 mM β-NADH as the co-reactant. This corresponds to approximately 95 ruthenium metal centres per gold nanoparticle. This is in agreement with the electrochemical studies on ruthenium metallopolymer-gold nanoparticle composites reported in Section 4.3.7 in Chapter 4.

The ECL emission intensity was recorded for the electrodes modified with pure ruthenium metallopolymer and metallopolymer-nanocomposite formed by dispersing gold nanoparticles at an Au NP:Ru molar ratio of 1.025×10^{-2}. Table 6.1 lists the average ECL intensities obtained for pure ruthenium metallopolymer film on glassy carbon electrode at various concentrations of β-NADH.

Table 6.1: ECL emission response of pure 20 μM $[Ru(bpy)_2PVP_{10}]^{2+}$ metallopolymer film at different concentrations of β-NADH.

Concentration of β-NADH (M)	Average ECL Intensity (a.u)	Standard Deviation (n=3)	Standard Error
blank	0.15	0	0
1000×10^{-6}	0.48	0.06	0.035
750×10^{-6}	0.42	0.009	0.005
500×10^{-6}	0.29	0.069	0.039
1×10^{-6}	0.31	0.063	0.036
1×10^{-9}	0.24	0.046	0.026

As shown in Table 6.1, the ECL response increase for the pure metallopolymer depends linearly on the concentration of NADH over a dynamic range of 500 μM to 1 mM with a detection limit of 1 nM. The ECL emission intensity of ruthenium metallopolymer nanocomposite at the optimum Au NP:Ru molar ratio of 1.025×10^{-2} was recorded with various concentrations of β-NADH. It is observed that the ECL emission intensity decreases with increasing concentration of β-NADH.

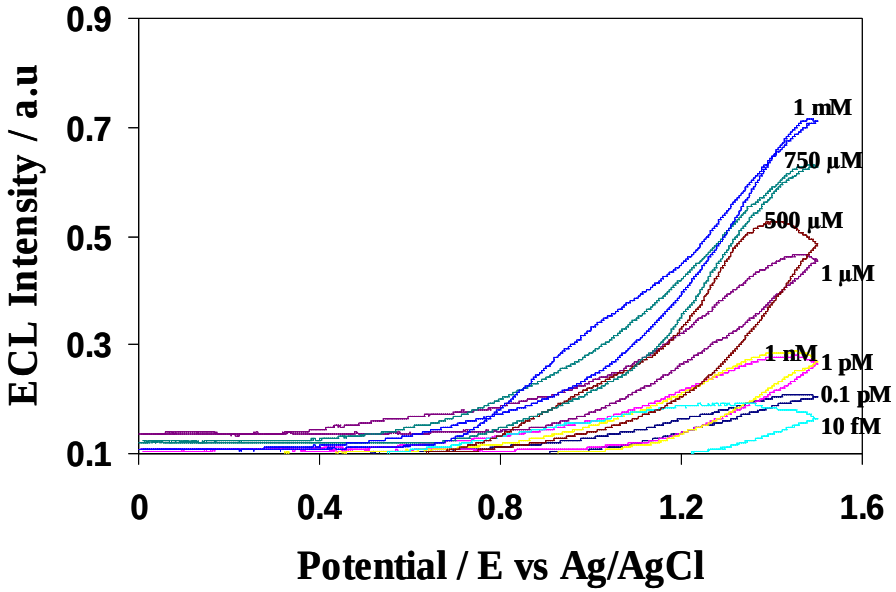

Figure 6.6: Dependency of ECL emission intensity of ruthenium metallopolymer-gold nanoparticle composite with various concentrations of β-NADH ranging from (top to bottom) 1 mM (—-blue line), 750 µM (—-green line), 500 µM (—-brown line), 1 µM (—-plum line), 1 nM (—-violet line), 1 pM (—-yellow line), 0.1 pM (—-pink line) and 10 fM (—-blue line), respectively.

The ECL emission intensity was recorded at various concentrations of β-NADH using ruthenium metallopolymer nanocomposite films formed by incorporating 12.5 nm DMAP-protected gold nanoparticles. Figure 6.7 shows the calibration curve of the maximum average ECL emission intensity of metallopolymer nanocomposite (♦) films *versus* the concentration of β-NADH.

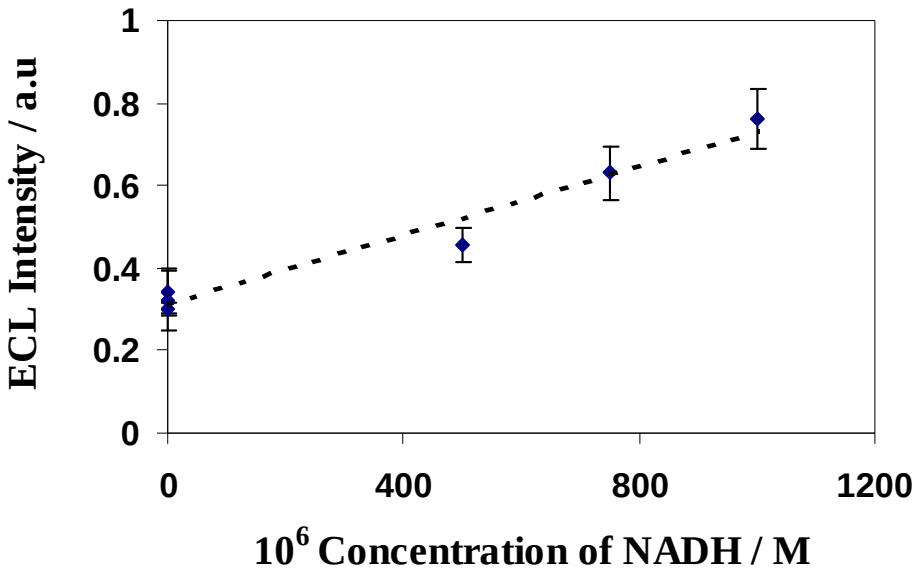

Figure 6.7: Calibration plot obtained from the ECL intensity *versus* [NADH] (various concentrations of β-NADH) for metallopolymer nanocomposite (♦) films. The ECL emission was recorded for metallopolymer-nanocomposite films at Au NP:Ru molar ratio of 1.025×10^{-2} formed on 3 mm glassy carbon electrode by drop-cast.

It is found that the presence of 12.5 nm DMAP-protected gold nanoparticles in the metallopolymer matrix enhances the emission intensity of the polymer and hence lowers the detection limit of β-NADH. Figure 6.8 shows the linear dependence of ECL emission intensity *versus* the concentration of NADH in the lower concentration range. The lower limit of detection must be greater than the sum of blank signal plus three times the standard deviation of the blank. The calibration curve shows that the ECL detection using nanocomposite-modified electrode is linear over a dynamic range of 1 μM and 1 mM. The detection limit was 10 fM. This shows that the limit of detection has been lowered due to the presence the 12.5 nm DMAP-protected gold nanoparticles.

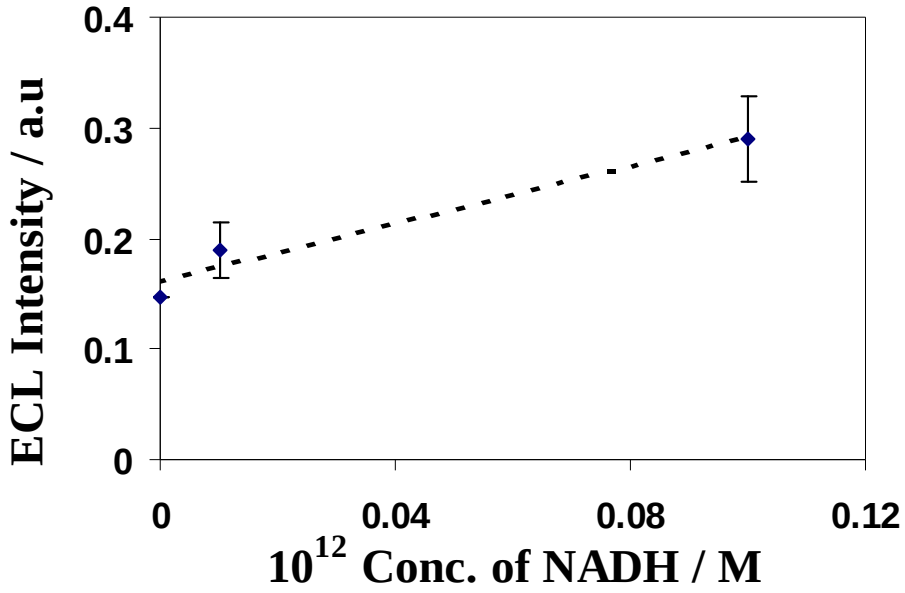

Figure 6.8: Expanded view of calibration plot obtained from the ECL intensity *versus* [NADH] for metallopolymer nanocomposite (♦) films.

This is a significant result in ECL based detection of β-NADH as the method shows nearly three orders of magnitude lower detection limit in comparison with pure metallopolymer films. Also it is found that the detection of β-NADH using metallopolymer nanocomposites shows much lower limits of detection compared to the earlier reports. Zhaung et al has reported the detection of NADH by immobilising $[Ru(bpy)_3]^{2+}$ in multi walled carbon nanotube / nafion composite membrane on a glassy carbon electrode. It was demonstrated that ECL signals can be detected over a concentration range of 1 μM to 16 μM with a detection limit of 820 nM.[29]

Dong and co workers have shown that much lower detection limits can be achieved using gold nanoparticles. They reported that using gold nanoparticles in a sol-gel network, ECL detection of NADH could be achieved as low as 1 nM.[15] Hence, much lower limits of detection can be achieved for the detection of β-NADH using ruthenium metallopolymer-gold nanocomposite films described in the present work. The higher sensitivity in the detection is significant when a quantitative analysis is required. The present work shows a sensitivity of about 1 pM sensitivity, which is a significant result in designing the biosensor for quantitative purpose. These

metallopolymer-gold nanocomposite systems can also be used to detect much more biologically important biomolecules like amino acids, antibodies etc.

6.4. Conclusion

Enhanced ECL based detection of reduced nicotinamide adenine dinucleotide (β-NADH) was demonstrated using modified electrodes. The glassy carbon electrodes were modified with ruthenium metallopolymer-gold nanocomposite films, which are formed by dispersing 12.5 nm DMAP-protected gold nanoparticles within the Ru polymer. The ECL emission intensity of $[Ru(bpy)_2PVP_{10}]^{2+}$ metallopolymer-gold nanocomposite decreases with the concentration of β-NADH. It has been demonstrated that lower limits of detection can be achieved by incorporating gold nanoparticles in the metallopolymer matrix. The detection limits achieved for the electrodes modified with nanocomposites and pure metallopolymer was 10 fM and 1 nM, respectively. The ruthenium metallopolymer nanocomposite showed nearly five orders of magnitude lower limits of detection with a sensitivity of 1 pM in comparison with the pure metallopolymer. These results are significant while designing the biosensors for the detection of biomolecular detection.

6.5. References

1 Tang, L.; Zeng, G.; Shen, G.; Zhang, Y.; li, Y.; Fan, C.; Liu, C.; Niu, C. *Anal. Bioanal. Chem*. **2009**, 393, 1677.

2 Gorton, L.; Dominguez, E. *Rev. Mol. Biotech*. **2000**, 82, 371.

3 Tang, L.; Zeng, G. M.; Wang, H.; Shen, G. L.; Huang, D. L. *Enzyme Microb Tech*. **2005**, 36, 960.

4 Balamurugan, A.; Ho, K-C.; Chen, S-M.; Huang, T-Y, *Colloids and Surfaces A: Physicochem. Eng. Aspects*, **2010**, 362, 1.

5 Dai, H.; Xu, H.; Lin, Y.; Wu, X.; Chen, G. *Electrochem. Commun*. **2009**, 11, 343.

6 Blaedel, W. J.; Jenkins,, R. A. *Anal. Chem*. **1975**, 47, 1337.

7 Bogachev, A. V.; Bertsova, Y. V.; Barquera, B.; Verkhovsky, M. I. *Biochem*. **2001**, 40, 7318.

8 Karyakin, A. A.; Ivanova, Y. N.; Revunova, K. V.; Karyakina, E. E.; *Anal. Chem*. **2004**, 76, 2004.

9 Somin, B. P.; Macanas, J.; Munoz, M.; Fabregas, E. *Talanta*, **2007**, 71, 2102.

10 Zhang, M.; Smith, A.; Gorski, W. *Anal. Chem*. **2004**, 76, 5045.

11 Chakraborty, S.; Raj, C. R.; *Electrochem. Commun*. **2007**, 9, 1323.

12 Vastarella, W.; Nicastri, R. *Talanta*, **2005**, 66, 627.

13 Curulli, A.; Valentini, F.; Padeletti, G.; Viticoli, M.; Cashera, D.; Palleschi, G. *Sens. Actuators. B.* **2005**, 111-112, 441.

14 Martin, A. F.; Nieman, T. A. *Biosens. Bioelectron*. **1997**, 12, 479.

15 Deng, L.; Zhang, S.; Shang, L.; Guo, S.; Wen, D.; Wang, F.; Dong, S. *Biosens. Bioelectron*. **2009**, 24, 2273.

16 Huang, X.; El-Sayed, I. H.; Yi, X.; El-Sayed, M. A. *J. Photochem. & Photobiology B: Biology*, **2005**, 81, 76.

17 Downey, T. M.; Nieman, T. A. *Anal. Chem.* **1992**, 64, 261.

18 Bergmeyer, H. U. *Methods of Enzymatic analysis*, Academic press, new york, **1974**, 1, 545.

19 Siegel, J. M.; *Arch. Biochem. Biophys.* **1959,** 82, 288.

20 Dawson, R. Ben. *Data for biochemical research* , **1985**, 3rd edition. Oxford: Clarendon Press. 122.

21 Lakowicz, J. R.; Szmancinski, H.; Nowaczyk, K.; Johnson, M. L. *Proc. Natl. Acad. Sci. U. S. A.* **1992**, 89, 1271.

22 Gorton, L.; Dominguez, E. *Electrochemistry of $NAD(P)^+$/NAD(P)H, in Encyclopedia of Electrochemistry*, Wilson, G. S. (Ed), Wiley-VCH, Weinheim, **2002.**

23 Jaegfeldt, H. *J. Electroanal. Chem.* **1980**, 110, 295.

24 Blaedel, W. J.; Jenkins, R. A. *Anal. Chem.* **1974**, 46, 1952.

25 Bartlett, P. *Bioelectrochemistry: Fundamentals, experimental techniques and Applications*, John Wiley & sons, **2008**, p. 161.

26 Chen, J.; Bao, J.; Cai, C.; Lu, T. *Anal Chim Acta*, 2004, 516, 29.

27 Clark, W. M. *Oxidation-reduction potentials of organic systems*, Williams and Wilkins, Baltimore, **1960**, 487.

28 Chovin, A.; Garrigue, P.; Sojic, N. *Bioelectrochemistry*, **2006**, 69, 25.

29 Zhaung, Y.; Ju, H. *Anal. Letters.* **2005**, 38, 2077.

Chapter 7

Conclusions and Future Work

7.1. Summary

This thesis focuses on developing highly sensitive electrochemiluminescence biosensors for the detection of biologically significant molecules. As the concentration of analytes and hence the biomarkers are extremely low at the early stage of any disease, an increased sensitivity and lower limits of detection are essential for successful detection. The sensitivity of ECL detection relies on several parameters and hence a complete understanding of the underlying kinetics and biomolecular interaction with ECL luminophores is essential. Thus, this work is focussed on studying the underlying charge transport mechanisms of ECL metallopolymers and nanocomposites.

Incorporation of metal nanoparticles with monomeric ECL luminophores showed an increase in the ECL intensity of luminophores.[1] A detailed investigation on such systems is significant to extend the applications of metal nanoparticles in ECL based point-of-care devices. Hence, metallopolymer-gold nanoparticle composites were developed to investigate the effects of nanoparticle incorporation on both optically and electrochemically driven emission. Ru and Os metallopolymers finds a wide range of applications in ECL biosensors due to their excellent electrochemical and photophysical properties.[2,3] The successful synthesis and basic characterisation of ECL active ruthenium and osmium-based metallopolymers are reported in Chapter 2. Future work will require the development of synthetic strategies to produce multi centred metallopolymers, which could be applicable to demonstrate the controlled generation of ECL signals at different wavelengths that could be used to detect a panel of biomolecules, i.e., multianalyte detection.

Gold nanoparticles with various size and shapes can be produced using well-established synthesis approaches. The influences of synthetic parameters on the morphology of gold nanoparticles are described in Chapter 3. Incorporating gold nanoparticles with various sizes and shapes modulated the charge transport properties

of Ru and Os based metallopolymers. It has been shown in chapter 4 that the ECL emission from luminophores increases with the loading and size of the diapersed nanoparticles. A maximum of seven-fold enhancement in the ECL emission intensity of Ru metallopolymers was observed by dispersing 12.5 nm DMAP-protected gold nanoparticles. However, the quenching nature of gold nanoparticles hinders the ECL enhancement at the higher loading and hence maximum ECL production was achieved at intermediate loadings due to the enhanced conductivity. Though the quenching nature of gold nanoparticles can be successfully used for designing quenching assays for the bio molecular detection, metal enhanced fluorescence is of our primary interest due to the possible ECL enhancement. Hence, further investigation will focus on the possibilities of reducing the quenching effects that has been observed from the nanoparticles so that the enhancement factor can be successfully increased. Also another interesting feature might be controlling the ruthenium and nanoparticles separation in the nanocomposites.

Os metallopolymer-gold nanorod composites were also developed. However, desorption of the C_{16}TAB protecting layer from the gold nanorods resulted in the formation of large aggregates. This resulted in complete insulation of gold nanorods from electrochemical activity. Moreover, the formation of aggregates affected the distribution of gold nanorods in the metallopolymer matrix and hence effective mediation of charge transport by osmium metal centres *via* gold nanorods was hindered. Thus, no ECL enhancement was achieved. It is found that the existence of a communicating network between the nanorods and metal centres is required to achieve enhanced ECL response. This leaves the possibility of continuing the research on surface modifications of gold nanorods in order to facilitate controlled dispersion that could enhance the percentage of electrochemically active area of gold nanorods.

The extension of these significant findings for the successful developmet of low-cost biosensors is crucial. Hence, the electrodes modified with ruthenium metallopolymer-gold nanocomposites were used for the detection of reduced nicotinamide adenine dinuclotide. The presence of gold nanoparticles enhanced the ECL emission intensity of Ru metal centres and hence a lower limit of detection of about 10 fM was achived with a sensitivity of 1 pM. The investigation will be

extended for the successful detection of proteins and antibodies using metallopolymers as the biomarkers.

7.2. References

1 Deng, L.; Zhang, L.; Shang, L.; Guo, S.; Wen, D.; Wang, F.; Dong, S, *Biosens. Bioelectron.* **2009**, 2273.

2 Bartlett, P. *Bioelectrochemistry: Fundamentals, experimental techniques and Applications*, John Wiley & sons, **2008**, p. 161

3 Dennany, L.; Forster, R. J.; Rusling, J. F.; *J. Am. Chem. Soc*. **2003**, 125, 5213.